A STUDY OF THE NEUTRAL FINAL STATES BETWEEN 1570 AND 1710 Mev/c^2 PRODUCED IN K^-p INTERACTIONS

Thesis

Submitted by

THOMAS BEGGS, B.Sc.,

for the degree of

Doctor of Philosophy

University of Edinburgh

MAY, 1973.

CONTENTS

C O N T E N T S (Contd.)

C O N T E N T S (Contd.)

CHAPTER 1

INTRODUCTION

The experiment described in this thesis is one which has been designed to study the isospin 0 and 1 resonances in the 1660 Mev/c^2 mass region, through an investigation of K^- meson interactions on protons, in a heavy liquid bubble chamber. Before describing the experimental technique itself, however, a brief explanation is given in this chapter of some of the particle classification schemes to provide an understanding of why this and other similar experiments have been performed.

1.1 Particle Classification - The Regge Scheme

During the past twenty years the considerable increase in the number of "elementary" particles has led to many attempts at finding some order among them in the hope that a better understanding of their nature might be gained. The situation is similar to that of the classification of the elements by Mendeleev or to the early studies of atomic spectral lines. In this latter case the empirical formulae deduced by Balmer and Rydberg were later explained by the Bohr model of the atom and the successful "quark" model may also provide a similar understanding of particle spectra.

In particle physics two main types of classification have survived - the "Regge" scheme and the "SU(3)" scheme. The first was introduced by Regge in 1959 as part of the much wider based "Regge pole" theory which has its main application in the study of particle dynamics in high energy collisions. In this scheme particles having the same isospin and strangeness were grouped in order of increasing spin, J,

and alternating parity, P, along "Regge trajectories", represented by lines on a spin versus energy squared plot or "Chew-Frautschi" plot. In figures 1.1(a), (b) the Regge trajectories linking some of the better established baryons and mesons are shown. A trajectory, which is the path of a "Regge pole" - a singularity in spin - energy squared space - gives rise to a meson bound state or resonance when it passes through an integral value of J ; for the baryons a bound state or resonance occurs when a trajectory passes through a one half integral value of J.

The discovery of resonances with large spin values seems to indicate that the linear progression may be naturally extended and predicts the existence of states with even higher spins and masses.

1.2 Symmetry Groups - SU(2)

Whereas the Regge classification groups particles of the same isospin and strangeness, the SU(3) scheme links particles with the same spin and parity but differing in isospin and strangeness. This second type of classification is based on the concept of symmetry, that is, the invariance of a particle state function with respect to certain transformations, and was developed using Group Theory methods. It has been very successful in accommodating the known mesons and baryons and in predicting the existence of new states. A brief description of its progress from the early SU(2) model, to SU(3) and eventually to SU(6), will now be given and the principal successes and failures will be outlined.

The fundamental idea underlying this classification is

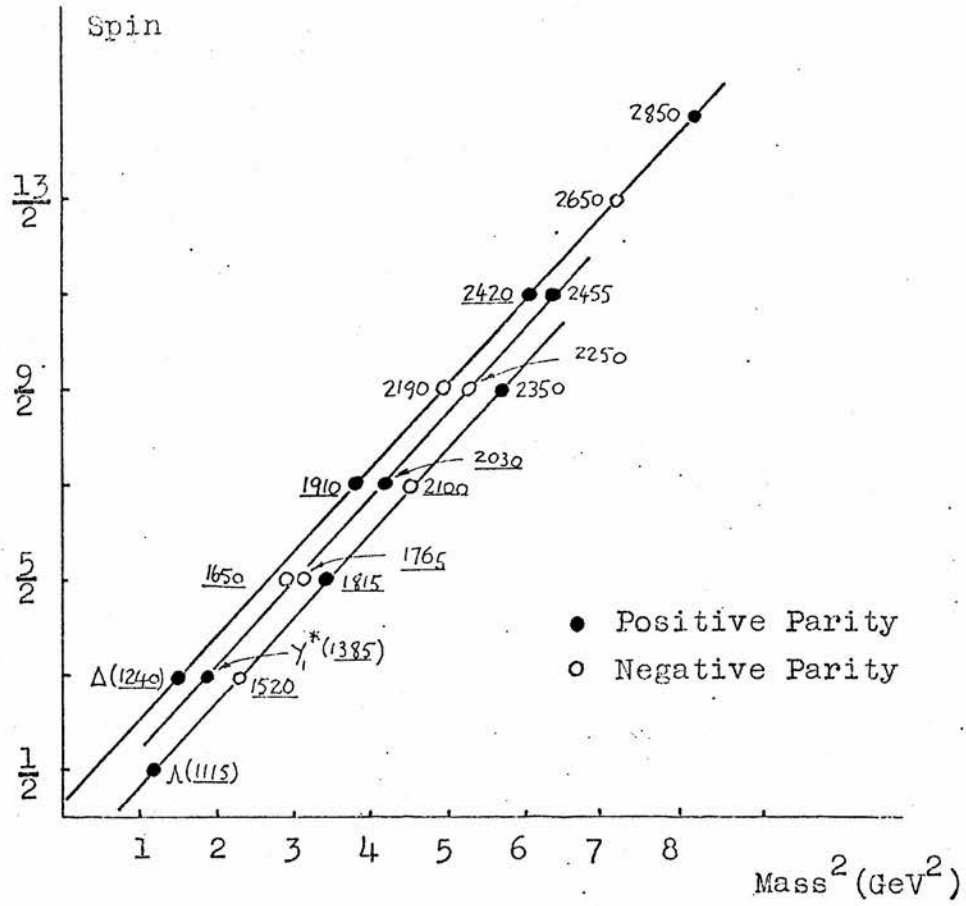

FIG. 1.1a) Plot of spin versus mass squared for a number of baryons, with Regge trajectories shown as straight lines. The particle mass is underlined if its spin and parity have been measured.

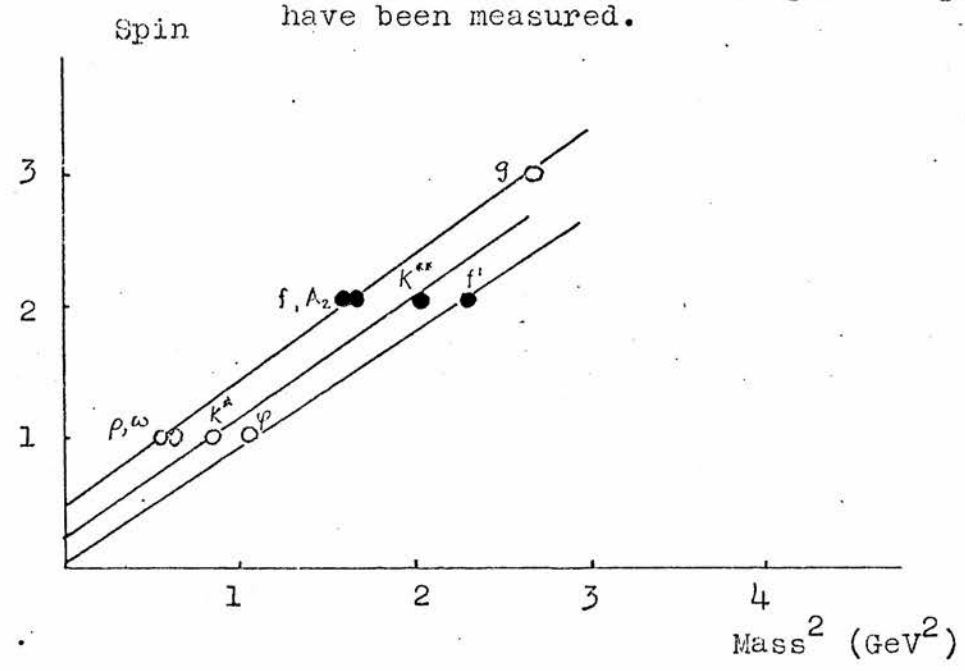

Fig. 1.1b) Plot of spin versus mass squared for a number of mesons with Regge trajectories shown as straight lines. All spins and parities have been measured.

that there exists a basic group of states from which all other states can be generated. In the early SU(2) classification, the basic multiplet was composed of the neutron and the proton which formed an isospin doublet. This choice was a reflection of the fact that the strong force seemed to be independent of charge or was "invariant under rotations in isospin space".

Ordinary rotations in 3-dimensional space are described by the action of the group of rotation operators, termed "R(3)" in group theory notation, on the angular coordinates of a particle wave function. There are an infinite number of such operators, but the situation may be simplified because each of these may be expressed in terms of only three basic operators - those of angular momentum - J_x, J_y, J_z. These are known as the "generators" of the group of space rotations and obey certain commutation laws:-

$$\left[J_x, J_y\right] = iJ_z \; ; \quad \left[J_y, J_z\right] = iJ_x \text{ , etc.}$$

They form what is known as a "Lie algebra", so called because of the pioneering group theoretical work of the Norwegian mathematician Sophus Lie in the nineteenth century.

The invariance of a Hamiltonian describing a system under rotations in 3-dimensional space can be expressed by saying that the Hamiltonian commutes with the group generators and leads to the law of conservation of angular momentum.

By analogy with the example of space rotations, the rotations in isospin space can be expressed in terms of a basic set of operators I_1, I_2 and I_3 which form the generators of the isospin rotation group and obey similar commutation rules to those of the angular momentum operators.

i.e. $[I_1, I_2] = iI_3$, etc.

They can be expressed in terms of operators τ_i, analogous to the Pauli spin operators σ_i , with $I_1 = \tau_{1/2}$ etc.

The group of rotations is called the "Special Unitary Group in two dimensions" - SU(2), because the operators, denoted U, are "special" in that they are unimodular (i.e. Det U = 1), unitary $(U^+ = U^{-1})$ and of dimension 2.

A similar law to that of the conservation of angular momentum - that of the conservation of isospin in strong interactions - arises because the strong interaction Hamiltonian commutes with the isospin rotation group generators. This implies that the neutron-proton doublet should be degenerate in energy and therefore both particles should have the same mass. This is similar to the degeneracy observed in states having the same angular momentum values. The fact that the masses are not the same is due to the "symmetry breaking" effect of the electromagnetic interaction, whose Hamiltonian does not commute with the group operators and hence gives rise to the observed small mass difference. This effect is similar to the splitting of atomic spectral lines in a magnetic field - the Zeeman effect.

From the basic isospin doublet (n,p) and its corresponding antiparticle doublet $(\bar{n},\bar{p})$ various other states can be generated. Using group notation these can be seen to form a singlet and a triplet, all with baryon number (B) = 0.

$$2 \otimes \bar{2} = 1 \oplus 3$$

		isospin 0	isospin 1	
$p\bar{n}$	$\longrightarrow \pi^+$	($I_3 = +1$: $\uparrow\uparrow$)		
$\frac{1}{\sqrt{2}}(p\bar{p} - n\bar{n})$	$\longrightarrow \pi^0$	($I_3 = 0$: $\uparrow\downarrow$)		$I = 1$
$n\bar{p}$	$\longrightarrow \pi^-$	($I_3 = -1$: $\downarrow\downarrow$)		
$\frac{1}{\sqrt{2}}(p\bar{p} + n\bar{n})$	$\longrightarrow \eta^0$	($I_3 = 0$: $\downarrow\uparrow$)		$I = 0$

The triplet states were immediately identified with the π^+, π^0 and π^- mesons, and the singlet with the η^0 meson, although at the time that this scheme was proposed by Fermi and Yang in 1949, the η^0 had not yet been found.

1.3 The SU(3) Group

The discovery of strangeness meant that the SU(2) scheme could no longer adequately describe the "elementary" particle spectrum, and so it was extended to become SU(3). In this case the basic multiplet became a triplet which contained the original neutron-proton doublet with zero strangeness quantum number, and included another particle with non-zero strangeness, taken to be the Λ hyperon ($S = -1$).

The original set of three 2×2 Pauli matrices of SU(2) now became a set of eight traceless 3×3 matrices which formed the generators of the group. The operators transformed the basic states into each other by producing rotations in isospin - hypercharge space, where hypercharge, Y, is related to the strangeness, S, and the baryon number, B, by the equation

$$Y = S + B .$$

These rotations can be illustrated by constructing a set of three axes, labelled "I-spin", "U-spin" and "V-spin" at 120° to each other. Along the I-spin axis hypercharge, Y, remains constant but charge varies (i.e. $p \longrightarrow n$ transitions). Along the U-spin axis charge is constant but Y

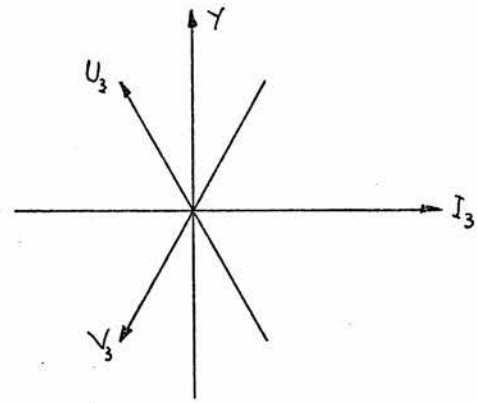

varies (i.e. $n \longrightarrow \Lambda$ transitions). There is no simple interpretation of the V-spin axis along which $p \longrightarrow \Lambda$ transitions occur.

A model of this type was proposed by Sakata in 1956. In a way analogous to that of SU(2) the meson states were generated by pairing the particle and antiparticle components of the basic triplet. In this case a singlet and an octet were formed.

$$3 \otimes \bar{3} = 1 \oplus 8 .$$

This can be shown graphically by representing the triplet and antitriplet states on a $Y - I_3$ "weight" diagram.

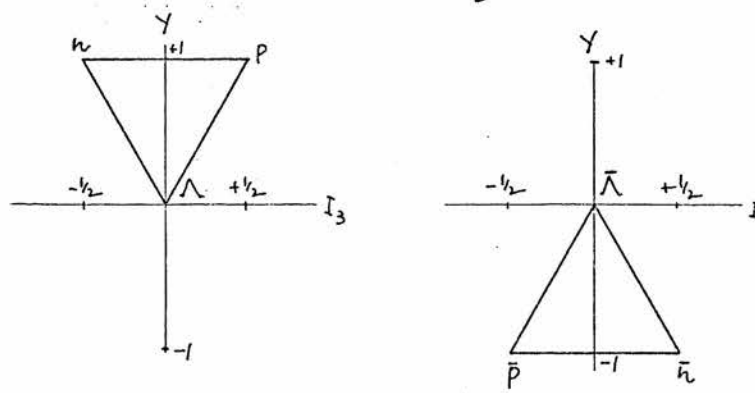

triplet antitriplet

The octet and singlet can be formed by placing the centre of gravity of one triplet on each member state of the other triplet in turn:-

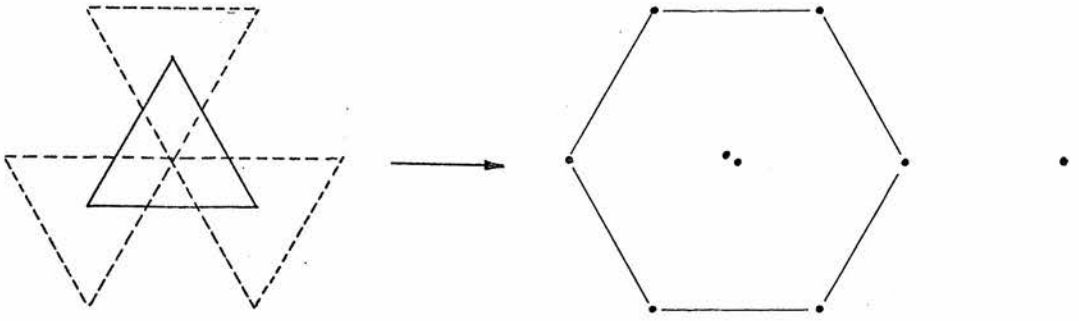

$3 \otimes 3$ $8 \oplus 1$

The resultant states can be associated with the pseudoscalar $J^P = 0^-$ mesons as shown:-

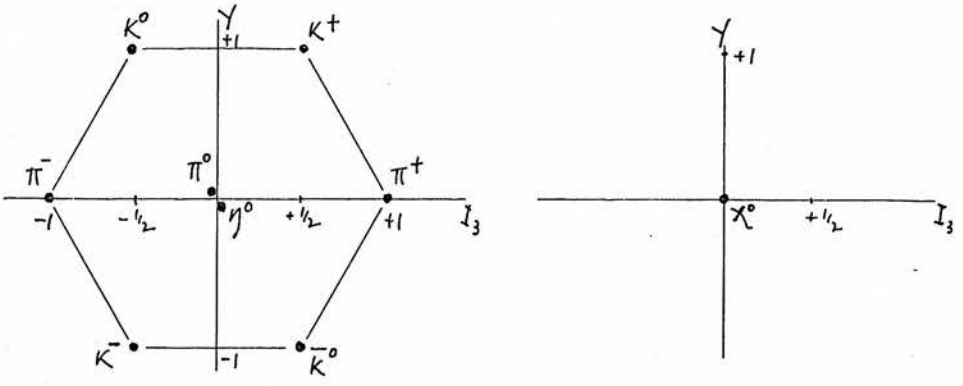

Octet Singlet

The other baryons were formed by combining the fundamental baryon triplet with the meson octet to form a "second generation" multiplet.

The Sakata model, although it worked well for the pseudoscalar mesons, fell out of favour for various reasons, one of these being the fact that it predicted the spin and parity of the Σ as $\frac{1}{2}^-$, whereas it was found experimentally to be $\frac{1}{2}^+$.

1.4 The Eightfold Way and Quark Model

Another classification based on SU(3) symmetry was that of the "Eightfold way" or "Octet" model introduced by Gell-Mann and independently by Ne'eman in 1961. In this model the J^P $\frac{1}{2}^+$ baryons also formed an octet. Such a scheme can be realised by postulating an elementary triplet composed, not of baryons as in the Sakata model, but of hypothetical particles called "quarks" which have non-integral baryon number. (This suggestion was made by Gell-Mann and Zweig in 1964.) The triplet was composed of 'p', 'n' and 'Λ' quarks, the nomenclature of the Sakata scheme being retained, having the quantum numbers as shown below:-

	I_3	Y	B	S	Q
n	$-\frac{1}{2}$	$\frac{1}{3}$	$\frac{1}{3}$	0	$-\frac{1}{3}$
p	$\frac{1}{2}$	$\frac{1}{3}$	$\frac{1}{3}$	0	$\frac{2}{3}$
Λ	0	$-\frac{2}{3}$	$\frac{1}{3}$	-1	$-\frac{1}{3}$
$\bar{n}$	$\frac{1}{2}$	$-\frac{1}{3}$	$-\frac{1}{3}$	0	$\frac{1}{3}$
$\bar{p}$	$-\frac{1}{2}$	$-\frac{1}{3}$	$-\frac{1}{3}$	0	$-\frac{2}{3}$
$\bar{\Lambda}$	0	$\frac{2}{3}$	$-\frac{1}{3}$	1	$\frac{1}{3}$

The quantum numbers of the antiquark triplet are also shown.

The meson states were formed by the product of a quark and an antiquark to form a singlet and an octet as before, and the baryons by the product of 3 quarks, to produce a

singlet, two octets and a decuplet.

i.e. $3 \otimes 3 \otimes 3 \longrightarrow 1 \oplus 8 \oplus 8 \oplus 10$.

This again can be shown geometrically:-

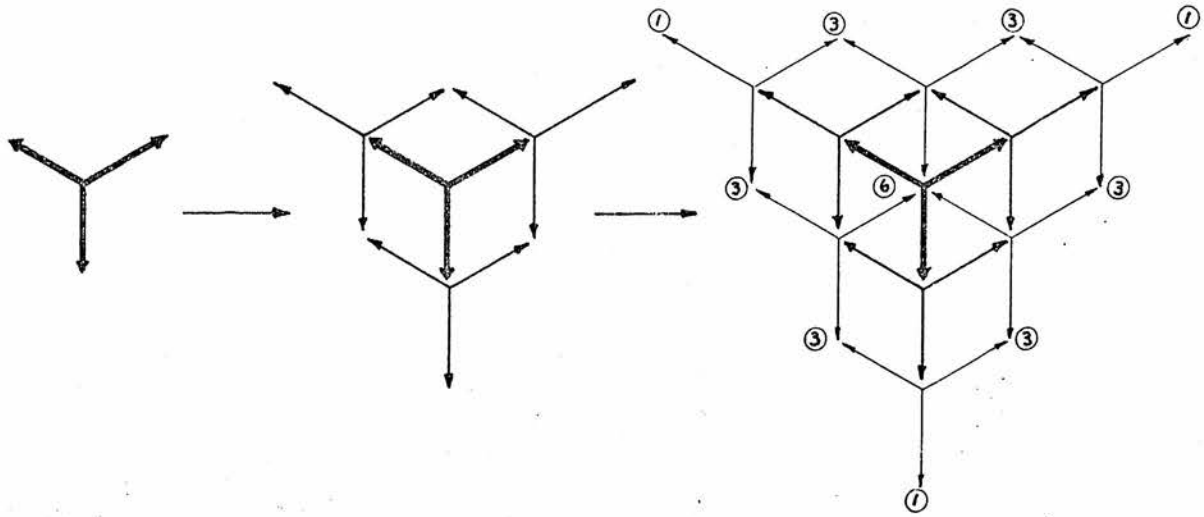

3 : $3 \times 3 \rightarrow \bar{3} + 6$: $3 \times 3 \times 3 \rightarrow 1 + 8 + 8 + 10$

(The multiplicity of each state is shown circled.)

By considering the multiplicity of the states it can be seen that the 27 states so formed by the $q\bar{q}q$ combination decompose into:-

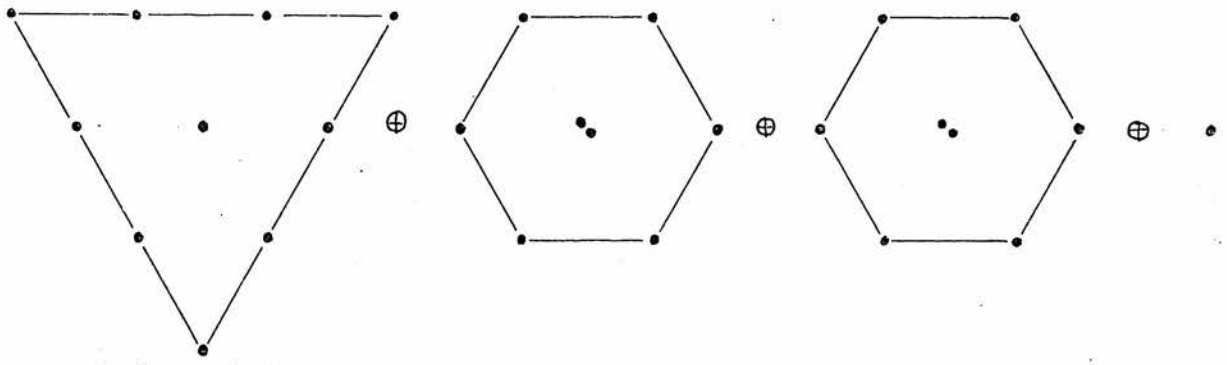

1 decuplet 2 octets 1 singlet

It was found that the $J^P = \frac{1}{2}^+$ baryons fitted into one of the octets, and the $J^P = \frac{3}{2}^+$ baryons into the decuplet.

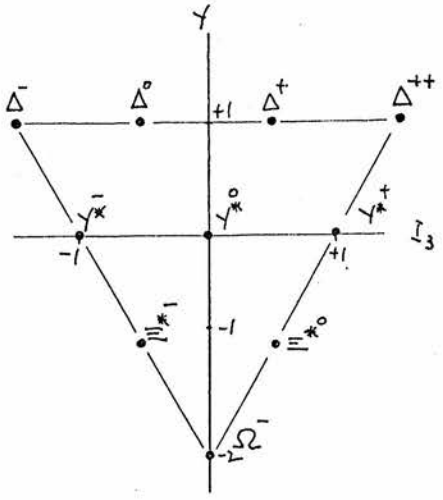

$\frac{3}{2}^+$ Baryon Decuplet

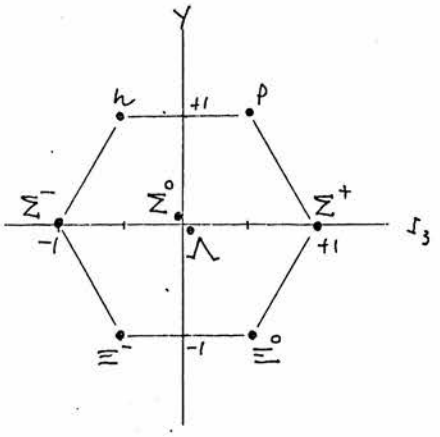

$\frac{1}{2}^+$ Baryon Octet

At the time the scheme was proposed not all of these particles had been discovered.

In the earlier SU(2) model the mass splitting within the isospin multiplet was explained by the symmetry breaking effect of the electromagnetic interaction. The much larger mass difference between the isospin sub-multiplets contained in the SU(3) multiplets showed that the SU(3) group was not a complete symmetry. This can be understood if it is assumed that the strong interaction Hamiltonian has two components, one of which commutes with the group operators, and the other - the "medium-strong" part - which does not, and hence provides the symmetry breaking. This can be expressed by saying that the medium-strong force is scalar in isospin and vector in U-spin, that is, has different eigenvalues for each U-spin multiplet. A consequence of this was the "equal spacing" mass rule for the decuplet:-

$$(M_{\Omega^-} - M_{\Xi^-}) = (M_{\Xi^-} - M_{Y^*}) = (M_{Y^*} - M_{\Delta})$$

which allowed the mass of the hitherto unknown "Ω^-" particle

at the apex of the decuplet to be predicted as 1675 Mev/c^2. The celebrated discovery of such a particle with mass 1672.4 Mev/c^2 in 1964 was one of the more spectacular successes of the SU(3) model.

A similar mass rule was formulated for the octets. Applied to the $\frac{1}{2}^+$ baryon octet the Gell-Mann - Okubo formula predicted[1]:-

$$\frac{M_n + M_{\Xi^\circ}}{2} = \frac{M_{\Sigma^\circ} + 3M_\Lambda}{4}$$

and was found to be in very good agreement with experiment. (LHS = 1127.2 $\pm$ 0.4 Mev/c^2, RHS = 1134.8 $\pm$ 0.1 Mev/c^2)

For the meson octets the Gell-Mann - Okubo formula was written with the masses squared and for the pseudoscalar mesons appeared as[2]:-

$$M_K^2 = \frac{M_\pi^2 + 3M_\eta^2}{4} .$$

The reason for this was that in the meson field equations e.g. the Klein-Gordon equation, the mass always appears in quadratic form and so it seemed reasonable that the same should apply for the mass formulae.

Another initial difficulty arose for the mesons when trying to decide which of the observed $Y = 0$, $I = 0$ states belonged to the singlet and which to the octet, for example, in the case of the $J^P = 1^-$ "vector" mesons where two $I = 0$, $Y = 0$ singlet states, the ϕ and the ω mesons, were found. To explain this apparent ambiguity, Sakurai in 1962 introduced the concept of "mixing" whereby the SU(3) states were composed of a mixture of the physical ϕ and ω

mesons, and calculated a "mixing angle" to describe the situation. The calculated $\phi - \omega$ mixing angle of 35° was found to be in very good agreement with the experimental value of $39.9^\circ \pm 1.1^\circ$. It was, however, later found that mixing is not confined only to the meson states but applies also to the baryons (for example in the case of $\frac{3}{2}^-$ singlet-octet mixing).

1.5 SU(6).

A natural extension of the SU(3) classification was made by assigning a spin ½ to each of the quark states, since the lowest lying meson states have spin 0 or 1 ($q\bar{q}$), and the lowest baryon states have spin ½ or $\frac{3}{2}$ (qqq). This idea, introduced by Gürsey, Radicati and by Sakita in 1964, led to a six component basic multiplet with three of the quarks having spin "up" and three having spin "down". This new scheme is represented by the SU(6) symmetry group.

The SU(6) states formed from the quark-antiquark pairs are now given by:-

$$6 \otimes \bar{6} = 1 \oplus 35$$

where the 35 component super-multiplet can be decomposed into sub-multiplets of the SU(2) and SU(3) systems. Using the notation (N, J) to denote a multiplet of dimension N and total spin J then:-

$$35 = (1, 1) \oplus (8, 0) \oplus (8, 1)$$

i.e. the 35-plet contains the vector singlet (ω), the pseudo-scalar meson octet (K, π, η), and the vector meson octet (K, ρ, ϕ).

As before the baryons are formed by combining 3 quarks:-

$$6 \otimes 6 \otimes 6 = 20 \oplus 56 \oplus 70 \oplus 70$$

to produce super-multiplets which again contain the SU(2) and SU(3) subgroups.

$$56 = (8, \tfrac{1}{2}) \oplus (10, \tfrac{3}{2})$$

$$70 = (1, \tfrac{1}{2}) \oplus (8, \tfrac{1}{2}) \oplus (8, \tfrac{3}{2}) \oplus (10, \tfrac{1}{2})$$

$$20 = (1, \tfrac{3}{2}) \oplus (8, \tfrac{1}{2}) \ .$$

In this case the 56-plet, composed of two $J = \frac{1}{2}$ octets and four $J = \frac{3}{2}$ decuplets (multiplicity = $2J + 1$), is interesting in that it unites the baryon $\frac{1}{2}^+$ octet and $\frac{3}{2}^+$ decuplet.

In addition to the multiplets of spin 0 and 1 mesons and of spin $\frac{1}{2}$ and $\frac{3}{2}$ baryons predicted by the SU(6) scheme it was found that mesons and baryons of higher spins could be grouped in a similar manner. An explanation of these higher order multiplets was offered by the "orbital-excitation" model of Dalitz in which the quarks were assumed to rotate about each other in a state of relative angular momentum, ℓ .

Besides providing a framework which contains the already successful SU(3) classification, the SU(6) model has led to a better understanding of the concept of mixing, mentioned earlier, and has made predictions concerning magnetic moment ratios, mass differences, interaction cross-sections and decay ratios, many of which have been verified experimentally. (For example the ratio of the neutron and proton magnetic moments $\mu n/\mu p$ was predicted to have a value of $-\frac{2}{3}$ and found experimentally to be - 0.685.)

An illustration of the current knowledge of the baryon spectrum is given in Figure 1.2[3], where the established states are shown as solid lines, and those less well known, as dashed lines. Figure 1.3[3] shows the success with which the SU(3) model has been able to accommodate these states in singlets, octets and decuplets. The missing pieces are indicated by dashed lines and the symbol ≀↓ shows that singlet-octet mixing occurs.

As mentioned above, this experiment has been performed to investigate the $I = 0, 1$ resonances in the 1660 Mev mass region. In the energy region covered - 1570 to 1750 Mev - only three well established $I = 0, 1$ resonances exist - the Λ (1670) belonging to the $\frac{1}{2}^-$ nonet, and the Λ (1690) and Σ(1670) belonging to the $\frac{3}{2}^-$ nonet. These are shown in Table 1.1 together with those resonances in this energy range whose status is still uncertain. The evidence for these states comes mainly from a single channel Partial Wave Analysis by Armenteros et al.[4] and from a multi-channel analysis by Kim[5]. It can be seen that the situation is somewhat confused, with the unconfirmed resonances outnumbering the established ones. Because of the lack of data on these unconfirmed states, no SU(3) assignments have yet been made.

It is hoped that this experiment, besides providing information on some of these states, will also allow a better determination of the branching ratios of the resonance decay channels which are at present not well known. This will allow a stricter comparison to be made with the SU(3) predictions for these ratios, and will provide a better constraint when making further fits to the SU(3) model.

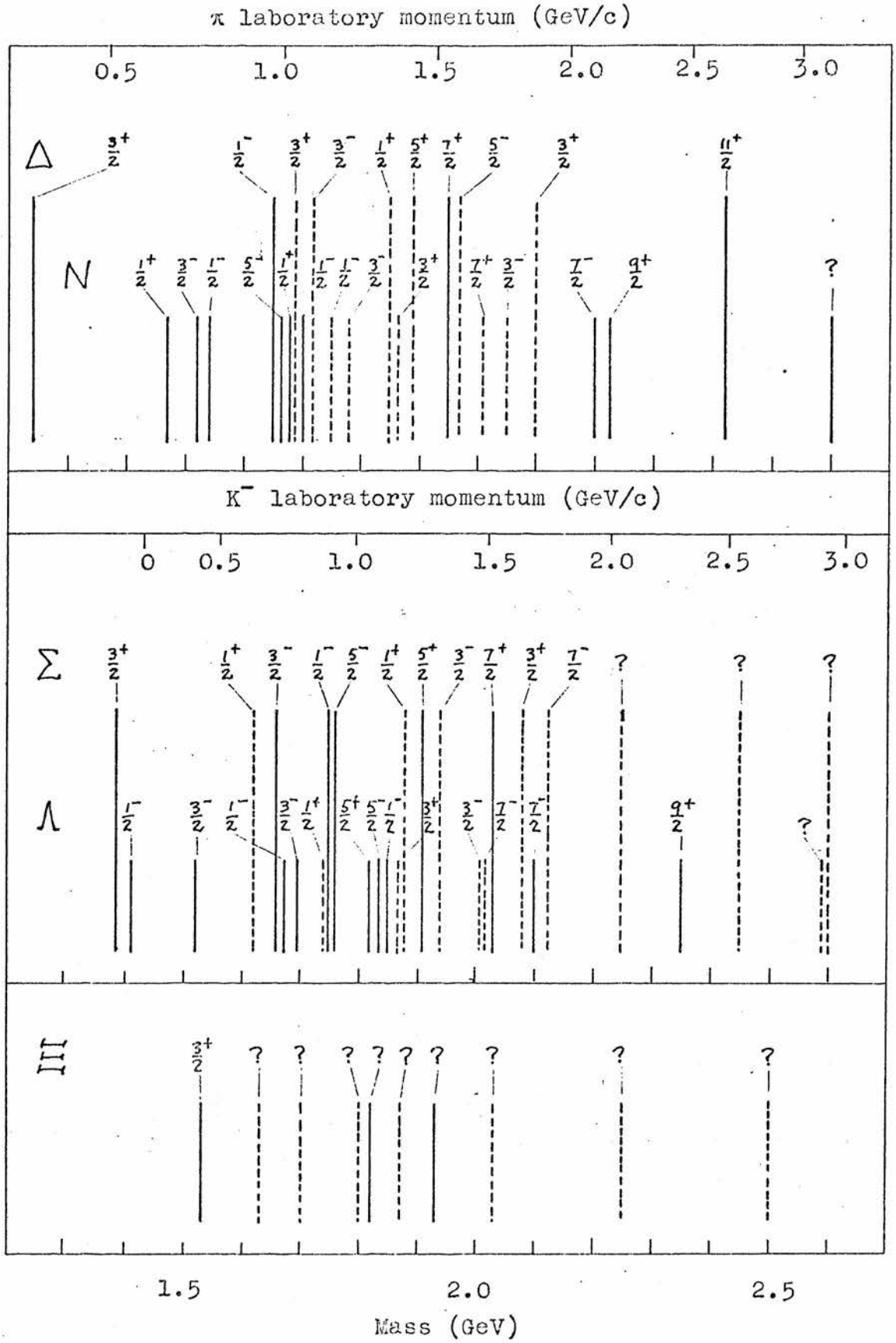

FIG. 1.2 Spectrum of Baryon resonances with established particles represented as solid lines and those of uncertain status as dashed. The value of J^P appears over each line.

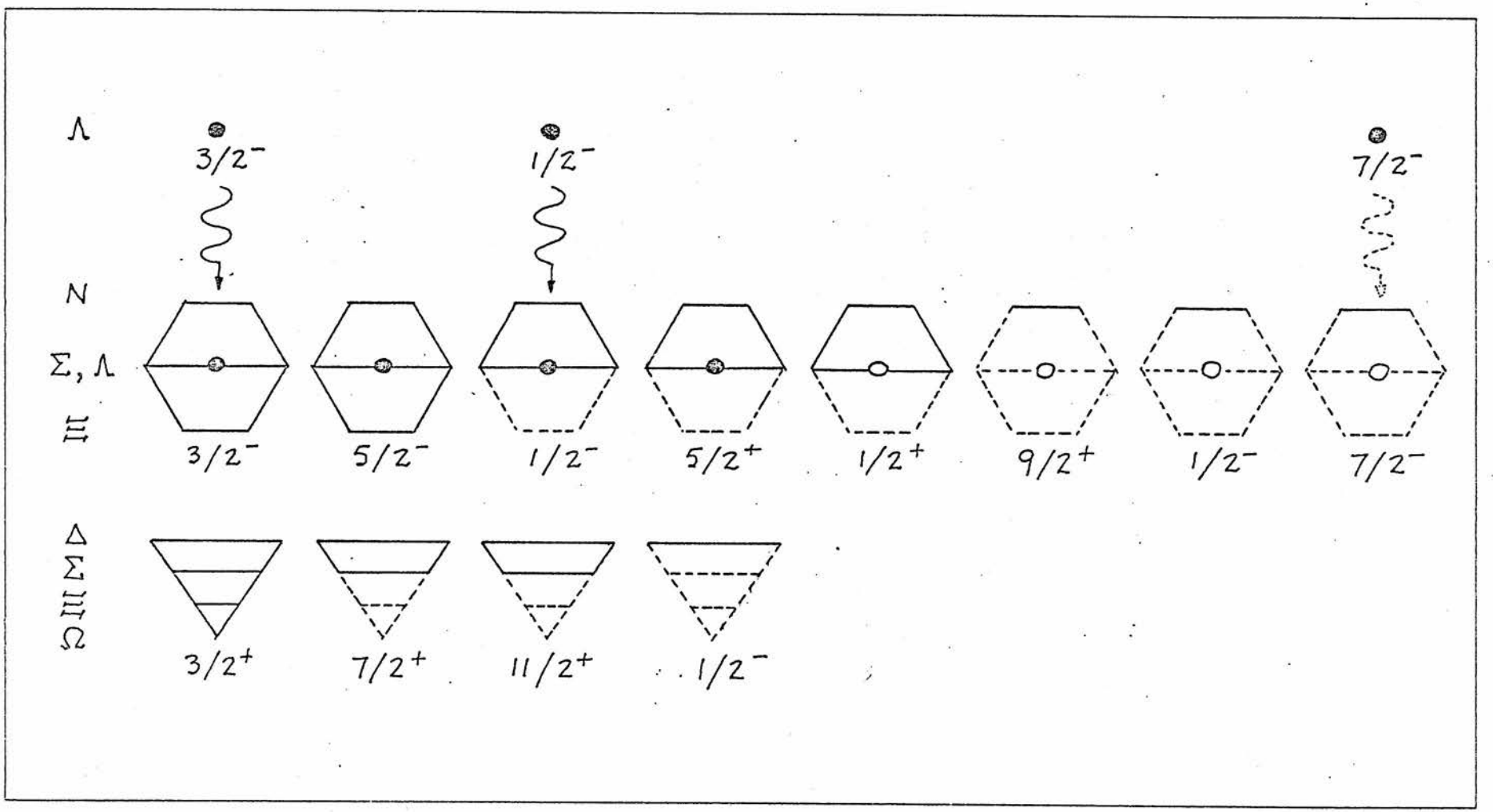

FIG. 1.3 The established SU(3) multiplets. The value of J^P is given under each multiplet and missing pieces shown as dashed lines. The symbol ≀ indicates singlet-octet mixing.

I = 0	L_{IJ}	DECAY MODE
$\Lambda(1670)$	S_{01}	$\bar{K}N$, $\Lambda\eta$, $\Sigma\pi$
$\Lambda(1690)$	D_{03}	$\bar{K}N$, $\Sigma\pi$, $\Lambda\pi\pi$, $\Sigma\pi\pi$
$\Lambda(1710)^{K}$	P_{03}	$\bar{K}N$, $\Sigma\pi$
$\Lambda(1720)^{K}$	D_{05}	$\bar{K}N$, $\Sigma\pi$
$\Lambda(1755)^{K,A}$	P_{01}	$\bar{K}N$, $\Sigma\pi$, $\Lambda\pi\pi$, $\Sigma\pi\pi$
$\Lambda(1780)^{K}$	S_{01}	$\bar{K}N$, $\Sigma\pi$, $\Lambda\pi\pi$
$\Lambda(1800)^{A}$	P_{01}	$\bar{K}N$
I = 1		
$\Sigma(1500\text{-}1600)^{A}$	P_{11}	$\Sigma\pi$
$\Sigma(1620)^{K}$	S_{11}	$\bar{K}N$, $\Sigma\pi$, $\Lambda\pi$, $\Sigma\pi\pi$
$\Sigma(1670)$	D_{13}	$\bar{K}N$, $\Lambda\pi$, $\Sigma\pi$, $\Lambda\pi\pi$, $\Sigma\pi\pi$, $\Sigma(1385)\pi$, $\Lambda(1405)\pi$
$\Sigma(1670)^{K}$	P_{11}	$\bar{K}N$, $\Sigma\pi$, $\Lambda\pi\pi$, $\Sigma\pi\pi$
$\Sigma(1750)$	S_{11}	$\bar{K}N$, $\Sigma\eta$, $\Lambda\pi$, $\Sigma\pi$
$\Sigma(1765)$	D_{15}	$\bar{K}N$, $\Lambda\pi$, $\Lambda(1520)\pi$, $\Sigma(1385)\pi$, $\Sigma\pi$, $\Sigma\eta$, $\Sigma\pi\pi$

TABLE 1.1

Confirmed and proposed resonances in the energy region 1600-1800 MeV. (The proposed resonances of Armenteros[4] - A - and Kim[5] - K - are shown underlined.

1.6 Quark Searches

The successes of the quark model in the domains of strong, electromagnetic and weak interactions have led many physicists to a belief that the quark is not merely a mathematical concept, but a physical entity, and various experiments have been performed in attempts to identify it. Most of these have been based on the fact that at relativistic velocities the ionisation produced by a particle as it passes through matter is proportional to its charge squared. Hence a relativistic quark with either $\frac{1}{3}$ or $\frac{2}{3}$ the electronic charge should produce $\frac{1}{9}$ or $\frac{4}{9}$ the ionisation of a singly charged particle travelling at the same velocity. Using accelerators and cosmic rays as possible sources of quarks, Cloud Chamber, Bubble Chamber and Spark Chamber techniques have been employed to detect them, but have so far been unable to produce any conclusive evidence for their existence.

Another approach, that of looking for quark accumulations in matter, for example in material taken from ocean floors, has been made on the assumption that quarks may have been produced over a long period of cosmic ray bombardment of the earth, and because of their fractional charges, have not been able to annihilate. Here again this method has been unsuccessful. However many new experiments are under way, for example in the Intersecting Storage Rings at CERN, and one of these may ultimately produce a quark to provide a physical basis for SU(3).

CHAPTER 2

EXPERIMENTAL METHOD

2.1 Introduction

In order to test fully the predictions of the SU(3) classification scheme, it is necessary to have as much experimental information as possible on the spectra of meson and baryon states. A considerable amount of data on one group of excited hyperon states - the $Y^*_{0,1}$ resonances, has been provided by recent experiments in which the K^- p system has been studied at low energies, notably in hydrogen filled bubble chambers. The use of hydrogen has the advantages of being able to provide clean proton targets on which the K^- mesons can interact and of allowing good momentum resolution of the incoming and outgoing charged particles. Many of these experiments[6,7,8] have spanned the mass region around 1660 Mev where considerable confusion still exists as to the resonance positions and quantum numbers. These experiments have studied directly the charged final states in this region, but because the γ ray materialisation probability in hydrogen is very low, certain neutral final states in which electromagnetic decays occur, are not directly accessible.

To enable a direct study of these neutral channels, which are important because of their pure isospin, a "heavy liquid" mixture of propane (C_3H_8) and freon (CF_3 Br) can be used instead of hydrogen, the propane to provide hydrogen targets and the freon to allow γ detection. The γ's materialise by either creating electron pairs:-

$$\gamma \longrightarrow e^+ e^-$$

or by producing Compton electrons

$$\gamma e^- \longrightarrow \gamma' e^- \quad .$$

This experiment was performed primarily to make a direct study of the K^-p neutral final states in the 1660 Mev region, and used a Heavy Liquid composition of 50°/o propane and 50°/o freon, by volume, allowing a 75°/o γ detection efficiency. The final states investigated were:-

$I = 0$: $\Sigma^0\pi^0$, $\Lambda\pi^0\pi^0$, $\Lambda\eta$.

$I = 1$: $\Lambda\pi^0$, $\Sigma^0\pi^0\pi^0$, $\Lambda\pi^0\pi^0\pi^0$, $\Sigma^0\eta$

all of which have pure isospin as shown. The principal decay modes of the final state particles accessible to this technique are:-

$\pi^0 \longrightarrow \gamma\gamma$ (98.84°/o)

$\eta^0 \longrightarrow \gamma\gamma$ (38.0°/o)

$\Sigma^0 \longrightarrow \Lambda\gamma$ (100°/o)

$\Lambda \longrightarrow p\pi^-$ (64.2°/o)

and by detecting the decay γ's the parent particles can be reconstructed. From this aspect, one of the important features of this experiment is therefore the ability to measure directly the $\Sigma^0\pi^0$ total and differential cross-sections, previously determined in Hydrogen, in the absence of γ detection, by making kinematic constraints to select the $\Sigma^0\pi^0$ events from the other channels. A detailed analysis of our results is given in Chapter 6, where a comparison is made with the Hydrogen data for both the $\Lambda\pi^0$ and $\Sigma^0\pi^0$ channels.

Two main drawbacks arise, however, from the use of heavy liquid. The first is that events are produced not only on

"free" hydrogen atoms, but also on protons which are bound in the heavy liquid nuclei (C, F, Br). Most of this nuclear event contamination is removed by the scanning and fitting processes, but not all, and a residual background remains in the fitted sample of "hydrogen" events.

A further background arises from events which are fitted in the wrong channel because of the inclusion in the fit of a "spurious" γ, that is, one which does not originate from the primary interaction, and/or because of the non-detection of one or more of the primary γ's in the bubble chamber.

Although representing major disadvantages in the use of heavy liquid, these important backgrounds can be reliably estimated and the separate investigations carried out to this end are described in detail in later chapters.

2.2 Experimental Details

(a) Beam

The exposure was made at CERN in the 1.2m heavy liquid bubble chamber, irradiated by a beam of negative kaons. A diagram of the secondary "K11" beam layout is shown in Figure 2.1. The kaon beam was produced by allowing the proton beam from the CERN proton synchrotron to strike an external copper target. The secondary particles were accepted from the target at 0°, and after a two stage electrostatic separation to remove unwanted particles, mainly negative muons and pions, the beam was directed into the chamber. The residual π, μ contamination was investigated by means of a "delta-ray count" described in Chapter 5.

The secondary beam was 32m. in length and was focussed

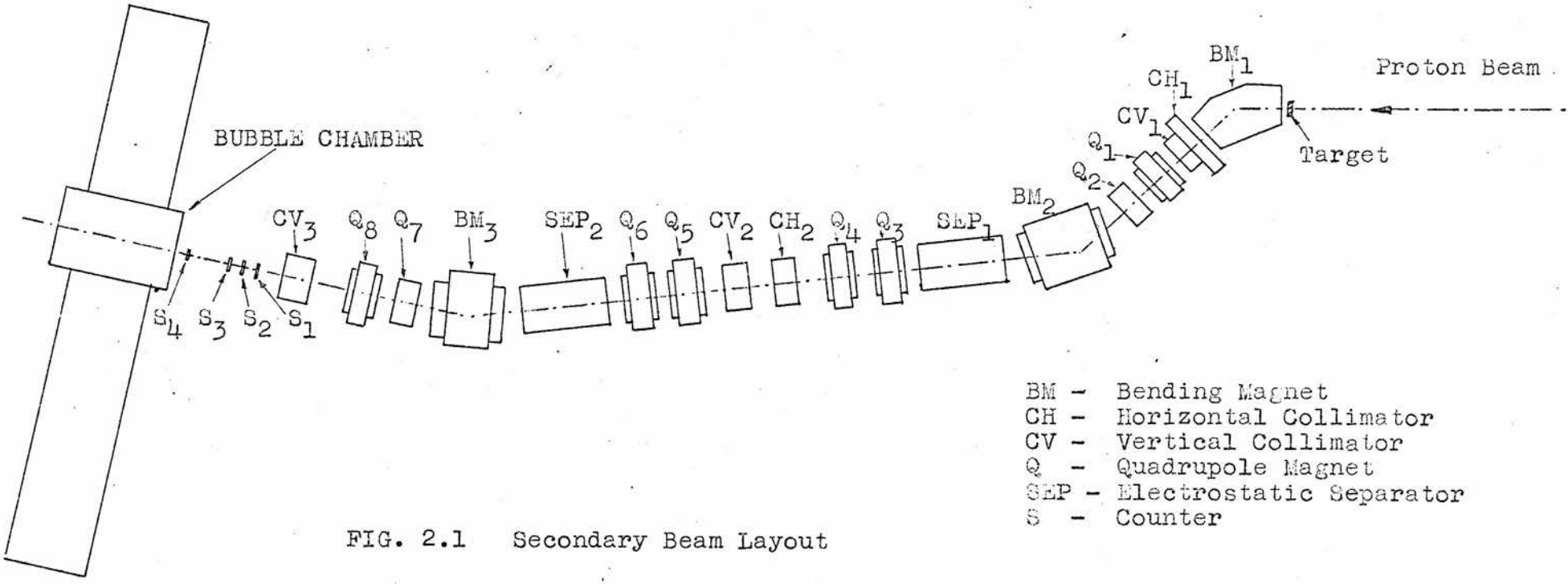

BM - Bending Magnet
CH - Horizontal Collimator
CV - Vertical Collimator
Q - Quadrupole Magnet
SEP - Electrostatic Separator
S - Counter

FIG. 2.1 Secondary Beam Layout

by a series of eight quadrupole magnets Q1 - Q8. The collimators CH1-2 and CV1-3 limited the flux entering the chamber to about 6-8 particles per burst. The flux was monitored just prior to entry into the chamber by counters S1 - S4.

A total of 1.3 million photographs (stereo triplets to allow three-dimensional reconstruction) was taken for four values of the beam momentum as shown in Table 2.1.

Run	P_{K^-} (Mev/c)	Photographs
1	808	300K
2	893	320K
3	975	480K
4	1035	210K

Table 2.1

The overlap between consecutive runs was approximately 30 Mev/c in momentum. The full exposure for each momentum interval was made up of three subruns - a, b, c - to allow for beam and chamber scheduling.

Because the analysing magnets were calibrated only to a precision of 1°/o an independent and more accurate measurement of the beam momentum was performed by adjusting the separators after each tuning to accept antiprotons, without altering the settings of the momentum analysing magnets. Photographs of the stopping antiprotons were taken and a measurement of their mean range and dispersion gavevalues of the central beam momentum and spread at the entrance to the chamber. The error on the central beam momentum was typically 0.2°/o and the

momentum spread about 0.8°/o. The mean ionisation energy loss for kaons in the liquid was about 1.0 Mev/cm allowing a range of incident momenta of about 150 Mev/c over the chamber for each run.

(b) Chamber and Liquid

The chamber was cylindrical in shape, 1.2 m.in diameter and 1.1 m in depth, as shown in Figure 2.2, and contained a mixture of equal volumes of propane and freon at a temperature of 38°C and at a pressure of 9.5 atmospheres. A magnetic field of 2.6 Tesla (26 Kilogauss) was applied uniformly over the chamber to provide charge identification, and to allow momentum determination from curvature measurement.

Illumination was provided by a bank of eight flash tubes placed at equal intervals around the chamber perimeter and photographs were taken by three synchronous cameras operated at a repetition rate of ~2 seconds.

A preliminary study revealed that in order to maximise the probability of interactions on hydrogen, together with the probability of γ detection in the 2, 3 and 4γ channels, the optimum liquid composition was 50-50°/o by volume propane to freon. The choice of liquid was made difficult because many competing factors had to be considered. A greater percentage of propane would have caused a decrease in the contamination due to interactions on protons bound in nuclei and would also have improved the momentum resolution because of the reduction in multiple scattering errors. On the other hand, the γ detection probability would be smaller, resulting in a corresponding decrease in fit statistics. On the

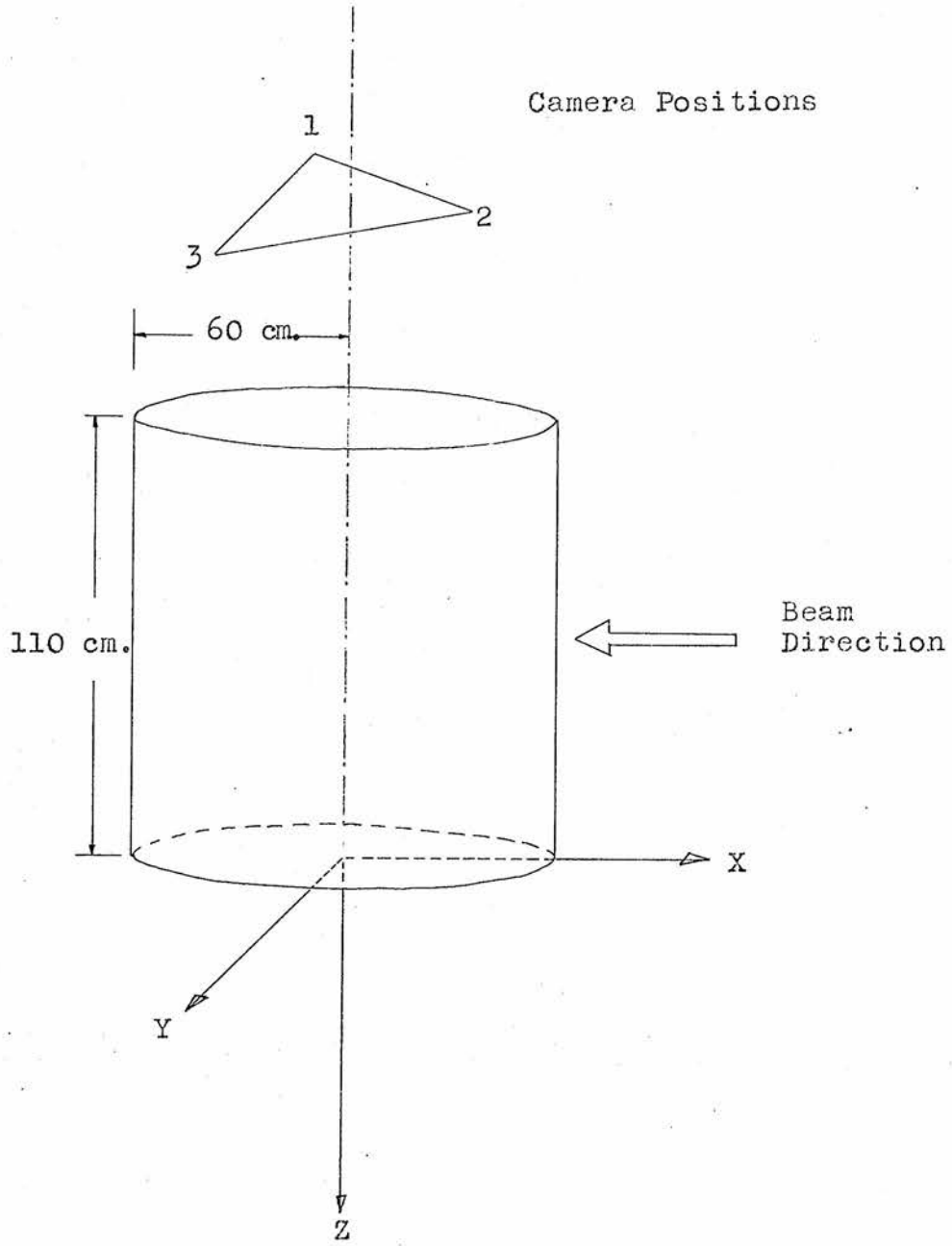

FIG. 2.2 Bubble Chamber Geometry

assumption that the free proton events could be successfully separated from the nuclear background, it was decided to take advantage of the greater γ materialising power of the 50-50 mixture. The estimation of nuclear background is dealt with in Chapter 4.

This liquid had a radiation length of 22 cms, giving a γ materialising efficiency of approximately 75°/o in the chamber. It was estimated that about 10°/o of the events would occur on free protons.

The liquid composition was determined before and after each run by a chemical analysis. Typical values are shown in Table 2.2.

Liquid Component	°/o By Weight
Propane (C_3H_8)	19.9
Freon (CF_3Br)	79.3
Ethane (C_2H_6)	0.1
Butane (C_4H_{10})	0.4
Nitrogen (N_2)	0.3

Density = 0.934g/cc.

Table 2.2

The number of atoms per cc. in such a mixture is given in Table 2.3.

Atom	No. of atoms/cc. ($\times 10^{22}$)
H	2.083
C	1.081
F	0.899
Br	0.300
N	0.008

Table 2.3

For each run a range versus momentum table was constructed from the known liquid composition and the known rates of energy loss in the separate components. Typical range-momentum curves are shown in Figure 2.3 for kaons, protons and pions.

(c) Liquid Density Measurement

The liquid density value actually used in the analysis was calculated from direct measurements made on the film. For convenience in computing, the originally measured density was used as a basis and was converted by means of the appropriate scaling factor to provide the correct value for each run. Depending on the run, one or more of three methods were used to make the correction.

For run 2a, a number of photographs was taken with a K^+ beam stopping in the chamber. About 300 $K^+ \longrightarrow \mu^+\nu$ decays at rest were measured and the mean μ^+ range, $\bar{L}_\mu$, found to be 69.47 ± 0.12 cm. From the known K^+ mass, the value of the μ^+ momentum from K^+ decay at rest was calculated to be 235.606 ± 0.057 Mev/c, where the error was due to the uncertainty in the kaon mass, and the range-momentum relation for the known liquid composition predicted the value of 73.324 ± 0.033 cm, as the muon range $\langle L_\mu \rangle$. After a small correction to allow for optical distortion the scale factor S_μ $(= \langle L_\mu \rangle / \bar{L}_\mu)$ was calculated as 1.0555 ± 0.0018.

For the remaining runs, in which no stopping K^+ photographs were taken, two methods were used to provide the density scaling. The first of these used normal photographs in which a Λ° was observed to decay to a proton and a pion,

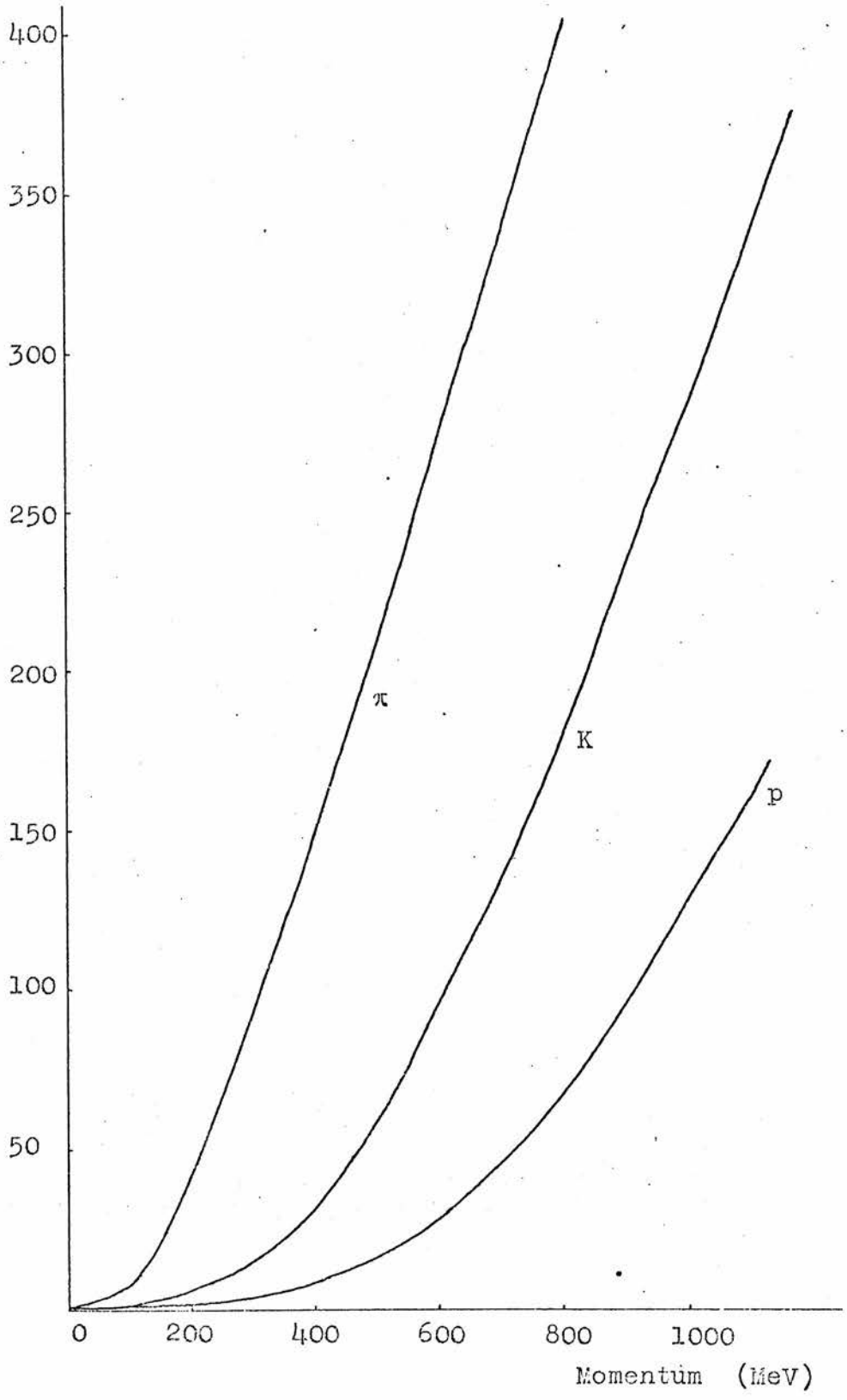

FIG. 2.3 Range versus momentum curves for K, π and p in 50-50 propane-freon mixture.

both of which stopped within the chamber. The secondary tracks were measured and the range-momentum relation used to provide accurate values for the momenta. The Λ 's were then fitted to the production vertex with the Λ mass a free parameter, to be determined by the fit. The density scaling factor, S_Λ , was calculated by comparing the fitted values to the accepted value of 1115.6 Mev/c^2.

With the second method, the density and hence the scaling factor were determined from a measurement of the observed refractive index of the liquid. This was done by reconstructing the fiducial marks on the back of the chamber, and by adjusting the value of the liquid refractive index till the mean reconstructed chamber depth was equal to the known value. The liquid density (d) was then related to the refractive index (n) using the Lorentz-Lorentz law:-

$$\frac{n^2 - 1}{n^2 + 2} = d \sum_i W_i R_i$$

where W_i is the fraction by weight and R_i the specific refractivity, of the i-th component of the liquid, and the scaling factor S_n calculated as:-

$$S_n = \frac{n^2 - 1}{n^2 + 2} \Big/ d \sum_i W_i R_i \quad .$$

These latter methods allowed the scaling factor to be determined to an accuracy of about 1°/o, as opposed to approximately 0.2°/o for the stopping K^+ method. The separate determinations of the scaling factor were compatible and values for run 2a, for each method are shown in Table 2.4, where the errors quoted are statistical only.

S_μ	S_Λ	S_n
1.0555 ± 0.0018 ($\sim .0006$)	1.0450 ± 0.0078 ($\sim .005$)	1.0697 ± 0.0025 ($> .0085$)

Table 2.4

An estimate of the systematic error in each case is given in parenthesis.

2.3 Scanning

The film was shared among the five laboratories and each was responsible for the scanning and measuring of its portion. We in Edinburgh were involved only in the scanning operation and sent all our film to CERN for measurement.

The scanners searched each photograph for events having a "zero-prong" interaction with an associated V_o (i.e. Λ or K^o) and any number of γ's. A typical event is shown in Figure 2.4. The Σ^o decays in $\sim 10^{-14}$ seconds and the π^o in $\sim 10^{-16}$ seconds and hence these particles do not travel any detectable distance in the chamber before decaying. The decay products of an event which contains a Σ^o or a π^o therefore point toward the interaction origin.

General rules were laid down by the collaboration to ensure uniformity in scanning although the actual methods employed varied from laboratory to laboratory. In some cases the V^o and the γ's were scanned for simultaneously, and in others separate scans were performed. The philosophy adopted for the CERN/Edinburgh scanning was to remove as much of the unwanted material as possible while allowing the rules to be elastic enough to accept doubtful events which could

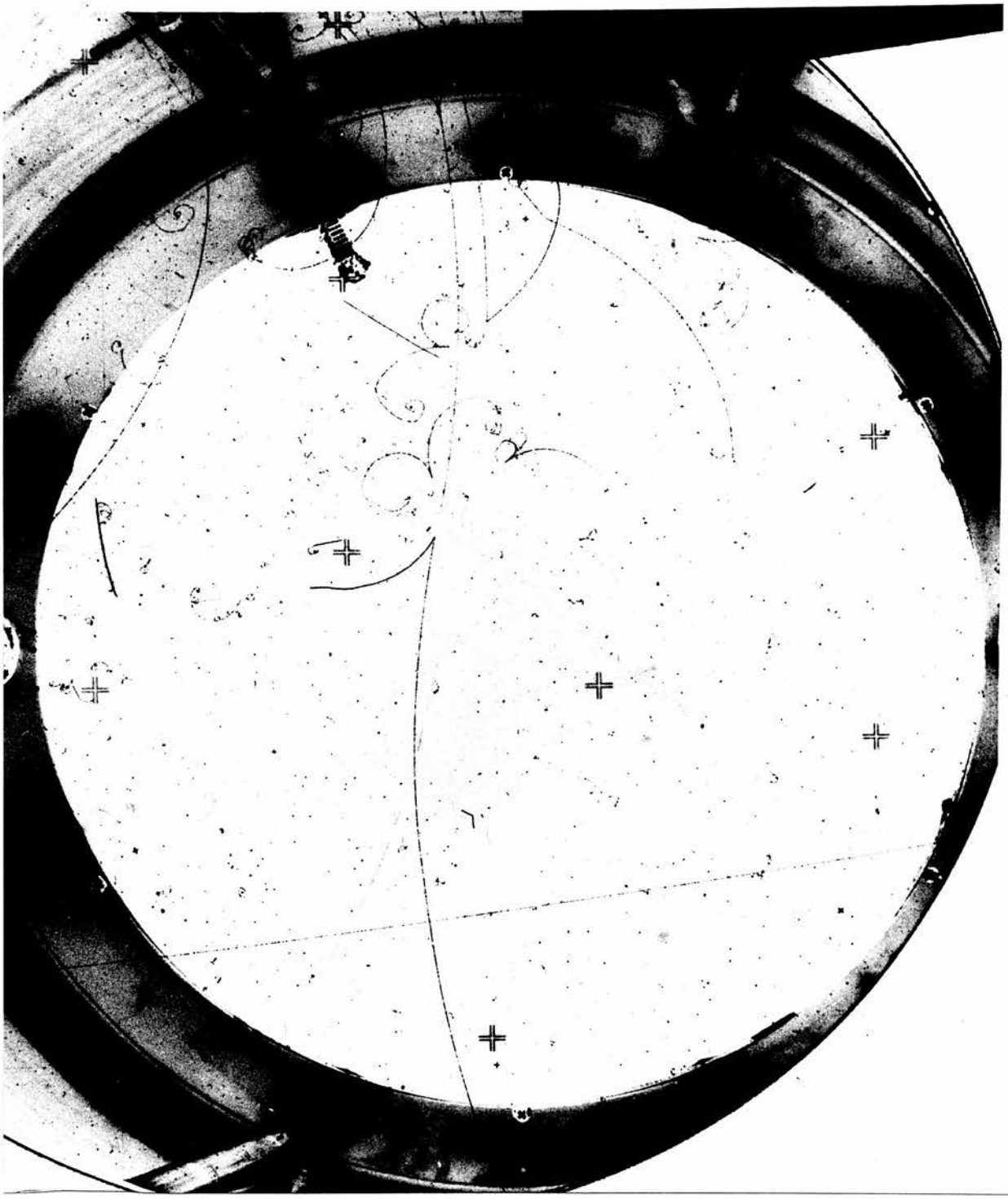

FIG. 2.4 Example of a $K^- p \longrightarrow \Lambda \pi^\circ$ interaction.

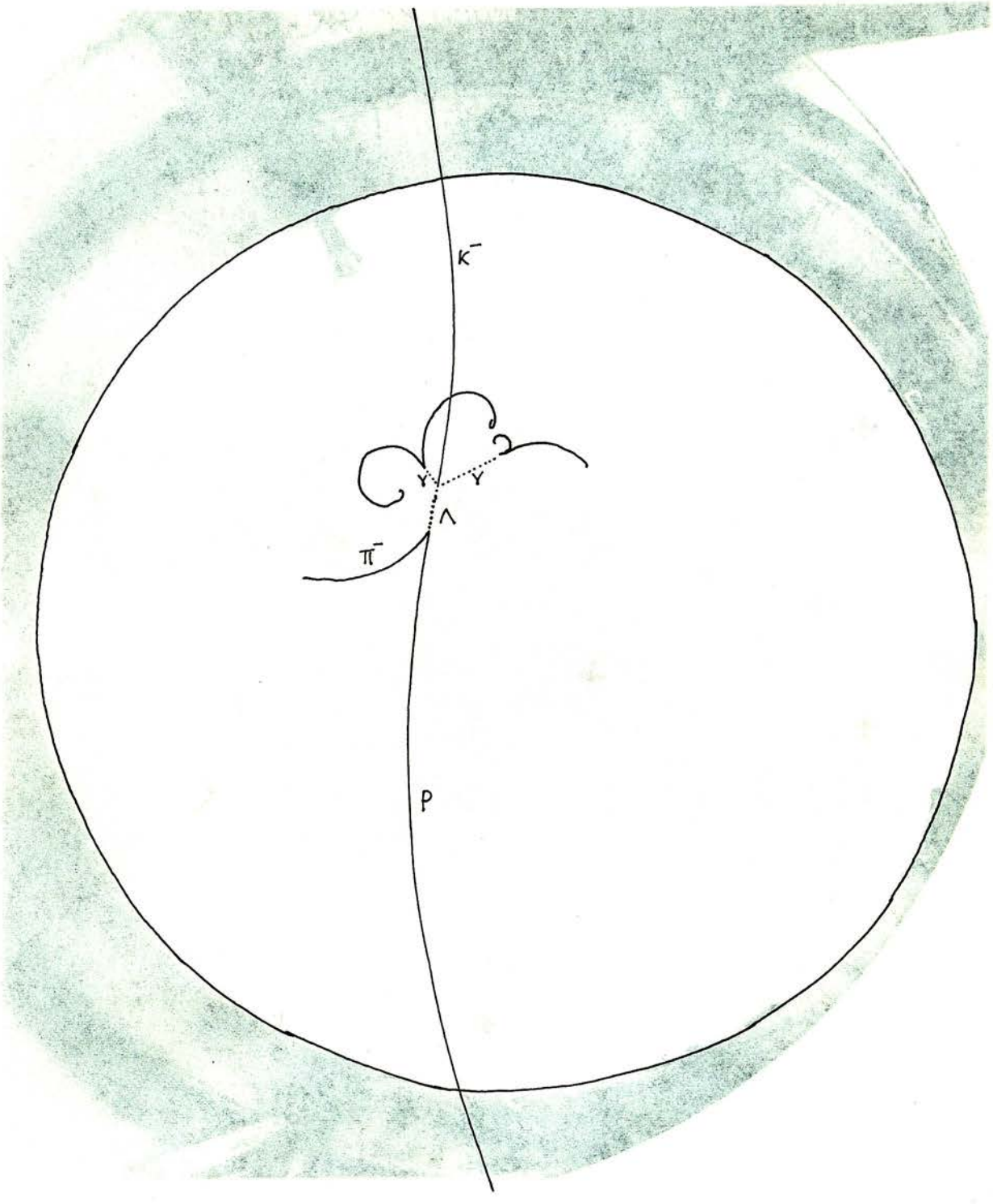
K⁻
γ
γ
Λ
π⁻
p

be rejected or accepted at a later stage.

Each frame was projected onto a flat horizontal table to appear about one half life-size. The "zero-prong - V^o" combination was scanned for on view 1 and the other two views used for verification, and to resolve ambiguities. Events were accepted if the interaction origin was visible in at least two views and fell within the "fiducial region" (i.e. within the circle defined by the base of the chamber as seen on view 1). Gamma rays materialising as pairs or Comptons were scanned for on all three views and accepted if visible on any part of at least one view.

The position of the interaction origin was recorded using a Cartesian grid centred on the fiducial marks, and a polar grid, centred on the origin to facilitate the subsequent measurement process, used for the V^o and γ vertices.

Certain conditions had to be fulfilled by each event before it was finally accepted by the scanner. Beam tracks were rejected if they did not enter by the window, if they were out of alignment by more than 10^o, or if a single scatter occurred at more than 10^o on any view. To avoid confusion the entire frame was discarded if the number of beam tracks was greater than 12. The nuclear event background was substantially reduced by rejecting those events with either two or more evaporation protons or with one proton of length greater than 2 mm. on the scan table (corresponding to a momentum of greater than $\sim$ 200 Mev/c). Origins having a small "blob" (less than 2 mm. in length) were retained for measurement because of the possibility that the blob was due to a stray bubble or to a small δ - ray and not to a nuclear interaction. It was estimated that even after the application

of this cut, about 50°/o of the events remaining were produced on bound protons.

A V^o was rejected as not pointing if the line of flight direction drawn from the origin to the V^o apex did not pass between its arms. V^o's having a total projected length less than 2 cms., or a line of flight distance greater than 15 cms., as seen on the scan table, were discarded. The first cut served to remove Λ^o's of low visibility, and the second reduced the background of Λ^o's originating from other interactions.

A V^o surviving these cuts was accepted, and no attempt was made by the scanners to discriminate between K^o's and Λ^o's. For each accepted V^o the scanner made a record which described the decay vertex and tracks, and included her opinion of the individual track endings. This latter information was important at the measuring stage, described in Section 2.4, where stopping and non-stopping tracks received different treatments.

Electron pairs and Compton electrons were accepted if they appeared to point to the origin. (Comptons to within 10^o). Possible bremsstrahlung gammas were recorded as such. Low visibility pairs or Comptons of energy less than 7 Mev/c^2 were eliminated, using a disc of diameter 1 centimetre.

All of the CERN/Edinburgh film was double scanned for the $K^- V^o \gamma$ combination to enable scan efficiency corrections to be made. The independent scan records for each frame were compared and discrepancies resolved by performing a "third scan". Here, each scanner rescanned those events which she had previously missed or had rejected, and which had been accepted by her counterpart. Final decisions were taken on these events, and, for those accepted, new scan descriptions

written. These "third scan" records were then merged with the information of the primary scans to form a final description of the event. This method, by allowing a rapid feedback to the scanner, demonstrated those areas in which weaknesses occurred and ultimately led to a much improved scan efficiency.

A set of computer programs to handle the scan data was developed at CERN and implemented at Edinburgh. The processing framework is shown in Figure 2.5. The scan information was transferred from written sheets to punched cards, an example of which is shown in Figure 2.6, and typographical and formatting errors searched for using the program "CHECK". The corrected scan card decks for the two independent scans were compared by "COMPARE" which produced lists of those events which required a rescan. The primary and rescan information was then ordered by the program "MERGE", and by selecting from all of these data, the final comprehensive scan summaries written on magnetic tape by "EVENTS" in such a way as to be compatible with the requirements of the measuring system.

2.4 Measurement and Reconstruction

The events were measured at CERN using the "DOLL"[9] (Direct-on-Line-Logic) system. Six measuring tables, each equipped with a coordinatograph and a three-view projector were served by a CDC 3100 computer on which the geometry programs were mounted. Geometrical checks were made on measured tracks and vertices, and a stereo reconstruction of the event attempted on-line, allowing immediate remeasurement

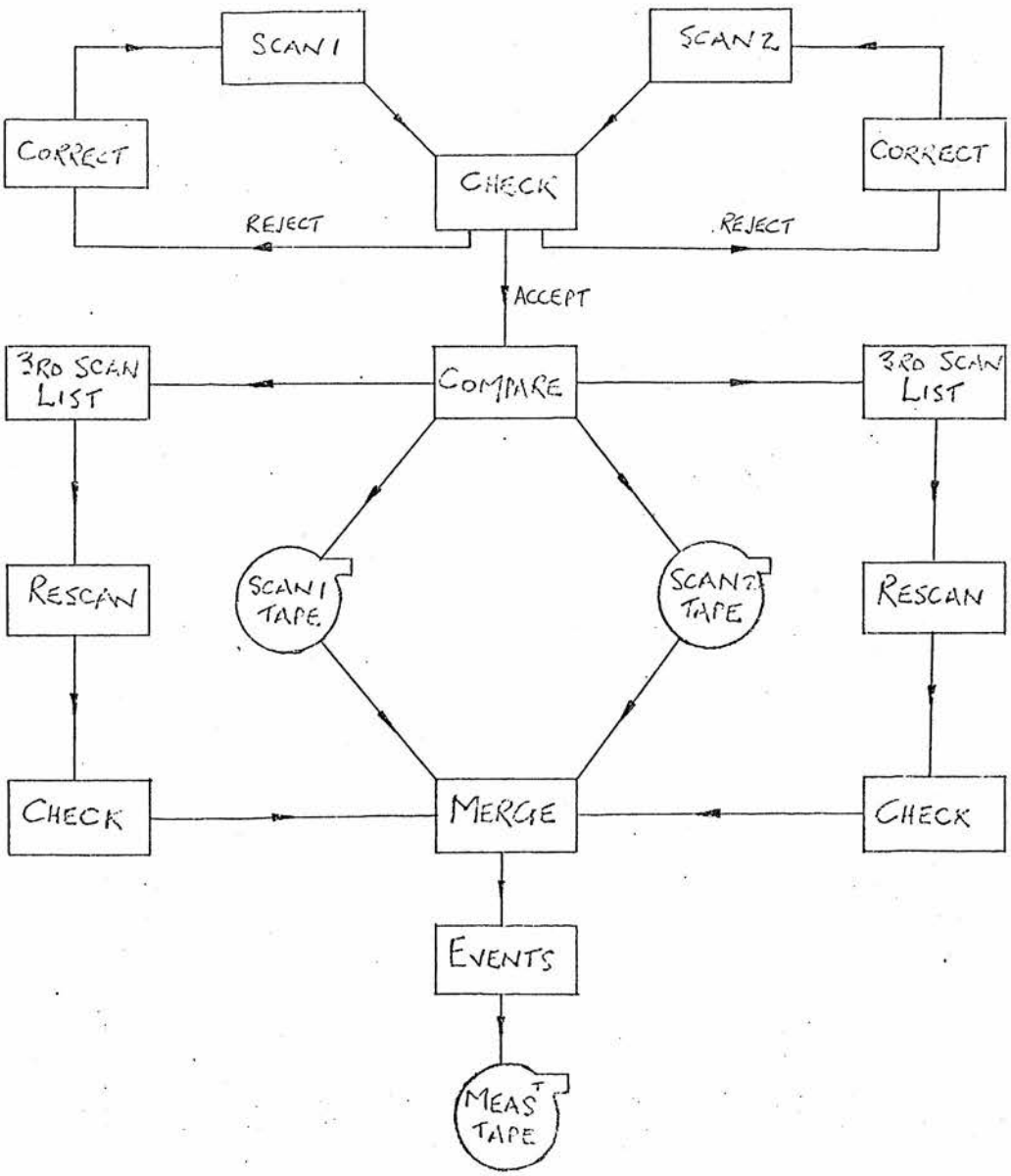

FIG. 2.5 Scan-card processing flow diagram.

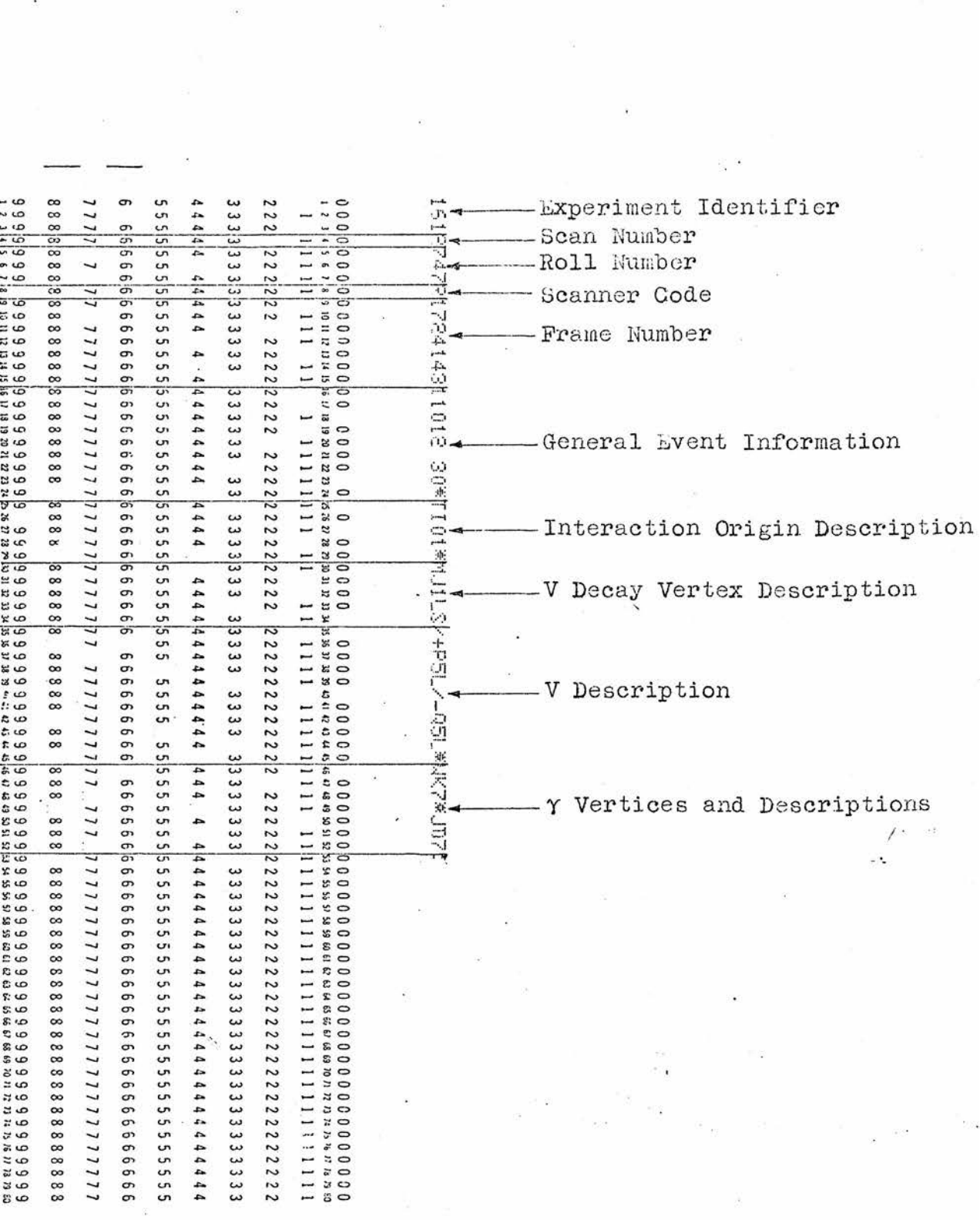

FIG. 2.6 Example of Scan Card.

if a failure occurred.

All the required details of an event, including the vertex positions and track labels, were taken from the magnetic tape prepared from the scanning information and given automatically to the measurer via an electric typewriter. The measurer recorded the positions of the fiducial marks on each view to provide a coordinate reference, and then measured the vertices and tracks in an order dictated by the system. An event was measured completely on all three views. A charged track was measured by recording the positions of many points along the track, the straighter the track, the more widely spaced the points, and vice versa. For stopping tracks, as indicated by the label, the position of the end point was always measured to enable a range determination to be made. For each view, as a new bubble position on a track was recorded, a geometrical check was performed by fitting a circle to the three last entered points, and testing the position of the new point relative to the circle. A point failing this test because of large measurement errors was remeasured.

Non-stopping tracks were reconstructed by making a "helix" fit. The measured points from each view (not necessarily corresponding to the same bubble on the track) were used to calculate the positions of "near corresponding points" in space, and these were fitted to a helix. The fit was not to the entire track, however, but only on that part for which the tangent to the track made an angle of less than about 60° to the initial track direction. Beyond this, energy loss became important and would have necessitated making assumptions about the mass of the particle. In the case of

a kinked track the fit was made only on the first segment. This fit then provided the initial direction of the particle and a momentum determination from curvature.

For stopping tracks a helix fit to the first five near corresponding points was made to provide the track angles, and the momentum determined by means of a "polygon" fit. Here the total range of the track was estimated by summing the length of the individual track segments between points. The momentum was then found from the range-momentum relation for the liquid, as illustrated above in Figure 2.3.

Only those events having at least two gammas were measured. A measurer had the power to reject a gamma or an event, if, in her opinion, it did not satisfy the scanning criteria. An event was "killed" only after verification by a physicist. No γ's or events were added by the measurers.

In heavy liquid the main sources of error, when determining particle momenta, arise from multiple Coulomb scattering. An overall error estimate was made by adding in quadrature the measurement error and the error from scattering (and from straggling in the case of stopping tracks).

For electron tracks, an estimate of the momentum was made from curvature by allowing for ionisation and for bremsstrahlung losses. The pair momentum was taken as the sum of the electron momenta and the direction as the weighted mean of the electron directions.

The kaon momentum at the interaction vertex was calculated from the theoretical value at the beam window by allowing for ionisation loss over the measured length in the chamber using the range-momentum relation.

Typical errors for the charged tracks, for the Λ , after a constrained fit to the interaction origin, and for γ's are shown in Table 2.5.

Particle	Percentage Momentum Error $\Delta P/P$ °/o	Dip Error λ (mr.)	Azimuth Error ϕ (mr.)
P	18°/o (1°/o if Stops)	30	20
π^-	22°/o (2°/o if Stops)	50	30
	11°/o (2°/o if Proton Stops)	20	10
K^-	0.8°/o	16	8
γ	20 °/o	10	3

Table 2.5

To describe the quality of the measurement each particle was assigned a "measurement code" of three letters, one for each of the parameters P, λ and ϕ. The parameters were set either "W" - "well measured" - or "U" - "unmeasured". The code was initialised to WWW and after an inspection of the measurement information by the Geometry program the codes were reset. A particle having the code WWW was one with all three parameters well measured. For any particle, an error in P of more than 50°/o caused the P code to be changed from W to U, and similarly, an absolute error of greater than 500 mr. in λ or ϕ resulted in a U code for those parameters. For γ's producing electron pairs the presence of an associated bremsstrahlung also altered the P code from W to U.

2.5 Fitting

The measured events were kinematically fitted using the program GRIND[10]. The fitting was a two-stage process in which the "V"-particle was firstly constructed by making fits of the type:-

a) $\Lambda \longrightarrow P\pi^-$ (3 constraint fit to the interaction origin)
b) $K^o \longrightarrow \pi^+\pi^-$ (" " " " ")
c) $\Lambda \longrightarrow p\pi^-$ (1 constraint fit without origin)
d) $K^o \longrightarrow \pi^+\pi^-$ (" " ")

It was found that for the sample of V's measured:-

80°/o fitted hypothesis a)
5°/o " " b) and not a)
11°/o " " c) and not a) or b)
0.5°/o " " d) and not a), b) or c)
3.5°/o fitted no hypothesis.

The majority of the 15°/o of V's making only unconstrained fits, or no fit at all, was explained by V's originating from other interactions. It was estimated that in the accepted Λ sample, the background of K^o's was less than 0.1°/o.

Only if fit a) above was successful (i.e. fit probability greater than 1°/o) did the second stage or "production fit" proceed. In this, the event was fitted to the hypotheses:-

$$K^- p \longrightarrow \Lambda\eta \quad (1)$$
$$\Lambda\pi^o \quad (2)$$
$$\Sigma^o\pi^o \quad (3)$$
$$\Lambda\pi^o\pi^o \quad (4)$$
$$\Sigma^o\pi^o\pi^o \quad (5)$$
$$\Lambda\pi^o\pi^o\pi^o \quad (6)$$

For an event containing n γ's, all γ fit combinations were attempted. γ's were then systematically dropped and all lower order fit combinations with n-1, n-2 .... down to 2 γ's tried, to allow for the presence of "spurious" γ's in the measured sample. In this context, "spurious" refers to those γ's not originating from the interaction vertex although accepted as pointing towards it.

No missing γ or missing π^o fits were included because of the large measurement errors in heavy liquid.

The philosophy adopted when fitting was to accept as many fits as were successful and to remove the backgrounds and resolve ambiguities in the post-fitting analysis, rather than impose possibly biassed conditions pre-fitting to reduce the number of fit candidates. One cut which was made in fitting, however, was to reduce the number of bremsstrahlung γ's. The emission angle of a bremsstrahlung γ is strongly peaked in the forward direction and often points to the K^- interaction. This is illustrated in Figure 2.7 where the distribution of the space angle, $\theta_{\gamma\gamma}$, between the lines of flight of pairs of γ's is seen to have a marked peak above 100 mr.

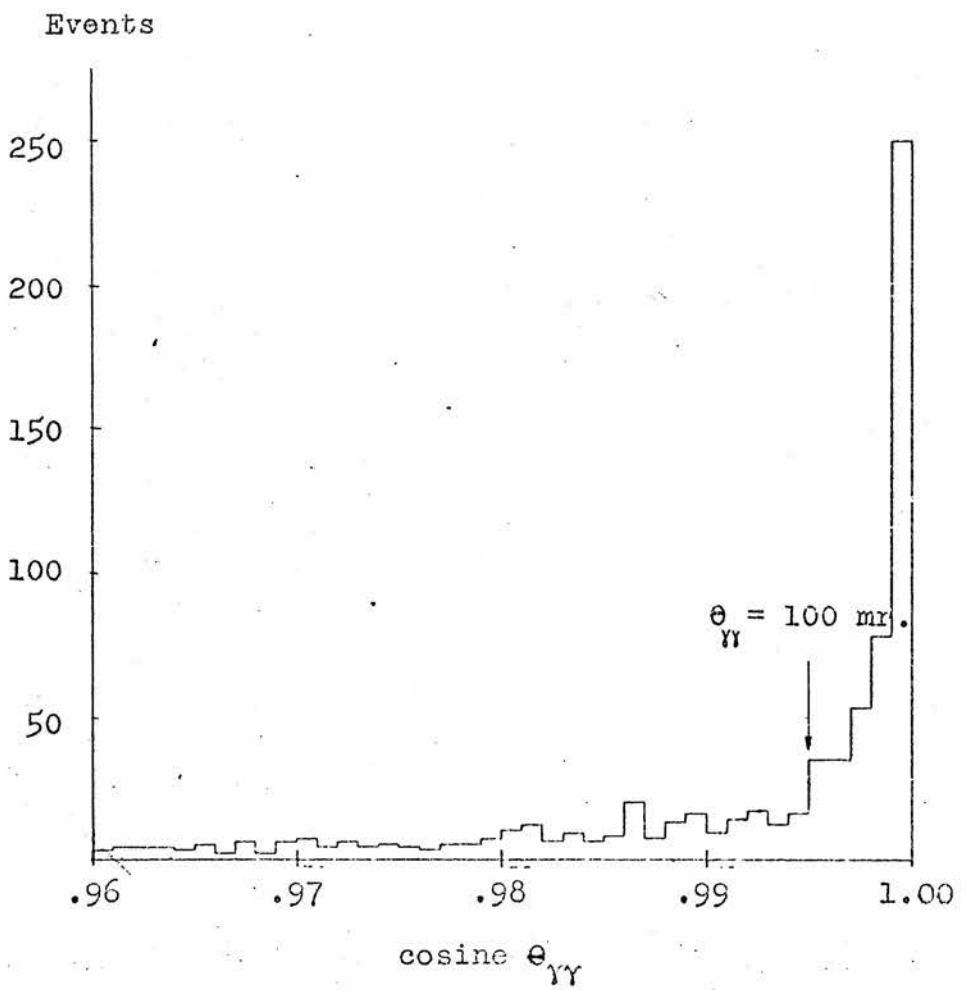

FIG. 2.7 Distribution of Cos $\theta_{\gamma\gamma}$.

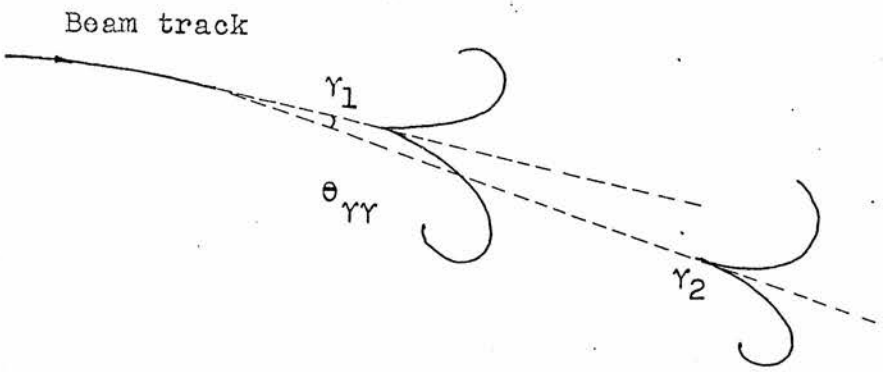

The cut was therefore applied by rejecting the further away of two γ's which had a value of $\theta_{\gamma\gamma}$ less than 100 mr. A larger cut of 300 mr. was later applied after fitting and is discussed in Chapter 3.

Several studies were made to estimate the fitting efficiency and to gain an insight into the various backgrounds. These included remeasuring and refitting a sample of events and making a comparison of the respective GRIND outputs, to see the effects of measurement errors on the fit. For some of the events nuclear fits of the type:-

$$K^- N_A \longrightarrow \Lambda \pi^\circ N_{A-1}$$
$$\longrightarrow \Sigma^\circ \pi^\circ N_{A-1}$$

where N_A and N_{A-1} are the target and recoil nucleus respectively, were attempted and the distribution of recoil momenta investigated. Those events having a nuclear fit with a small recoil momentum, and which also fitted the free proton hypothesis were studied in order to test for fit convergence problems.

Fits of the type:-

$$K^- p \longrightarrow \Lambda \gamma\gamma$$

in which some of the mass constraints were dropped were also tried and the backgrounds in the $\Lambda\pi^o$, $\Lambda\eta^o$ and $\Sigma^o\pi^o$ channels investigated from an inspection of the $\gamma\gamma$ and $\Lambda\gamma$ invariant mass distributions. The $\gamma\gamma$ invariant mass distribution is given in Figure 2.8 and shows a marked peak well centred on the π^o mass. The shaded portion shows those fits which also fit $K^-p \rightarrow \Lambda\pi^o$ and the narrow width of the peak (~ 20 Mev) is an indication that the channels may be resolved by kinematic fitting.

A detailed investigation of GRIND errors and distortions was made by fitting a sample of events generated by a Monte Carlo process using information from those events already measured by way of "look-up" libraries of beam tracks, protons, pions, and γ's. This study also provided useful information on expected distributions and on the effect of cuts and was used to estimate the backgrounds of fits with spurious and missing γ's. A description of this analysis is given later in Chapter 6.

In addition to the above internal checks, frequent comparisons were made with the fit results of the other collaborators to ensure uniformity.

From the findings of the above tests, many modifications were made to the original GRIND program, and it was estimated that the final version used at CERN had an overall production fit efficiency of about 90°/o.

The data on the GRIND output tape was made more manageable by writing the relevant parts in a simpler form on a "data summary tape" (D.S.T.). The format of this tape was agreed upon by the collaborators, and designed to facilitate

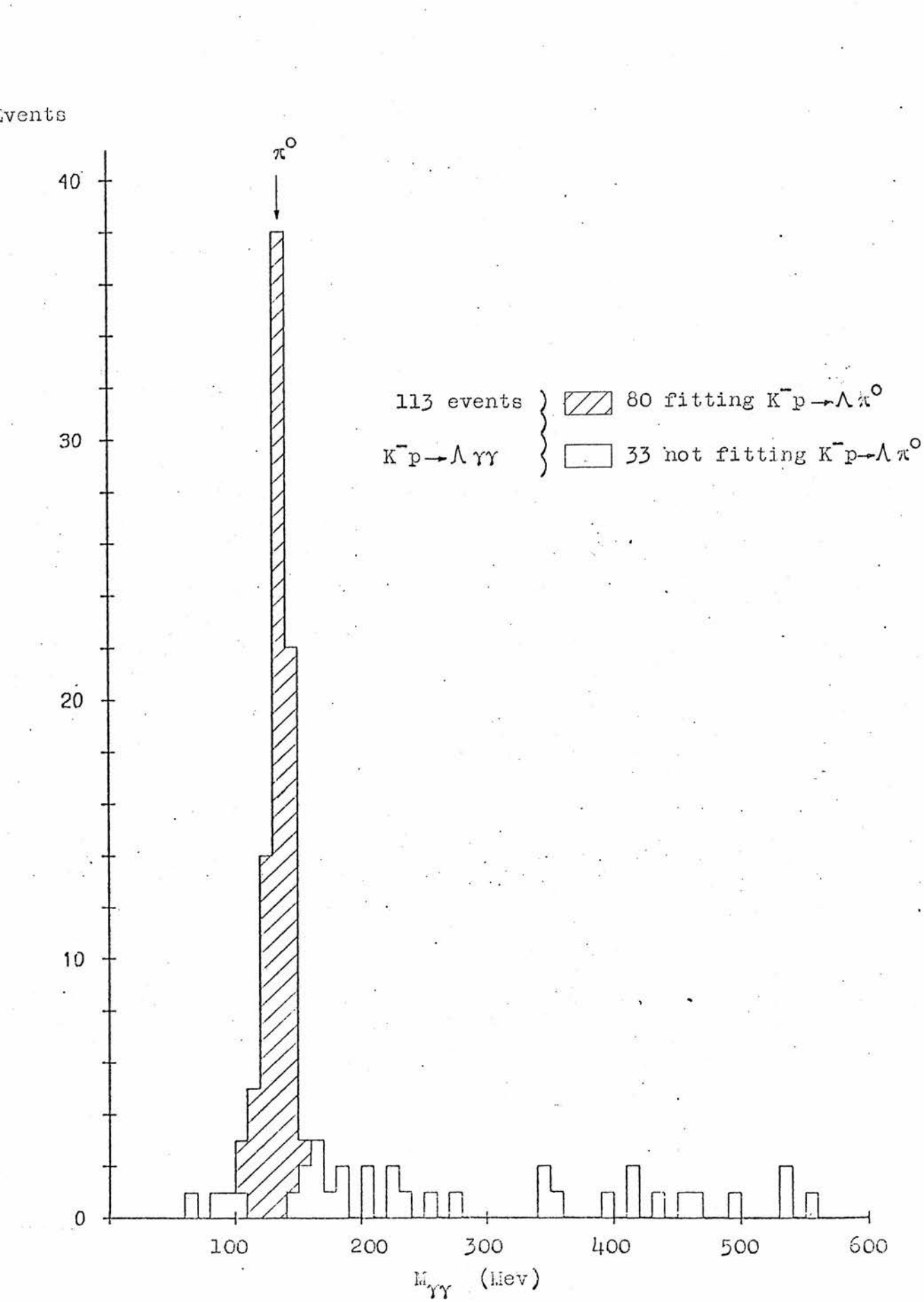

FIG. 2.8 Distribution of the invariant $\gamma\gamma$ mass after fitting a sample of Λ 2γ events to the hypothesis $K^-p \rightarrow \Lambda\gamma\gamma$.

the transfer of data among the laboratories. Tapes of this type then formed the basis for further analysis.

2.6 Analysis

In order to separate acceptable hydrogen events from the backgrounds of badly measured, spurious, and nuclear fits, a series of cuts was devised, and appropriate corrections made to allow for the loss of good events. A detailed description of the cutting and weighting technique is given later in Chapter 3. The selected sample of hydrogen events will then be used as the basis of an investigation to discover information on the resonances which are thought to exist in the energy range covered by this experiment.

There are two basic experimental approaches[11, 12] to the study of resonances. The first, the "production" experiment, involves the investigation of the effective mass spectra of two or more of the particles emitted in certain reactions. A significant enhancement above phase-space is taken as evidence of the decay of a resonance. The disadvantage of this method is that in situations where several resonances are produced simultaneously, the accurate assignment of the quantum numbers becomes difficult.

In a "formation" experiment such as this one, these complications do not arise. Resonances are investigated by allowing an appropriate beam of mesons to strike a proton target, such that the mass of the resonance is equal to the total centre of mass (c.m.) energy. Instead of probing the invariant mass spectra, the angular distributions and

polarisations of the final states are studied to provide information on the resonance parameters. This information is usually extracted by means of a "Partial Wave Analysis".

For $K^- p$ interactions, a spin-parity 0^- particle is incident on a $\frac{1}{2}^+$ target. The scattering amplitude can be expressed as the sum of a "spin flip" amplitude, $f(\theta)$, and a "spin non-flip" amplitude, $g(\theta)$. The squares of these amplitudes represent the respective probabilities that the spin of the outgoing baryon is anti-parallel or parallel to the initial spin of the proton. Both $f(\theta)$ and $g(\theta)$ can be expanded in terms of the c.m. scattering angle θ and are given by:-

$$f(\theta) = {}^{1}/_{K} \sum_{\ell} [(\ell+1) T_{\ell}^{+} + \ell T_{\ell}^{-}] P_{\ell} (\cos \theta)$$

$$g(\theta) = {}^{i}/_{K} \sum_{\ell} [T_{\ell}^{+} - T_{\ell}^{-}] P_{\ell}' (\cos \theta)$$

where K is the c.m. momentum, $P_{\ell}(\cos \theta)$, $P_{\ell}'(\cos \theta)$ are Legendre and first associated Legendre polynomials in cosine θ, and $T_{\ell}^{\pm}$ are the complex "partial wave" amplitudes. The subscript ℓ refers to the orbital angular momentum state, and the superscript to the spin direction, indicating the value of the total angular momentum J $(= \ell \pm \frac{1}{2})$. Using the above expressions for $f(\theta)$ and $g(\theta)$, the differential cross-section and the polarisation $\vec{P}$ of the final baryon may be written :-

$$\frac{d\sigma}{d\Omega} = f(\theta)^2 + g(\theta)^2$$

$$= \lambda^2 \sum_{n} a_n P_n (\cos \theta)$$

$$\vec{P} \frac{d\sigma}{d\Omega} = \hat{n} \cdot 2\mathrm{Re} (f^* g)$$

$$= \hat{n} \lambda^2 \sum_{n} b_n P_n' (\cos \theta)$$

where $\lambda = {}^{1}/_{K}$ and $\hat{n}$ is the normal to the production plane. The coefficients a_n and b_n can be expressed in terms of the $T_\ell^{\pm}$ and have been tabulated, for example, by Tripp[11]. In order to reduce the number of parameters, the series is truncated at some convenient angular momentum value, but care must be taken not to exclude any higher partial wave, which, although not observable, may have an appreciable effect on the solution, because of its interference with lower order partial waves.

To determine the partial wave parities it is not sufficient to use only the angular distribution data. Under a "Minami Transformation" in which the parity changes, e.g. $S_{1/2} \longrightarrow P_{1/2}$, the angular distribution remains invariant but the polarisation changes sign. Hence to resolve this ambiguity the polarisation data must also be utilised. However, the "complex conjugation" operation, equivalent to a time reversal, causes each amplitude to change into its complex conjugate and has the same effect as the Minami Transform. It therefore becomes necessary to have some additional knowledge of the behaviour of the partial wave amplitudes as expressed for example by the "Wigner Condition" to allow an unambiguous determination of the resonance properties. The Wigner Condition, arising from causality, states that as the energy increases through the resonance position, the amplitude moves along a circular locus in the complex plane in an anti-clockwise direction.

A partial wave analysis can be performed in one of two ways - the "energy independent" approach or the "energy dependent" approach. If sufficient data of the correct type are available at particular energies within the range covered,

the energy independent analysis can be performed. For this method to be successful only data from elastic or slightly inelastic channels can be used so that the condition of unitarity can be applied as a constraint. In this case separate solutions are found for each energy and the condition of continuity then imposed to obtain a unique solution.

With the energy dependent method the data from all energies are used simultaneously. It is therefore necessary to make some assumptions about the energy dependence of the partial waves and they are generally parametrised as the sum of a rapidly varying resonance contribution (e.g. Breit-Wigner) and a slowly varying background. The advantage of this method is that the condition of continuity is automatically obeyed, and the effect of low statistics in any region no longer serious. The main disadvantage stems from the fact that assumptions must be made in order to reduce the number of free parameters to make the analysis feasible.

In this experiment, because of the large degree of inelasticity in the interactions studied, and because of the limit set by statistics, it is proposed to perform an energy-dependent fit to each channel separately using a Maximum Likelihood method. In this case no binning is involved, and all available information is utilised to its fullest extent. The individual event weights, the derivation of which is explained in Chapter 3, will not however be used explicitly in the Partial Wave Analysis. Instead, a detection efficiency function in terms of the centre of mass energy and scattering angle will be generated, by observing

the effect of applying the same cuts, developed for the real events, to a large sample of Monte Carlo events. In this way the results of the analysis will be made much less prone to individual event weight fluctuations.

As a preliminary to this analysis, the angular distributions for the $\Lambda\,\pi^{o}$ and $\Sigma^{o}\pi^{o}$ channels have been fitted to Legendre polynomial expansions in the cosine of the centre of mass scattering angle and values of the expansion "A" coefficients so determined are compared in Chapter 6 with the results from the analysis of hydrogen data, as a check of the experimental method.

CHAPTER 3

DATA ANALYSIS

3.1 Introduction

The kinematic fitting procedure described above, by making the constraints of energy and momentum conservation, and by imposing additional constraints on invariant mass, allowed a considerable separation of the events produced on free proton targets from those occurring on heavy nuclei. The fitted events were further purified, to produce a sample of free proton fits with acceptable errors and a minimum of background, by requiring each to satisfy certain criteria before being selected. Individual cuts were made on the K^-, the Λ, and the γ parameters to remove unwanted particles with either poor measurement or with low detection efficiency, and to reduce areas in which remaining backgrounds were large. In the case of each of the cuts applied, a method was devised to compensate for the loss of good events. The weight given to an accepted event was the inverse of the probability that it would be observed and was taken as the product of the separate weight factors calculated for each particle. In the following sections the cuts applied to each type of particle and the contributions to the final event weight are summarised. The estimation of the γ scan efficiency and materialisation weights are dealt with in detail in the latter part of the chapter.

3.2 Cutting and Weighting

The cuts and corrections applied to each type of particle in an event were as follows:-

i) K^-

To ensure that the beam momentum and direction were known to a reasonable precision at the interaction origin, certain cuts were made on the K^- parameters. At the scanning stage a template was used to reject those beam particles which did not enter the chamber through the beam window, and hence suffered a large, and unknown, energy loss in the chamber wall. This condition was applied more stringently by making a geometrical cut on the measured beam coordinates at entry. In addition, a cut was made on the dip angle at the window to remove non-Gaussian error tails, and the "kink" cut reapplied to reject tracks with scatters greater than 8^o. Only those tracks with good angle measurement were accepted, by making separate cuts on the dip and azimuth errors.

The interaction origin fiducial volume was limited by cuts made on the K^- track length, to accept only those events with a beam track length S_K, in the region 25.0 cm. $< S_K <$ 98.0 cm. (measured from the reference plane, x = + 62 cms, at the entrance window).

The effect of the above cuts can be directly correlated with the beam length and a parametrised "flux-reduction factor" (which also allowed for the residual π, μ contamination in the beam), folded in with the expression for the natural beam attenuation to provide a corrected value for the flux.

ii) Λ^0

The following cuts were made on the Λ parameters:-

a) Length Cuts

Both maximum and minimum cuts were made on the Λ line of flight distance from the origin. A maximum length cut, corresponding to five mean Λ lifetimes was made to reduce the background of Λ's originating from other interactions. However, if the Λ "potential length", the line of flight distance from the interaction origin to the Λ fiducial volume boundary, was less than the lifetime cut, then this was chosen as the maximum length. (The fiducial volume for the Λ decay vertex was defined as a cylinder of radius 50 cm and height 90 cm centred on the chamber coordinate origin.)

When the Λ line of flight length was of the order of the average distance between neighbouring bubbles on a K^- track the Λ and the $\pi^+\pi^-$ two-prong topology could be easily misidentified. The minimum length cut to resolve this ambiguity was applied by requiring that the Λ^0 apex should appear on at least one view, outside an ellipse centred on the interaction origin, with the major axis along the beam direction and the minor axis perpendicular to the light ray to the camera. The size of the ellipse was laboratory dependent and for CERN/Edinburgh, the lengths of the semi-major and semi-minor axes were chosen to be 0.5 cm and 0.3 cm respectively.

The weight, W_D, applied to a Λ, observed between the distances X_{min} and X_{max}, to allow for unobserved $\Lambda \longrightarrow p\pi^-$ decays and for Λ interactions was given by:-

$$W_D = \frac{\lambda_D}{\lambda_T(e^{-x_{min}/\lambda_T} - e^{-x_{max}/\lambda_T})}$$

where λ_D is the mean decay length and λ_T the total attenuation length given by

$$\frac{1}{\lambda_T} = \frac{1}{\lambda_D} + \frac{1}{\lambda_I} \quad .$$

For a Λ of mass M_Λ and momentum, P_Λ, the decay length, λ_D, can be expressed as :-

$$\lambda_D = \frac{P_\Lambda (c\tau_\Lambda)}{M_\Lambda}$$

where $c\tau_\Lambda$ is the mean decay length. The mean interaction length of the Λ, λ_I, was taken as that of the proton. The justification for this choice is explained later in this section.

b) Λ Decay Phase - Space Cuts

These cuts were designed to eliminate those Λ decay configurations which had either low visibility or were undetectable because: i) the proton or pion tracks were very short, which is the case when one or other is emitted backwards in the Λ centre of mass with almost the same velocity as the Λ or ii) the opening angle, $\theta_{P\pi^-}$, is large and the Λ appears as a background track with a slight kink. The secondary momenta and opening angle in the laboratory frame for a Λ of a particular momentum are determined by the angle θ_{Dec}, between the direction of the proton in the Λ centre of mass and the Λ direction in the laboratory frame. For all channels θ_{Dec} should be uniformly

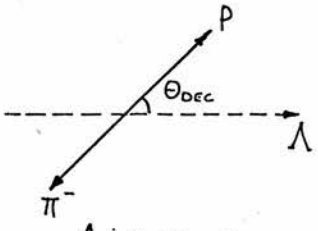

Λ C.M. frame

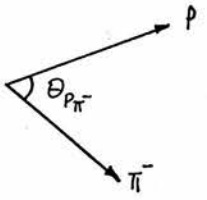

Lab. frame

distributed. An investigation of this distribution for the seen Λ 's suggested cuts on the secondary momenta to reject protons of momentum less than 150 MeV/c (corresponding to a length cut at 0.23 cm) and pions of momentum less than 0.54 Mev/c (length cut 0.7 cm), and a maximum opening angle cut at 140°. The correction was made from the Θ_{Dec} distribution, and also allowed for the effect of a cut, originally made at the scanning stage (see Section 2.4) requiring the combined length of the proton and pion tracks to be greater than 2 cm. (as seen on the scan table) to remove low visibility Λ 's.

c) Secondary Interactions

The above length cuts on the secondary tracks were applied to remove low momentum protons and pions. A further correction, however, was necessary to allow for those Λ 's which were lost because of interactions on the secondary tracks near the decay vertex within these length cuts. This correction was made using the proton and pion interaction probabilities, calculated for our liquid by scaling from Hydrogen and Carbon measurements.

d) Dip Cut

In some cases a cut was also applied to the Λ dip

angle to remove low momentum Λ 's with large dips and poor visibility. The correction was made using the knowledge that the azimuthal distribution of the Λ about the beam K^- direction is isotropic.

It was found that after the application of the above cuts, the selected sample of Λ 's had a double scan efficiency of $\sim 99^{o}/o$ which was virtually independent of momentum.

In Figure 3.1 the detection efficiency for $\Lambda \longrightarrow p\pi^-$ is shown as a function of the Λ momentum. At low momenta (< 175 Mev/c) the detection efficiency was very small and consequently the detection weights became large and unreliable. It was therefore decided to reject all events having a Λ with momentum less than 175 Mev/c. This value corresponded to a cut on the centre of mass scattering angle, θ^* at $\cos\theta^* = 0.9$ for the $\Lambda\pi^o$ and $\Sigma^o\pi^o$ channels. Here θ^* is defined as the angle between the incoming proton

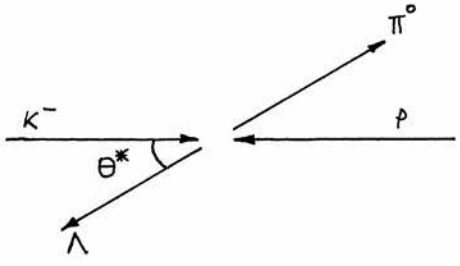

and the outgoing baryon directions in the reaction centre of mass frame. The contribution to the total cross-section of those events lost because of this cut is dealt with in Chapter 6.

To test the effectiveness of the above cuts on the removal of background, the "Q-distributions" in the decay length (ℓ) and angle (θ_{Dec}) were drawn. For a variable, x, with a probability distribution, P(x), normalised within

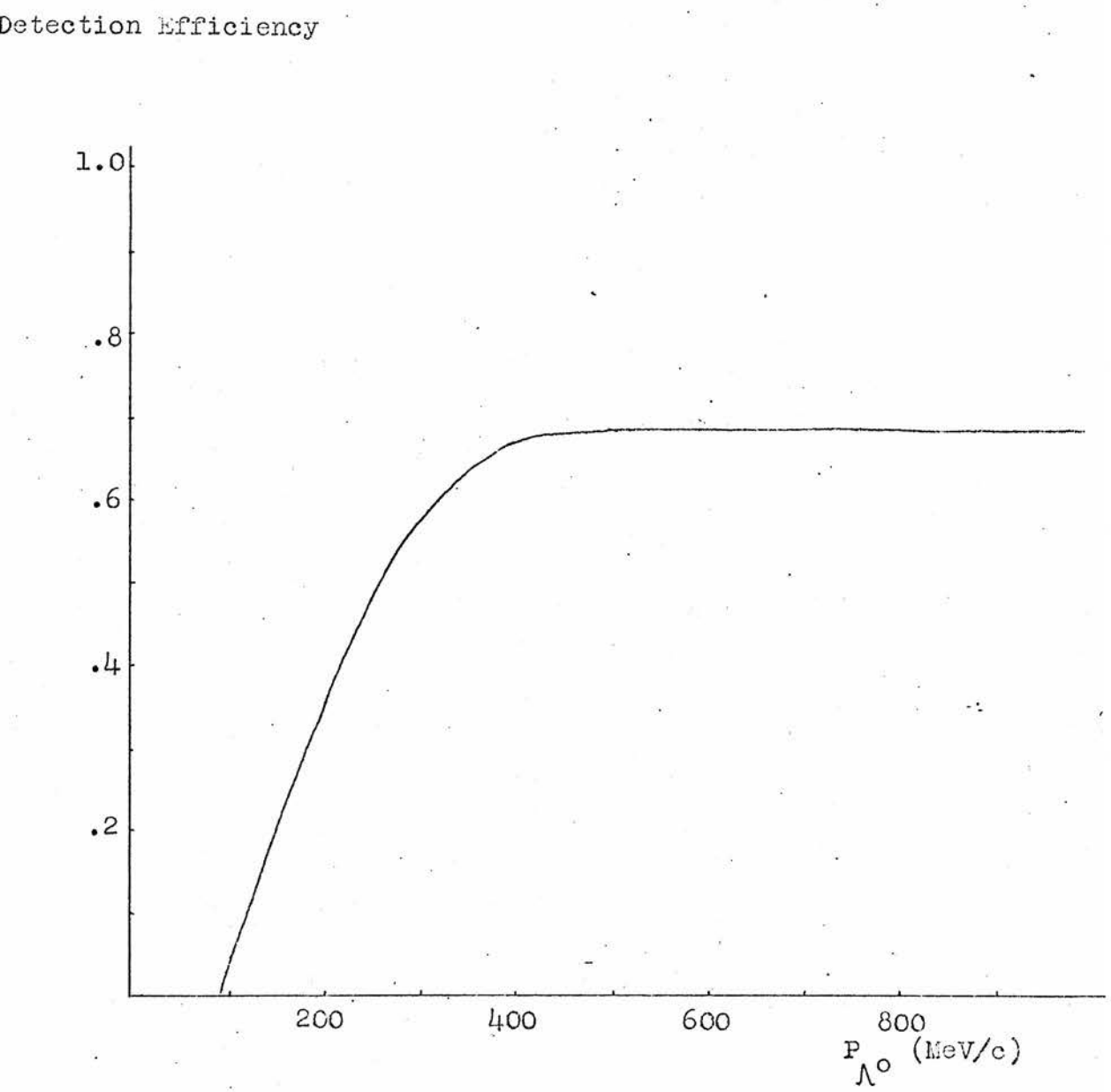

FIG. 3.1 Detection efficiency for $\Lambda \rightarrow p\pi^-$ as a function of the Λ momentum.

the physical limits x_1 and x_2, one can define another variable

$$Q(x) = \int_{x_1}^{x} P(x)\,dx$$

which is by definition uniformly distributed between 0 and 1. The use of such "Q-distributions" provided a convenient way of studying backgrounds. The experimental distributions in ℓ and $\cos(\theta_{Dec})$ are shown in Figures 3.2 and 3.3. Histograms a, b, c refer to the Λ sample, before cuts, after cuts, and after a successful production fit. It can be seen from histograms c that there is little evidence of background in the sample of Λ's in accepted fits.

A Maximum Likelihood fit to determine the mean Λ lifetime was made using a sample of Λ's selected by these cuts, and yielded a value of $2.44 \pm 0.07 \times 10^{-10}$ sec. After a correction to allow for Λ interactions (as mentioned earlier in this section) the value was calculated as $2.52 \pm 0.07 \times 10^{-10}$ sec. in good agreement with the world average of $2.52 \pm 0.02 \times 10^{-10}$ sec.[13] The compatibility of these figures was an indication that the choice of the proton reaction cross-section to describe Λ interactions had been correct.

iii) γ

For the γ's the cuts can be categorised into four main groups:-

a) Length Cuts

As with the Λ, minimum and maximum cuts were made on the line of flight length from the origin. A fixed minimum

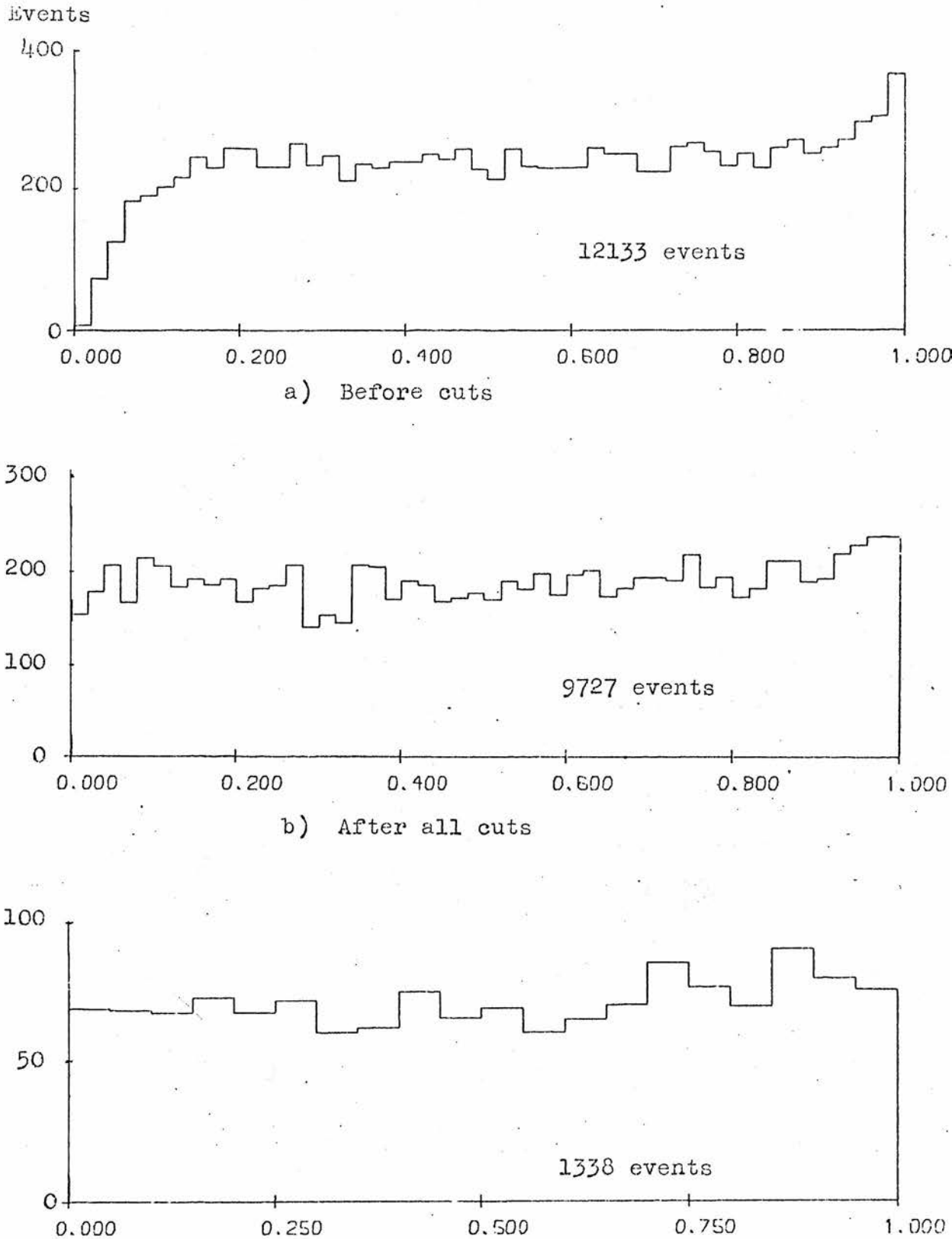

FIG. 3.2 Distributions in $Q(\ell)$ for the Λ line of flight length, ℓ, for the Λ sample a) before cuts, b) after all cuts and c) after a successful production fit.

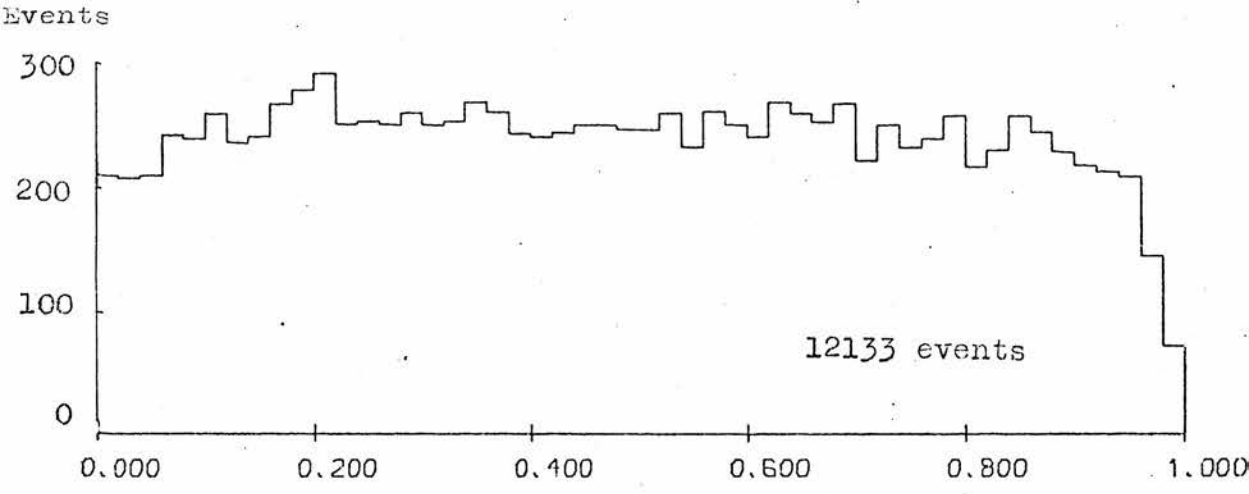

a) Before cuts

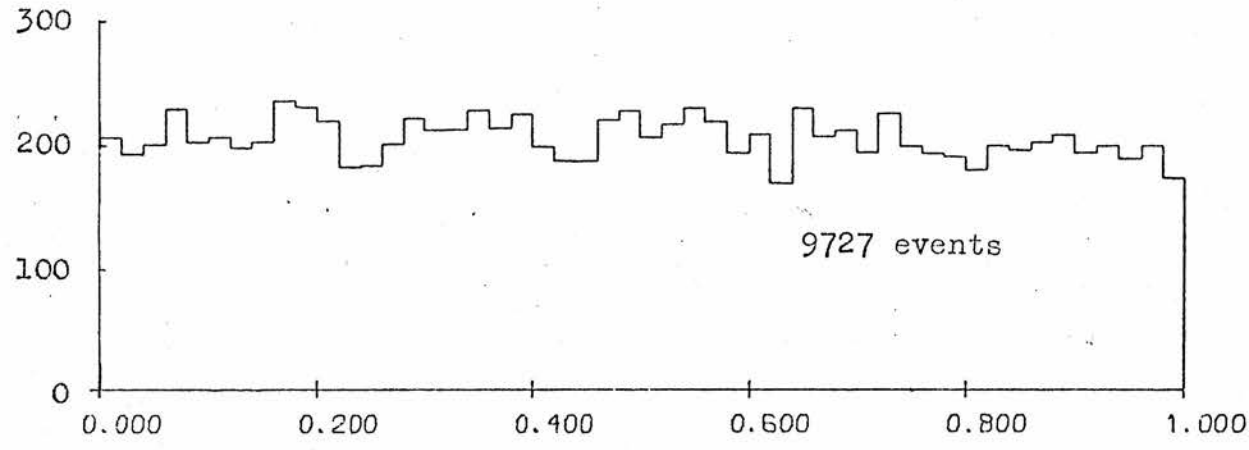

b) After all cuts

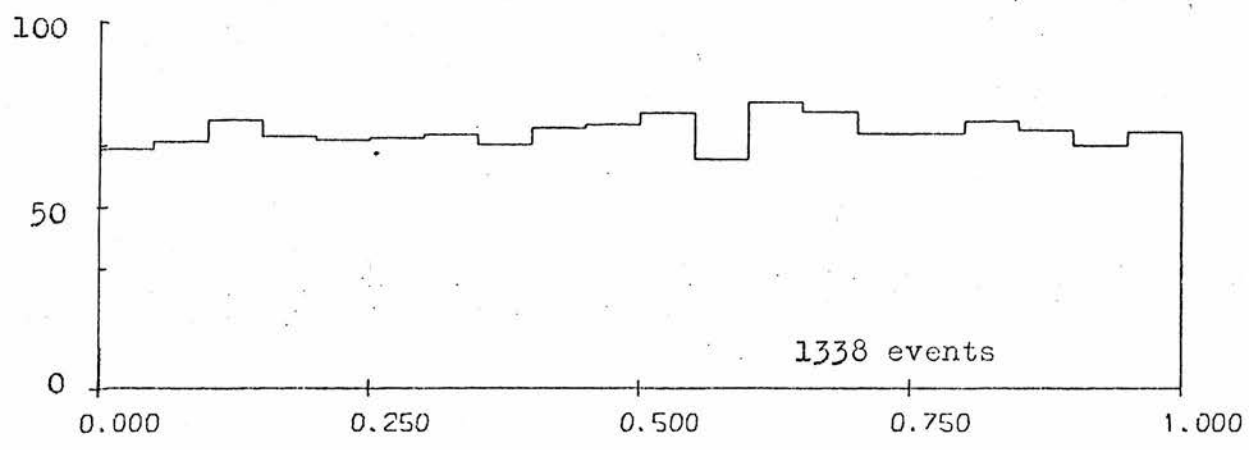

c) After production fit.

FIG. 3.3 Distributions in $Q(\cos \Theta_{Dec})$ for Θ_{Dec}, the angle between the proton in the Λ centre of mass and the direction in the laboratory. The histograms a), b) and c) refer to the same samples as in Fig. 3.2.

length cut at 1 cm. reduced the numbers of pairs with badly measured angles, because of their proximity to the origin and also removed any confusion with Dalitz pairs.

The type of maximum length cut used depended on the channel being considered. This cut was applied to remove γ's with low scan efficiency at large distances from the origin, and to reduce the background due to spurious γ's, which again occurred predominantly far from the origin. For the $\Lambda\pi^0$ and $\Sigma^0\pi^0$ channels where the spurious γ problem was found not to be serious (see Section 3.8) only the loss due to low scan efficiency near the chamber walls was considered and the maximum length cut taken as the smaller of the γ potential length, and the length from the origin, which, for that particular γ momentum, the scan efficiency became unreliable (see Section 3.5). Here the γ potential length is defined similar to that of the Λ in sub-section ii), that is, the line of flight distance from the interaction origin to the γ fiducial volume boundary - a cylinder of radius 52 cms and height 94 cms, centred on the chamber coordinate origin.

For the $\Lambda\pi^0\pi^0$, $\Sigma^0\pi^0\pi^0$ and $\Lambda\pi^0\pi^0\pi^0$ channels, where the number of $\Lambda\gamma$ and $\gamma\gamma$ combinations was much larger than for the other channels, a stronger maximum length cut was used to diminish the spurious γ background. This cut, which was variable, was calculated as a function of the γ emission angle, the pointing probability of the γ, and the measurement errors on the electron angles. The application of the cut, (which varied between 20 and 80 cms) to the three- and four-body channels greatly decreased the spurious γ background and provided a sample of γ's in

accepted events with a flat $Q(\ell)$ distribution as shown later in Figures 3.4 and 3.5.

b) Bremsstrahlung Cuts

Prior to fitting, a conservative cut of 100 mr. was made on $\theta_{\gamma\gamma}$, the angle subtended at the interaction origin by the lines of flight of two γ's, in order to reduce the number of bremsstrahlung γ's. This cut was reapplied after fitting at an increased value of 300 mr., after an inspection of the experimental distribution of $\theta_{\gamma\gamma}$ for a large sample of γ's had shown a marked increase over phase space below 300 mr. The π^o and η^o decay opening angles are both larger than this value in the energy range covered in this experiment, and hence no events from the $\Lambda\pi^o$ and $\Lambda\eta$ channels were lost as a result of the cut. The loss of events due to the interference of γ's from two π^o's or from a Σ^o and a π^o was compensated by a correction calculated from the known angular distributions of γ's from π^o and Σ^o decay. The average losses for the $\Sigma^o\pi^o$, $\Lambda\pi^o\pi^o$, $\Sigma^o\pi^o\pi^o$ and $\Lambda\pi^o\pi^o\pi^o$ channels were found to be 3°/o, 8°/o, 16°/o and 28°/o respectively. A correction was also made to allow for the loss of primary γ's because of "shadowing" by a spurious γ, i.e. the rejection of a primary γ by the bremsstrahlung cut because a spurious γ lay nearer the origin, within the 300 mr. angle. In the channel $K^-p \rightarrow \Lambda\pi^o\pi^o$, for example, the loss was ~ 3°/o.

c) Dip Cut

γ's with large dips were prone to bad measurement or to incorrect reconstruction. A cut was therefore made to remove all γ's with lines of flight within 10° of the optic axis, and it was estimated that the event loss due to this cut was about 4°/o. A correction was made from the knowledge that the azimuthal distribution of γ's about the beam direction was symmetric.

d) Cuts on Comptons

A correction was made using the Klein-Nishina formula to allow for cuts made at the scanning stage to reject Compton electrons of kinetic energy less than 7 Mev/c and produced at angles greater than 10° (see Section 3.6). The spurious γ background was reduced by rejecting all Compton electrons occurring at distances greater than 30 cms from the origin. This cut superseded an earlier cut made on the Compton pointing probability but which proved to be somewhat unreliable.

The Q distributions in the γ conversion length, ℓ_{γ}, are shown separately for pairs and Comptons in Figures 3.4 and 3.5. In histograms a) only the 300 mr cut on the $\gamma\gamma$ space angle was applied to remove bremsstrahlung, and the background of spurious γ's is seen to be large. In histograms b) all cuts were applied and the spurious γ background decreased considerably. Histograms c) show that for γ's belonging to an accepted fit, the $Q(\ell)$ distributions are almost flat, with little evidence of spurious γ background.

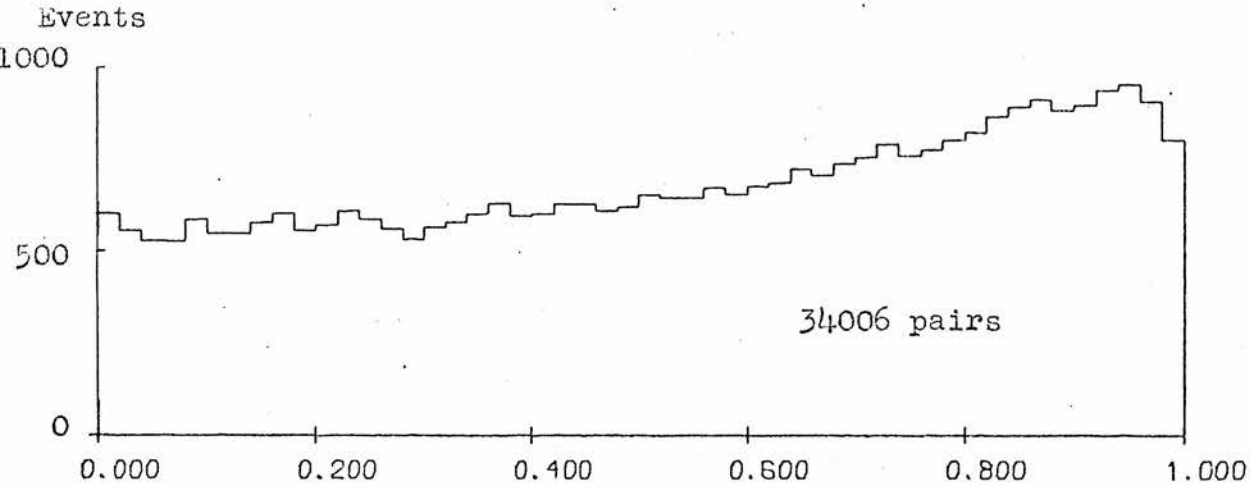

a) After 300 mr. bremsstrahlung cut.

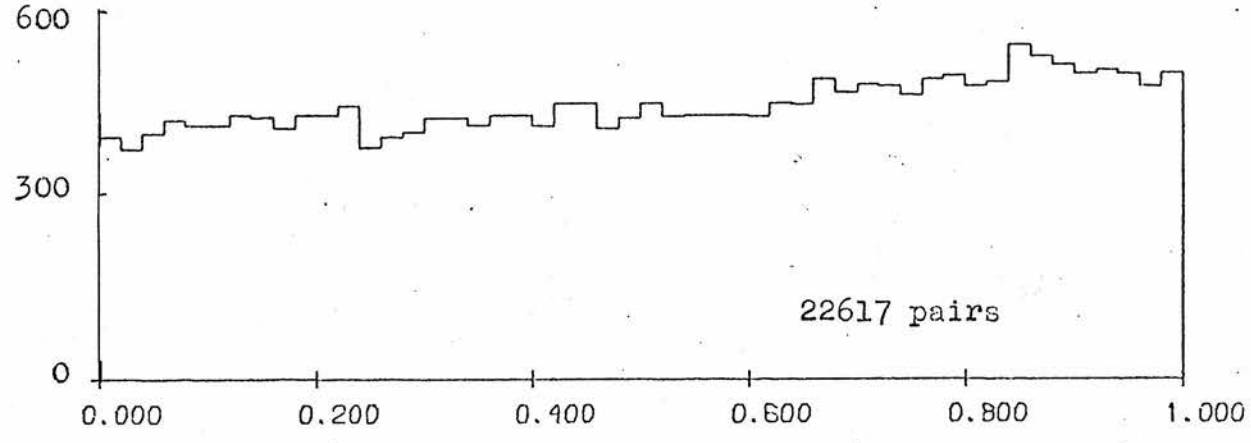

b) After all cuts.

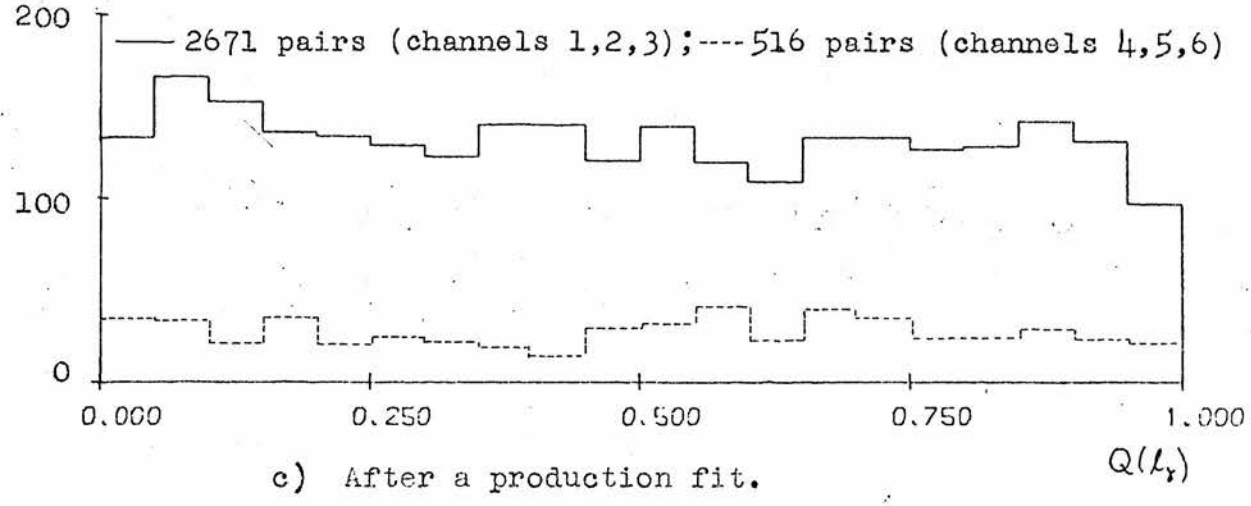

c) After a production fit.

FIG. 3.4 Distribution in $Q(\ell_\gamma)$ for the γ line of flight length, ℓ_γ, for pairs:— a) After only the bremsstrahlung cut, b) after all cuts, c) after a production fit.

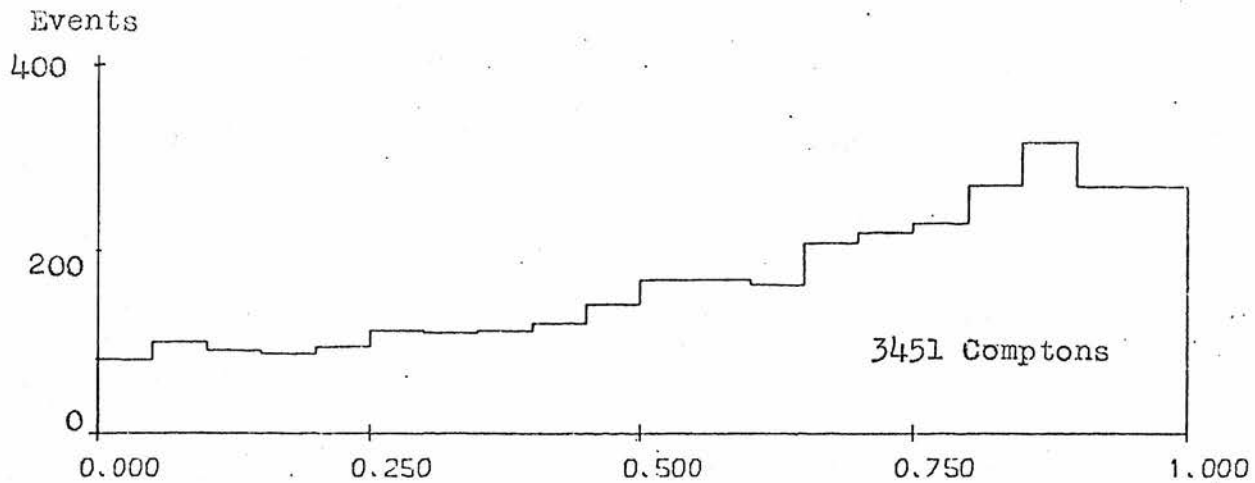

a) After 300 mr. bremsstrahlung cut.

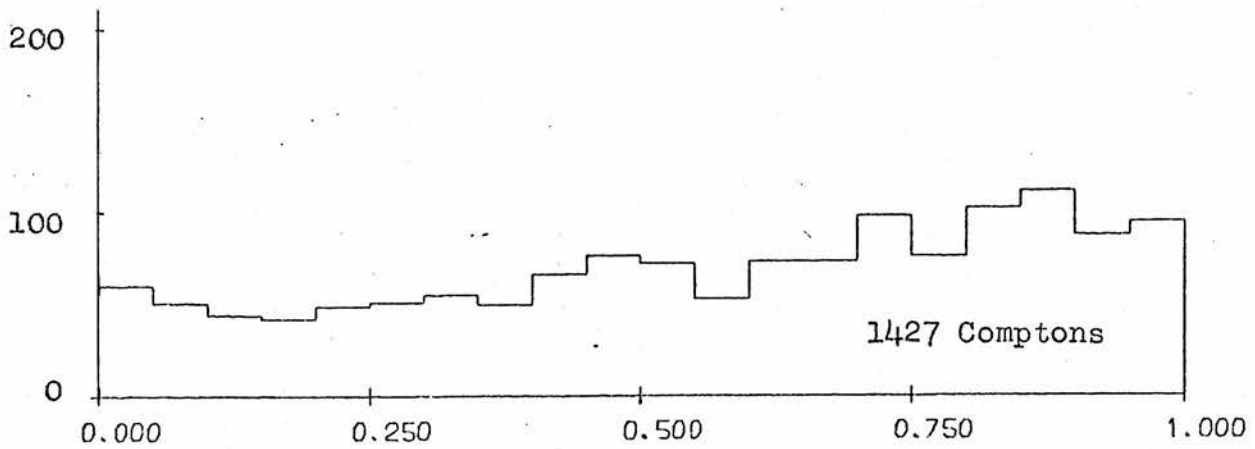

b) After all cuts.

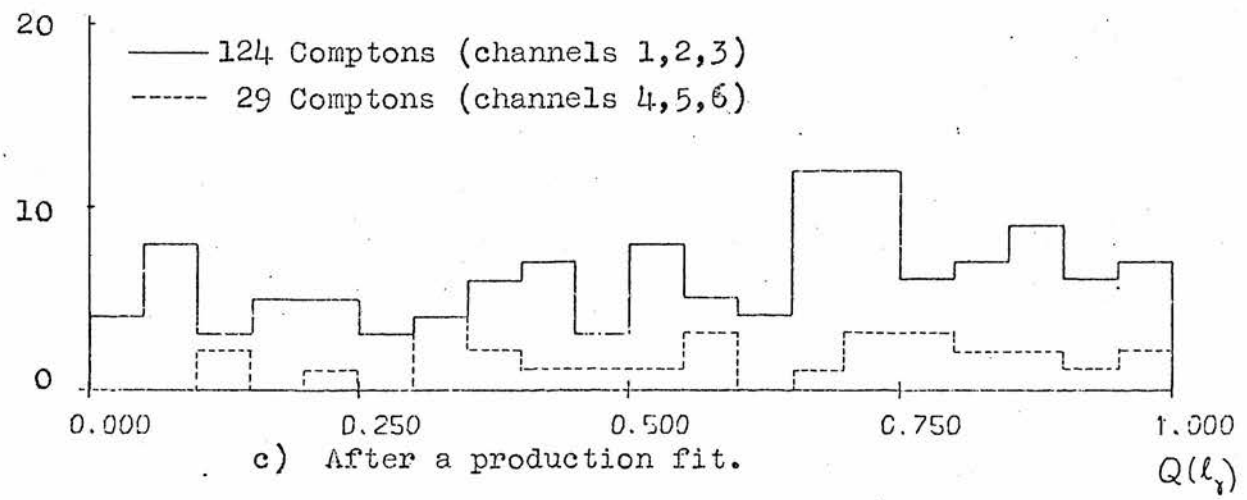

c) After a production fit.

FIG. 3.5 Distribution in $Q(\ell_\gamma)$ for the γ line of flight length, ℓ_γ, for Comptons. Histograms a), b), c) refer to the same samples as in Fig. 3.4.

The detection probability correction was applied to allow for γ detection, either as a pair or as a Compton within the limits set by the cuts described above. The detailed calculation of the detection weight is dealt with in Section 3.4 et. seq.

3.3 Fit Selection

Only those fits having a probability greater than 0.1°/o were initially accepted. (For the $\Lambda\,\pi^{o}$ channel this was later increased to 1°/o as explained in Section 6.2). It was found, however, that for some events the technique of fitting and cutting was not sufficient to resolve certain "hard-core" ambiguities among the surviving fits, and, so a final selection had to be made on the basis of fit probability. In the case of an event having several fits, each with the same number of γ's, that fit with the highest probability was chosen.

The first approach to this problem for ambiguous fits with different numbers of γ's was to select that fit with the greatest number of γ's subject to the condition that its fit probability was not less than one fifth that of any other fit. This choice was made on the assumption that if a more complex fit was successful, it was the most likely representation of the true event.

It was found, however, from an investigation of Monte Carlo event distributions (discussed later in Chapter 6) that for the $\Lambda\,\pi^{o}$ and $\Sigma^{o}\pi^{o}$ channels, the background arising from fits containing spurious γ's was substantially reduced by choosing on the basis of minimum complexity (i.e.

fewest γ's) and this method was therefore adopted for the selection of real events in these channels.

3.4 Gamma Detection Weight

As mentioned above, the total weight applied to an event was taken as the product of the weight factors calculated for each of its component particles. Unlike the Λ or the K^-, which occurred only once in an event, the γ could appear several times, and its weight, especially for the multipion events, was therefore of considerable importance.

The weight applied to each accepted γ was designed to compensate for those γ's lost because of:-

i) Scanning inefficiency

ii) Non-materialisation in the fiducial volume

iii) Cuts.

The development of the scan efficiency and materialisation corrections is dealt with in the following sections and an expression for the overall γ detection weight is derived. The scan efficiency correction is considered first.

3.5 Scan Efficiency Correction

The information transferred to the D.S.T. for an event contained a record of the scan history of each of the γ's measured, indicating the number of times it had been found by the scanners. The scan efficiency values were estimated directly from this data by making use of the coincidence technique of Geiger and Werner[14]. The double scan efficiency

η, was given by this method as:-

$$\eta = \frac{(N_1 + N_2 + N_{12}) \times N_{12}}{(\frac{N_1 + N_2}{2} + N_{12})^2}$$

where N_1, N_2 and N_{12} are respectively the numbers of γ's found by scanners 1 and 2 separately, and the number found in common.

A sample of approximately 15,000 measured γ's taken from an early D.S.T. was used in this study. The number of bremsstrahlung was reduced by applying a cut to the γ-γ angle, as mentioned above in Section (2.5). (At the time at which this analysis was performed the earlier value of the cut, 100 mr., was in operation.)

In order to reduce the spurious γ contamination, cuts were also made on the γ pointing probabilities at $\frac{1}{4}$°/o for pairs and 1°/o for Comptons, below which values the corresponding probability distributions showed large peaks. It was estimated that these cuts removed about one quarter of the total sample of γ's, but only about 2°/o of the true primaries. Those γ's surviving the cuts were regarded as representative of the primary sample and were used as input to the scan efficiency calculation.

Scan efficiency values were determined separately for pairs and Comptons. An overall estimate of the double scan efficiency showed the pairs to have a value of 95°/o and the Comptons of 85°/o. The ratio of pairs to Comptons was about 10 to 1 and the resultant lack of statistics for Comptons proved troublesome at a later stage when binning was introduced.

The dependence of the scan efficiency on certain γ parameters was next investigated with the aim of expressing the efficiency in terms of the significant variables. To this end the scan efficiency was calculated separately for:-

i) P - the γ momentum

ii) λ - the γ dip angle

iii) ϕ - the γ azimuth angle

iv) R - the distance from the origin to the conversion point

v) $R_p = R \cos \lambda$ - the distance R projected onto the scanning plane

vi) Z - the Z coordinate of the γ conversion point

vii) $P(\chi^2)$ - the γ pointing probability.

The variation of the double scan efficiency with each of these parameters is shown in Figures3.6, 3.7(a-g). An inspection revealed that the dependence on dip, azimuth and pointing probability was small, and in relation to the others could be disregarded.

To study the variation with each of the remaining four parameters - P, R, R_p and Z - separately, the scan efficiency plot for one variable was redrawn using only those γ's which lay on the flat portions of the other three. In this way the scan efficiency, expressed in terms of one variable, was made relatively independent of the others. These plots are shown as dashed lines in Figures 3.6, 3.7 (a-g). By making reference to the distributions, shown in Figure 3.8 (a-g), it was found that for about 95% of the pairs, the Z and R dependences were small, and fell off only near the chamber walls. A reduction in the effective chamber dimensions allowed the scan efficiency dependence on these variables to be disregarded, and the materialisation

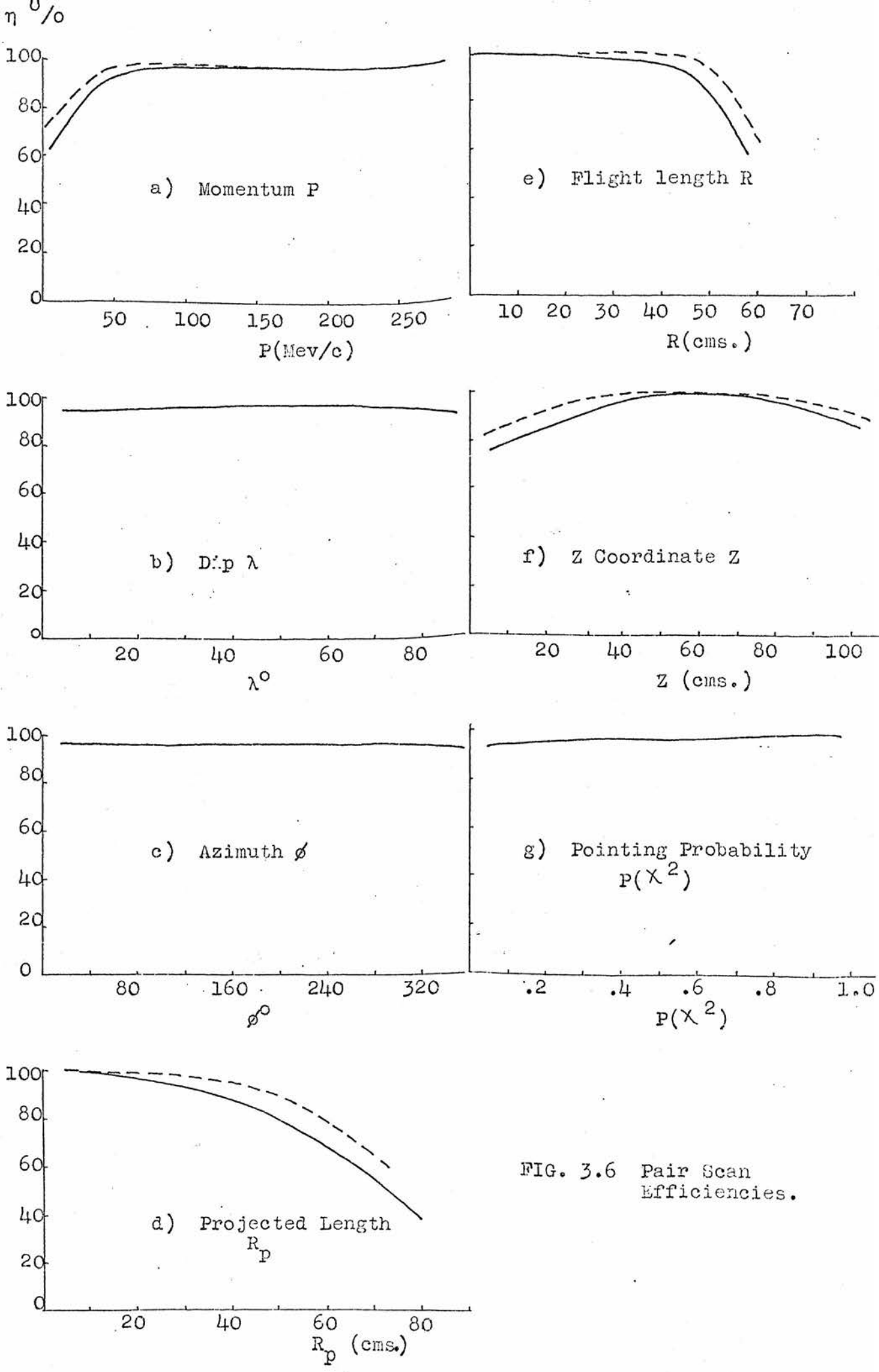

FIG. 3.6 Pair Scan Efficiencies.

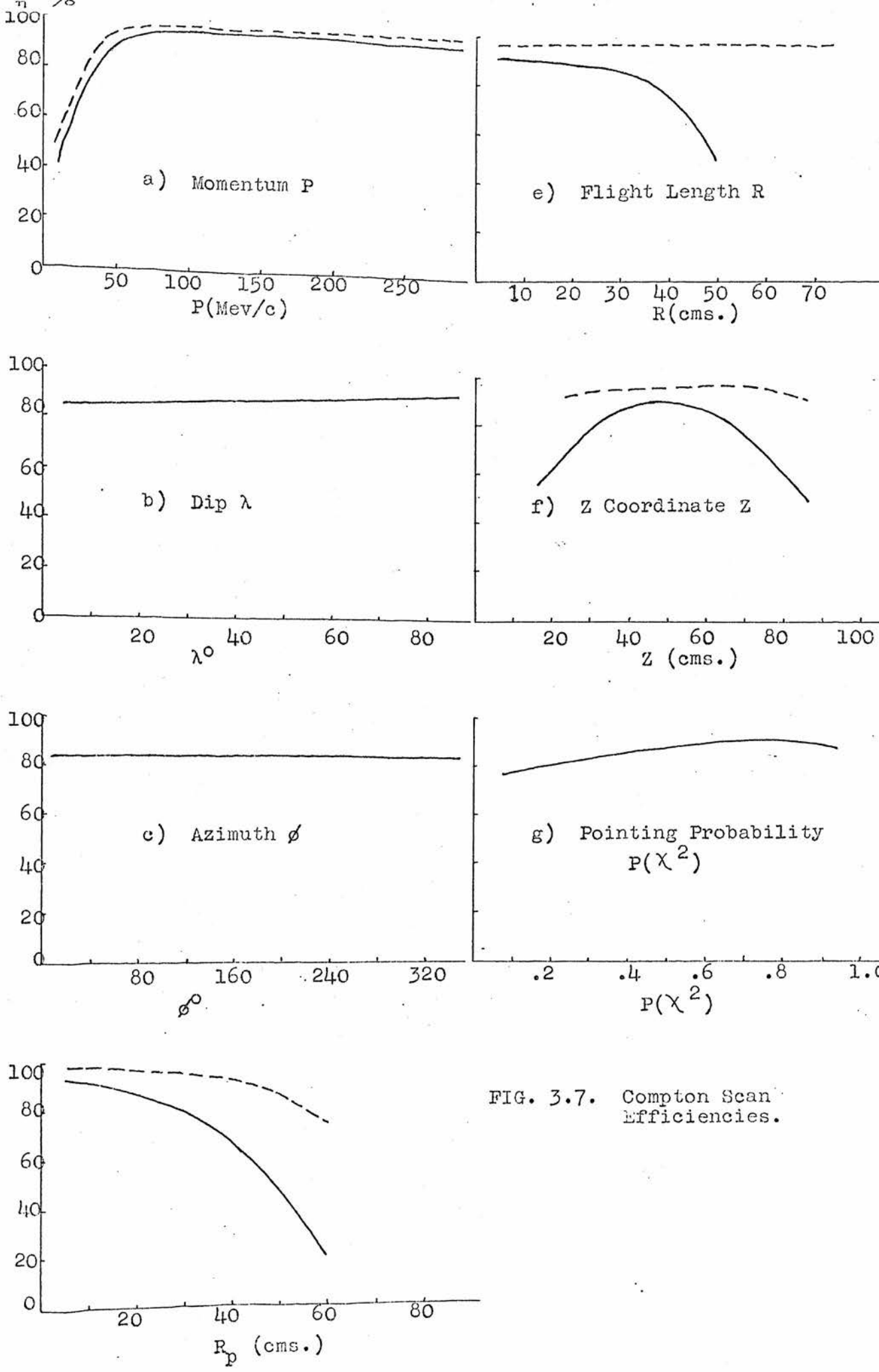

FIG. 3.7. Compton Scan Efficiencies.

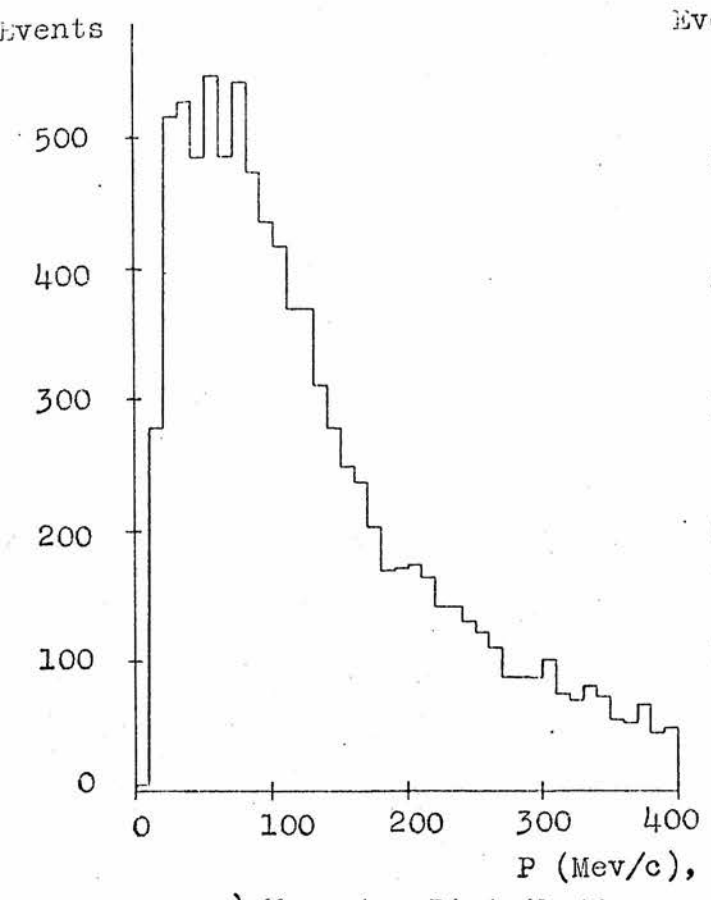

a) Momentum Distribution

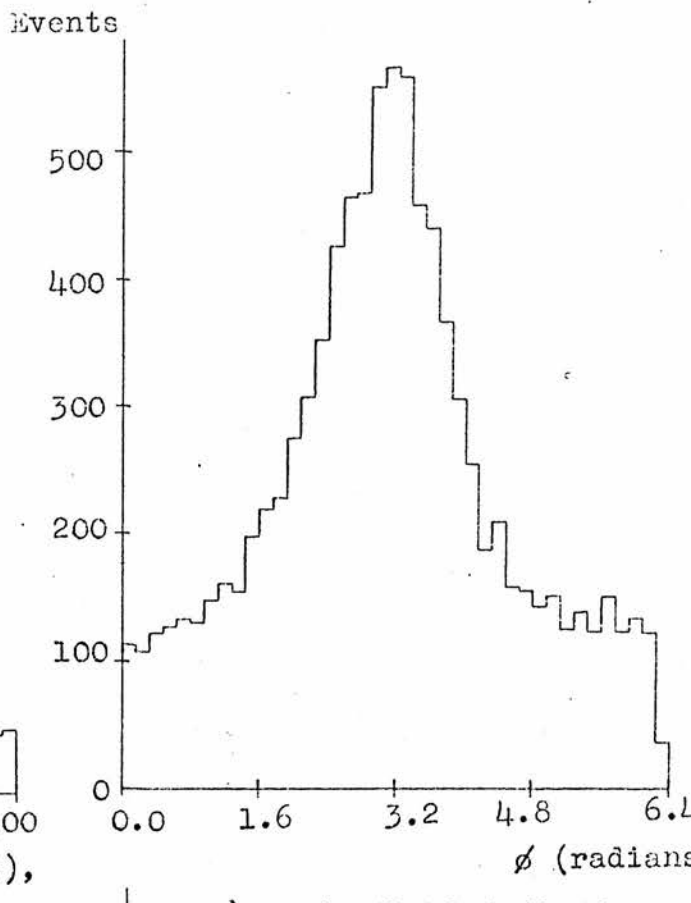

c) Azimuth Distribution

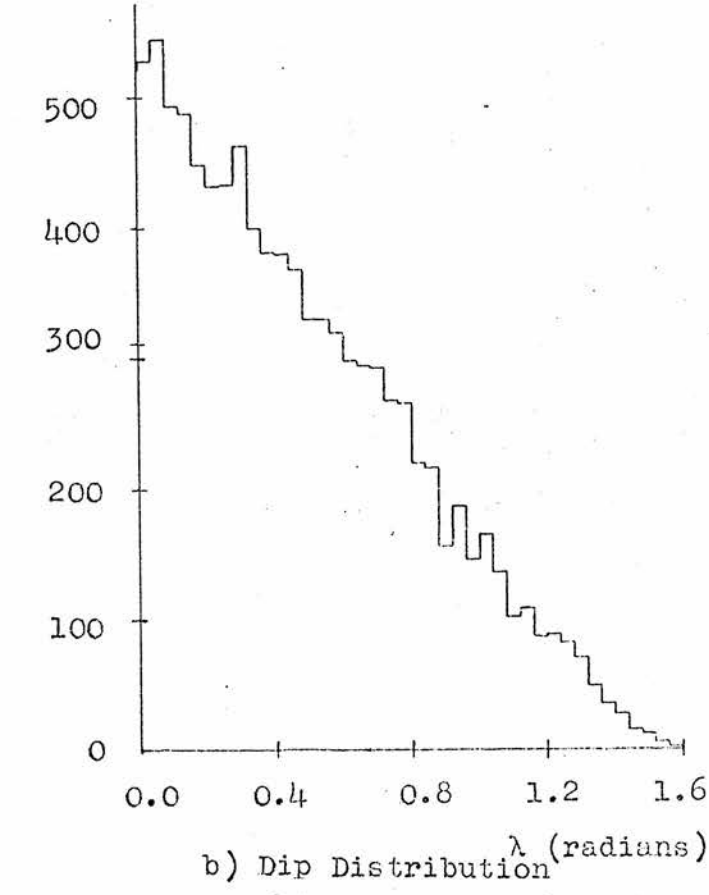

b) Dip Distribution

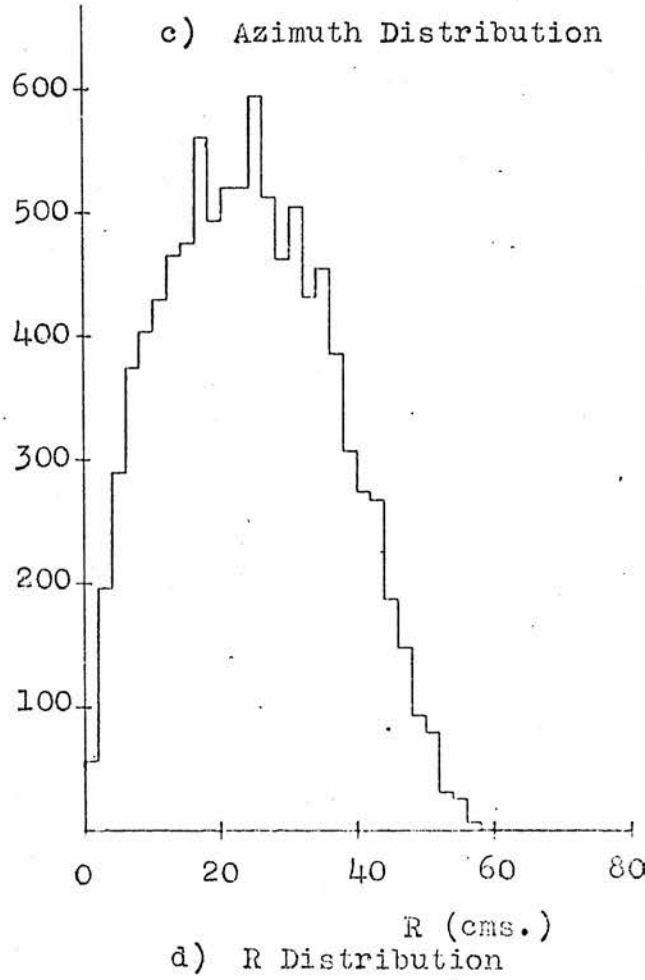

d) R Distribution

FIG. 3.8 Pair Distributions.

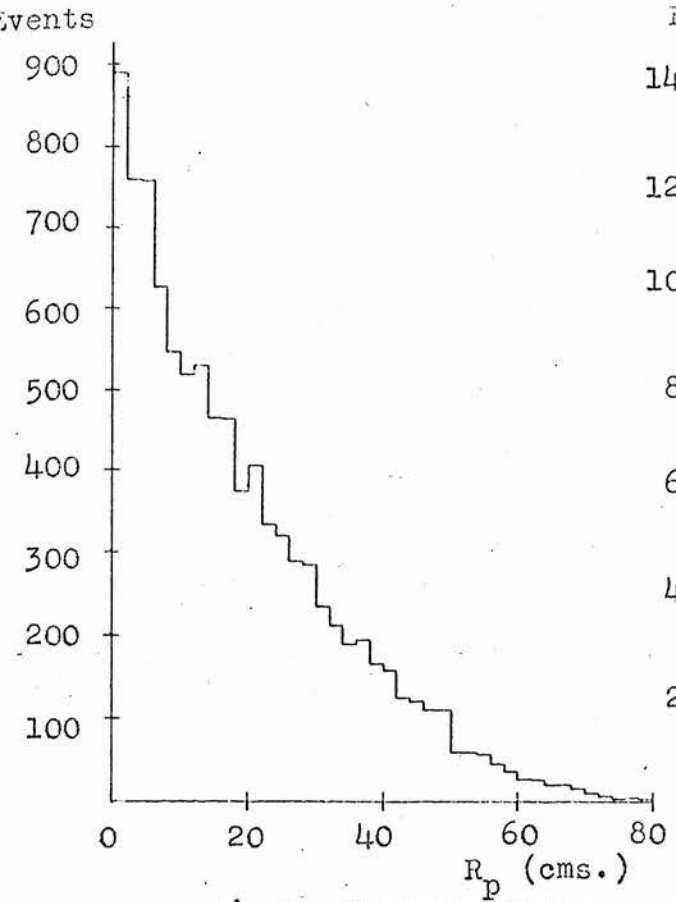

e) R_p Distribution

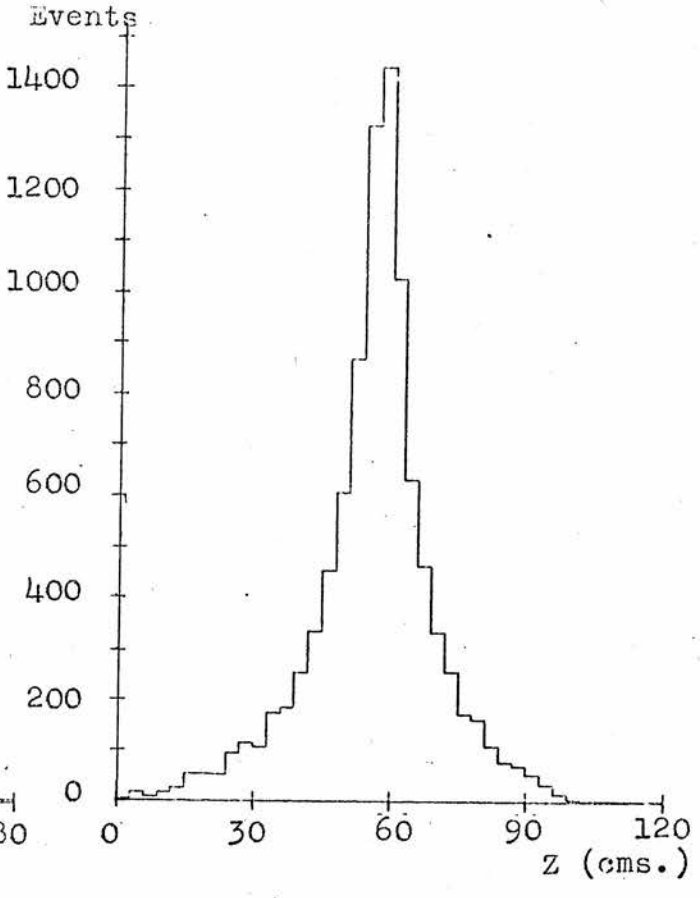

g) Z Distribution

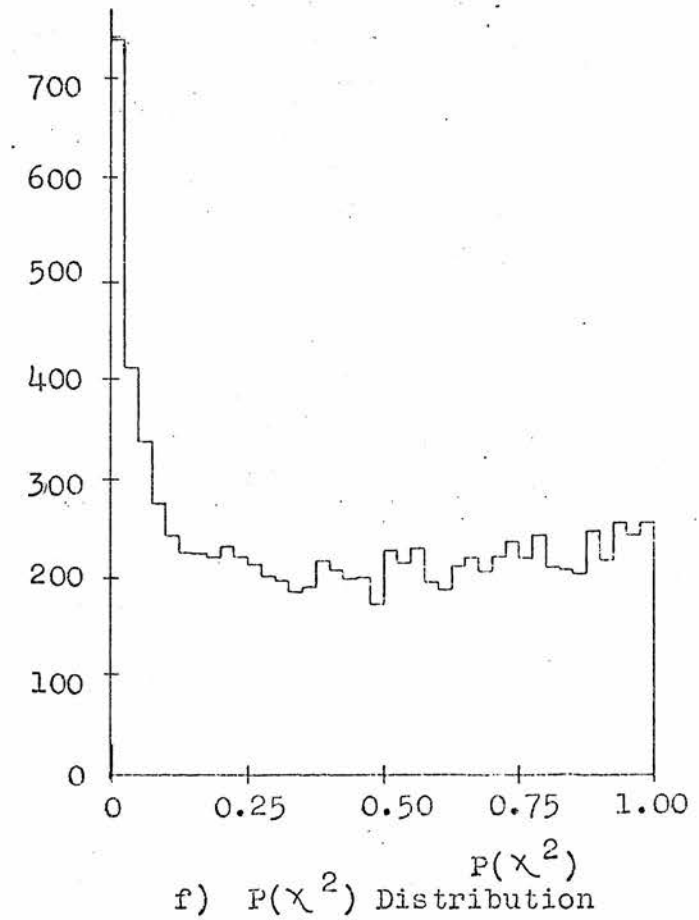

f) $P(\chi^2)$ Distribution

Fig. 3.8. Pair Distributions (Contd.).

weight was adjusted to compensate for the loss of good gammas (see Section 3.6). Hence from the seven quantities originally considered, two, P and R_p, emerged as being those mainly responsible for the variation in scan efficiency.

Scan efficiency tables for pairs and Comptons separately were constructed in terms of these two variables. The ranges of each of the parameters were partitioned so as to allow good statistics in each individual bin (minimum contents generally not less than 20), and to ensure a relatively fine resolution, particularly in areas where the scan efficiency showed large variations. The numbers of doubly and singly found γ's were accummulated for each bin, and, using the expression given above, the scan efficiency values calculated.

The variation of the scan efficiency with R_p is shown in Figures3.9, 3.10 for each of the momentum bins. Here smooth curves have been fitted by eye, by ensuring that the fitted values were consistent for both the P and R_p projections. Error bars on each of the points were drawn on the assumption that the distributions were Poissonian. As was mentioned above, the lack of statistics in many of the Compton bins produced a rather uneven distribution, making smoothing difficult, and for both pairs and Comptons, the low scan efficiency regionsat large values of R_p were very sparsely populated.

One important aspect of this method was that to a large degree the γ's in a particular bin each had the same "visibility". (The visibility of a γ is defined as the probability that it will be found by an average scanner),[15]

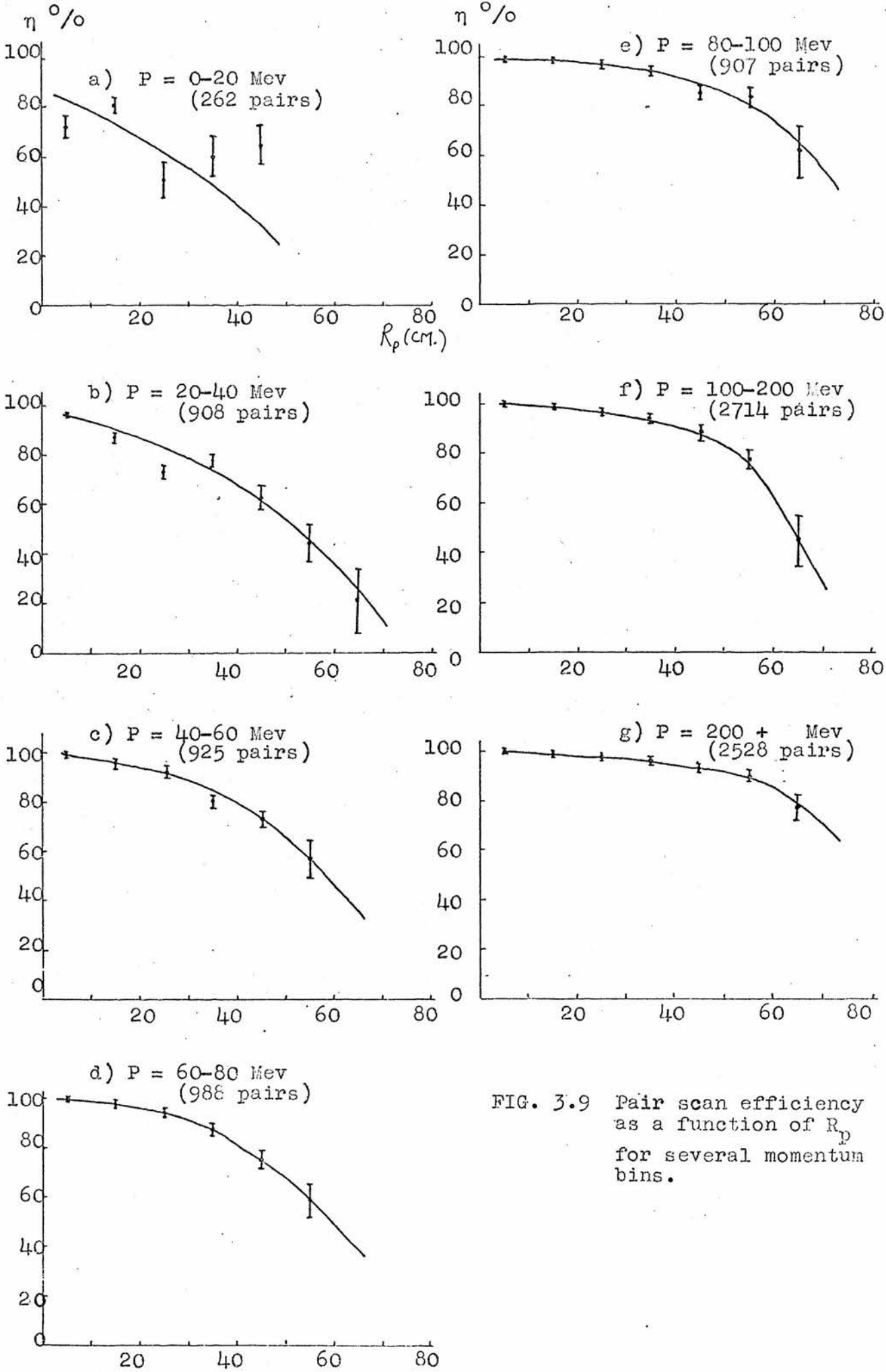

FIG. 3.9 Pair scan efficiency as a function of R_p for several momentum bins.

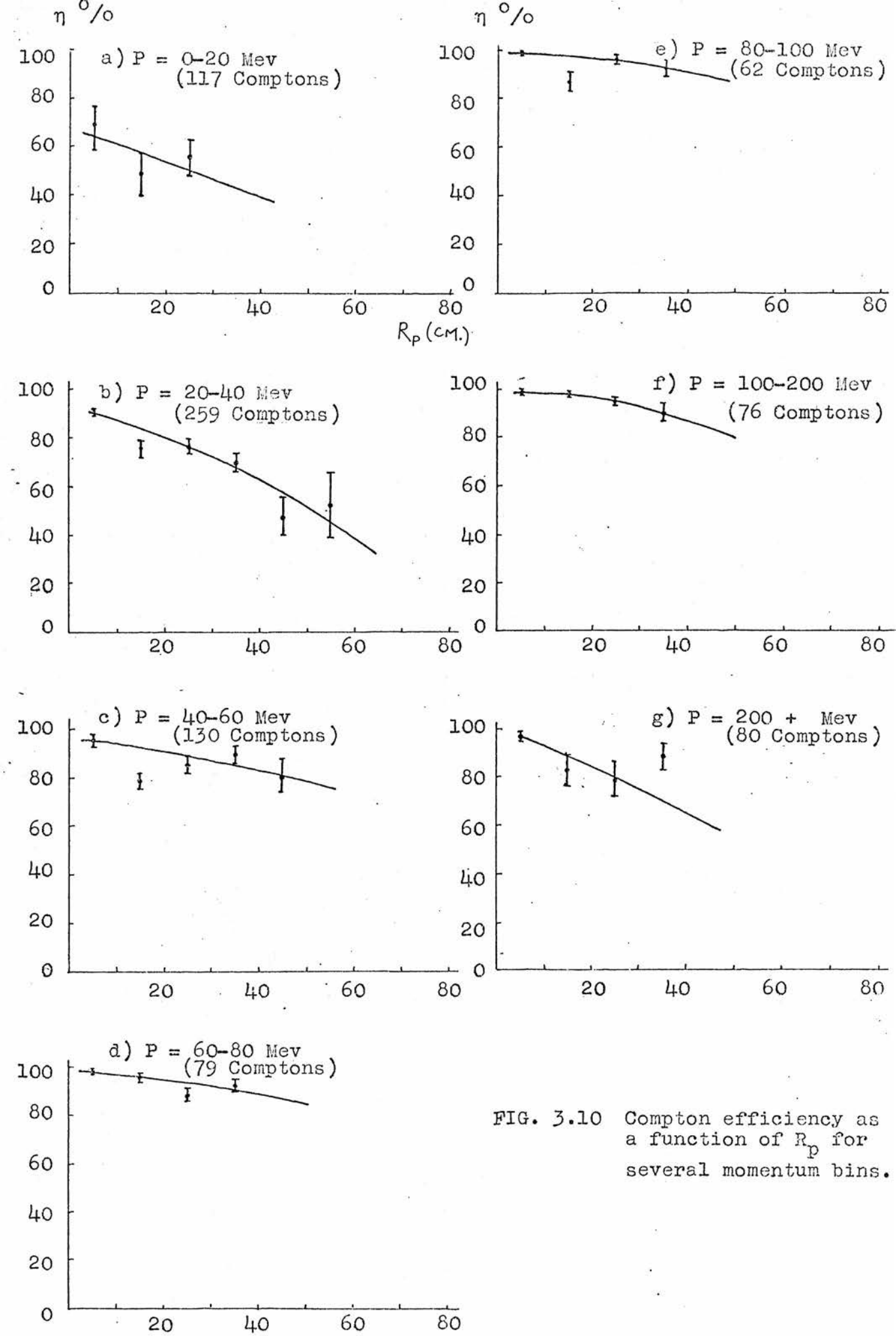

FIG. 3.10 Compton efficiency as a function of R_p for several momentum bins.

i.e. in any bin, no one γ was more difficult to see than any other. In this way the method fulfilled the basic assumption which underlay the use of the Geiger-Werner technique, that is, that all γ's have equal a priori probabilities of being observed.

It was found that in some bins with large values of R_p, the error in the scan efficiency became large, because of poor statistics, and so it was decided to reject all γ's falling into such a bin by means of a momentum dependent cut on the γ projected length. The loss of primary γ's due to this cut was allowed for by a correction applied to the γ materialisation probability as explained in the next section.

3.6 Materialisation Correction

The radiation length of 22 cms and a mean flight length of about 50 cms., allowed approximately 75°/o of the γ's produced to materialise within the chamber. A correction was applied to each accepted γ to compensate for the loss of those γ's which materialised outwith the maximum and minimum length cuts outlined above in Section 3.2(iii). The probability that a γ materialises within a distance x_{min} and x_{max} from the origin is:-

$$P_\gamma = e^{-x_{min}/\lambda} - e^{-x_{max}/\lambda}$$

where λ is the γ conversion length in the liquid. x_{min} was taken as 1 cm. and x_{max} the smaller of the γ potential length and the length corresponding to the point at which the scan efficiency became unreliable.

Separate weights were calculated and applied to each γ to allow for materialisation by producing either an electron pair or a Compton electron. The cross-sections for pair production in the liquid were derived analytically using the formula of Bethe and Heitler[16]. For pair production in the field of a nucleus, the probability that a photon of energy E, traversing a thickness dx g.cm^{-2} of material, produces a pair in which the positron has a kinetic energy between E' and E' + dE' is:-

$$\phi_{pair}(E, E')dE' = 4\alpha N \frac{Z^2}{A} r_e^2 \frac{dE'}{E} G(E,v)$$

where $\alpha = e^2/hc = 1/137$.

N is Avogadro's Number.

Z, A are the charge and mass numbers of the material.

r_e is the classical radius of the electron.

v is the fractional energy of the positron given by:-

$$v = \frac{E' + m_e c^2}{E}$$

and G(E,v) is given by:-

$$G(E,v) = \left[v^2 + (1-v)^2 + \tfrac{2}{3}v(1-v)\right]\left[\ln \frac{2E}{m_e c^2} \times v(1-v) - \tfrac{1}{2} - C(\gamma)\right].$$

$C(\gamma)$ is a factor which takes into account the screening effect of the atomic electrons on the electric field of the nucleus.

The probability that a photon of energy E undergoes a Compton scatter in a thickness dx g.cm^{-2} and the scattered

photon has an energy between E' and $E' + dE'$ is given by Klein and Nishina[17] as:-

$$\phi_{compton}(E,E')dE' = \frac{Cm_e c^2}{E} \cdot \frac{dE'}{E'} \left[1 + \left(\frac{E'}{E}\right)^2 - \frac{E'}{E} \sin^2\theta \right]$$

$$\text{for } E > E' > \tfrac{1}{2}m_e c^2 ,$$

where:-

C is a constant $(= 0.150\ Z/A)$.

m_e is the electron mass.

θ is the emission angle of the electron with respect to the original photon direction,

and c is the speed of light.

Separate materialisation probabilities were calculated for each run and in Figure 3.11 typical values are shown for all γ's, for pairs, and for Comptons, as a function of the γ momentum, calculated for a γ with a potential length of 45 cms.

The Compton contribution to the materialisation weight using the above formula also allowed for the cuts already described in Section 2.3 by which Compton electrons of energy less than 7 Mev and produced at angles greater than 10° were rejected. (The correction for pairs removed by the 7 Mev energy cut was found to be negligible and was not made.)

3.7 Gamma Weight Expression

Having calculated these corrections the next problem was to combine them to form an overall γ weight. In the first approach the final γ weight, or "separated" weight, was taken as the direct product of the individual correction

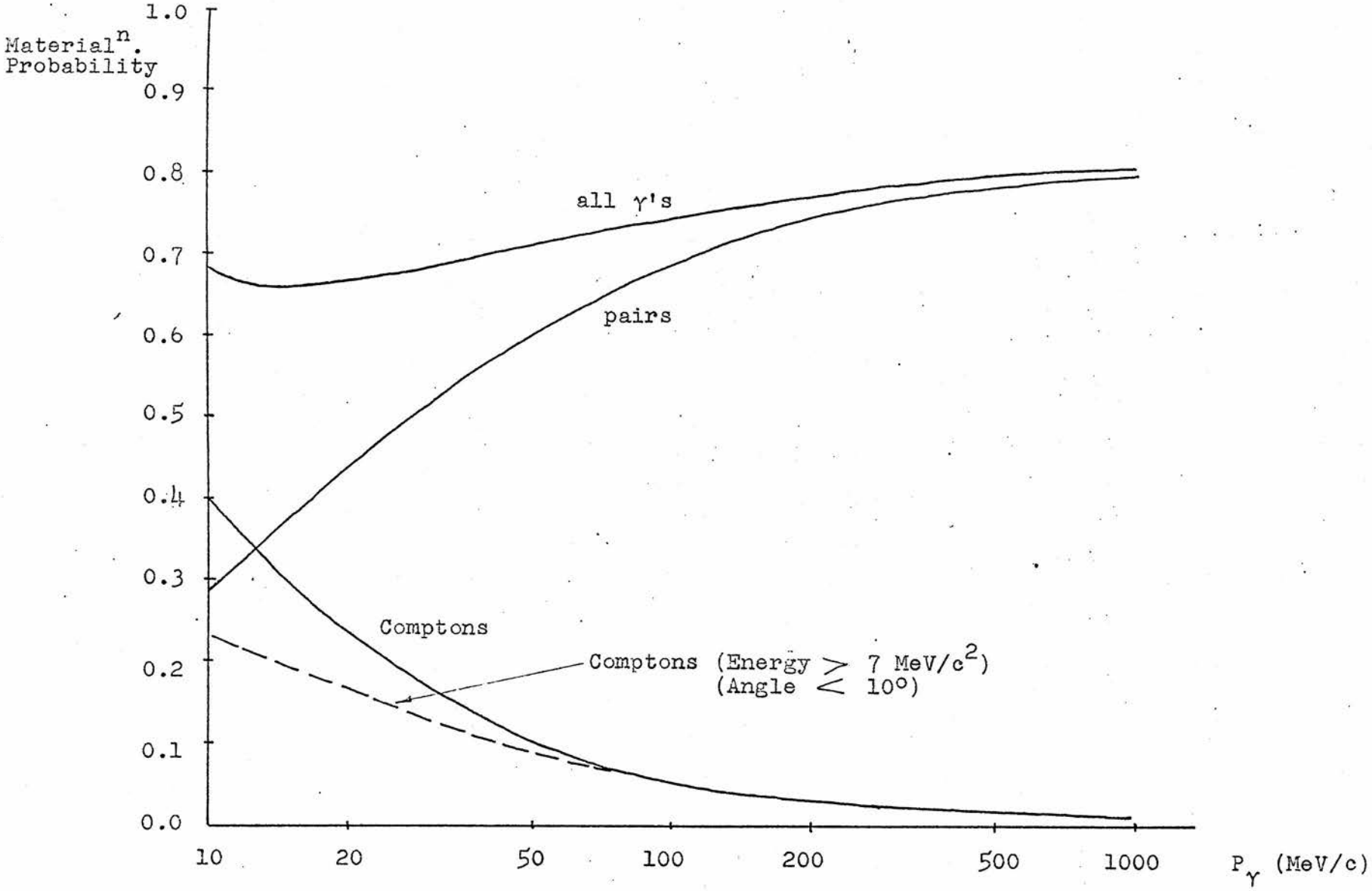

FIG. 3.11 Probability of materialisation within the chamber for pairs. Comptons and all γ's as a function of γ momentum, calculated for a γ with a potential length of 45 cm.

factors,

i.e. W_γ = W(materialisation) × W(scan efficiency) × W(cuts).

However, although this method provided acceptable weights, it was eventually replaced by the "Integrated Weight" method which combined the corrections in a different manner and offered several advantages over the first approach. An appreciation of this method can be gained from the following.

If one considers a beam of γ's of fixed momentum travelling along the x-axis and if there are N_o at $x = 0$, then the number materialising, dN_{mat}, and the number observed, dN_{obs}, within an interval dx at x are given by:-

$$dN_{mat} = {}^{N_o}/_{\lambda}\ e^{-x/\lambda}\ dx \qquad (1)$$

$$dN_{obs} = {}^{N_o}/_{\lambda}\ \eta(x)\ e^{-x/\lambda}\ dx \qquad (2)$$

where λ is the conversion length and $\eta(x)$ is the scan efficiency, as a function of length. If n γ's are observed between $x = x_{min}$ and $x = x_{max}$, then, if their conversion points are x_i :-

$$N_{T(obs)} = n$$

$$N_{T(mat)} = \sum_{i=1}^{n} {}^{1}/_{\eta(x_i)}$$

From equations (1) and (2):-

$$N_{T(mat)} = \sum_{i=1}^{n} {}^{1}/_{\eta(x_i)} = \int_{x_{min}}^{x_{max}} dN_{mat}$$

$$= N_o\left[e^{-x_{min}/\lambda} - e^{-x_{max}/\lambda}\right] \qquad (3)$$

$$N_{T(obs)} = n = \int_{x_{min}}^{x_{max}} dN_{obs}$$

$$= N_o/\lambda \int_{x_{min}}^{x_{max}} \eta(x)\, e^{-x/\lambda}\, dx \quad . \qquad (4)$$

From equations (3) and (4) estimates can be made of N_o, say N_1 and N_2 respectively.

$$N_1 = \sum_i 1/\eta(x_i) \Big/ \left[e^{-x_{min}/\lambda} - e^{-x_{max}/\lambda} \right]$$

and therefore the weight applied to each event, W_1, is given by

$$W_1 = 1/\eta(x) \left[e^{-x_{min}/\lambda} - e^{-x_{max}/\lambda} \right] .$$

Likewise:-

$$N_2 = n \Big/ \int_{x_{min}}^{x_{max}} \eta(x)\, e^{-x/\lambda}\, d(x/\lambda)$$

and the weight W_2 given by:-

$$W_2 = 1 \Big/ \int_{x_{min}}^{x_{max}} \eta(x)\, e^{-x/\lambda}\, d(x/\lambda) \quad .$$

W_1 is the "separated weight" mentioned above, and W_2, the "integrated weight", is the inverse of the probability of detecting the γ, integrated over its potential length, and is in fact the Maximum Likelihood estimate. Both methods give the same average γ weight but the integrated method has the advantage of producing a smaller dispersion about the mean.

With the separated method the weight given to a spurious γ which survived the cuts was usually large because such a γ generally fell into a low scan efficiency region, and the effect of this was to upset the overall event weight. This problem was, however, removed by the use of the integrated weights in which the presence of the exponential factor $e^{-x/\lambda}$ in the integral kept the value small and made the contribution to the total event weight from residual spurious γ's much less significant.

The average weight using the integrated method was 1.35 with a standard deviation of 0.30 (s.d. = 0.38 with the separated method). Histograms of the weights applied to a sample of γ's using both methods are shown in Figure 3.12.

3.8 Note on Spurious γ's

The application of the pointing cuts of $^1/_4{}^\circ/o$ for pairs and $1^\circ/o$ for Comptons, and the bremsstrahlung cut at 100 mr. was an early attempt at dealing with the background of spurious gammas. Because of the poor statistics of fitted γ's, the sample of all measured γ's was used to test the effectiveness of the cuts. It was found that the histograms of the conversion lengths of the surviving γ's showed a large departure from the exponential distribution expected if the cuts had been successful in rejecting the background. Similar effects were observed at the other laboratories, and several independent studies were undertaken to find the most suitable way of treating the problem.

The background was found to predominate at low momenta (below 100 Mev/c) and at large distances from the origin.

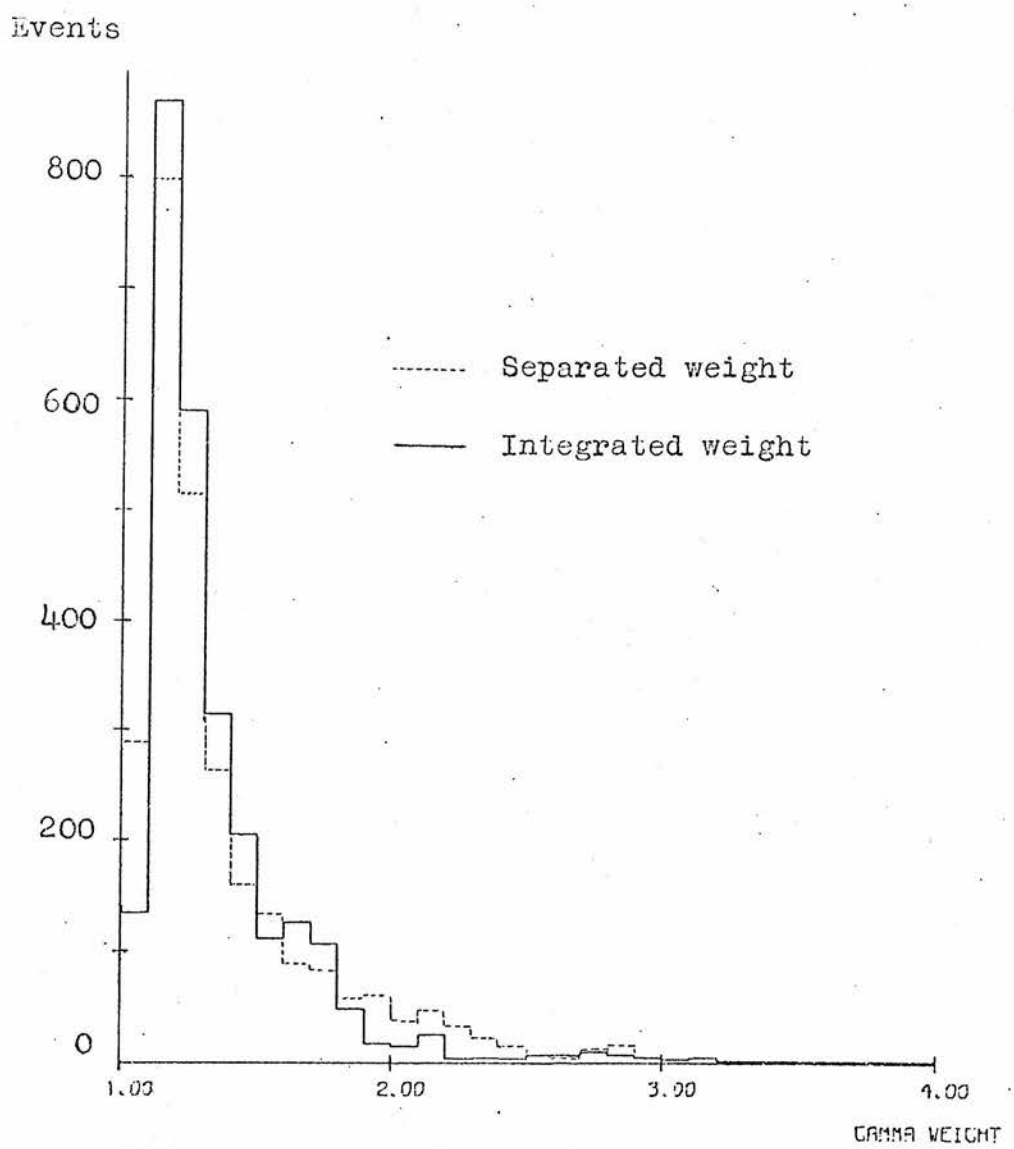

FIG. 3.12 Histograms showing gamma weights calculated using "separated method" (dashed line) and "integrated method" (solid line).

At Edinburgh, an attempt to devise a series of momentum dependent pointing cuts to replace the existing ones however proved unsuccessful, and a further investigation aimed at parametrising the background from a study of the $P(\chi^2)$ and χ^2 distributions also failed, although it did serve to define a better $\frac{1}{2}^{o}/o$ cut on pair pointing probability.

With increased fit statistics, and with an improved cutting, weighting and selection technique, it was found that the spurious γ problem was not as critical as was first thought.

For the two-body channels the minimum complexity selection procedure (see Section 3.3) allowed most of the spurious γ background to be rejected, and for the higher channels the application of more restrictive cuts on the γ maximum length as described in Section 3.2(iii) had the same effect.

The extent of the remaining background of accepted fits in the $\Lambda\pi^{o}$ and $\Sigma^{o}\pi^{o}$ channels, containing spurious γ's was investigated by adding "tagged" spurious γ's to Monte Carlo generated events and by fitting, cutting and weighting these events in the normal way. This analysis is described in more detail in Chapter 6.

CHAPTER 4

NUCLEAR EVENT BACKGROUND

4.1 Introduction

The use of a heavy liquid mixture in this experiment enabled the detection of gammas and from this aspect it had a considerable advantage over hydrogen. One of the drawbacks, however, was the fact that interactions occurred not only on the hydrogen atoms in the mixture but also on target protons which were bound in the liquid nuclei, and which therefore had unknown Fermi momenta. Such events violated the assumption made when fitting that the target particle was at rest in the laboratory frame, and were usually rejected when the constraints of energy and momentum conservation were applied. A background arose, however, from those nuclear events in which the momentum unbalance was not sufficiently large to destroy the fit, and which were therefore accepted as occurring on hydrogen.

A preliminary Monte Carlo study indicated that about 10°/o of the interactions were expected to occur on free protons and about 45°/o on bound protons, the remainder being on neutrons. It was estimated that approximately three-quarters of those events with bound proton targets, and producing a Λ and n γ's ($n \geqslant 2$), would have visible evaporation proton tracks, allowing them to be rejected at the scanning stage. Hence the signal to noise ratio after scanning was $^{10}/_{45} \times 4 \doteq 1$ and it was hoped that this ratio would be substantially increased by fitting.

To have an estimate of the magnitude of the residual

background of events occurring on bound protons in the fitted "hydrogen" sample, a portion of the film was scanned for essentially nuclear events of the type - negative one prong, V^o, $n\gamma$ ($n \geqslant 0$) - occurring on neutron targets (e.g. $K^- n \longrightarrow \Lambda \pi^-$). The equivalent numbers of events in the corresponding nuclear proton channels (e.g. $K^- p_{nuclear} \longrightarrow \Lambda \pi^o$) were calculated by taking account of the various differences, for example in cross-section, and in target density, between the two types of interaction. The background of nuclear events in each channel was therefore found by a comparison of the estimated number of bound proton fits with the number of accepted hydrogen fits in that channel.

Throughout scanning, measurement and analysis, the nuclear event data were dealt with in a way which resembled as closely as possible that used for the hydrogen events, in an attempt to reduce to a minimum any biasses which might have occurred from dissimilar treatments.

4.2 Scanning and Measurement

The nuclear event topologies were scanned for on about 16,000 frames of run 2 film (beam momentum 650-820 Mev/c). A typical configuration is shown in Figure 4.1. The scan rules employed were based on those used for the original scanning of the hydrogen events, described in Section 2.3, with only minor modifications to accommodate the π^- track from the interaction origin. Those events having visible evaporation proton tracks at the origin were rejected using the same criteria as in normal scanning. The scan data were

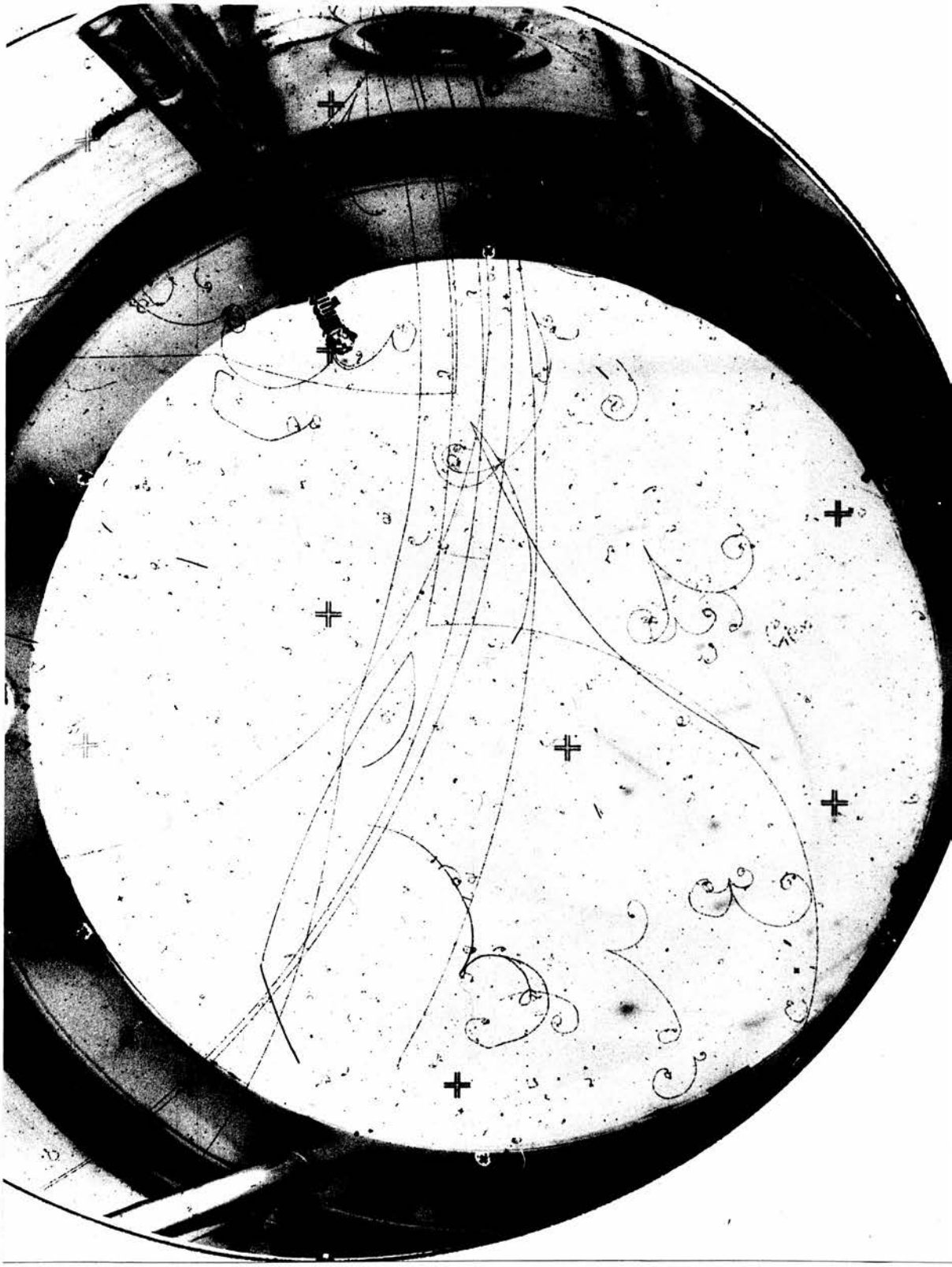

FIG. 4.1 Example of a $K^- n \longrightarrow \Lambda \pi^-$ interaction.

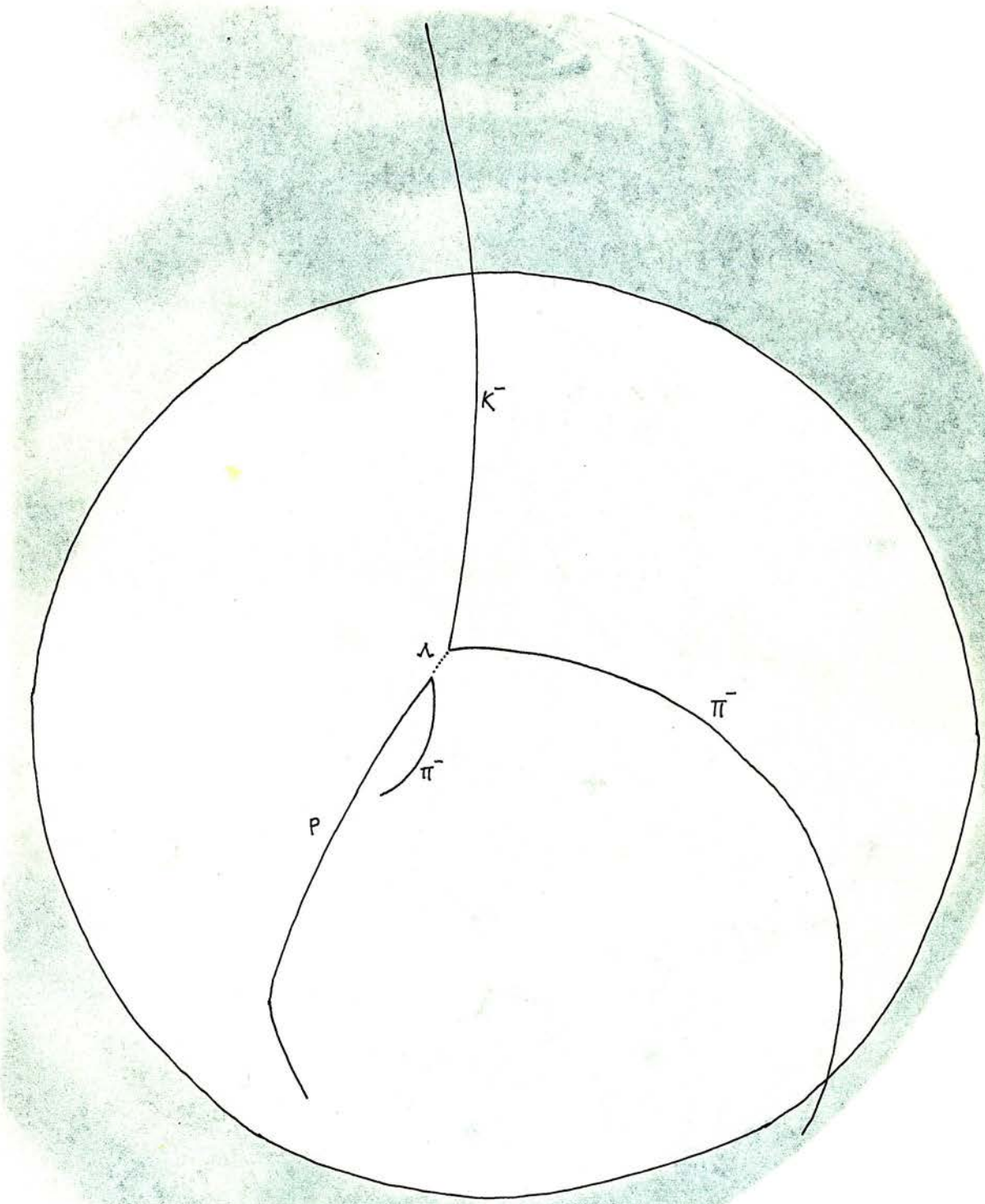
K⁻
Λ
π⁻
π⁻
p

processed by a program chain similar to that described in Section 2.3, and the events measured at CERN using the DOLL system.

4.3 Analysis - Correction Factors

When trying to estimate the number of bound proton events, N_p, from the number of neutron events actually present in a particular sample of film, N_n, it was necessary to correct for the basic differences between the two types of interaction. The relation between N_p and N_n can be written:-

$$N_p = R_T \times R_x \times R_A \times N_n$$

where R_T expresses the target density ratio $\rho_{proton}/\rho_{neutron}$ in the liquid nuclei; R_x is the cross-section ratio between the K^-p and K^-n interactions; and R_A the ratio of the reabsorption probabilities of the π^o and π^- produced in the primary interactions. Each of these corrections is now considered in detail.

i) Target density

More explicitly the factor R_T gives the relative probabilities that a kaon interacts on a nuclear proton or neutron. For kaons of momentum $\sim$ 800 Mev/c the mean free path in nuclear matter is of the order of 1 fermi, and it is therefore reasonable to assume that the interactions will occur predominantly in the surface regions of the heavy nuclei.

Using a naïve model of the nucleus one might expect that Coulomb forces would tend to spread the protons around the surface because of their mutual repulsion. Further consideration,

however, indicates that the effect of the Coulomb repulsion is to raise the proton potential well relative to that of the neutron, and thereby create a region at the surface available to neutrons and not to protons. Hence in this

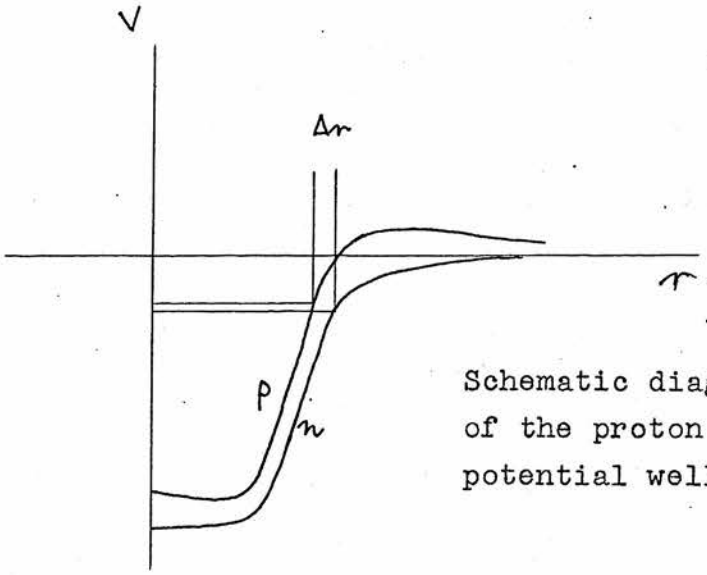

Schematic diagram of the proton and neutron potential wells

more sophisticated model, one would expect to find more neutrons in the surface than protons.

A certain amount of information relevant to this problem was gained from experiments which studied separately the "matter" and "charge" distributions in the nucleus. More recently, however, experiments have been performed to provide information specifically on the proton/neutron distributions in the outermost regions of the nucleus, mainly using π and K mesons as probes.

An early experiment by Abashian et al.[18] in 1956 measured the total π^+ and π^- absorption cross-sections on lead, and the results suggested that the neutron and proton root-mean-square (r.m.s.) radii were equal.

In the last few years, however, K^- absorption experiments have produced evidence to suggest that a neutron excess

does exist in the surface region. Aslam and Rook[19] analysed the data of Wiegand[20] (1969), obtained by observing K^-- mesonic X-ray spectra in medium and heavy elements, and by correlating the absorption coefficients for particular orbits with a model for the nuclear mass distribution, they estimated that for heavy nuclei the neutron r.m.s. radius was approximately 0.3 fermi greater than that for the protons.

An experiment by Davis et al.[21] in 1967 investigated the absorption of stopped K^- mesons in nuclear emulsions. They calculated the ratio of K^-p to K^-n interactions for both the lighter elements (H, C, N, O) and the heavy elements (Ag, Br) in the emulsion. The assumption was made that in the lighter elements - C, N, O - having equal numbers of neutrons and protons, the neutron and proton distributions would not differ. Hence the interactions on these nuclei formed a control experiment. The value found for the ratio $\frac{(K^-n/K^-p)\ \text{heavy}}{(K^-n/K^-p)\ \text{light}}$ was $5 \pm \begin{matrix}1.2\\0.8\end{matrix}$ and this was interpreted by Burhop[22] as indicating that the neutron surface thickness or "transition region", that is, the width of that region where the density varies from 90°/o to 10°/o of the value at the centre of the nucleus was 50°/o larger than for the proton distribution, assuming the mean radii equal. This analysis was, however, criticised by Bugg et al.[23], mainly on the basis that the method of event selection may have been prone to bias (98°/o of the events were rejected).

A very recent experiment by Allardyce et al.[24] (1972) in which the ratio of the π^+ and π^- reaction cross-sections have been measured for a series of nuclei, from carbon to lead, over the momentum range 0.7 to 2.0 GeV/c, has shown, however,

that the difference between the neutron and proton root-mean-square radii is very small (less than 0.1 fermi).

The situation is therefore somewhat confused with evidence for and against a neutron excess in the nuclear surface. In the case of those experiments which lend support to the neutron "skin" hypothesis, the assumptions made concerning the various processes utilised to study the nuclear distributions have given rise to large uncertainties, and hence no conclusive evidence for the existence of such a skin has been produced[25]. In view of this it was assumed for this experiment that the proton and neutron distributions were identical in all regions of the nucleus. The value of R_T was therefore taken as the ratio of the numbers of protons to neutrons averaged over the C, F and Br nuclei in the liquid, and was calculated to be 0.86.

ii) Cross-section ratio

The calculation of R_X, the cross-section ratio, was made from a knowledge of the transition amplitudes describing the reactions, and is dealt with later in detail for each channel.

iii) Reabsorption probability

The relative probabilities of absorption of the outgoing π^o and π^- produced in the primary K^-p and K^-n interactions by the nucleons of the same nucleus was expressed by the factor R_A. The value of this factor depends on both the proton and neutron distributions in the nucleus and on the π^o N cross-sections. On the assumption made above that

the proton and neutron distributions are identical, the rescattering should depend only on the π° cross-sections. It was assumed that these cross-sections were equal and hence the value of R_A was taken as unity. No allowance was made for the relative probabilities of the π° and π^{-} to produce detectable protons (of momentum greater than 200 Mev/c) by reinteraction, i.e. to produce a signal whereby events from one type of interaction would be preferentially rejected by the cut made on proton length (see Section 2.3). The magnitude of this correction was considered small in relation to the others.

4.4 Background Estimation

Method I

Apart from the fact that the interactions occurred on different target particles, the main distinguishing feature between the proton and neutron events, as far as the fitting was concerned, was that a π° was produced in one case and a π^{-} in the other. In order to keep the analyses of both types of event as similar as possible, the differences between the π° and the π^{-} were investigated from the viewpoint of their respective fit input error matrices, upon which the outcome of the fit largely depended, with the aim of superimposing the π° resolution on the π^{-} prior to fitting. The 3×3 error matrix for each track, containing the measurement errors, in the momentum, ΔP, in the dip, $\Delta \lambda$, and in the azimuth, $\Delta \phi$, was of the form

$$\begin{matrix} \langle \Delta P^2 \rangle & \langle \Delta P \Delta \lambda \rangle & \langle \Delta P \Delta \phi \rangle \\ \langle \Delta \lambda \Delta P \rangle & \langle \Delta \lambda^2 \rangle & \langle \Delta \lambda \Delta \phi \rangle \\ \langle \Delta \phi \Delta P \rangle & \langle \Delta \phi \Delta \lambda \rangle & \langle \Delta \phi^2 \rangle \end{matrix} .$$

The first order approach to making the π^- appear as a π^o was to take no account of the differences between the respective correlation terms ($\Delta P \Delta \lambda$ etc.), on the assumption that their influence on the fit was negligible, and to alter only the diagonal elements of the π^- matrix.

To have some idea of the values of the π^o matrix elements, several hundred π^o's were constructed by pairing γ's from a previous measurement in 0-constraint and 1-constraint fits. The distributions in momentum, P, of the fitted π^o errors in P, λ, and ϕ, were compared with the corresponding distributions for the measured π^- parameters.

It was found that the π^o error distributions were much more widely spread than those of the π^-, as can be seen in Figures 4.2, 3, 4, although the centres of gravity of corresponding distributions lay in approximately the same region. An initial attempt at improving the overlap was made by multiplying each of the π^- error terms by a factor of $\sqrt{2}$ and in the case of a stopping π^-, the momentum error was increased by a factor of 2. These factors were then used to distort the measured π^- diagonal error terms, and the central values of each of the parameters randomised within the increased spread.

The assumption inherent in this method of comparing the π^o and π^- error matrices was that the π^o could be constructed prior to the production fit from its decay γ's, and its error matrix inspected. When fitting the hydrogen events, however, the π^o was generated from its decay γ's during, and not before, the production fit, and as such its input error matrix could not be known exactly.

In addition to the above changes, the position of the

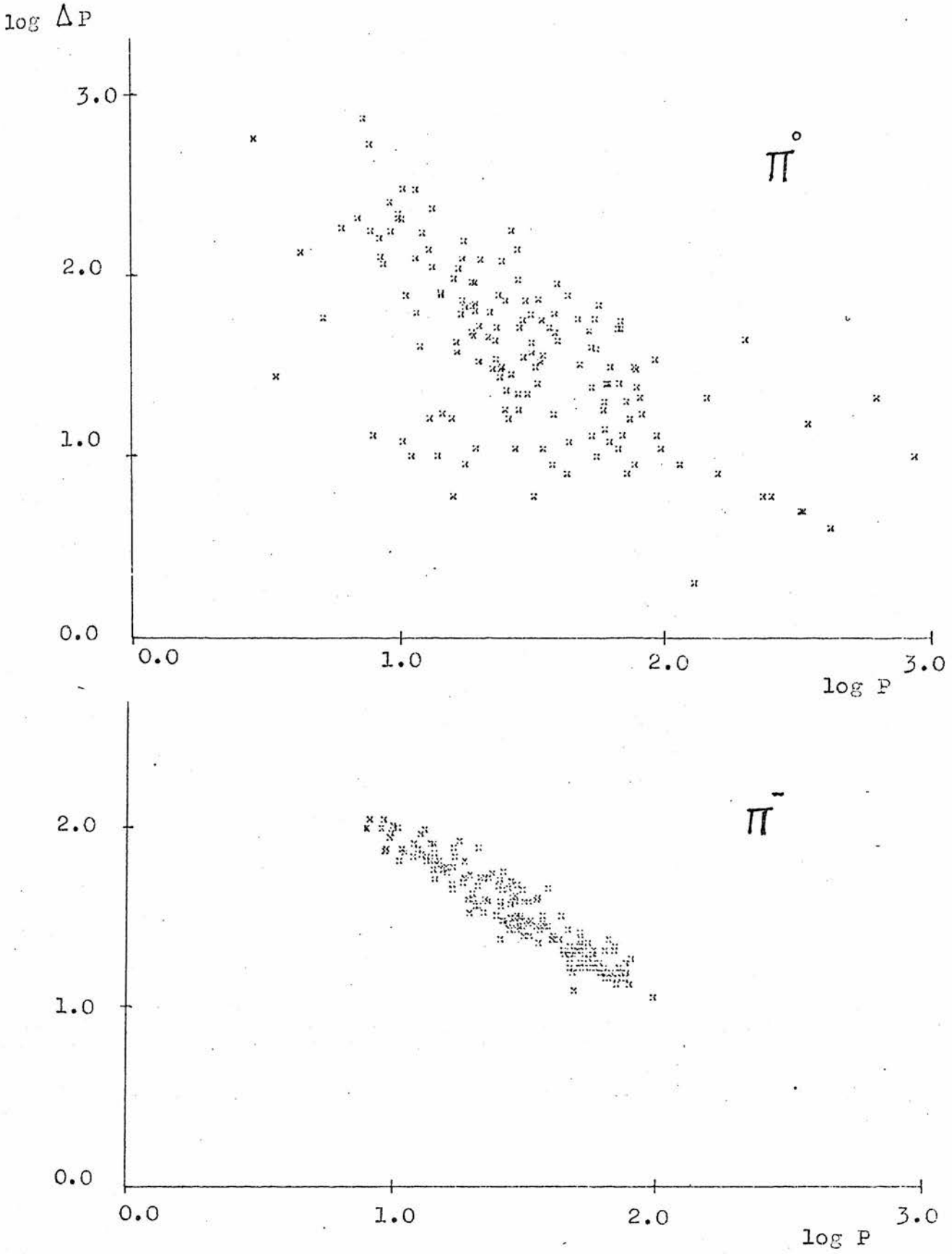

FIG. 4.2 log (ΔP) versus log P.

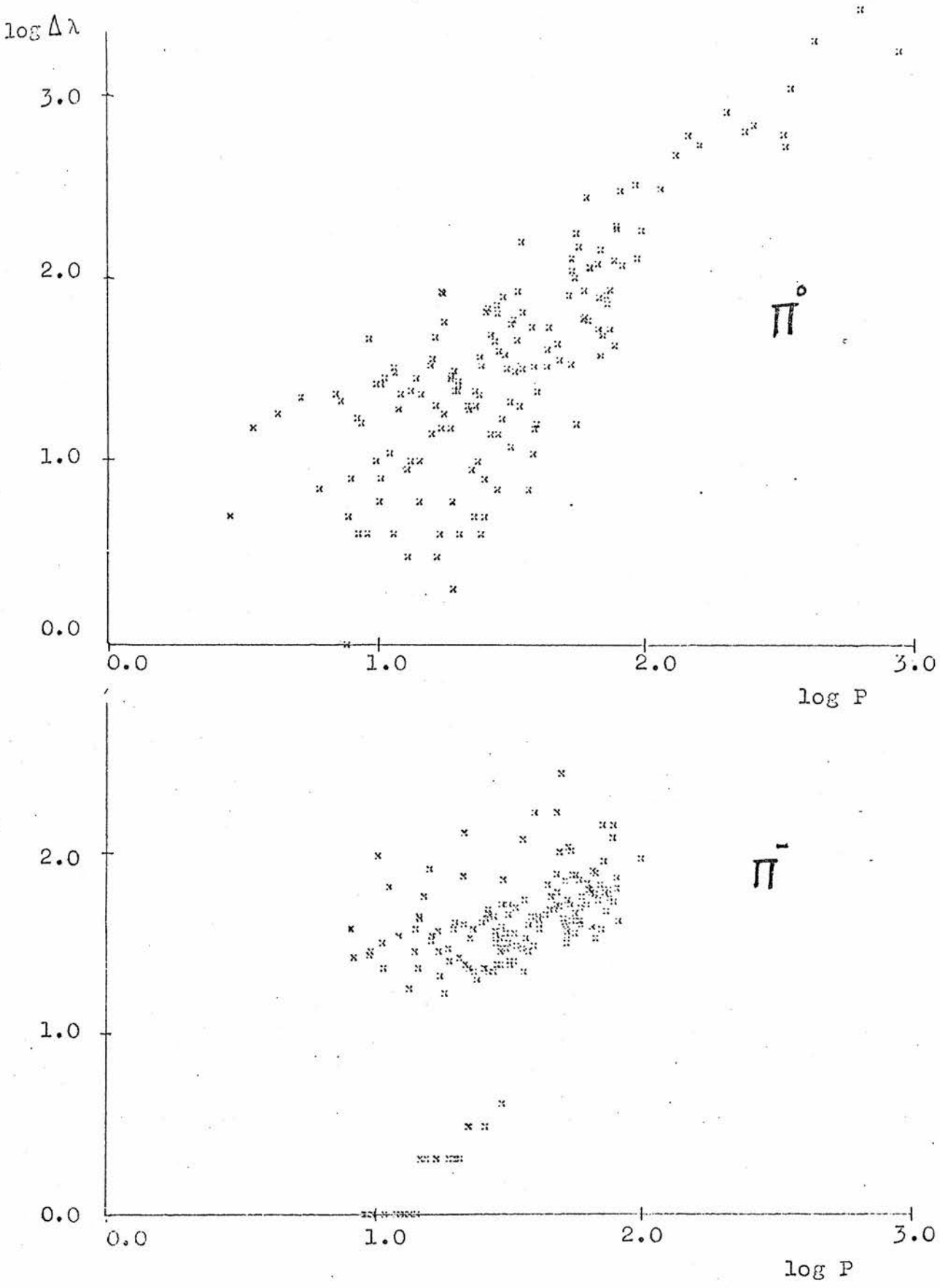

FIG. 4.3 log ($\Delta\lambda$) versus log P.

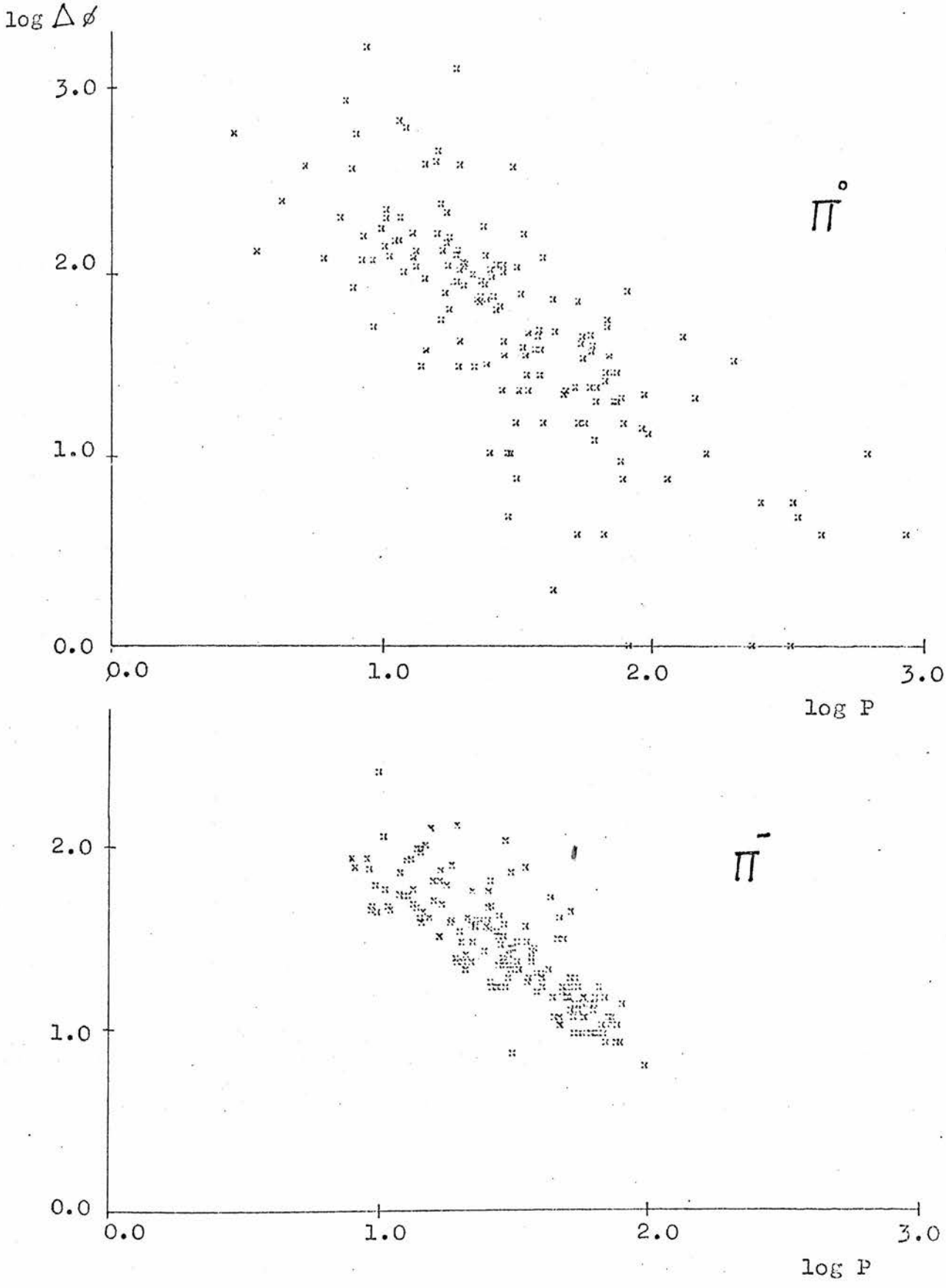

FIG. 4.4 log (Δø) versus log P.

interaction origin was altered in such a way as to reproduce the treatment given to the hydrogen events. Here, to allow for bubble density, the origin was repositioned one mean bubble diameter ($\sim\frac{1}{18}$ cm) beyond the measured endpoint of the beam track. To imitate this situation, the more precisely known K^-n interaction vertex was stepped forward along the kaon line of flight direction, a distance $(1-x)D$ centimetres, where x is a random number distributed exponentially between 0 and 1, and D, one mean bubble diameter. The errors on each of the vertex coordinates were increased accordingly.

Fits to the hypotheses - $K^-n \rightarrow \Lambda\pi^-$, $\Sigma^0\pi^-$, $\Lambda\pi^0\pi^-$ etc. - with the target neutron assumed at rest, were attempted, and the fitted events cut and weighted in analogy with the method used for the hydrogen events. The π^0 weight was replaced by a corresponding weight for the π^-. This allowed for a cut at 2 cms. on the projected π^- track length to remove short tracks which interacted near the origin. No explicit allowance was made for the possible loss of events because of non-detection of fast or slow π^-'s. The minimum π^- momentum was about 220 Mev/c (for the $\Sigma^0\pi^-$ channel), corresponding to a range of about 45 cms., thereby making unnecessary any correction for slow π^-.

A cut on the reaction centre of mass scattering angle, θ^*, at $\cos\theta^* = 0.9$ to remove slow Λ's of low visibility, as mentioned in Section 3.2, also made unnecessary a separate correction for the non-detection of fast π^-'s because of emission at small angles. For $\cos\theta^* = 0.9$, the π^- laboratory angle was approximately 10°, easily visible to the scanner, and the event made more obvious by the proximity

of the Λ^0 to the origin.

To determine the equivalent number of nuclear proton events, the corrections described above in Section 4.3 were applied to the final weighted number of neutron fits. In terms of isospin, I, and its third component, I_3, the various initial and final states can be expressed as combinations of states with precise isospin i.e. $|I, I_3\rangle$ with the appropriate Clebsch-Gordan coefficients:-

i.e.

$$|K^-p\rangle = \frac{1}{\sqrt{2}}|1,0\rangle - \frac{1}{\sqrt{2}}|0,0\rangle$$

$$|\Lambda\pi^0\rangle = |1,0\rangle$$

$$|K^-n\rangle = |1,-1\rangle$$

$$|\Lambda\pi^-\rangle = |1,-1\rangle \quad .$$

The conservation of isotopic spin implies that the transition amplitudes describing a reaction connect only those states with the same isospin, and are independent of charge (or I_3). Denoting the isospin 1 transition amplitude by A_1 it can be seen that:-

$$A(K^-p \longrightarrow \Lambda\pi^0) = \frac{1}{\sqrt{2}} A_1$$

and $$A(K^-n \longrightarrow \Lambda\pi^-) = A_1 \quad .$$

The cross-sections for these processes are proportional to the squares of the transition amplitudes and hence the cross-section ratio:-

$$R_x = \frac{\sigma(K^-p \longrightarrow \Lambda\pi^0)}{\sigma(K^-n \longrightarrow \Lambda\pi^-)} = \frac{1}{2} \quad .$$

The necessity of performing a separate normalisation for the nuclear events to obtain a cross-section was removed by determining the background directly from a comparison of the number of nuclear events with the number of hydrogen events in that channel occurring in the same sample of film.

Using this method the nuclear background in the $K^- p \rightarrow \Lambda \pi^0$ channel was found to be approximately 9.8°/o.

The effect on the resultant number of fits of altering the correlation terms in the π^- input matrix was then investigated by setting each of the off-diagonal elements to an "extreme" value of 0.9 times its maximum. (The maximum value of the off-diagonal term is the geometric mean of the corresponding diagonal terms). The sign was chosen randomly. The events were then refitted in GRIND and the fits processed as described above.

Contrary to the original assumption that the effect of the correlation terms was negligible compared with that of the diagonal terms, it was found that in the $\Lambda \pi^0$ channel the background decreased from $\sim$ 9.8°/o to $\sim$ 5.8°/o when the "extreme" correlation terms were included. This implied that a more careful study of these terms was required if this method was to be used.

In view of the assumptions mentioned above, however, concerning the construction of the π^0 input error matrix prior to the production fit, it was decided to accept the limits 5.8 - 9.8°/o as giving only an approximate figure for the background, and to adopt a new approach to provide a more accurate determination, as explained in Section 4,6.

4.5 K^- - Nucleus Fits

In addition to the fits where the target neutron was assumed to be at rest, fits were also made to the hypotheses:-

$$K^- N_A \rightarrow \Lambda \pi^- N_{A-1}$$

$$K^- N_A \rightarrow \Sigma^0 \pi^- N_{A-1}$$

and the "missing" momentum, Q, of the target neutron determined by the fit. Figures 4.5, 4.6 show the distributions of the target momenta for the $\Lambda \pi^-$ and $\Sigma^0 \pi^-$ events. Also shown is the target momentum distribution for those events which also fitted the rest neutron hypotheses. As expected these events fall at low Q values (below 125 Mev/c) in both cases.

These histograms also relate to another method by which the nuclear event background was determined for the channel $K^- p \rightarrow \Lambda \pi^+ \pi^-$ (26) and used as an estimate of the background in the $\Lambda \pi^0 \pi^0$ and $\Sigma^0 \pi^0 \pi^0$ channels. For this channel fits were made to both the hydrogen and nuclear target hypotheses, and in Figure 4.7 the fitted target momentum distributions are shown. The shaded portion of the histogram indicates those fits which also fit the free hydrogen hypothesis, and hence the remainder were assumed to occur on a nuclear proton. Although referring to a different channel it can be seen that the target momentum distribution for the nuclear events in the $\Lambda \pi^+ \pi^-$ channel is similar to the corresponding distributions for the $\Lambda \pi^-$ and $\Sigma^0 \pi^-$ channels.

In the case of the $\Lambda \pi^+ \pi^-$ events it was assumed that the target momentum distribution could be described by a

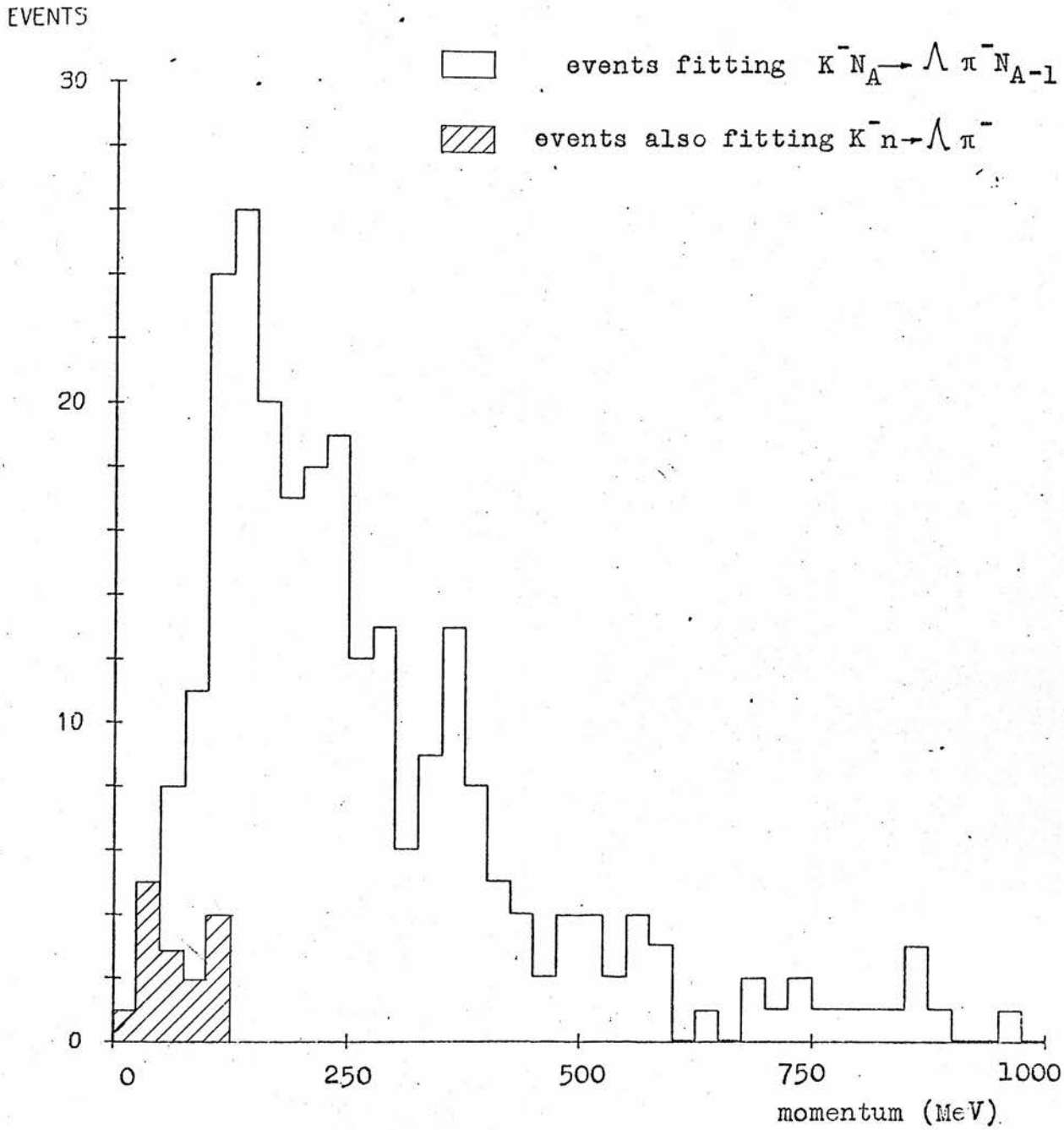

FIG. 4.5 Distribution of the fitted momentum of target neutron for events fitting $K^- N_A \longrightarrow \Lambda \pi^- N_{A-1}$.

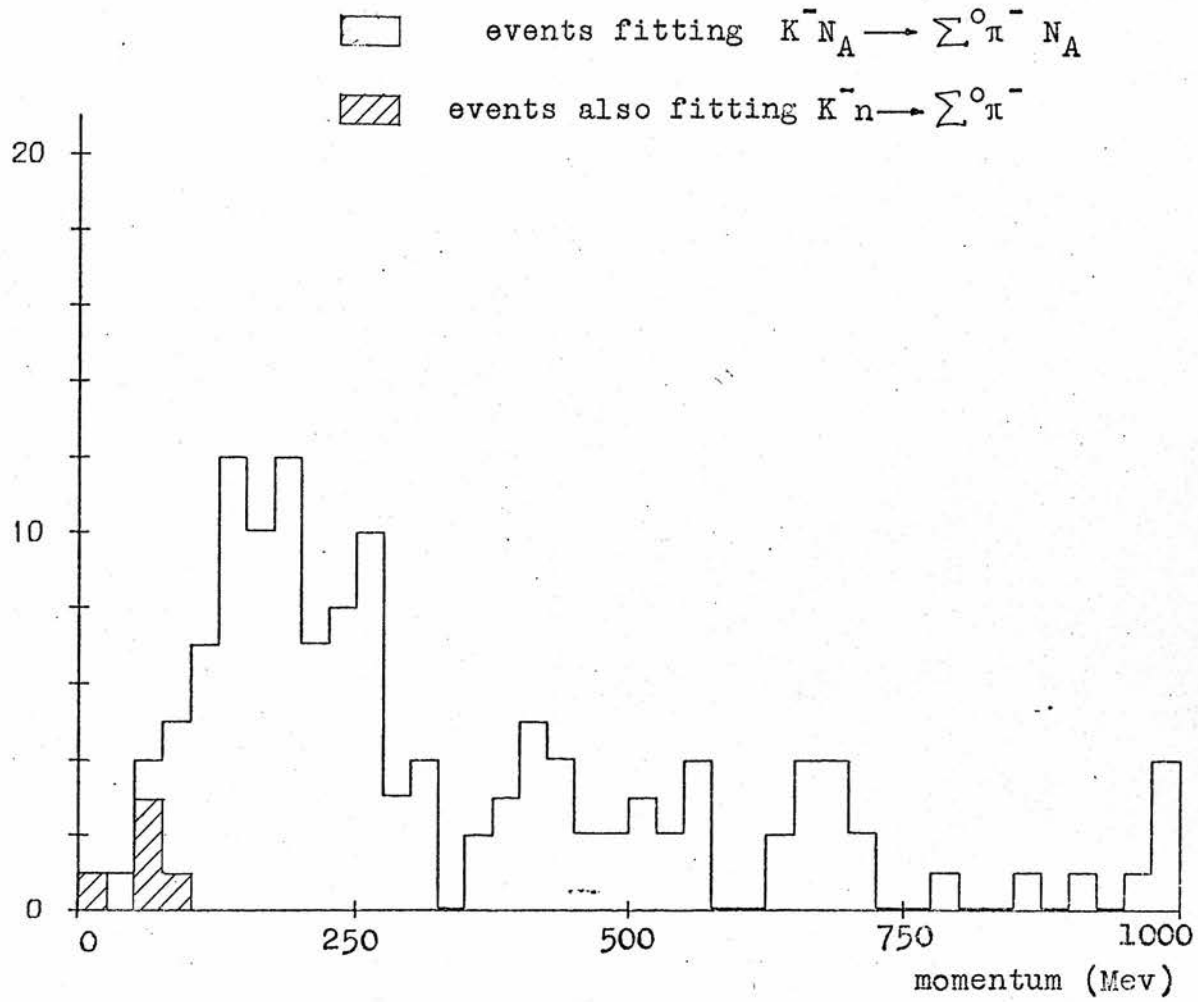

FIG. 4.6 Distribution of the fitted momentum of target neutron for events fitting $K^- N_A \longrightarrow \Sigma^0 \pi^- N_{A-1}$.

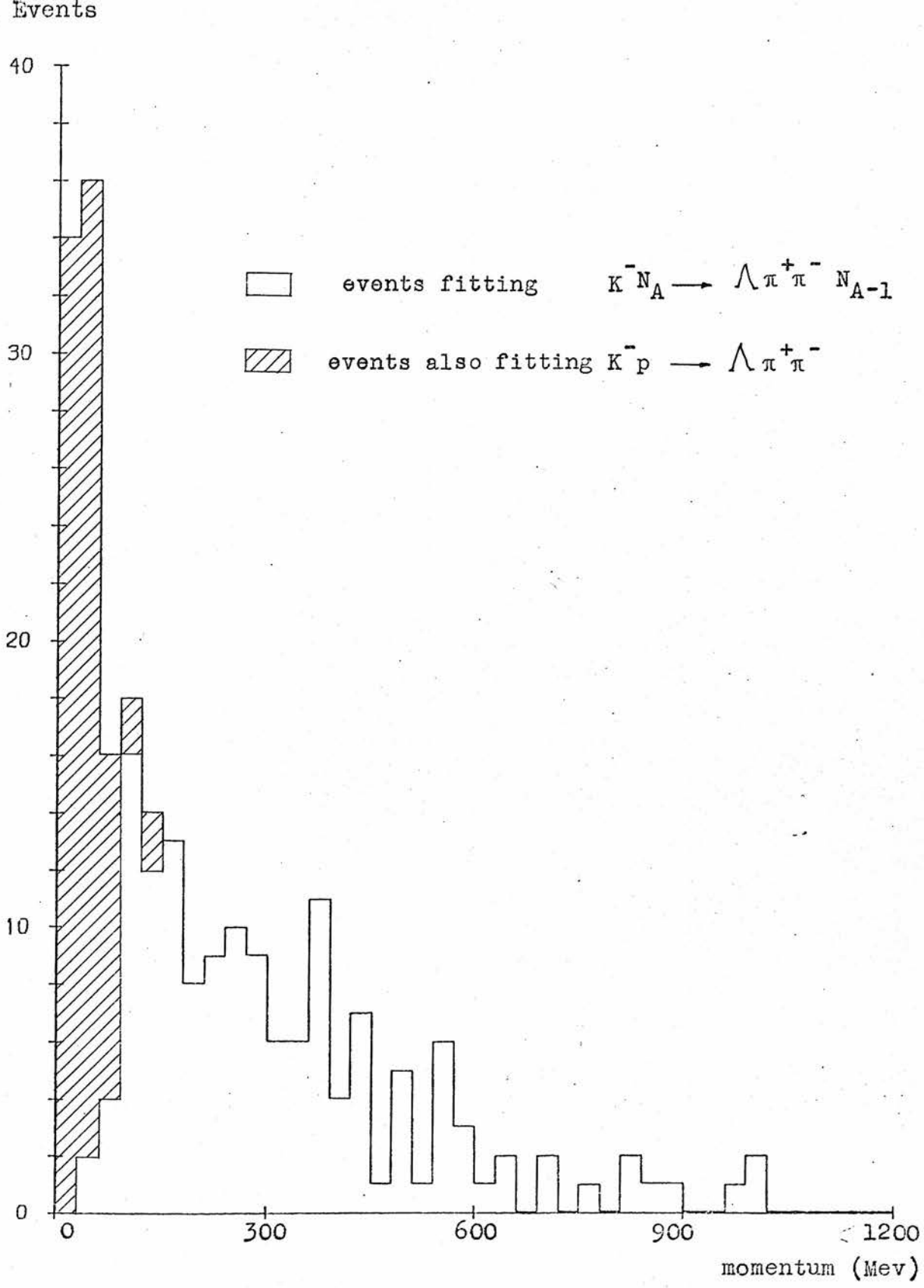

FIG. 4.7 Distribution of the missing momentum "Q" for events fitting $K^- N_A \longrightarrow \Lambda \pi^+ \pi^- N_{A-1}$. The shaded portion shows those events fitting $K^- p \longrightarrow \Lambda \pi^+ \pi^-$.

contribution from nuclear target events where the primary reaction products underwent secondary interactions in the nucleus (large Q values greater than~300 Mev/c) and from events in which no secondary interactions occurred (smaller Q values, less than~300 Mev/c). The nuclear event background in this channel was estimated by fitting the Q distribution to a model which allowed for nuclear interactions on both the light and heavy nuclei in the liquid by using a combination of the Fermi Gas and Shell models. The value was found to be $7.7 \pm 3.1^{o}/o$.

4.6 Method II

In this new method of fitting, a "pseudo-event" corresponding to the real scanned event was constructed by replacing the target neutron by a proton, and the π^-, created at the interaction origin, by two γ's from an equivalent π^o of the same vector momentum. The π^o decay γ's were generated by Monte Carlo, and for each one a similar real γ was selected from a "look up" library containing measurement and fit information for about 1200 real γ's taken from previously accepted hydrogen fits. The selection was made by means of a chi-squared (X^2) test on the momenta and the dip angles of the Monte Carlo and real γ's. For each Monte Carlo γ, all of the real γ's in the library were tested, and that with the minimum X^2 value considered as the best match. This method ensured that the real γ's chosen were not selected preferentially from any region of the momentum or dip distributions.

The measurement code (explained in Section 2.4) describing which of the real γ parameters had been set "measured"

or "unmeasured", together with the complete error matrix of the selected real γ, were then transferred intact to the Monte Carlo γ. The central value of each of the Monte Carlo γ parameters, $V_{m.c.}$, was then distorted to a new value $V'_{m.c.}$ given by

$$V'_{m.c.} = V_{m.c.} + (V_{real}(\text{measured}) - V_{real}(\text{fitted}))$$

to produce realistic fit input values.

The new γ's were then added to those already present in the event and these pseudo-events passed through the normal hydrogen fit chain, as outlined in Section 2.5. As with Method I, the position of the interaction origin was artificially distorted to allow for the bubble density correction. The subsequent cutting and weighting procedure for the fitted events differed from the hydrogen event method only in that the Monte Carlo generated γ's were assumed to lie within the chamber and were hence given no detection weight.

This approach had the important advantage over the previous method of making no assumptions about the form of the π^o error matrix and also allowed a more "hydrogen-like" treatment of the K^-n events.

A sample of events approximately half as large again as that used for Method I was used in this study. To test for possible biasses, and to extend the statistics, a new set of pseudo-events was generated with different Monte Carlo γ's, and these were then refitted in GRIND. The results of the separate analyses for the $\Lambda\,\pi^o$ and $\Sigma^o\pi^o$ pseudofit channels are shown in Table 4.1. The minimum complexity method, referred to in Section 3.3 in connection with choosing

between ambiguous hydrogen fits, was also used for the selection of nuclear fits.

Channel	Run 1 Fits		Run 2 Fits		Mean Fits	
	Raw	Weighted	Raw	Weighted	Raw	Weighted
$\Lambda\pi^0$	13	34.0	16	45.6	14.5	39.8
$\Sigma^0\pi^0$	4	17.3	7	26.7	5.5	22.0

Table 4.1

4.7 Results of Method II

i) $\Lambda\pi$ Channel

The fit probability distribution for the $\Lambda\pi^0$ pseudofits is shown in Figure 4.8 (fits from both Monte Carlo runs have been included). As expected, the majority of fits fall at low probability. Of the 36 fits made, 25 have probability less than 5°/o and 16 less than 2½°/o. Upon increasing the fit probability cut from 0.1°/o to 1°/o (to correspond with the 1°/o cut made on the $\Lambda\pi^0$ hydrogen fits to reduce the wrong-fit backgrounds, as explained later in Chapter 6), 7 fits with probability less than 1°/o were removed, leaving a total of 29. The average number of accepted pseudofits was therefore 14.5, which rose to 39.8 after weighting. These represented the total number of "free" neutron target events present in the film scanned, and were scaled by the target density factor

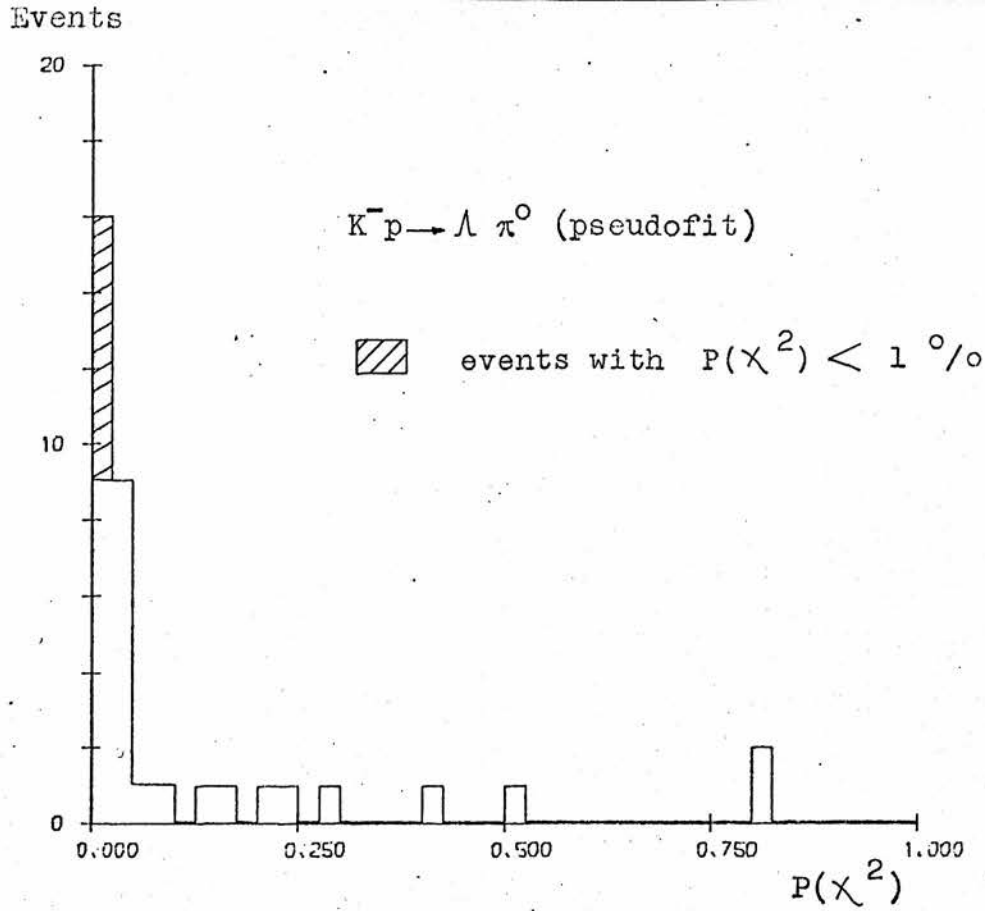

FIG. 4.8 Fit probability distribution for $K^- p \rightarrow \Lambda \pi^0$ pseudofits.

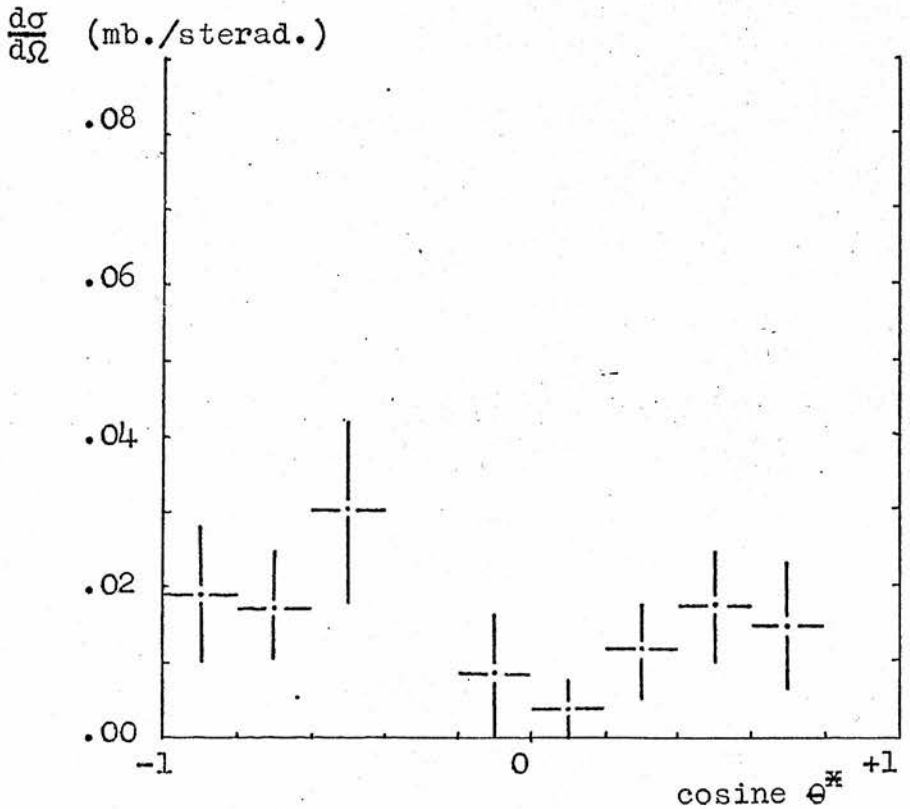

FIG. 4.9 Differential cross-section versus cos θ^* for $K^- p \rightarrow \Lambda \pi^0$ pseudofits.

of 0.86 and by the cross-section ratio of 0.5, as in Method I, to obtain the equivalent number of nuclear proton events, N_p. The nuclear event background in the $\Lambda\,\pi^o$ channel was estimated by comparing the resultant value of N_p - 17.1 - with the number of weighted hydrogen events with fit probability greater than 1°/o, in the same sample of film - 248.8. The background value was found to be 0.07 ± 0.03.

The $\Lambda\,\pi^o$ pseudofit differential cross-section shown in Figure 4.9 is relatively flat and because of the low statistics, no attempt was made at a parametrisation. The nuclear background subtraction was therefore made on the assumption that the distribution was isotropic.

ii) <u>$\Sigma\,\pi$ Channel</u>

In the case of the $\Sigma\,\pi$ channel, no simple ratio exists linking the $K^-p \longrightarrow \Sigma^o\pi^o$ and $K^-n \longrightarrow \Sigma^o\pi^-$ transition amplitudes, and the relation between the cross-sections must be derived indirectly from experimental measurements. The amount of data on the $K^-n \longrightarrow \Sigma^o\pi^-$ reaction is somewhat limited, but by making an isospin decomposition of the initial and final states, the cross-section can be related to better known values for other channels. The expression used to provide the cross-section was:-

$$\sigma(K^-n \rightarrow \Sigma^o\pi^-) = \sigma(K^-p \rightarrow \Sigma^+\pi^-) + \sigma(K^-p \rightarrow \Sigma^-\pi^+) - 2\sigma(K^-p \rightarrow \Sigma^o\pi^o).$$

The $\Sigma^+\pi^-$ and $\Sigma^-\pi^+$ cross-sections were calculated as the weighted means of the averages over the centre of mass energy range from 1630 - 1710 Mev/c^2 (Run 2 range) of data from references 6, 7, 8. For the $\Sigma^o\pi^o$ cross-section, the

estimate of this experiment was also included in the average, and the CHS errors were increased by a factor of two. The values calculated were:-

$$\sigma(K^- p \longrightarrow \Sigma^+ \pi^-) = 2.69 \pm 0.12 \text{ mb.}$$

$$\sigma(K^- p \longrightarrow \Sigma^- \pi^+) = 3.08 \pm 0.20 \text{ mb.}$$

$$\sigma(K^- p \longrightarrow \Sigma^\circ \pi^\circ) = 1.60 \pm 0.09 \text{ mb.}$$

The value of the $K^- n \longrightarrow \Sigma^\circ \pi^-$ cross-section was therefore 2.57 ± 0.3 mb and the cross-section ratio $\frac{\sigma(K^- p \longrightarrow \Sigma^\circ \pi^\circ)}{\sigma(K^- n \longrightarrow \Sigma^\circ \pi^-)}$ taken as 0.62 ± 0.16.

The $\Sigma^\circ \pi^\circ$ pseudofit probability distribution is shown in Figure 4.10. Here again a peak is seen at low values with 6 events out of a total of 11 with probability less than $2\frac{1}{2}^\circ/o$. The mean number of 5.5 pseudofits, which increased to 22.0 after weighting, was scaled using the above values for the target density and cross-section ratios to give the value of N_p as 11.7. The weighted number of $\Sigma^\circ \pi^\circ$ hydrogen events with fit probability greater than $0.1^\circ/o$ in the same film was 127.0, and the nuclear event background estimated as 0.09 ± 0.05.

As with the $\Lambda \pi^\circ$ pseudofits the $\Sigma^\circ \pi^\circ$ pseudofit differential cross-section was consistent with being isotropic as shown in Figure 4.11.

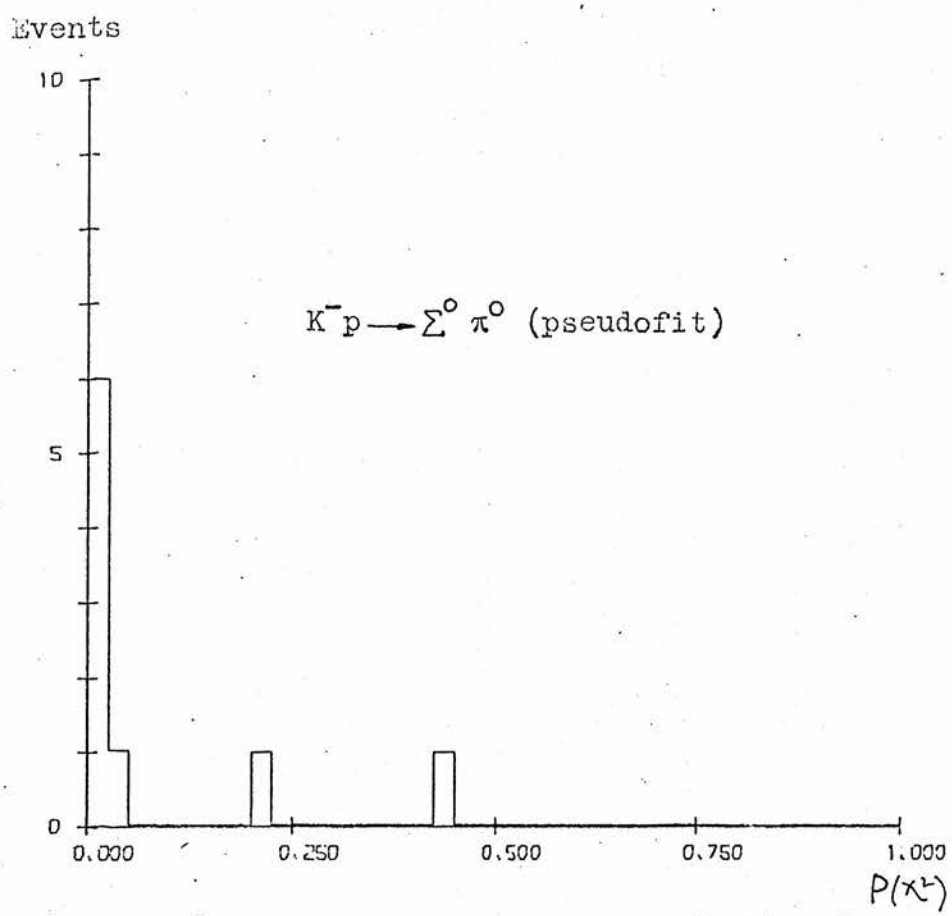

FIG. 4.10 Fit probability distribution for $K^- p \longrightarrow \Sigma^0 \pi^0$ pseudofits.

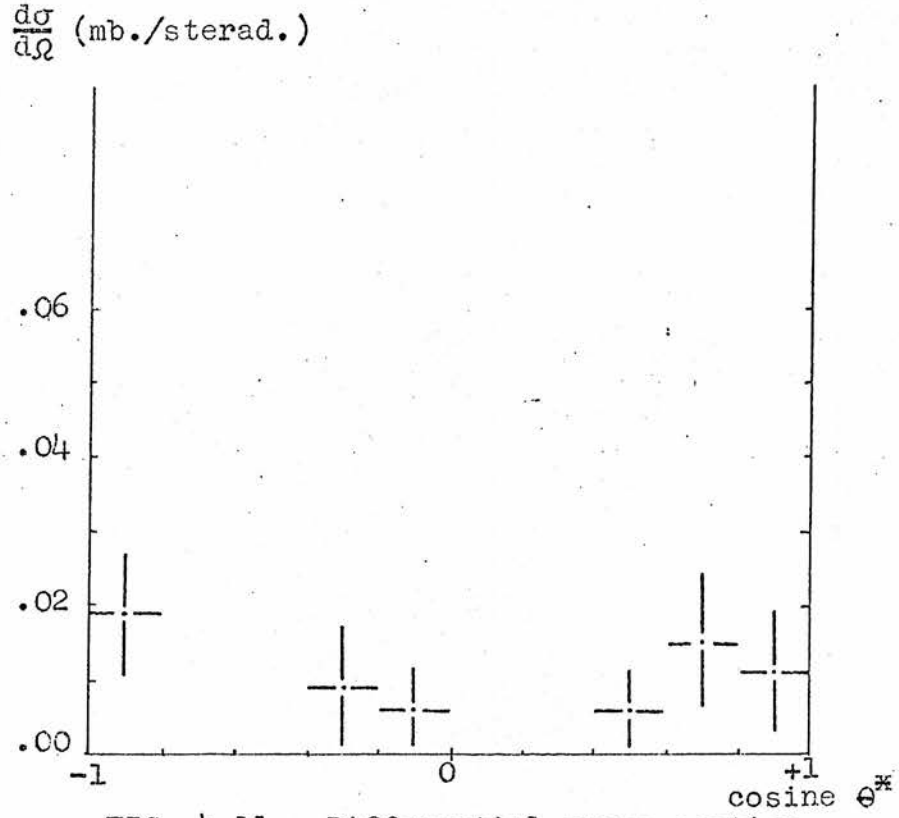

FIG. 4.11. Differential cross-section versus $\cos\theta^*$ for $K^- p \longrightarrow \Sigma^0 \pi^0$ pseudofits.

CHAPTER 5

BEAM CONTAMINATION

5.1 Introduction

The cross-sections for the hydrogen events were normalised by making a direct measurement of the incoming K^- flux by way of a beam count. This procedure was used instead of the method of scanning for τ decays as commonly used for experiments performed in hydrogen, because of the background of other three-prong interactions in heavy liquid.

A correction must be made, however, to the value of the flux measured in this way to allow for the fact that not all the tracks recorded in the beam count were kaons. The estimation of the contamination, assumed to be of negative pions and muons, was made using a "delta-ray count" performed at Edinburgh. This method provided the means whereby the K, π and μ fractions of the beam could be effectively separated, and also allowed the K^- attenuation length to be determined.

5.2 Delta-Ray Method

The contamination arises mainly from K^- decay in the final 9.5 m. of the beam line leading from the second separator to the chamber. The principal kaon decay modes are:-

$$K^- \longrightarrow \mu^- \nu \quad (64\%)$$
$$\longrightarrow \pi^- \pi^0 \quad (21\%) \ .$$

Some of these π's and μ's entered the chamber at the same momentum and direction as the on-beam kaons, and in the

heavy liquid the three particles were indistinguishable in track density. A means of separating the particles, however, was that of looking at the "knock-on" electrons or "δ-rays" which they produced as they traversed the chamber, the maximum energy of the δ-ray being a function of the mass of the particle creating it. The relation between the δ-ray kinetic energy T_δ and the particle mass M is given by

$$T_\delta = \frac{2m_e P^2 \cos^2\theta}{(m_e + \sqrt{P^2+M^2})^2 - P^2\cos^2\theta}$$

where m_e is the mass of the electron, P is the momentum of the incident particle, and θ is the laboratory emission angle of the electron with respect to the direction of the incident particle. As the emission angle, θ, decreases to zero, the value of T_δ tends toward a maximum given by:-

$$T_\delta(\max) = \frac{2m_e P^2}{m_e^2 + M^2 + 2m_e\sqrt{P^2+M^2}} \quad .$$

For K's, π's and μ's the variation of $T_\delta(\max)$ with the incident momentum, P, is shown in Figure 5.1. At 820 Mev (the run 2 beam momentum at the entrance to the fiducial volume) the maximum energies of the K, π and μ induced δ-rays were respectively 3, 34 and 57 Mev/c^2. By counting only those δ-rays of energy greater than 3 Mev/c^2 on both interacting and non-interacting tracks, and by using the laws governing the production of δ-rays and the probability of interaction, a maximum likelihood method was devised to calculate values for the beam composition.

On the initial assumption that the rate of energy loss

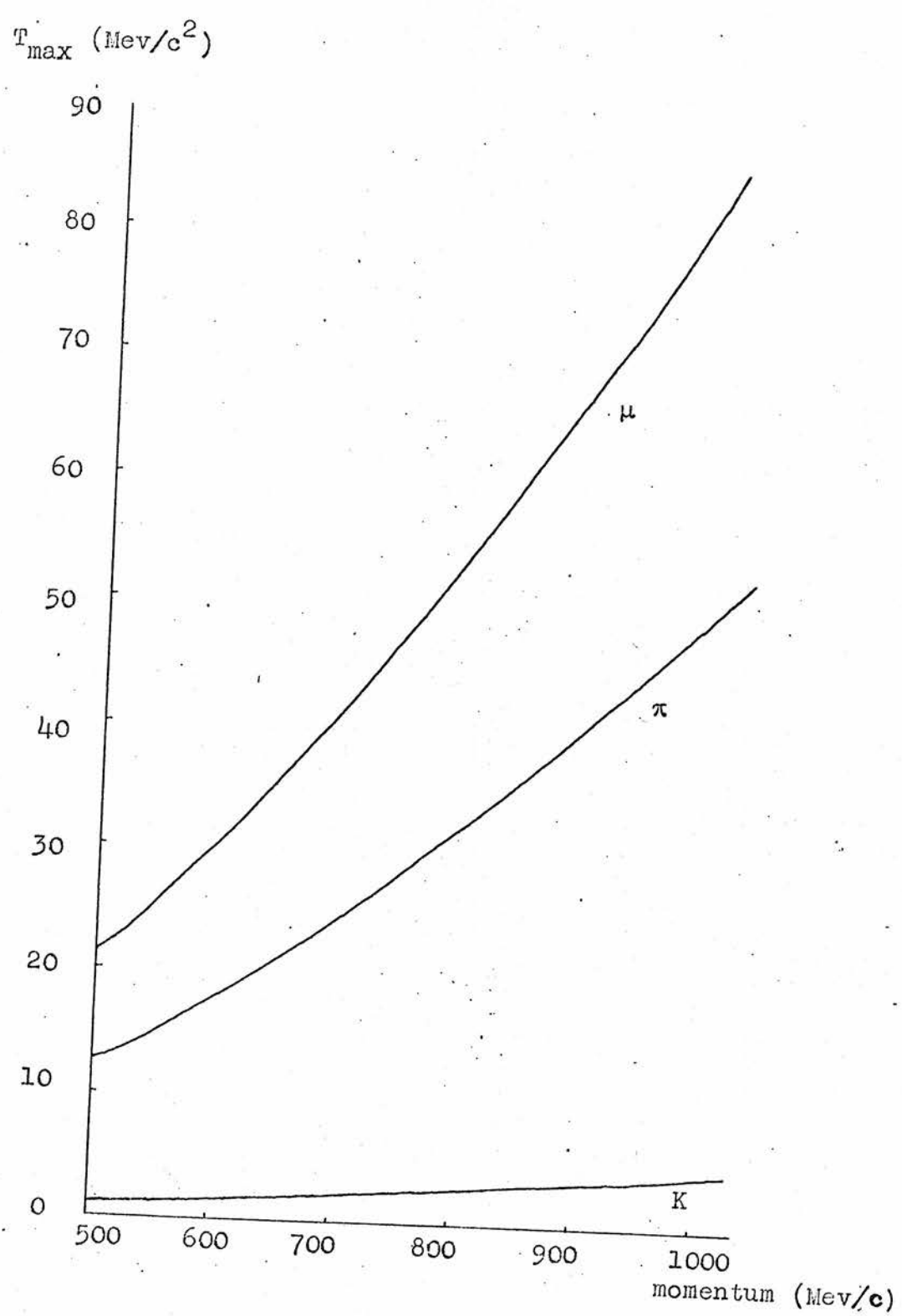

FIG. 5.1 Maximum δ-ray energy T_δ for K, π and μ versus beam momentum.

was negligible, the maximum diameter of a K^- δ-ray as seen on the scan table was 0.5 cms. To ensure that only the δ-rays produced by π's or μ's were counted, those having a maximum diameter less than 1.0 cm. were rejected. This corresponded to an energy cut at approximately 6.5 Mev/c^2. The relation between the radius of curvature, ρ_δ, and the kinetic energy T_δ of a δ-ray is given by

$$\rho_\delta = \frac{\sqrt{T_\delta(T_\delta + 2m_e)}}{0.3 \times B \times D} ,$$

where m_e is the mass of the electron, B is the magnetic field strength, and D the demagnification factor from the chamber to the scan table. For the Edinburgh scanning the value of D was 1.8.

The δ-ray total length and the initial curvature were also considered as criteria whereby the tracks could be differentiated, but it was felt that the measurement of the length would be difficult and time consuming, and that by discriminating on the basis of the initial curvature of a very short portion of track, large errors would be introduced, and particularly so in cases where large angle single scattering occurred near the δ-ray origin. Although the method of measuring the maximum δ-ray diameter was more prone to multiple scattering errors, it was assumed that the net effect was symmetric, in that as many contaminant δ's (i.e. π or μ induced) of energy greater than the minimum would be lost because of inward scattering to a maximum diameter less than 1 cm., as δ's of energy less than the minimum would be gained because of outward scattering to a diameter greater than 1 cm.

The diameter cut was applied by the use of a 1.0 cm. diameter "scanning circle", as illustrated in Figure 5.2. The circle was placed over the δ- ray and only those which were not completely enclosed were recorded. On the assumption that the scanners could place the circle to within 1 mm. of the optimum position, an error of approximately 10°/o in the cut was implied. The use of a smaller circle, although increasing the statistics, would have led to larger errors.

As a check on the consistency with which the cut was applied, it was decided to collect data on a different sample of δ - rays - those not covered by a 1.2 cm. diameter circle (corresponding to a kinetic energy of 8 Mev/c^2). This new cut was placed relatively close to the 1.0 cm. cut to ensure that the resultant loss in statistics by going to the higher energy was not too large.

The assumption made above that the rate of energy loss was unimportant, i.e. that the δ- ray followed an approximately circular path in the magnetic field, was reconsidered. An electron can lose energy by ionisation or by the emission of bremsstrahlung radiation. For low energy electrons (less than 15 Mev/c^2), however, radiation loss is small in the heavy liquid mixture ($\sim$ 0.25 Mev per cm.) compared with ionisation loss ($\sim$ 2 Mev per cm.) and therefore only ionisation loss was considered. Using the range-momentum table for the heavy liquid, calculated from the Bethe-Bloch[28] equation, the loci of δ- rays of initial energy ranging from 6 to 15 Mev/c^2 were plotted in 1 mm. path length steps, and in this way the maximum δ- ray diameters - the maximum distance from the point of creation on the beam track to a point on the δ- ray track - were found. Figure 5.3 shows the δ- ray

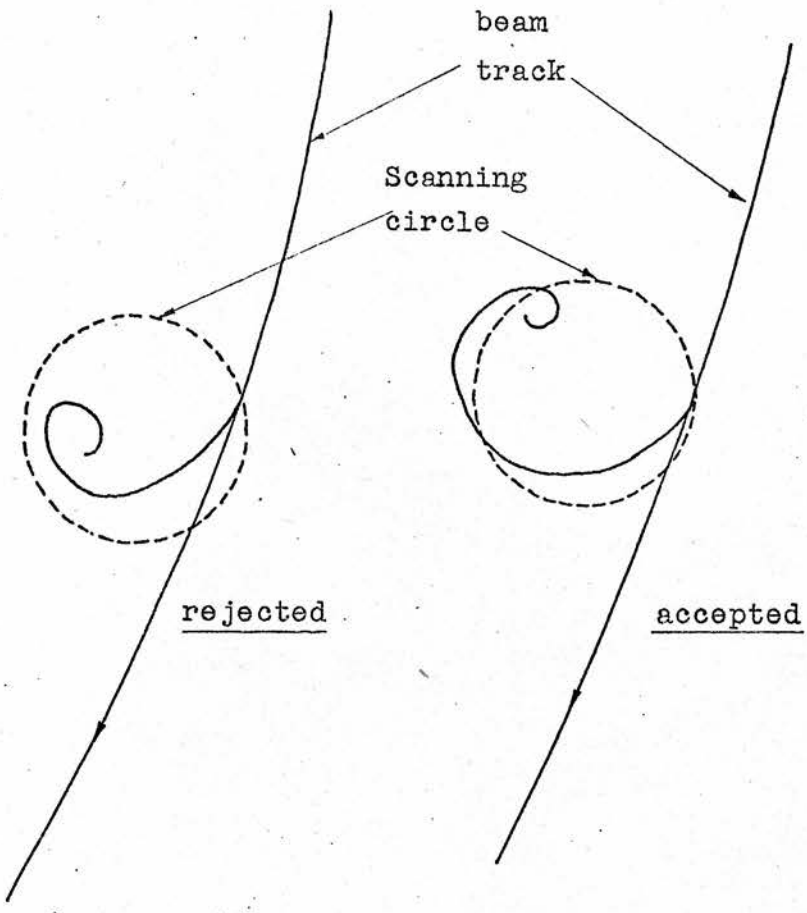

FIG. 5.2 Application of the δ-ray scanning circle.

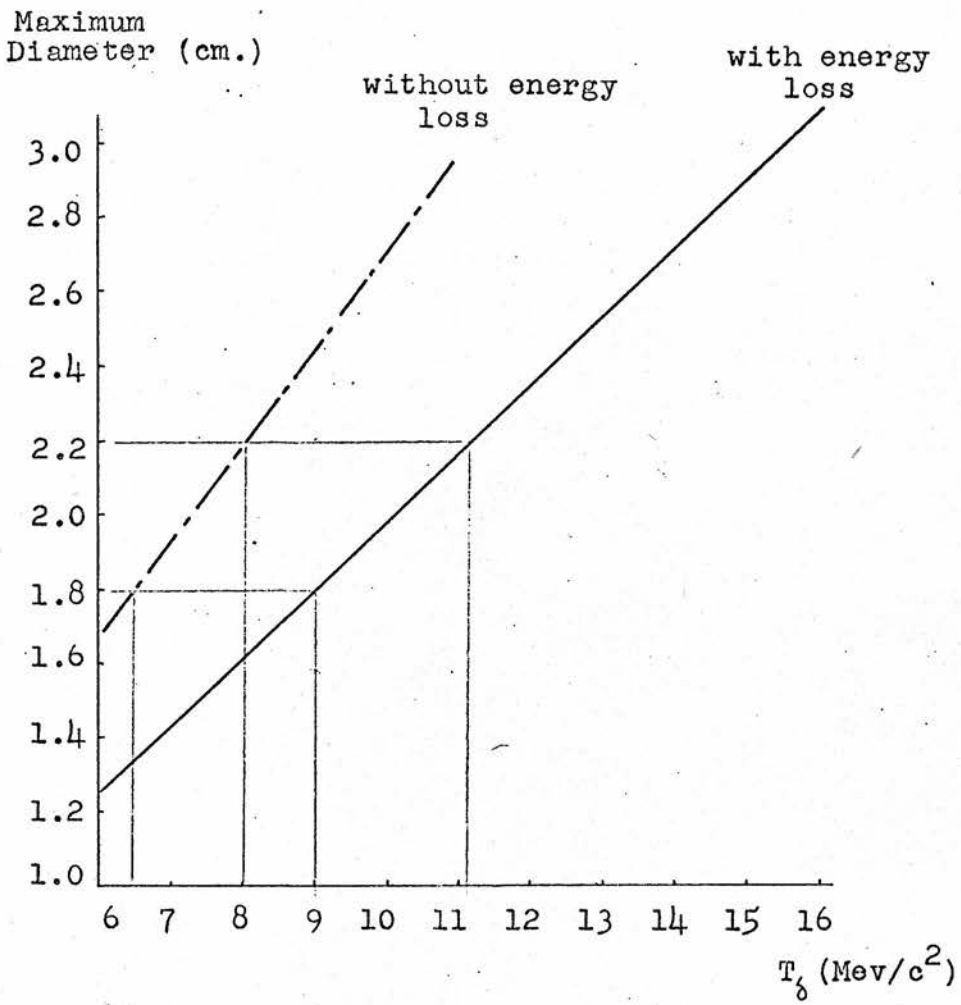

FIG. 5.3 δ-ray maximum diameters (in space) versus δ-ray kinetic energy.

maximum diameters in space, as a function of the δ - ray kinetic energy, with and without energy loss taken into account. From this it can be seen that the diameters of 1.0 and 1.2 cms. on the scan table, that is 1.8 and 2.2 cms. in space (table demagnification factor = 1.8) correspond to δ - ray kinetic energies of approximately 9 and 11 Mev/c^2 respectively (instead of 6.5 and 8 Mev/c^2 as found previously).

Although this was of little concern in the scanning where only the consistency of application of the cut was of importance, it was significant for the ensuing analysis in which the ratio of the π and μ "δ-ray length" - the mean track lengths of these particles to produce a δ - ray of energy greater than the minimum value - was fixed and used as a constraint in fitting the data, to reduce the number of free parameters.

The underlying assumption that the δ-ray plane was parallel to the scanning plane and that no distortion in the energy measurement was caused by strongly dipping δ's is justified by an inspection of Figure 5.4. Here it can be seen that 9 Mev δ-rays are produced at an angle of $\sim 15^{\circ}$ to the beam direction for both π's and μ's, and in this case over 95°/o of the δ-ray momentum is in the forward direction.

The probability of the production of a δ - ray by a specific particle is expressed by the parameter δ, its "δ-ray length" mentioned above. For a given minimum δ - ray energy, T_{min}, it is the average track length required to produce one δ - ray of energy $T_{\delta} > T_{min}$. An expression for δ, valid for both spin 0 and spin ½ particles is given

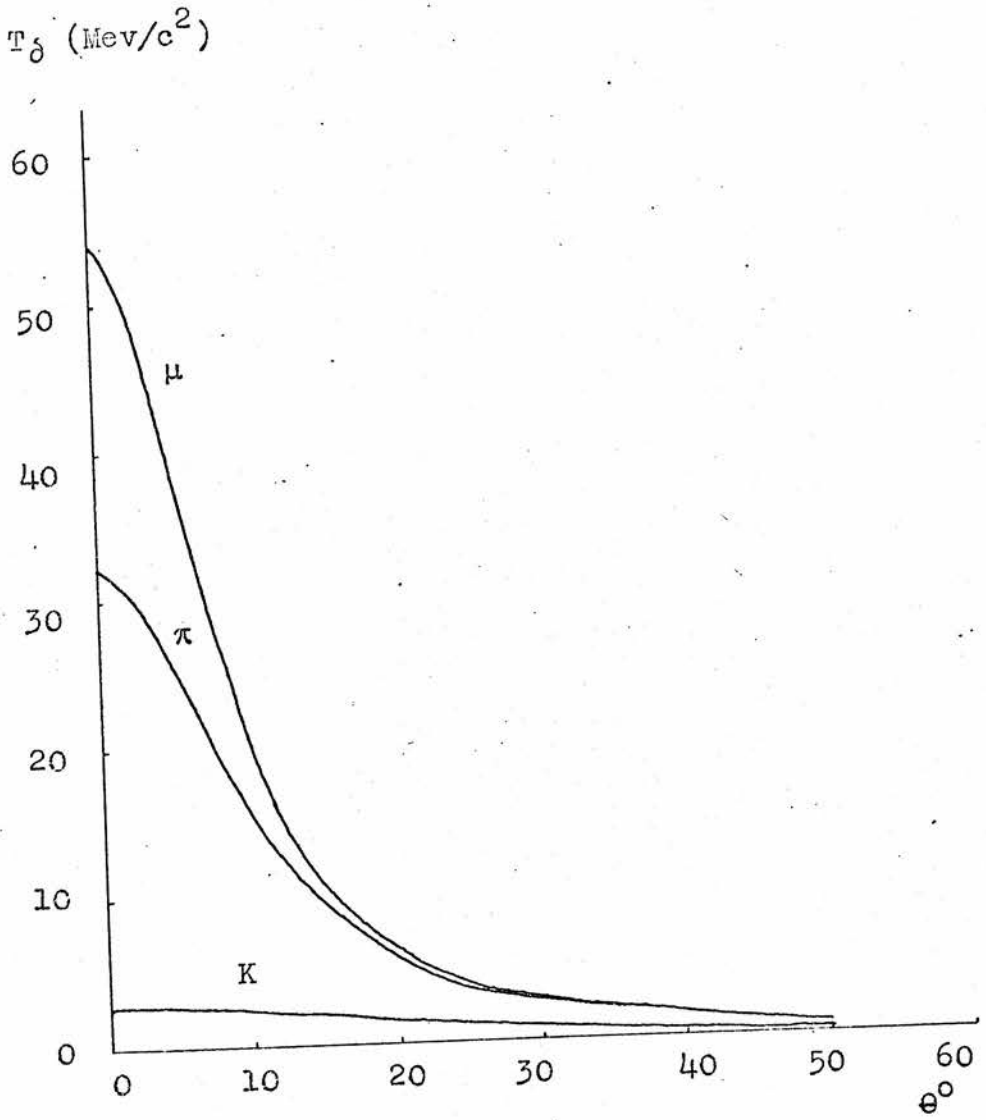

FIG. 5.4 δ-ray kinetic energy as a function of emission angle θ.

by[27]:

$$\delta = \beta^2/C' \left[1/T_{min} - 1/T_{max}(1 + \beta^2 \ln(T_{max}/T_{min})) \right]$$

where C' is a constant given by:-

$$C' = 2C\, m_e \rho^2 \text{ Mev/cm.}$$

$$C = \pi N \, Z/A \, r_e^2 = 0.150 \, Z/A \, g^{-1} \, cm^2 .$$

C is a constant representing the total "area" covered by the electrons in 1 gram of the material, each electron considered as a sphere of radius r_e; Z and A are the charge and mass numbers of the material, N is Avogadro's number, ρ the density, and r_e $(= e^2/m_e c^2)$ is the classical radius of the electron; β is the velocity of the particle expressed as a fraction of the speed of light $(\beta = v/c)$. For the liquid used in this experiment, values of δ were calculated using the known composition.

The probability of producing n δ-rays each with a kinetic energy greater than T_{min} on a length of track ℓ is given by the Poisson Law:-

$$P_n = \frac{e^{-\ell/\delta} (\ell/\delta)^n}{n!} .$$

For the analysis it was assumed that the probability of observing 6 or more δ-rays on the maximum length of track was negligible.

In order to separate the pion and muon contributions to the contamination, it was necessary to take into account the interaction probabilities of the particles. The probability that a track travels a distance ℓ without interacting is given by:-

$$P(\ell) = e^{-\ell/\lambda_I}$$

where λ_I is the "interaction length". Because of the extremely low muon interaction probability only the π and K interaction lengths are involved.

5.3 Scanning

The film was scanned mainly using only one view although a second view was available to resolve ambiguities. Samples of film from three different runs were scanned, and values for the beam composition calculated separately for each.

The same beam acceptance criteria as were used for both the normal scanning (see Section 2.3) and for the beam count, were employed for the δ-ray scan. The scanners were asked to count and to record the number of acceptable beam tracks entering the fiducial volume, and for each of these tracks to:-

a) record it as "Leaving" if it left the fiducial volume without interacting, or as "Interacting", if it interacted or kinked at an angle greater than 10^{o};

b) record the number of δ-rays not completely enclosed by placing the 1.0 cm. diameter scanning circle over them. These are referred to as 'A' type δ-rays;

c) do exactly the same for the 1.2 cm. diameter circle. These were called 'B' type δ-rays.

Frames with either zero or with 13 or more beam tracks were discarded. A preliminary double scan of a small portion of film revealed that the number of tracks without acceptable δ-rays was large compared to those with one or more, and that

the scan efficiencies for the tracks with δ- rays was significantly lower than for those without. On the basis of these results we decided to double scan all the film to have a reasonable estimate of the scan efficiencies for each category of track (with 0, 1, 2, 3, 4, 5 δ-rays). As with the normal scanning, the separate scan records were compared and a rescan performed on those frames in which disagreement occurred, to provide an accurate scan description.

The mean length of the leaving tracks, required for the analysis, was determined separately for each run, by measuring the lengths of several hundred leaving tracks distributed over the film.

Scan Program Chain

A chain of programs to manage the scanning and to analyse the data was developed at Edinburgh. A flow diagram of this scheme is shown in Figure 5.5, and is similar to that used to handle the normal scan data. The data were recorded on scan sheets and later transferred to punched cards, an example of which is shown in Figure 5.6. The card decks for each scan were then "cleaned" using a program "CHECK", which searched for typographical errors and ensured that the cards were in sequential order. The two independent records for each frame were compared and those frames, for which the correspondence was not complete, listed by "COMPARE". The rescanned data were merged with those of the primary scans, using "UPDATE", to form a final summary and from this, the program "STATS" extracted the numbers of leaving and interacting tracks with 0, 1, 2, 3, 4, 5 δ-rays.

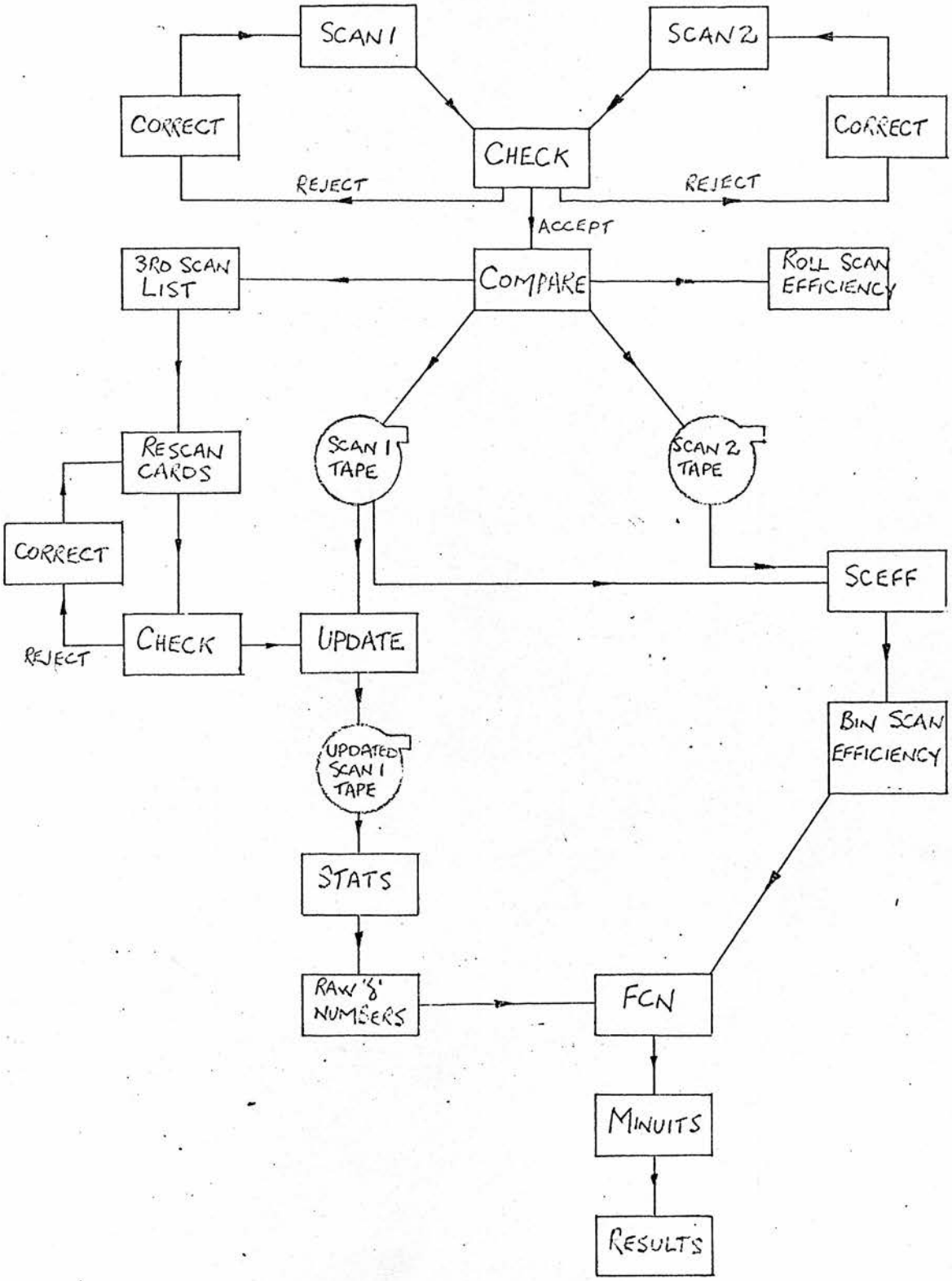

FIG. 5.5 δ-ray scan card processing flow diagram.

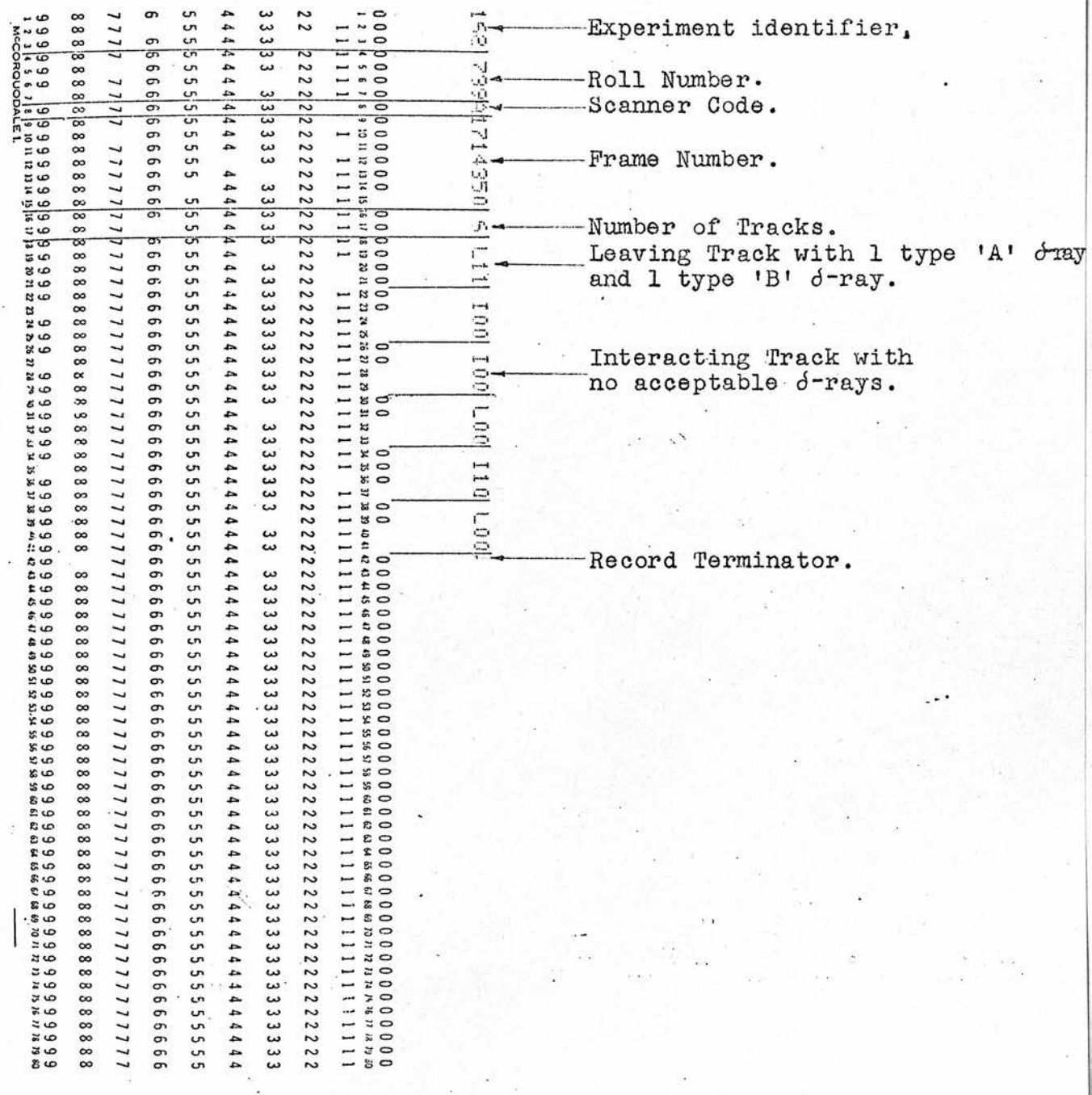

FIG. 5.6 Example of δ-ray scan card.

This information, together with the scan efficiencies, calculated by "SCEFF", formed the input to the subroutine "FCN", used with the minimising program "MINUITS"[29] to produce values for the beam composition.

5.4 Scan Results and Analysis

The results of the scanning are shown in Table 5.1. For each run, the appropriate scan data, both δ-ray numbers and scan efficiencies, together with the probability laws outlined above in Section 5.2, were used to calculate, by a method of Maximum Likelihood, the relative proportions of K, π and μ in the beam, and the K^- attenuation length, λ_K, required for the normalisation. Separate analyses were performed for the A and B type δ-rays to check for consistency, and the final values obtained by utilising both sets of data.

For the analysis it was assumed that the beam contained only K's, π's and μ's, and that the interaction lengths were independent of energy over the range covered by each run. During the scanning the lengths of the interacting tracks were not measured, and as a consequence, the pion attenuation length, λ_π, and hence the percentage of pions in the beam, were poorly determined. The fit was improved by constraining the value of λ_π to be within one standard deviation of the known value.

It was further assumed that the ratio of the δ-ray lengths, δ_π/δ_μ, as calculated from the equation given in Section 5.2 above, was constant for each run. Figure 5.7 shows the variation of the ratio δ_π/δ_μ for several values of T_{min}, and it can be seen that over the momentum ranges

	Run 2a				Run 2b				Run 3b			
	Leaving		Interacting		Leaving		Interacting		Leaving		Interacting	
N_δ	A	B	A	B	A	B	A	B	A	B	A	B
0	14212	14694	17347	17384	19302	19906	23121	23173	9814	10089	12227	12254
1	1050	709	76	44	1317	853	95	50	635	423	62	38
2	184	61	9	4	188	64	9	3	95	39	5	2
3	20	3	0	0	20	5	1	0	8	1	0	0
4	1	0	0	0	1	0	0	0	0	0	0	0
5	0	0	0	0	0	0	0	0	0	0	0	0
0	99.8	99.8	99.9	99.9	99.7	99.8	99.8	99.9	99.9	99.9	99.9	99.9
1	96.8	97.4	85.5	90.6	95.4	96.6	82.6	86.4	98.0	98.4	83.7	86.1
2	95.3	95.4	90.0	0	91.5	95.6	80.3	83.3	97.6	97.2	93.8	0
3	96.9	0	0	0	89.6	84.0	0	0	92.6	0	0	0
4	0	0	0	0	0	0	0	0	0	0	0	0
5	0	0	0	0	0	0	0	0	0	0	0	0

TABLE 5.1

Numbers of tracks with 0, 1, 2, 3, 4, 5 δ-rays and corresponding scan-efficiencies, for three separate runs.

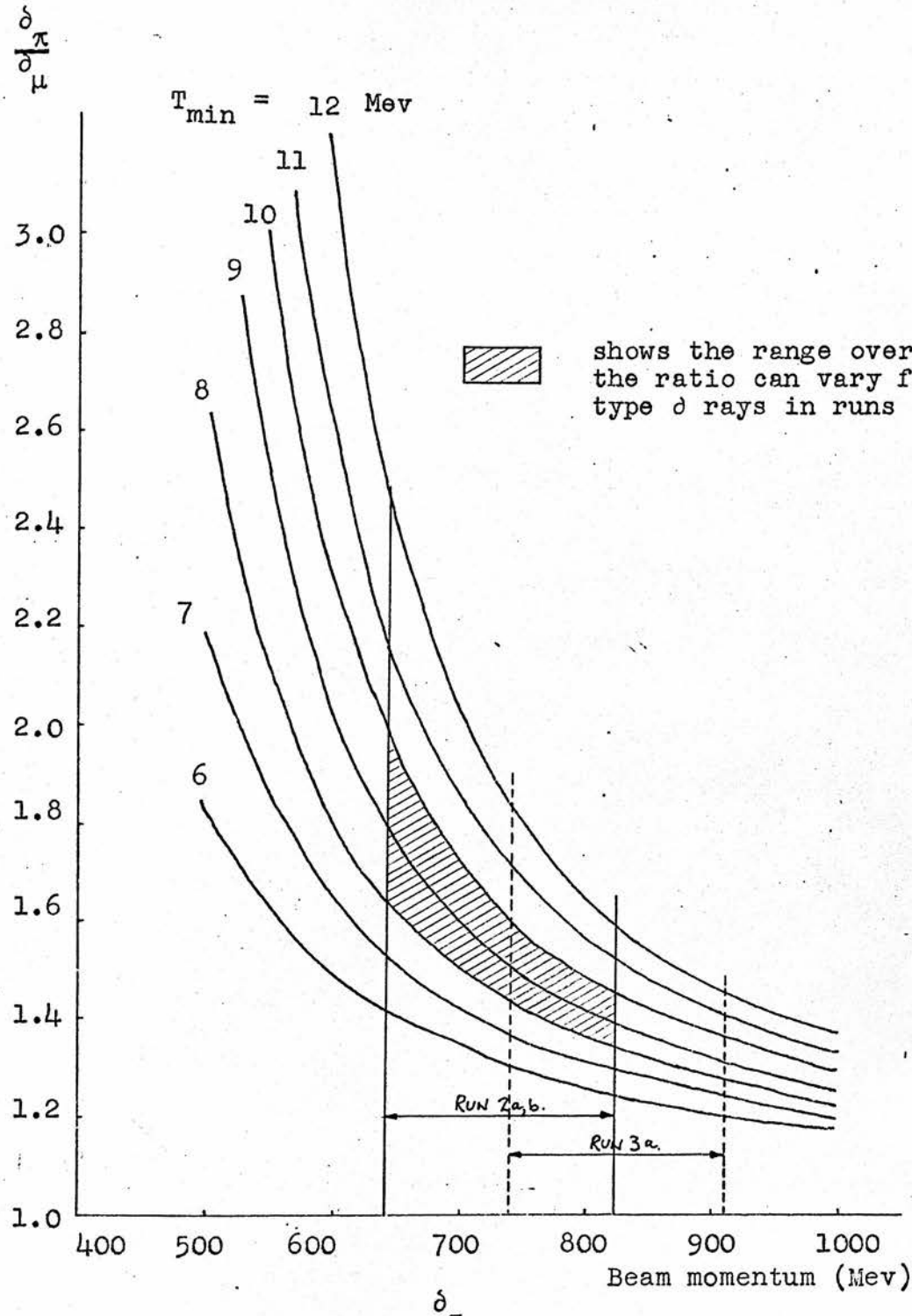

FIG. 5.7 The ratio $\frac{\delta_\pi}{\delta_\mu}$ as a function of beam momentum, for several values of T_{min}.

of the runs, the ratio in fact changes appreciably. However it was found that when a fit was made to the data with the ratio $\delta\pi/\delta\mu$ fixed at different values within its extreme limits, as determined by the range of beam momentum for the particular run, and allowing for an error of $\pm$ 1 Mev/c^2 in the application of the δ- ray energy cut, the beam composition and the K^- attenuation length did not appear to be sensitive to the value of the ratio, and remained relatively stable. Hence the ratio was fixed at a "mid-range" momentum and allowed to vary between its extreme values. This was taken as 1.56 ± 0.50 for the A type δ's and 1.74 ± 0.80 for the B type, in runs 2a and 2b. The values for run 3b were 1.40 ± 0.24 and 1.52 ± 0.32 respectively.

The Maximum Likelihood fit to the data for each run was made with the above constraints and with the fractions of K^- and π^- in the beam, the K^- interaction length, and the π^- δ- ray length as free parameters. The "raw" results of the fit are shown in Table 5.2. A check on these results was made by comparing the fitted values of the π and μ δ-ray lengths with the values calculated from the equation given in Section 5.2. For each run the values were found to be compatible.

5.5 Corrections

Two corrections were applied to the "raw" figures to compensate for processes not observed by the scanners, because they occurred at small angles. The first was made to the beam composition to allow for the probability that a kaon decay to a π or a μ was not observed, and at least one acceptable δ-

	Run 2a	Run 2b	Run 3b
% K	83.6 ± 1.0	83.2 ± 1.7	83.2 ± 1.4
% π	4.6 ± 1.0	4.6 ± 1.6	6.4 ± 1.0
% μ	11.8 ± 1.4	12.2 ± 2.3	10.4 ± 1.7
δ_π 'A'	283.4 ± 73	309.0 ± 104	360.3 ± 50
δ_π 'B'	586.8 ± 168	653.1 ± 241	652.1 ± 104
δ_μ 'A'	225.6 ± 7	262.6 ± 8	259.1 ± 16
δ_μ 'B'	393.1 ± 15	463.8 ± 14	430.6 ± 32
λ_π	84.7 ± 8.5	85.0 ± 9.5	82.7 ± 8.5
λ_K	86.6 ± 1.2	87.9 ± 1.2	88.6 ± 1.4

TABLE 5.2

Fitted values of the δ-ray parameters.

% K	84.1 ± 1.0	83.7 ± 1.7	83.7 ± 1.4
% π	4.5 ± 1.0	4.5 ± 1.6	6.3 ± 1.0
% μ	11.4 ± 1.4	11.8 ± 2.3	10.0 ± 1.7
λ_K	82.5 ± 1.2	83.6 ± 1.2	84.2 ± 1.4

TABLE 5.3

Corrected values of the δ-ray parameters.

ray was detected on the decay track. In this case the kaon

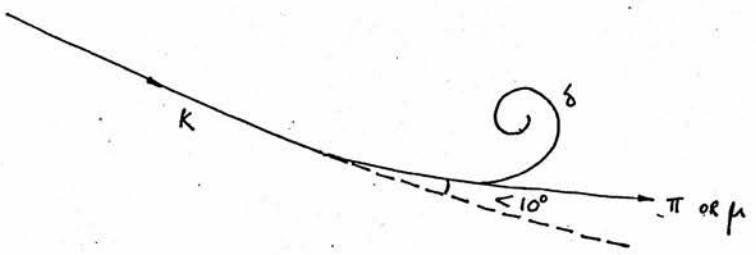

would be mistaken as a contaminant and the beam purity underestimated. The probabilities that a K^- decays at an angle less than 10^o to a π or a μ, and a δ-ray is seen on the decay track, are approximately 5.0×10^{-3} and 1.1×10^{-3} respectively. With these figures taken into account the beam composition was modified. The new values are shown in Table 5.3.

The K^- attenuation length required for the normalization (λ_{atten}) was that for kaon decays at <u>all</u> angles and for interactions at angles greater than 10^o. The attenuation length produced by the analysis of the δ-ray data (λ_{meas}) accounted only for decays and interactions at angles greater than 10^o and hence a correction was necessary to restore the small angle decays.

The expression for the attenuation cross-section, σ_{atten}, for decays and interactions at <u>all</u> angles is:-

$$\sigma_{atten} = \underbrace{\sigma_{el} + \sigma_{inel}}_{\sigma_I} + \underbrace{\sigma_{K\mu} + \sigma_{K\pi} + \sigma_{others}}_{\sigma_D}$$

where the total interaction cross-section, σ_I, is given as the sum of the elastic and inelastic interaction cross-sections,

σ_{el} and σ_{inel}, and the decay cross-section, σ_D, as the sum of the partial decay modes of which $\sigma_{K\pi}$ and $\sigma_{K\mu}$ are the most prominent. The expression can be written:

$$\frac{1}{\lambda_{atten}} = \frac{1}{\lambda_D} + \frac{1}{\lambda_I} \quad .$$

The kaon beam was attenuated if an interaction occurred, if there was a scatter at an angle greater than 10^o (during the scanning process, for a scatter at an angle less than 10^o the kaon was still regarded as acceptable), or if the kaon decayed (a pion or a muon could not produce the interactions required). Hence the required attenuation length can be written as:

$$\frac{1}{\lambda_{atten}} = \frac{1}{\lambda_D} + \frac{1}{\lambda_I}(1 - \Gamma_{el} P_{el}) \qquad (1)$$

where Γ_{el} is the elastic branching ratio $(= \sigma_{el}/\sigma_I)$ and P_{el} is the probability of an elastic interaction at an angle less than 10^o.

The measured attenuation length is given by:-

$$\frac{1}{\lambda_{meas}} = (1-fy)\left[\frac{1}{\lambda_D}(1 - \Gamma_{k\pi}P_{K\pi} - \Gamma_{K\mu}P_{K\mu}) + \frac{1}{\lambda_I}(1 - \Gamma_{el}P_{el})\right] \qquad (2)$$

where $\Gamma_{K\mu}$ and $\Gamma_{K\pi}$ are the branching ratios for the decays $K^- \longrightarrow \mu\nu$ and $K^- \longrightarrow \pi^-\pi^o$ respectively, and $P_{K\mu}$ and $P_{K\pi}$ are the probabilities that the decays occur at angles less than 10^o, and are therefore unobserved. The factor $(1 - fy)$ allows for that fraction of the track length, which

although starting out as kaon, is in fact pion or muon. Solving equations (1) and (2) gives:-

$$\frac{1}{\lambda_{atten}} = \frac{1}{\lambda_{meas}}\left[\frac{1}{1-fy} + \frac{\lambda_{meas}}{\lambda_D}\left(\Gamma_{K\mu} P_{K\mu} + \Gamma_{K\pi} P_{K\pi}\right)\right] .$$

Using the measured value, λ_{meas}, and the calculated values of the other parameters, the corrected attenuation lengths for the different runs were determined. The effect of the correction was to lower the measured attenuation length by about 5°/o. The new values are shown in Table 5.3.

As a check on the parameter values determined by this analysis, a comparison was made of the measured value of the K^- interaction length for run 2b, as given by the fit, with the value calculated for the liquid using the known K^-P and K^--Carbon cross-sections and scaling, using the "$^2/_3$ power law", to obtain the cross-sections on Fluorine and Bromine. The expression used was:-

$$\frac{1}{\lambda_{calc}} = \sigma_H n_H + \sigma_C \left\{ n_C + n_F \left(\frac{A_F}{A_C}\right)^{2/3} + n_{Br} \left(\frac{A_{Br}}{A_C}\right)^{2/3} \right\}$$

where σ_H and σ_C are the K^-P[30] and K^-C[31] cross-sections, n_H, n_C, n_F and n_{Br} are the numbers of Hydrogen, Carbon, Fluorine and Bromine atoms per cc. and A_C, A_F, A_{Br} are the atomic masses of Carbon, Fluorine and Bromine.

Averaged over the run 2b energy range a value for λ_{calc} of 81.5 $\pm$ 6.0 cm. was obtained. This value applied to interactions at all angles and for a valid comparison to be made another correction to restore the small

angle scatters must be made to the measured interaction length. The corrected "measured" value of 91.0 $\pm$ 6.0 cm. compared well with the calculated value.

It can be seen from Figure 5.8 that the calculated K^- interaction length varies by only a few per cent over the experimental momentum range, thereby providing justification for the fact that no allowance was made during the analysis for any variation.

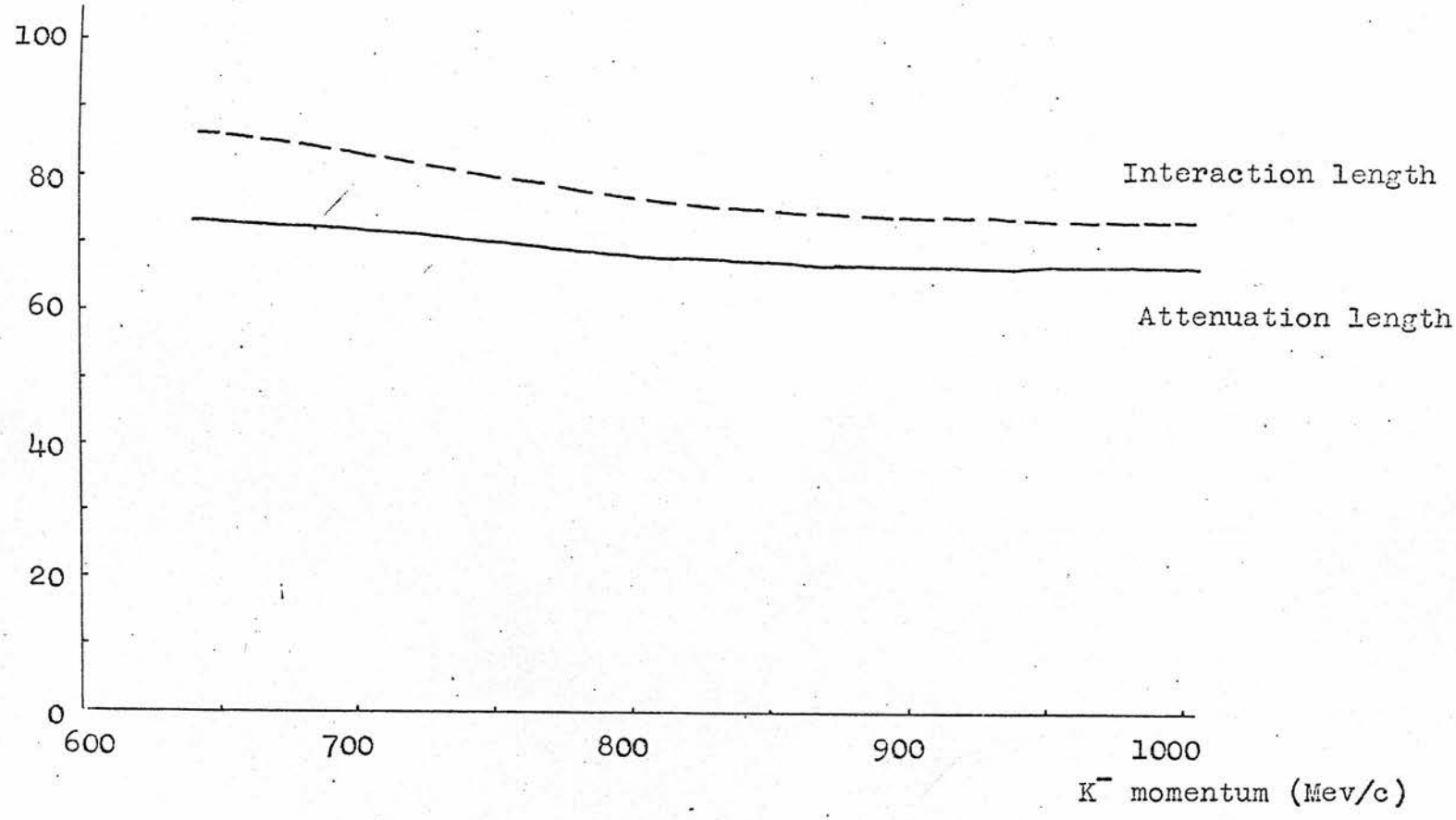

FIG. 5.8 K^- attenuation and interaction lengths as a function of momentum.

CHAPTER 6

ESTIMATION OF CROSS-SECTIONS

6.1 Flux Normalisation

In heavy liquid, a difficulty arises if trying to normalise cross-sections to the number of τ decays, as is done in hydrogen, because of the background due to 3-prong interactions. The beam-track flux was therefore measured directly by means of a beam count. For the count, only those photographs in which an event occured were used and the flux calculation was facilitated by taking the data directly from the D.S.T. This method used the same beam acceptance criteria as were used in normal scanning to define a "good" beam track - i.e. the track had to enter the chamber by the beam window and reach the beginning of the event fiducial volume without interacting or scattering by a projected angle of more than 10°.

An independent check of the value obtained for the run 2a film was made by "manually" counting the numbers of tracks on every twentieth frame over a large sample of film, irrespective of whether it contained an event. The compatibility of the results of the two methods for the beam track average (7.42 ± 0.06) and 7.34 ± 0.04 tracks per frame respectively) indicated that by restricting the count to event frames only, no bias was introduced, and this method was therefore used to provide the normalisation in the other runs.

A "flux factor" derived from the beam count allowed the

number of observed events in a particular channel to be converted into a cross-section. Expressed as a function of the centre of mass energy, ω^*, this was defined as:-

$$f(\omega^*) = N_K(S)\sigma_H\left(d\omega^*/dS\right)^{-1} \text{ events per mb per Mev}$$

where $N_K(S)$ is the number of beam tracks at the distance S ($\equiv S(\omega^*)$) from the reference plane at $x = +62$ cms. (at the beam window), σ_H the density of free protons estimated from the known liquid composition (typically $2.1 \pm 0.005 \times 10^{22}$ cm.$^{-3}$), and $d\omega^*/dS$ is the change in centre of mass energy ω^* due to ionisation loss of the incoming K^- (about 1 Mev per cm.).

Allowance was made when calculating $N_K(S)$ for a beam contamination of negative pions and muons of approximately 16% (see Chapter 5) and for beam losses because of cuts and book-keeping errors, by including in it a "flux reduction factor", expressed as a function of S.

The flux factor expression actually used was derived from the one given above, which applies to the ideal case, where the beam momentum can be described as a δ-function at the reference plane. This was generalised to a more realistic situation, by allowing for both a natural momentum spread at entry and for a variation in the central value across the entrance window. The latter correction was made after an analysis of stopping antiproton photographs, taken for each run, indicated that for certain runs, the beam momentum depended not only on the distance from the entrance window but also on the position in the window at which the particle had entered.

The net effect of including these considerations was to round off and to extend the limits of the flux range, as can be seen in Figure 6.1(a), where the flux factor for run 2a is shown as a function of ω^*. The overall flux factor used in the cross-section calculations, to be discussed later, was obtained by combining the separate flux factors for each run from which data were taken and is shown in Figure 6.1(b).

6.2 Additional Losses and Backgrounds

The event weighting procedure discussed in Chapter 3 took into account the loss of events due to the inefficiency of the bubble chamber and the visual scanning process as a means of detecting Λ's and γ's. Further corrections, however, must be applied before cross-sections can be calculated, to allow for additional losses and backgrounds occurring in the processing of event data post scanning, that is, in measurement, fitting and selection. Such losses and backgrounds arise from:-

1. Kinematic fitting failures.
2. Fits in the wrong channel.
3. Measurement mistakes.
4. Book-keeping losses.
5. Nuclear events.

A further "phase-space" correction, to allow for the loss of events because of the cuts made on the Λ and Σ° momenta at 175 Mev/c, mentioned above in Section 3.2, must also be included.

The background of nuclear events in the $\Lambda\pi^\circ$ and $\Sigma^\circ\pi^\circ$

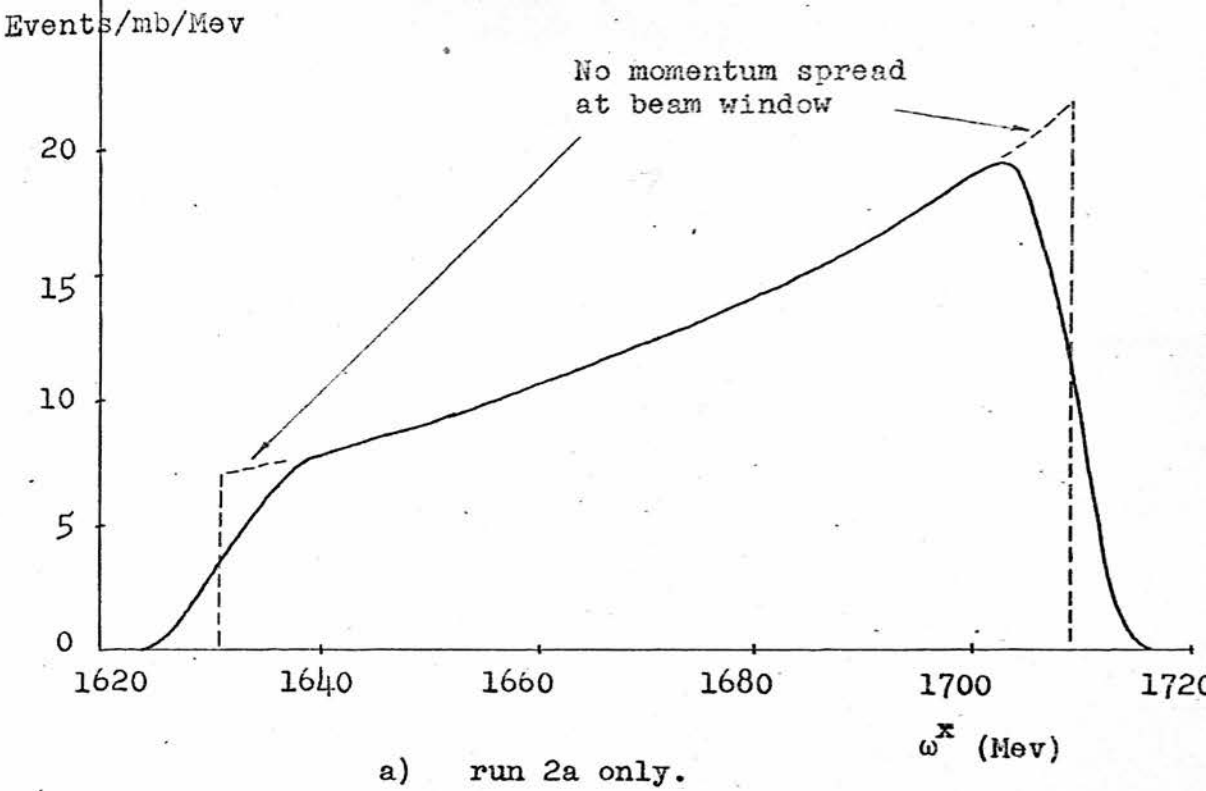

a) run 2a only.

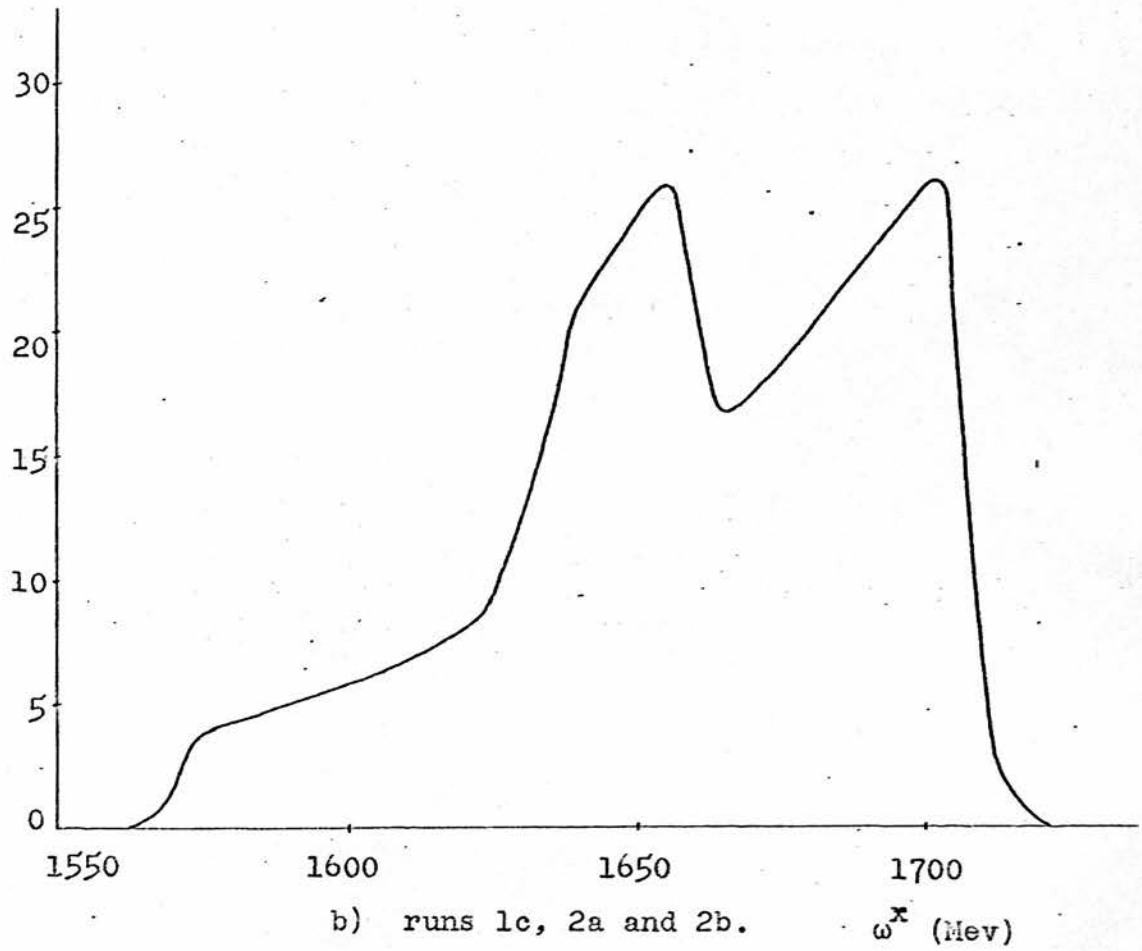

b) runs 1c, 2a and 2b.

FIG. 6.1 Flux factor, $f(\omega^x)$, as a function of centre of mass energy, ω^x.

channels has already been dealt with in Chapter 4. The methods used to estimate the other losses for these channels are described below.

Monte Carlo Study

Because of the fact that spurious γ's are present in our event sample, and because of the method used to fit and select events, certain "wrong-fit" backgrounds arise. These originate from:-

a) events which contain residual spurious γ's (after cuts have been applied) and which are successfully fitted and selected in a higher channel (e.g. a true $\Lambda\,\pi^o$ event plus one spurious γ may become an accepted $\Sigma^o\pi^o$ event) and

b) events which are fitted and selected in a lower channel either because one or more of its γ's are not detected or because of the γ dropping procedure in normal fitting (see Section 2.5), e.g. a true $\Lambda\,\pi^o\pi^o$ event may become an accepted $\Sigma^o\pi^o$ event upon losing or dropping a γ.

These "wrong-fit" backgrounds and the backgrounds of events in the correct channel with one or more of the true primary γ's replaced by spurious γ's, were determined for the $\Lambda\,\pi^o$ and $\Sigma^o\pi^o$ channels, by means of a Monte Carlo study, which also provided an estimate of the kinematical fitting efficiency for good events.

For each of these channels a large number of artificial events was constructed by using, as a basis, the beam track and interaction vertex of a real $\Lambda\,\pi^o$ event, previously measured, fitted, and selected as $K^-p \longrightarrow \Lambda\,\pi^o$. A Monte Carlo event of the required type - either $\Lambda\pi^o$, $\Sigma^o\pi^o$

or $\Lambda\pi^0\pi^0$ - was then generated at the vertex by assuming angular distributions derived from the CERN-Heidelberg-Saclay (CHS) experiment[6]. The $\Lambda\pi^0\pi^0$ events were included to allow an estimate of the background of true $\Lambda\pi^0\pi^0$ events which were accepted as $\Lambda\pi^0$ or $\Sigma^0\pi^0$ events. The simulation also provided converted γ's from Σ^0 and π^0 decay, and only those events with all γ's materialising within the chamber were retained.

In order to investigate the backgrounds arising from the presence of spurious γ's in as realistic a way as possible, the spurious γ's from the original real $\Lambda\pi^0$ event (i.e. those γ's observed in scanning but not used in the final fit) were added to those produced by the Monte Carlo. It had been found previously that for the $\Lambda\pi^0$ and $\Sigma^0\pi^0$ channels, the numbers of spurious gammas per event were equal ($\sim$ 1.5 γ's per event). The parameters of each Monte Carlo generated particle were then matched with values from a library containing measurement information on real particles from previous fits, and the Monte Carlo values distorted within the associated real measurement errors which were assumed to be Gaussian. The $\Lambda\pi^0$ and $\Sigma^0\pi^0$ events, each with its complement of spurious γ's, and the $\Lambda\pi^0\pi^0$ events (no spurious γ's added) were then fitted in the normal way.

For ambiguous fits in the same channel, that with the maximum probability was selected. Two methods were considered to resolve ambiguous fits in different channels. Fits were selected by "maximum complexity" (i.e. that with the most γ's chosen), and by "minimum complexity" (i.e. that with the fewest γ's chosen). The maximum complexity

choice was that which had previously been used in the real event selection. It was found, however, that by choosing the Monte Carlo events on the basis of minimum complexity, the background in the accepted fit sample due to fits with an additional spurious γ was greatly reduced (with only a small change in the background from higher channels) and it was therefore decided to adopt this selection procedure for the real events.

The kinematic fitting and selection efficiency was calculated by comparing the numbers of input Monte Carlo events at a particular centre of mass energy and angle $(\omega^*, \cos\theta^*)$ with the numbers of fits ultimately selected in the correct channel at the same $(\omega^*, \cos\theta^*)$. A similar comparison with the numbers of fits selected in different channels gave values for the "wrong-fit" backgrounds.

It was found that the dependence of the fitting efficiency and "wrong-fit" backgrounds on ω^* was small, and this was therefore disregarded. The variations with cosine θ^* are shown in Figures 6.2, 6.3. Further, it was found that the background of true $\Lambda\,\pi^o\pi^o$ events in the $\Lambda\,\pi^o$ channel (i.e. 2 γ's dropped) was insignificant and it was assumed from this, that the background in any channel from another displaced upwards by more than 1 γ was negligible. From the fact that the background of $\Lambda\,\pi^o$ events with one spurious γ added, in the $\Sigma^o\pi^o$ channel was so small ($\sim 2^o/o$), it was assumed that for any channel the background from another displaced downwards by more than 1γ was also negligible.

To estimate the loss of events because of non-Gaussian measurement errors and because of gross measurement mistakes, a complete remeasurement of a large number of the accepted fits was performed and the efficiency of obtaining the same

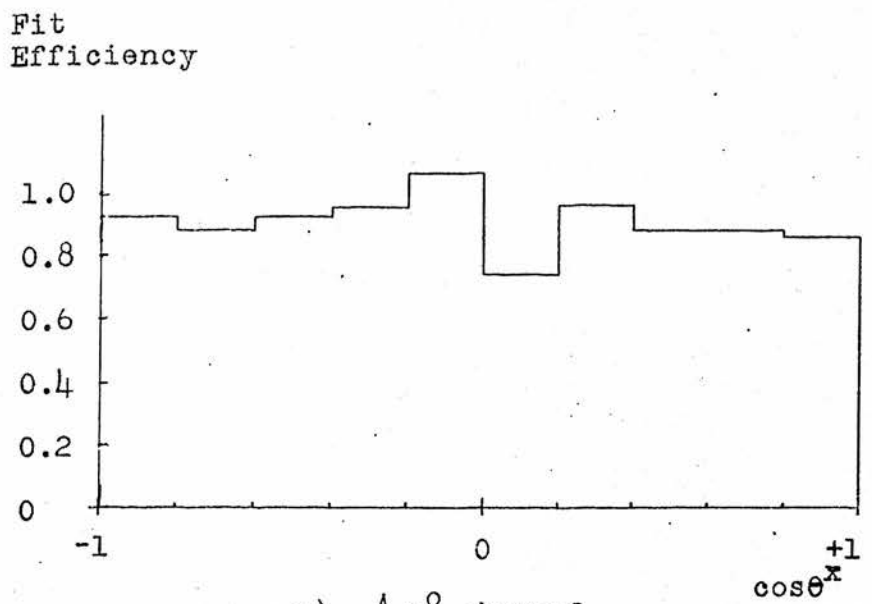

a) $\Lambda\pi^{\circ}$ channel

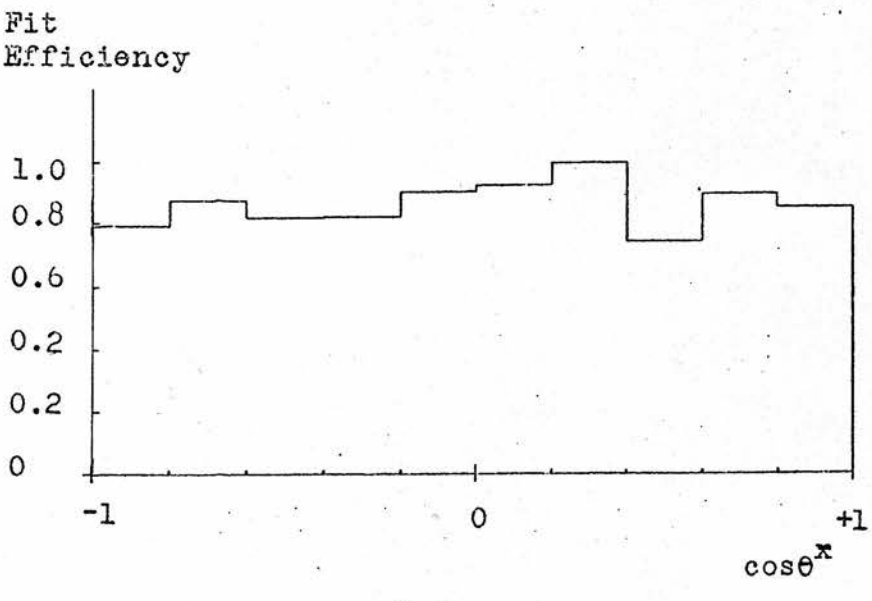

b) $\Sigma^{\circ}\pi^{\circ}$ channel

FIG. 6.2 Fit-efficiency as a function of $\cos\theta^{*}$ for the $\Lambda\pi^{\circ}$ and $\Sigma^{\circ}\pi^{\circ}$ channels.

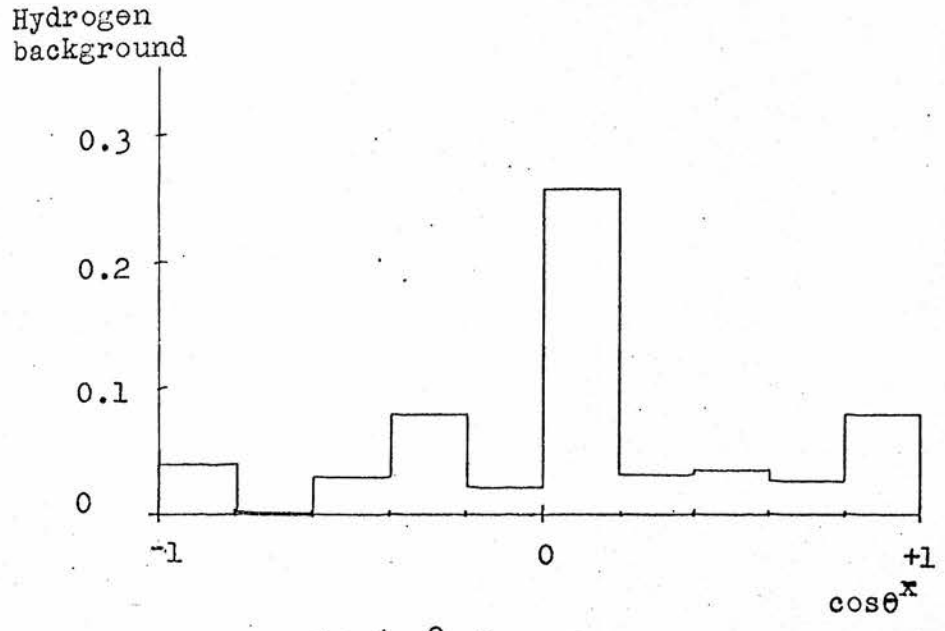

a) $\Lambda\pi^{\circ}$ channel

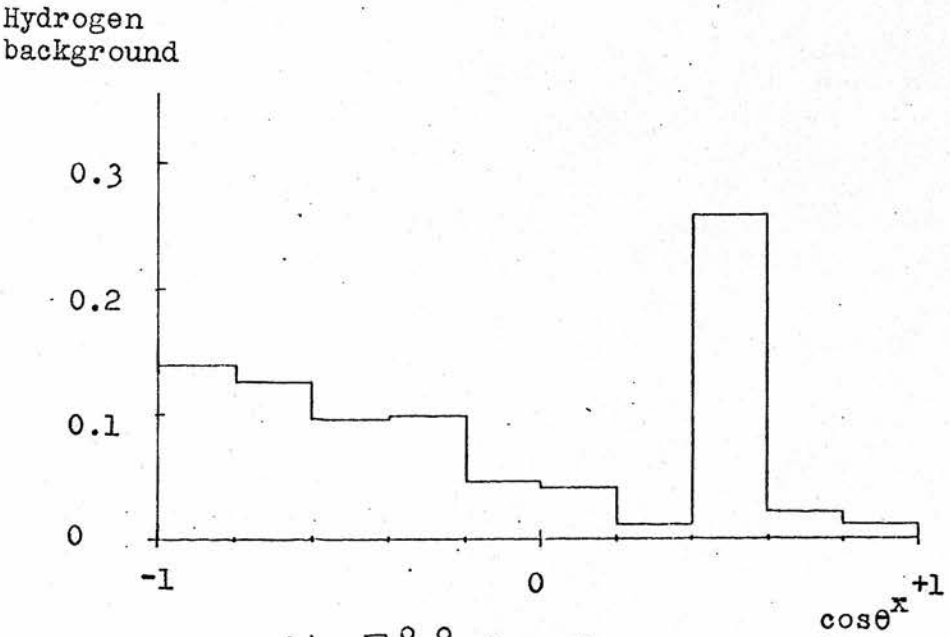

b) $\Sigma^{\circ}\pi^{\circ}$ channel

FIG. 6.3 Hydrogen background as a function of $\cos\theta^{*}$ for the $\Lambda\pi^{\circ}$ and $\Sigma^{\circ}\pi^{\circ}$ channels.

fit on remeasurement was calculated. The difference between this number and the fit-plus-selection efficiency calculated from the Monte Carlo study represented the additional loss of events during the real measurement process.

The estimates of the fit-plus-selection efficiency, the wrong-fit backgrounds, and the measurement efficiency for the $\Lambda\,\pi^o$ and $\Sigma^o\pi^o$ channels are presented in Table 6.1, where the values quoted correspond to the range $-1 < \cos\theta^* < +1$. For completeness the nuclear background estimates are also shown.

An overall correction factor was calculated from the above efficiencies and backgrounds to scale the cross-sections. The distribution in cosine θ^* is shown in Figures 6.4a and 6.4b. For both the $\Lambda\,\pi^o$ and $\Sigma^o\pi^o$ channels the distributions are flat with average values 1.009 ± 0.064 and 1.073 ± 0.117 respectively.

In addition to the above corrections, a book-keeping loss of $\sim 4^o/o$ for both the $\Lambda\,\pi^o$ and $\Sigma^o\pi^o$ channels occurred between scanning and the final D.S.T. An adjustment was made to the normalisation to allow for this.

For the 3-body ($\Lambda\pi^o\pi^o$ and $\Sigma^o\pi^o\pi^o$) channels a detailed background analysis has not as yet been performed and only nominal corrections of $10^o/o$ for nuclear background and $80^o/o$ fit-plus-selection efficiency have been made in each case.

Phase-Space Correction

The cross-sections have also been corrected to allow for the fact that events having Λ's and Σ's of momentum

Channel	Fit & Selection Efficiency	Wrong Fit Background	Measurement Efficiency	Nuclear Background	Overall Correction Factor
$\Lambda\pi^\circ$	0.894 ± 0.014	0.05 ± 0.01	0.97 ± 0.05	0.07 ± 0.03	1.009 ± 0.064
$\Sigma^\circ\pi^\circ$	0.867 ± 0.021	0.09 ± 0.02	0.90 ± 0.08	0.09 ± 0.05	1.073 ± 0.117

Table 6.1

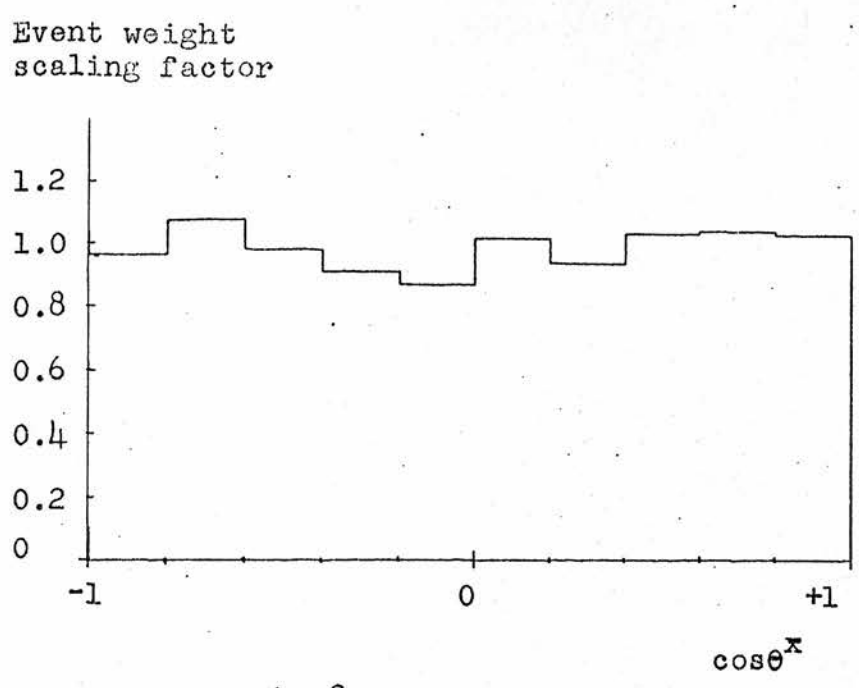

a) $\Lambda\pi^{\circ}$ channel

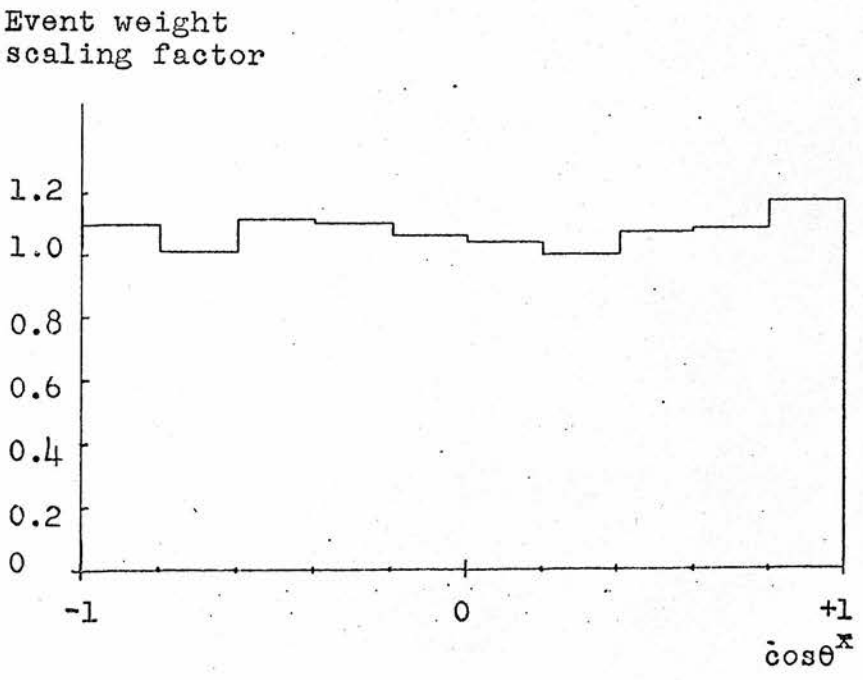

b) $\Sigma^{\circ}\pi^{\circ}$ channel.

FIG. 6.4 Event weight scaling factor as a function of cos θ^{*} for the $\Lambda\pi^{\circ}$ and $\Sigma^{\circ}\pi^{\circ}$ channels.

less than 175 Mev/c were rejected because of their low detection efficiency (see Section 3.2). For the $\Lambda\,\pi^{o}$ and $\Sigma^{o}\,\pi^{o}$ channels, this corresponded to a cut on the centre of mass scattering angle at cosine θ^{*} = 0.9, and the correction was made by fitting the differential cross-section to a Legendre Polynomial expansion and extrapolating into the undetectable region. For the $\Lambda\,\pi^{o}\pi^{o}$ and $\Sigma^{o}\pi^{o}\pi^{o}$ channels the correction was based on the extrapolation of the Λ and Σ^{o} momentum distributions as given by phase space. For the 3-body channels the correction was small (1°/o for $\Lambda\,\pi^{o}\pi^{o}$, and negligible for $\Sigma^{o}\pi^{o}\pi^{o}$) but for the 2-body channels it was appreciable (for $\Lambda\,\pi^{o}$ it varied from 5°/o to 20°/o over the energy range and from 1°/o to 10°/o for $\Sigma^{o}\pi^{o}$).

6.3 Total Cross-Sections

Using the flux factor expression given in Section 6.1, the weighted event statistics were converted into cross-sections. The data were separated into four energy bands, each containing approximately equal statistics and for each channel cross-sections calculated as averages over the bands. For a centre of mass energy range ω_1^{*} to ω_2^{*} the average cross-section was given by:-

$$\bar{\sigma} = \frac{1}{\omega_2^{*} - \omega_1^{*}} \int_{\omega_1^{*}}^{\omega_2^{*}} \sigma(\omega^{*})\,d\omega^{*}$$

$$= \sum_{i=1}^{n} \frac{W_i}{(\omega_2^{*} - \omega_1^{*}).f(\omega^{*})}$$

where W_i is the detection efficiency weight for the i-th event. This value was then scaled by the appropriate correction factor for that channel, to allow for the additional losses and backgrounds described in the previous section, and the phase space correction made to give the final cross-section.

The corrected cross-section values for each channel are given in Table 6.2, where the errors quoted are statistical only. The contribution to the cross-section from the phase-space correction is shown in parenthesis. It was estimated that there was in addition a total systematic error of $\sim 10^{o}/o$ arising from flux normalisation and from the channel dependent background corrections and fit losses. A more detailed analysis of these results is made in the following sections.

6.4 Analysis of the 2-Body Channels

i) $\bar{K}^- p \longrightarrow \Lambda \pi^o$

In the film analysed to date, representing about $50^{o}/o$ of the total exposure, 890 acceptable $\Lambda \pi^o$ fits remained after cutting. A mean weight factor of 5.7 was applied to correct for the loss of good events because of cuts.

As mentioned above, the fit selection procedure was such that an ambiguous event fitting both the $\Lambda \pi^o$ and $\Sigma^o \pi^o$ hypotheses was normally accepted as $\Lambda \pi^o$ (minimum complexity selection). Hence the main source of wrong-fit background in the $\Lambda \pi^o$ channel arose from true $\Sigma^o \pi^o$ events making spurious $\Lambda \pi^o$ fits, because of the loss or

Channel	Events	Average Weight Factor	Cross-Sections (mb.)			
			Band I	Band II	Band III	Band IV
			P_K - (MeV/c) → 525-670	670-720	720-770	770-820
			ω^* (MeV/c^2) → 1574-1639	1639-1662	1662-1685	1685-1709
$K^-p \to \Lambda\eta$	50	12.6	-	-	0.45 ± 0.11	0.20 ± 0.08
$K^-p \to \Lambda\pi^o$	890	5.7	2.42 ± .32 (0.43)	2.61 ± .22 (0.35)	2.70 ± .24 (0.41)	2.84 ± .24 (0.55)
$K^-p \to \Sigma^o\pi^o$	434	8.6	1.88 ± .23 (0.04)	1.63 ± .19 (0.07)	1.42 ± .16 (0.02)	1.40 ± .18 (0.14)
$K^-p \to \Lambda\pi^o\pi^o$	170	14.4	.69 ± .25 (.005)	1.14 ± .27 (.01)	1.10 ± .28 (.01)	1.75 ± .37 (.02)
$K^-p \to \Sigma^o\pi^o\pi^o$	29	29.8	.33 ± .33 (0)	.23 ± .13 (0)	1.01 ± .35 (0)	.25 ± .14 (0)
$K^-p \to \Lambda$ + neutrals (sum of the above channels)	1573	8.1	5.31 ± .62	5.61 ± .44	6.68 ± .56	6.44 ± .52

Table 6.2

Cross-section values for channels 1-5 averaged over four energy bands.
The contribution from the phase-space correction is shown in parenthesis.

exclusion of one γ. This background was substantially reduced by raising the fit probability cut from 0.1°/o to 1.0°/o for the $\Lambda\ \pi^0$ channel only. The fit probability distribution after the application of this cut is shown in Figure 6.5 and is flat, apart from a peak at low values. From an analysis of remeasurement data this low probability peak was attributed mainly to events with non-Gaussian errors either because of poor measurement or unobserved small angle scatters.

As shown in Table 6.1 subtractions of 7°/o for nuclear background and 5°/o for wrong-fit backgrounds were made.

Several measurements of the $K^-p \rightarrow \Lambda\ \pi^0$ cross-section have been made in recent hydrogen experiments in this energy range, and these provide a useful check of our results. In hydrogen, where the neutral pion is not observed, the $\Lambda\ \pi^0$ events can be separated from the other channels by selecting on the missing mass squared to the Λ (Armenteros et al.[6] chose those events with a missing mass squared less than 0.04 Gev^2, illustrated as cut 'A' in Figure 6.13). A compilation of the hydrogen data is shown in Figure 6.6 together with the cross-sections from this experiment as given above in Table 6.2 and it can be seen that the values are compatible.

The differential cross-section for each energy range is shown in Figures 6.7 to 6.10, together with a fourth order Legendre Polynomial fit to the data points. As was mentioned above, this fit was used to correct for the $\Lambda\ \pi^0$ cross-section loss above $\cos\theta^* = 0.9$. The most significant of these plots is that for the centre of mass energy range

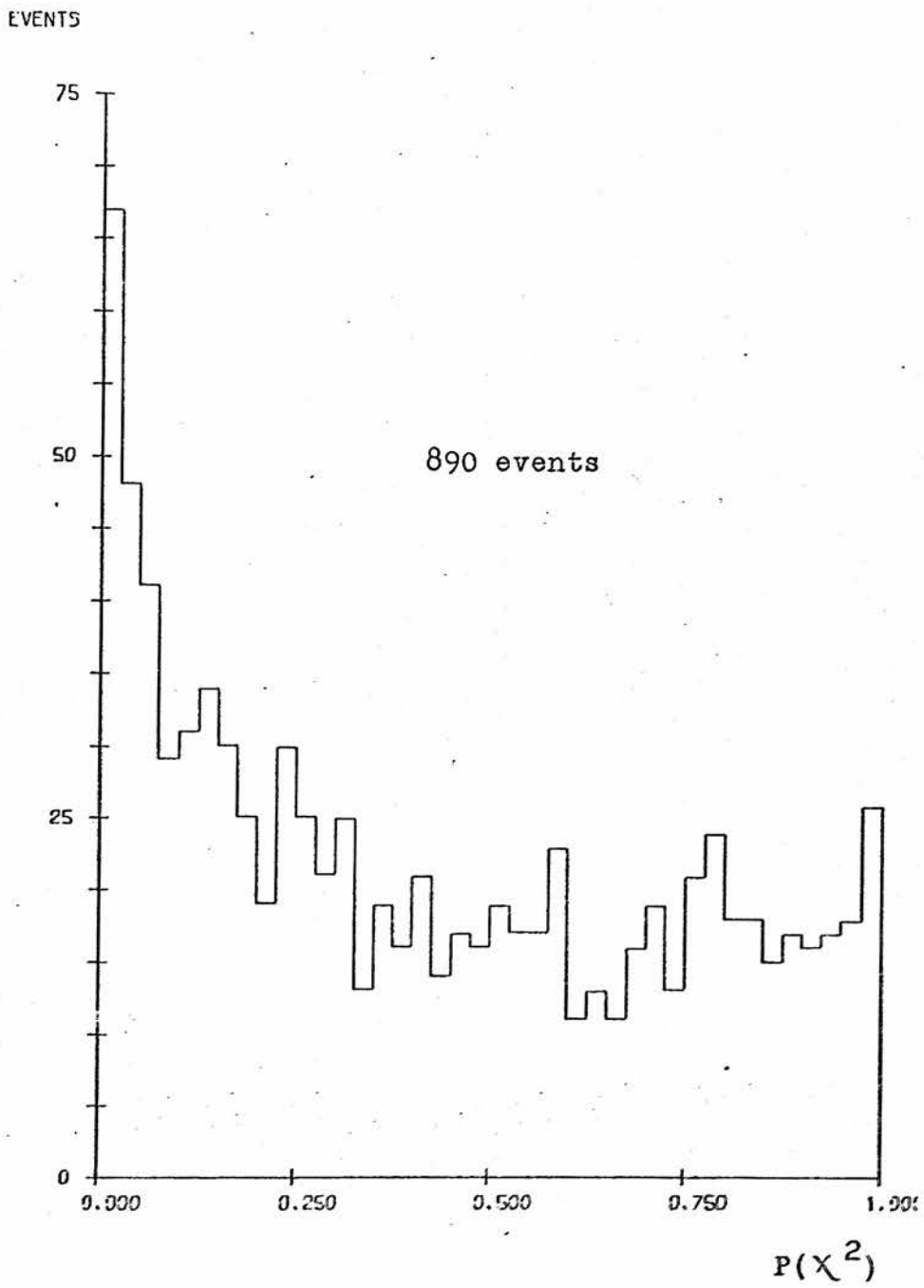

FIG. 6.5 Fit probability distribution for events fitting $K^- p \longrightarrow \Lambda \pi^o$.

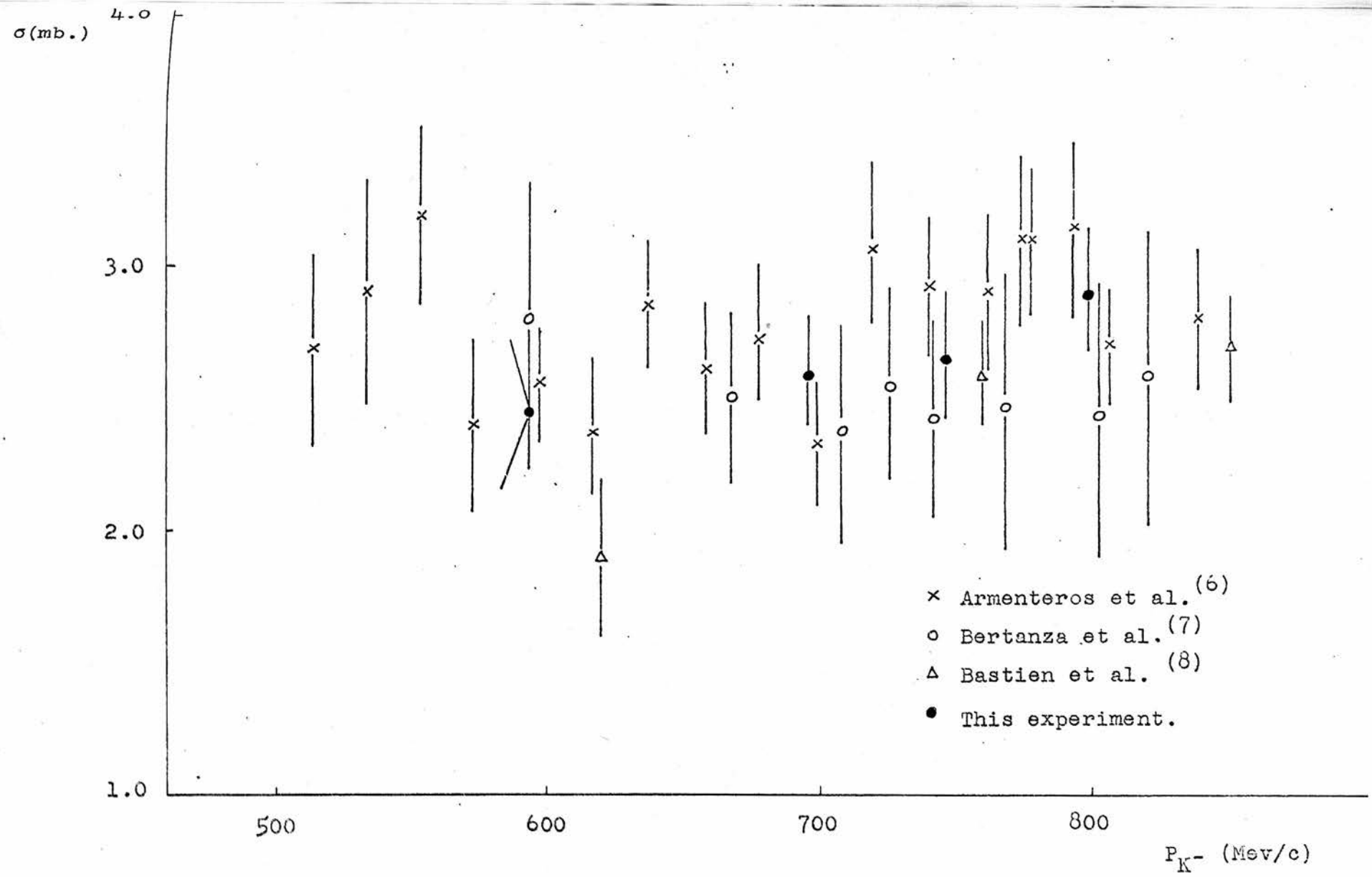

FIG. 6.6 Total cross-section versus K^- momentum for $K^-p \longrightarrow \Lambda\pi^o$ for the 4 momentum bands of this experiment, compared with previous hydrogen results.

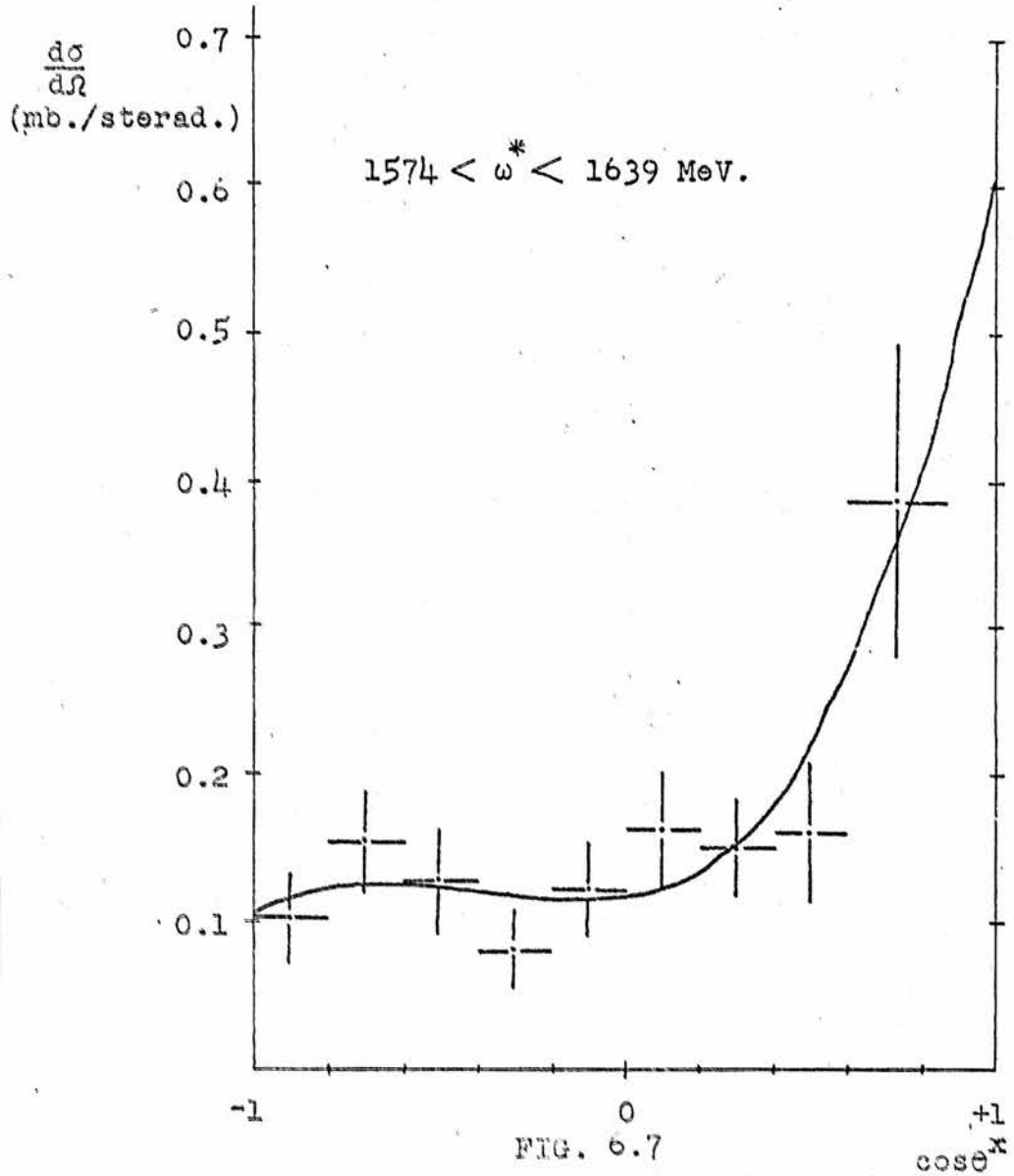

FIG. 6.7

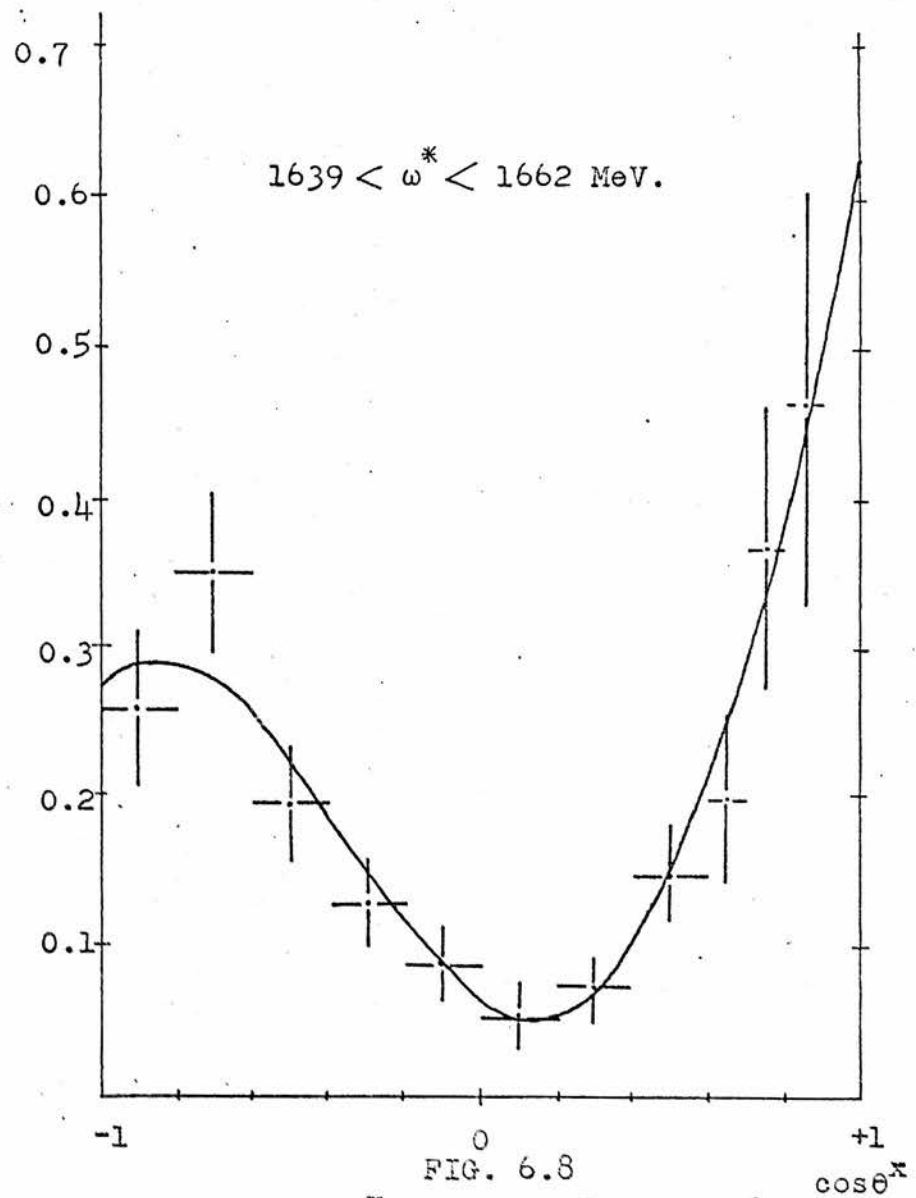

FIG. 6.8

FIGS. 6.7 to 6.10 show the differential cross-sections versus $\cos\theta^x$ for the $K^- p \longrightarrow \Lambda \pi^\circ$ channel in each of the 4 momentum bands.

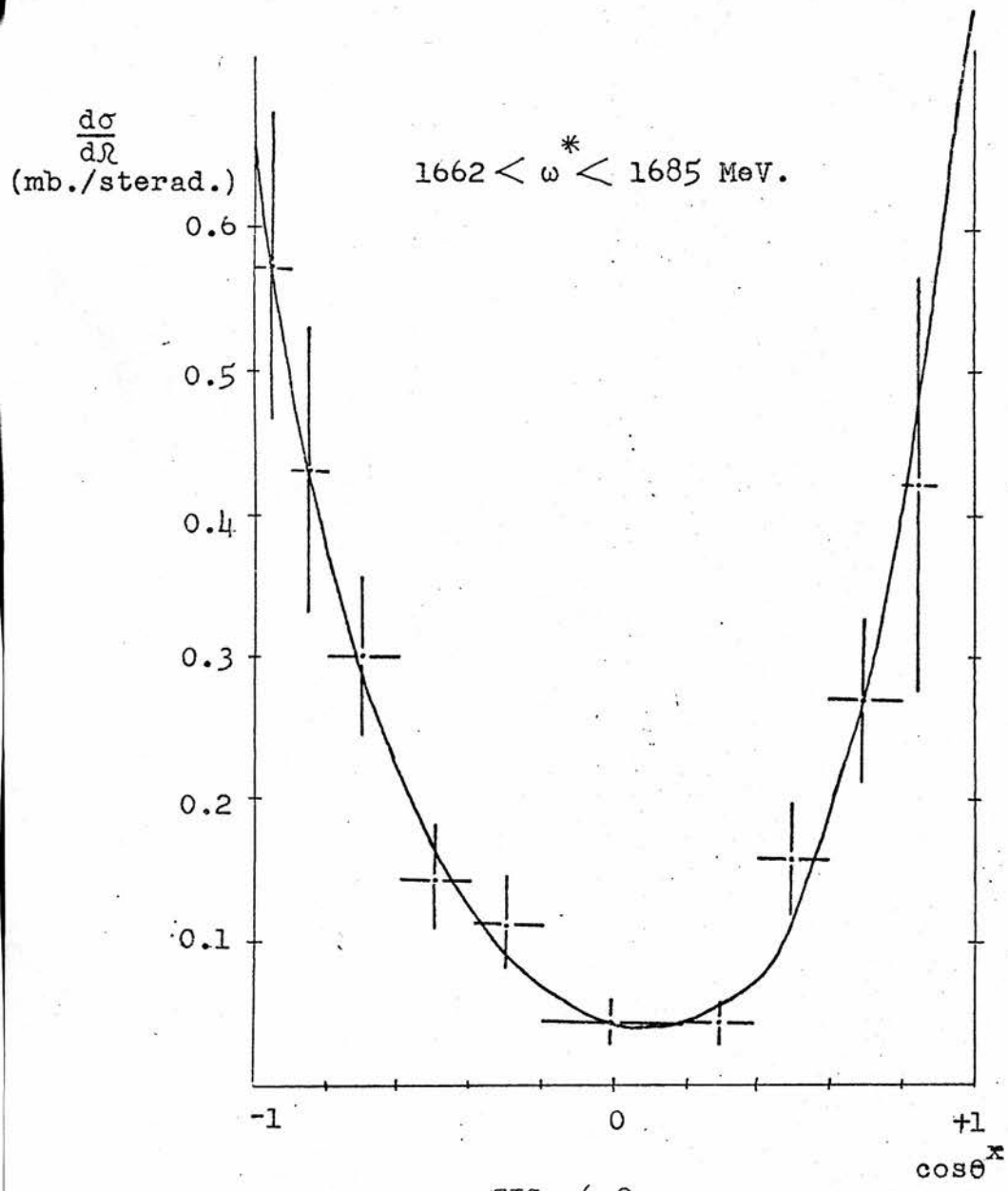

FIG. 6.9

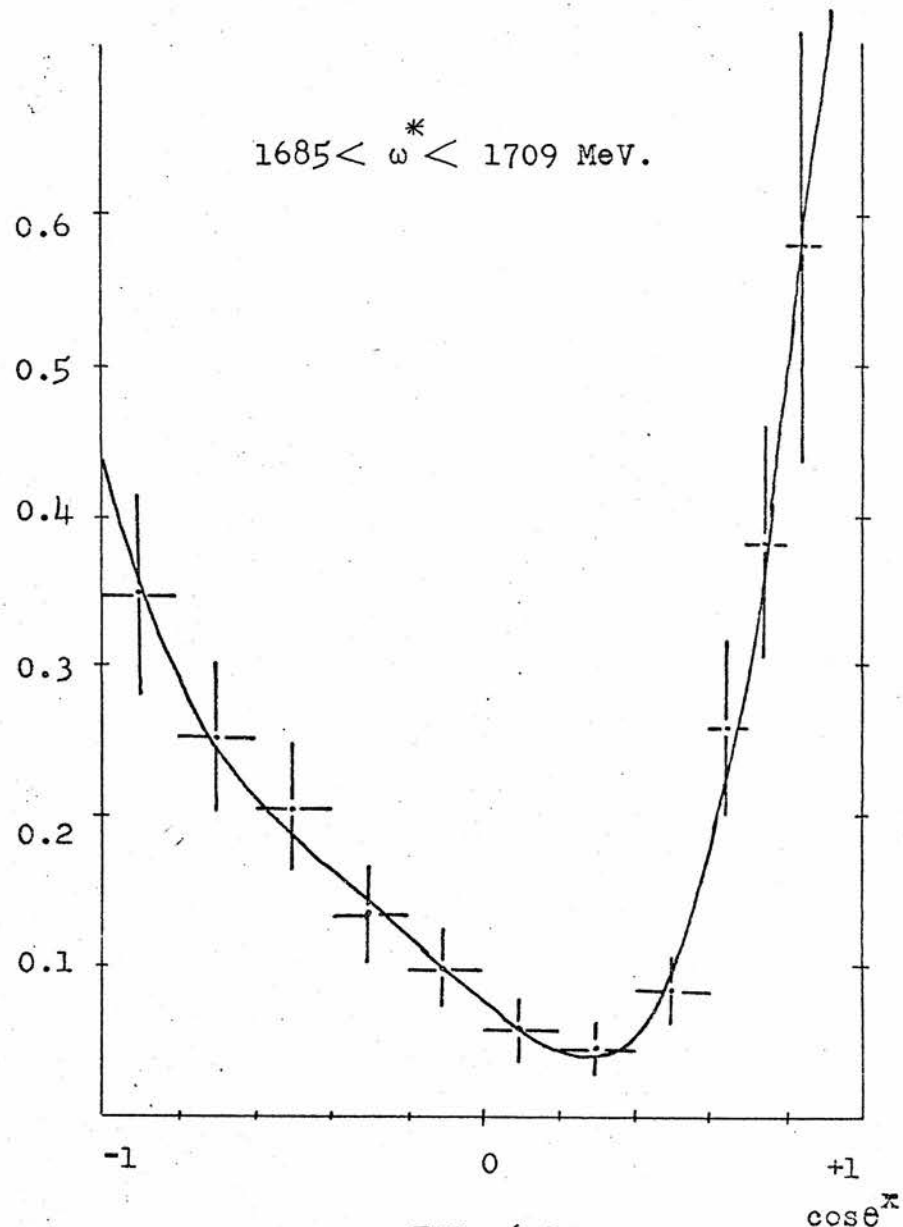

FIG. 6.10

1662-1685 Mev/c^2, approximately centred on the $\Sigma^*(1670)$, where the fit is consistent with an almost pure $D_{3/2}$ wave, and also indicates that the background in this channel is low.

For this experiment, and for several hydrogen experiments, the normalised 'A' coefficients of the Legendre polynomial fits to the $\Lambda\pi^o$ differential cross-section, averaged over the four energy bands, are shown in Figure 6.11. It can be seen that the general agreement is good. The coefficients A_1/A_o, A_3/A_o, and A_4/A_o are small and show little structure. In all cases, however, evidence is seen for a rapid increase in the D-wave amplitude with increasing energy.

As yet no polarisation measurements have been made for either the $\Lambda\pi^o$ or $\Sigma^o\pi^o$ channels and so a similar comparison of the Legendre 'B' coefficients is not possible. It is hoped, however, that this data will be available at a later date.

ii) $\underline{K^-p \longrightarrow \Sigma^o\pi^o}$

The total number of accepted fits in this channel was found to be 434 with an average weight factor of 8.6. The fit probability distribution after a cut at 0.1°/o is shown in Figure 6.12 and is similar to that for the $\Lambda\pi^o$ channel, with a peak at low values. This was again attributed to events with non-Gaussian errors.

To allow for nuclear and wrong-fit contaminations in the accepted fit sample, background subtractions of 9 ± 5°/o and 9 ± 2°/o respectively were made.

In order to test our cross-section results for the

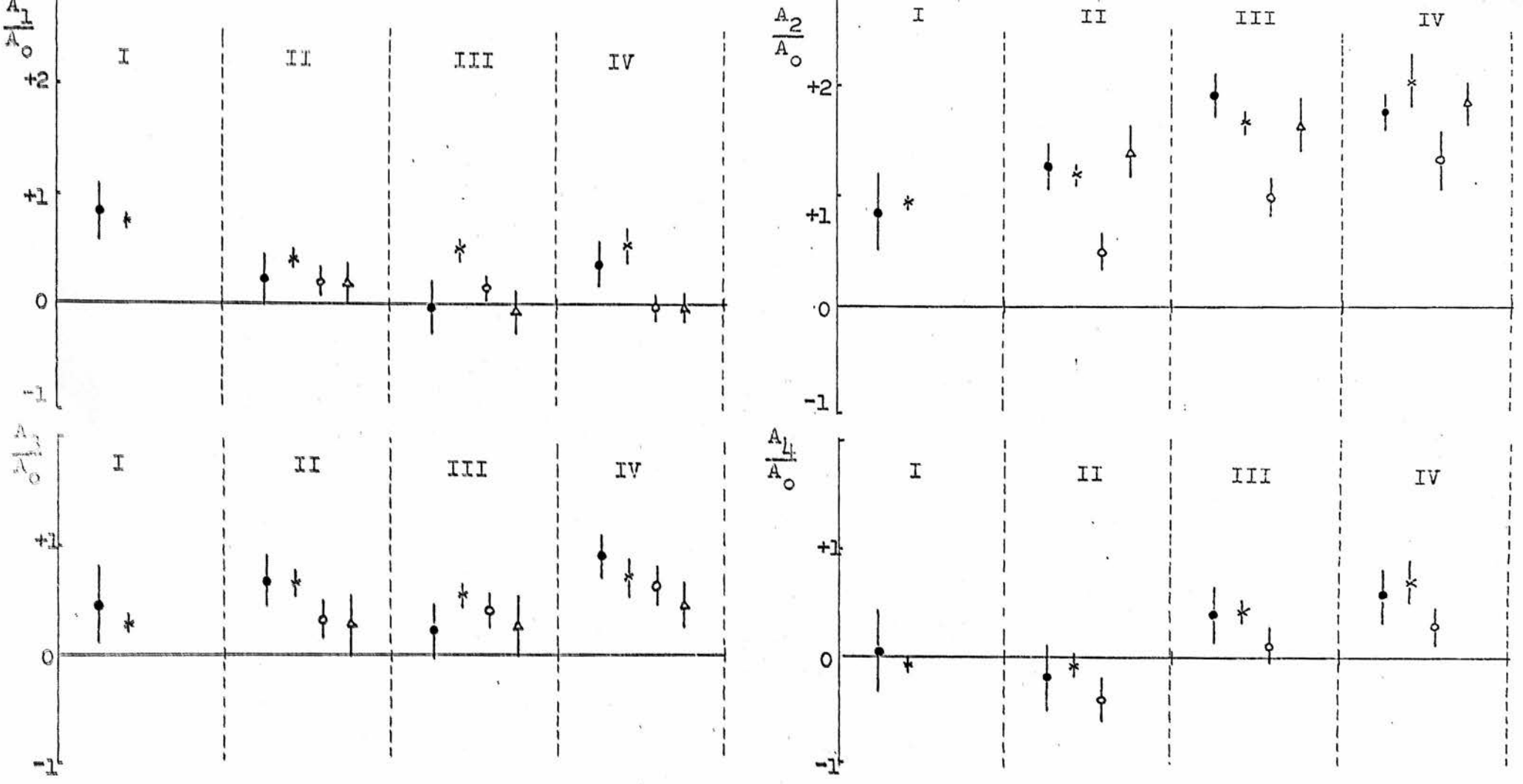

FIG. 6.11 The Legendre 'A' Coefficients from the $K^- p \longrightarrow \Lambda \pi^0$ differential cross-section fit in each of the 4 energy bands are compared with hydrogen values.

× Armenteros et al.[6]

∘ Bertanza et al.[7]

△ Bastien et al.[8]

• This experiment.

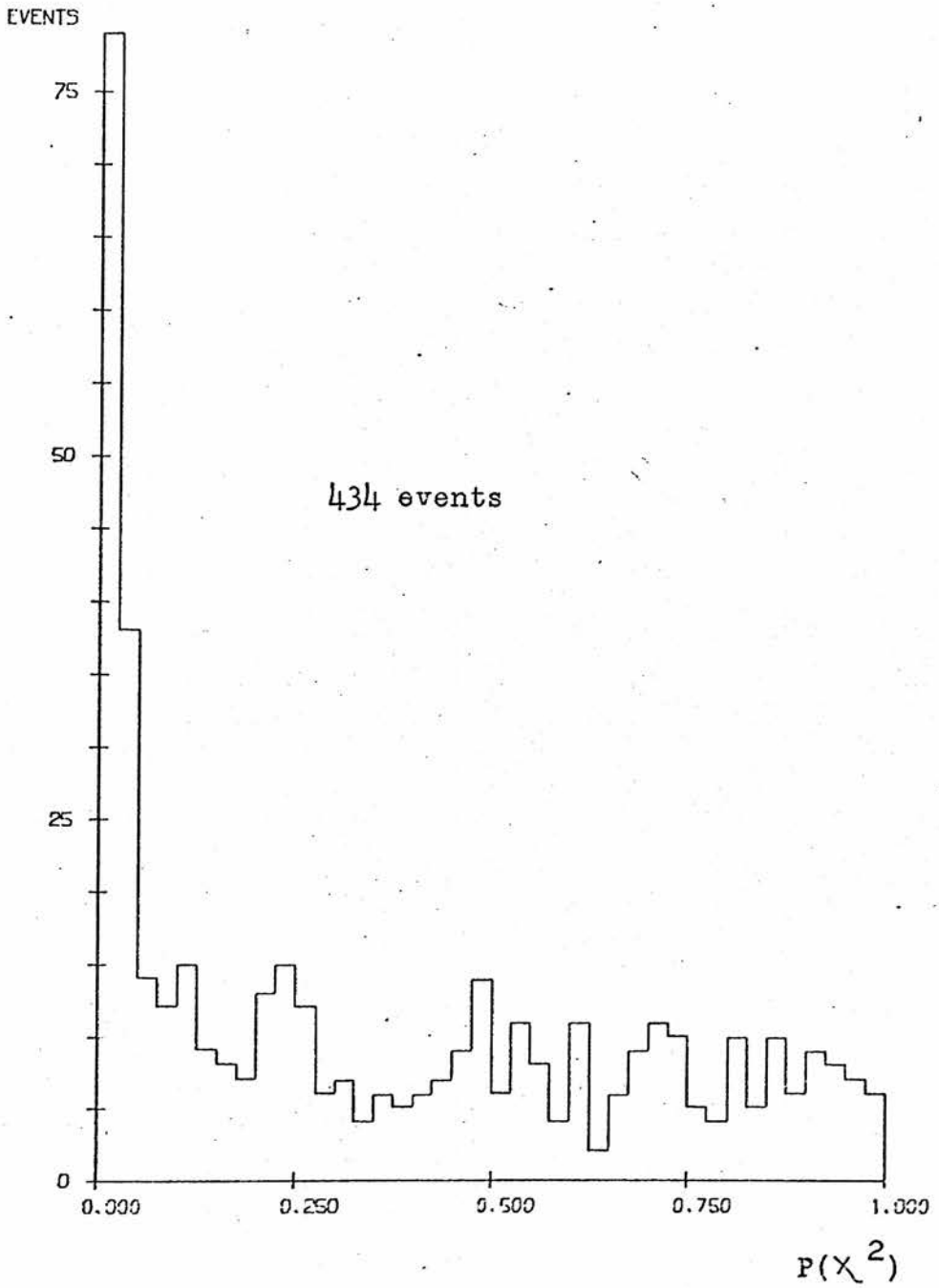

FIG. 6.12 Fit probability distribution for events fitting $K^- p \longrightarrow \Sigma^0 \pi^0$.

$\Sigma^0\pi^0$ channel, a comparison was made with the existing hydrogen data. As with the $\Lambda\pi^0$ events it is not possible to make a direct fit to $K^-p \longrightarrow \Sigma^0\pi^0$ in hydrogen because no γ's are observed, and it is therefore separated from the $\Lambda\pi^0$ and multiple π^0 channels by making a kinematic selection on the missing mass squared to the Λ. A typical missing mass distribution for the reaction $K^-p \longrightarrow \Lambda X$ is shown in Figure 6.13 together with a phase space calculation representing the result of an ideal experiment with perfect resolution. The π^0 and η^0 peaks can be seen above the smeared out contributions from the $\Sigma^0\pi^0$, $\Lambda\pi^0\pi^0$ and $\Sigma^0\pi^0\pi^0$ channels. The method used by Armenteros et al. when calculating the total cross-sections, was to make a least squares fit to the missing mass spectrum, for each energy bin, allowing the contribution from each final state to vary. Measurement errors were taken into account by describing the π^0 and η^0 peaks by Gaussian distributions and for the other channels by modifying the phase-space distributions by the experimental resolution.

It was claimed by Bertanza et al.[7] that the assumption that the three-body distributions followed phase space was probably incorrect. They presented evidence of a marked deviation from phase space in the form of a $\pi^+\pi^-$ missing mass distribution from reactions of the type $K^-p \longrightarrow \Lambda\pi^+\pi^-$ in analogy with the $\pi^0\pi^0$ distribution from $K^-p \longrightarrow \Lambda\pi^0\pi^0$ and concluded that, although the reactions did not correspond exactly, it was unrealistic to attempt a prediction of the $\pi^0\pi^0$ distributions. Instead,

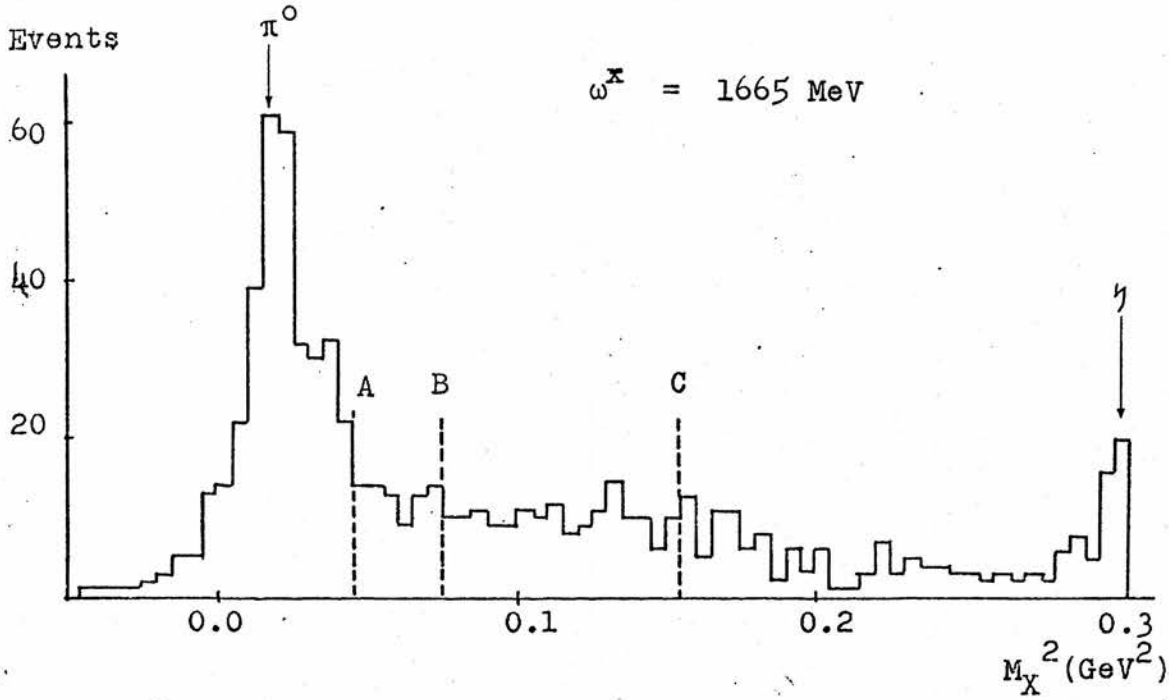

FIG. 6.13 a) Typical experimental missing mass squared distribution for the reaction $K^-p \rightarrow \Lambda X$. The cuts used by the CHS collaboration to separate the channels are shown as dashed lines.

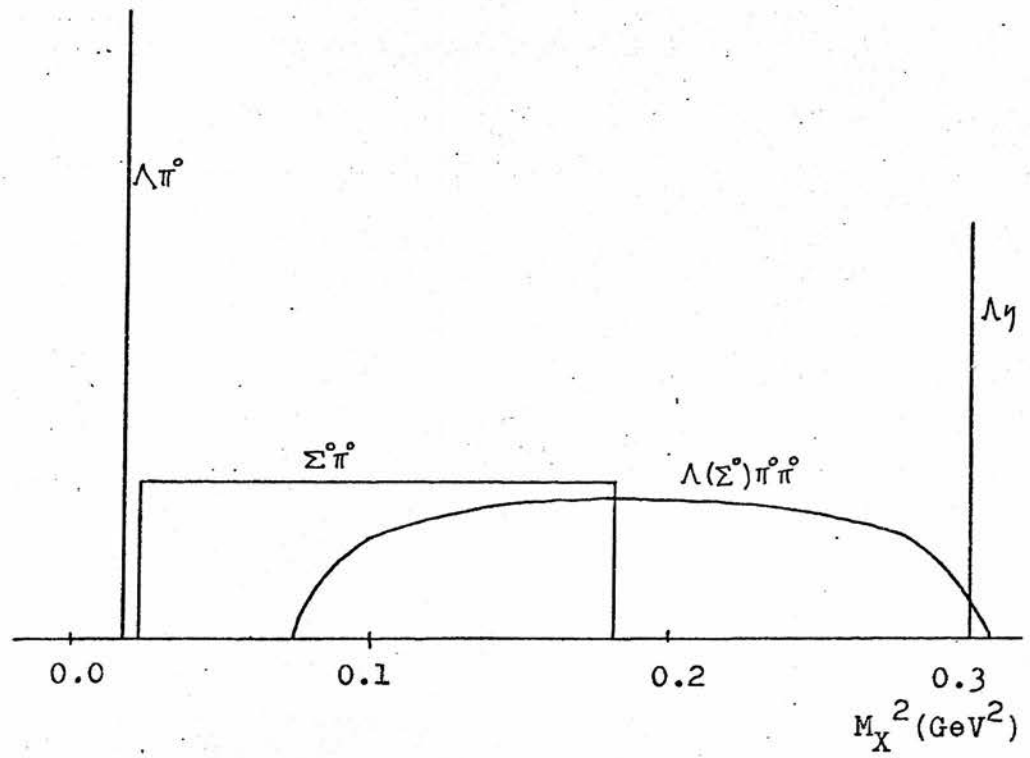

FIG. 6.13 b) Diagram showing contributions to the missing mass squared distribution from the various channels assuming perfect resolution.

they used a method which took into account the uncertainty in the $\Lambda\pi^o$ and $\Sigma^o\pi^o$ resolution by ascribing a $\Lambda\pi^o$ and a $\Sigma^o\pi^o$ "moment" to each event, and, to obtain an estimate of the systematic errors, calculated two values of the $\Sigma^o\pi^o$ cross-section by assuming extreme distributions for the $\pi^o\pi^o$ events, one peaking at high masses, giving a low 3-body background, and the other at low masses corresponding to a large background.

The method used by Bastien et al.[8] in an earlier experiment (1963) to separate the neutral channels, was similar to that of Armenteros et al.

A comparison of the $\Sigma^o\pi^o$ cross-section values of this experiment with those of the above hydrogen experiments is shown in Figure 6.14. There is reasonable agreement with the values of Bertanza et al. and of Bastien et al., but the cross-sections of Armenteros et al. are considerably higher (up to 1 mb.) in the region 1650-1700 Mev/c^2. That this effect is not due to normalisation is shown in Figure 6.15 where the $K^-p \longrightarrow \Lambda$ + neutrals (i.e. $\Lambda\pi^o + \Sigma^o\pi^o + \Lambda\eta_{neutrals} + \Lambda\pi^o\pi^o + \Sigma^o\pi^o\pi^o + \Lambda\pi^o\pi^o\pi^o$) cross-sections are shown, and here it can be seen that the agreement with the Armenteros values is good. A possible explanation of the significantly larger $\Sigma^o\pi^o$ cross-sections is that the Armenteros data may contain a substantial 3-body background.

For the differential cross-sections, Armenteros et al. used the method of selecting $\Sigma^o\pi^o$ events with a missing mass squared to the Λ, greater than 0.04 Gev^2 - cut A in Figure 6.13(a) - to exclude $\Lambda\pi^o$ events and less than an

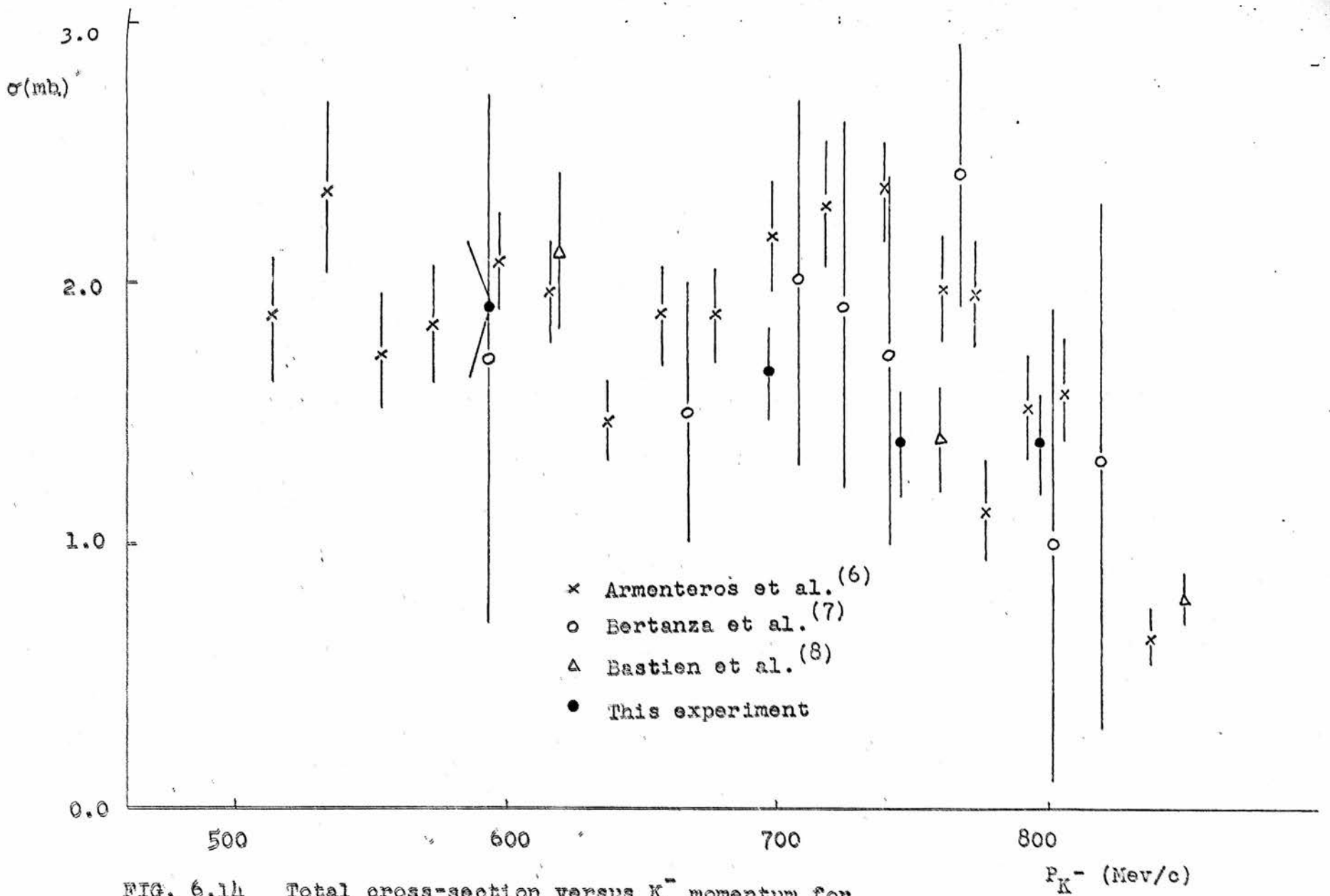

FIG. 6.14 Total cross-section versus K^- momentum for $K^-p \longrightarrow \Sigma^0\pi^0$ for the 4 momentum bands of the experiment, compared with previous hydrogen results.

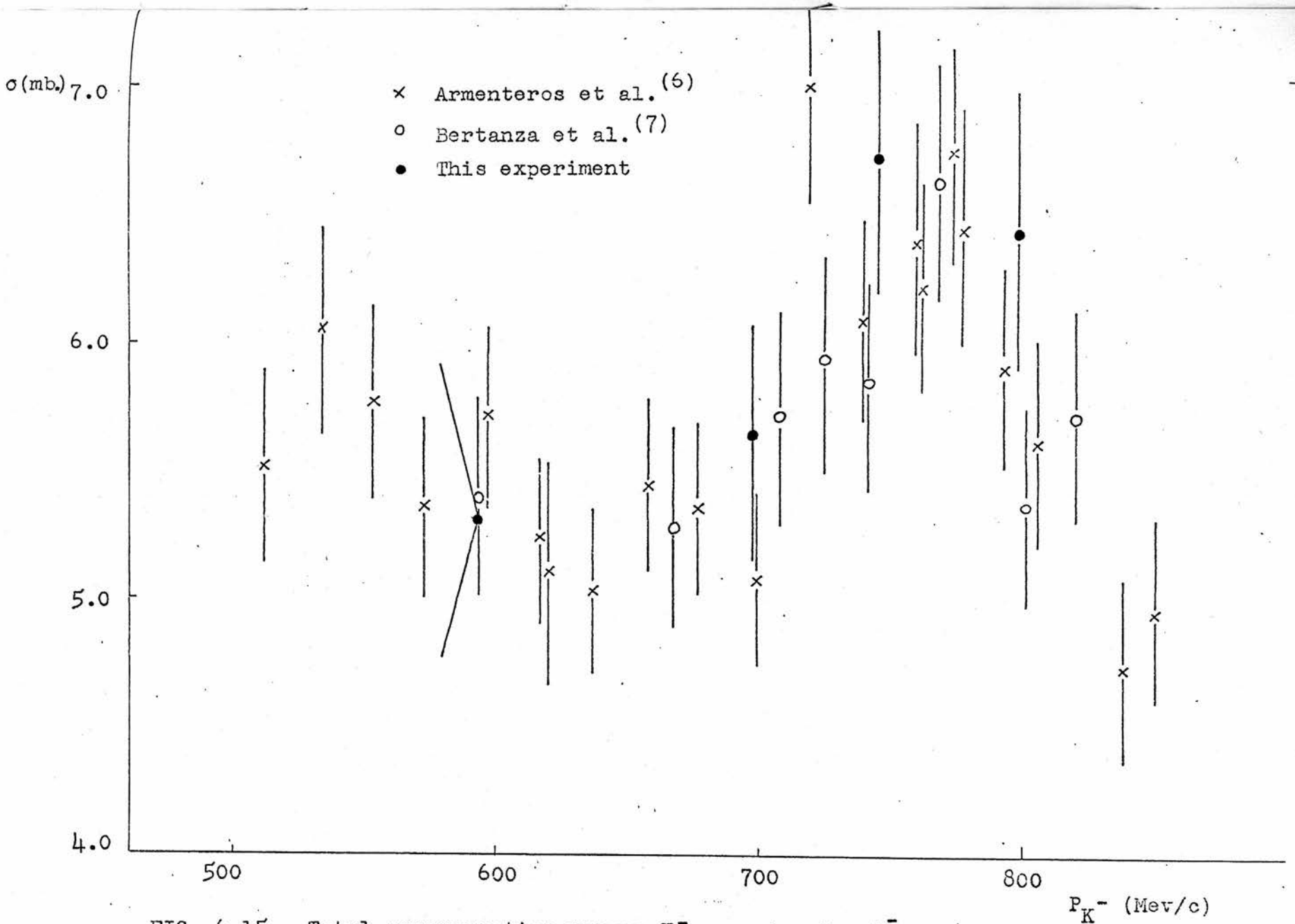

FIG. 6.15 Total cross-section versus K^- momentum for $K^- p \rightarrow \Lambda$ + neutrals for the 4 momentum bands of this experiment, compared with previous hydrogen results.

upper cut chosen at 0.16 Gev^2 - cut C - to provide reasonable statistics, although with a background of 3-body events. A check was made on the extent of the background by placing a harsher upper cut at 0.073 Gev^2 - cut B - to exclude all the 3-body contamination and, although the errors increased in this case because of the drop in statistics, the fact that the angular distributions did not change significantly was taken as evidence that the background was small. In hydrogen, neither the Σ^o nor π^o is seen, and the Σ^o direction was therefore taken as that of the Λ. The error due to this was claimed to be less than 0.2 in cosine θ^*.

The $\Sigma^o\pi^o$ differential cross-sections are shown in Figures 6.16 to 6.19 together with a third-order Legendre polynomial fit. As with the $\Lambda\pi^o$ channel, the fit was used to correct for the loss of events above cosine $\theta^* = 0.9$. This correction varied from 1°/o to 10°/o over the four energy ranges.

In Figure 6.20 the $\Sigma^o\pi^o$ Legendre 'A' coefficients of this experiment, and those of Armenteros et al. are compared in each of the four energy bands. Here again the agreement is reasonable within the errors, although in the region 1662-1685 Mev/c^2 the Armenteros values are somewhat smaller. This effect may be due to the 3-body background in the Armenteros data, implied from the total cross-section comparison.

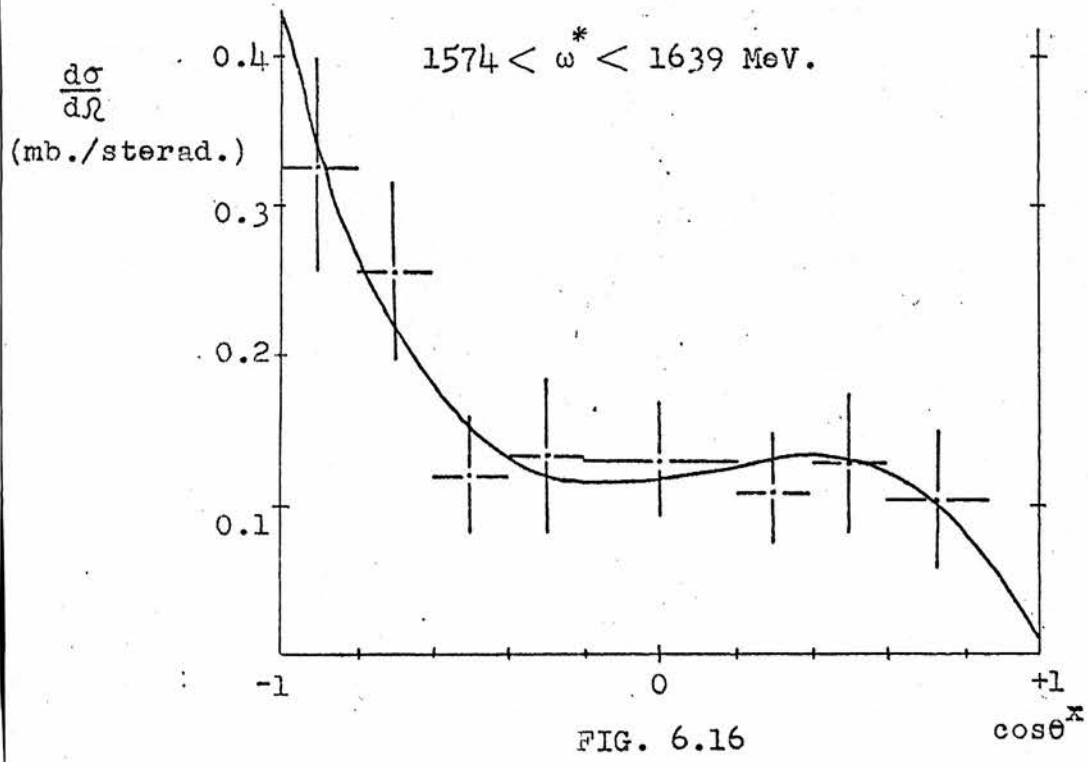

FIG. 6.16

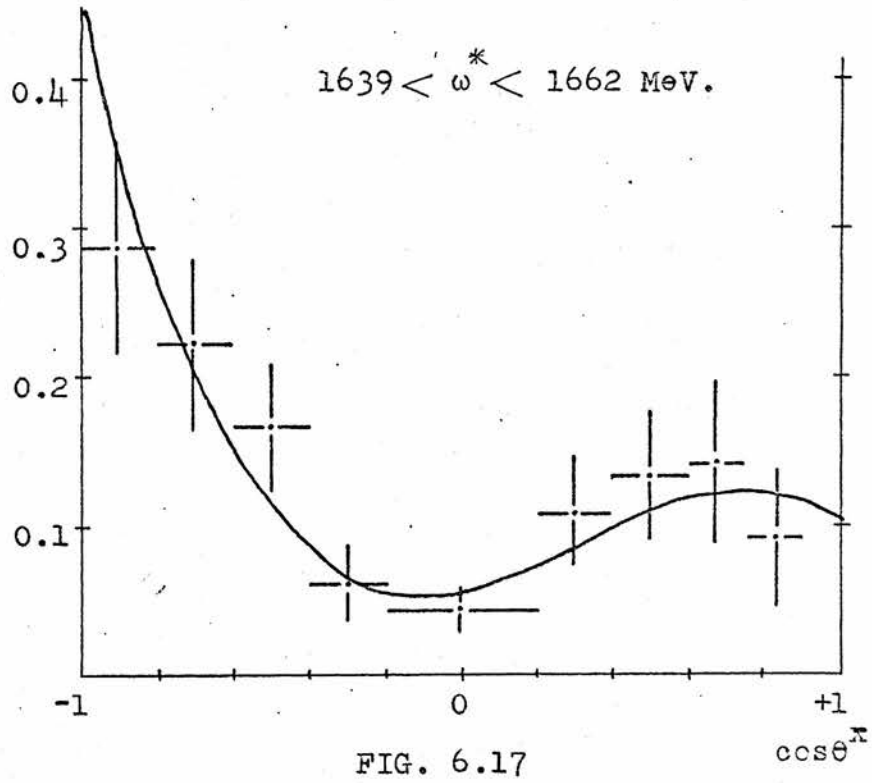

FIG. 6.17

FIGS. 6.16 to 6.19 show the differential cross-section versus $\cos\theta^*_\pi$ for the $K^- p \longrightarrow \Sigma^\circ \pi^\circ$ channel for each of the 4 momentum bands.

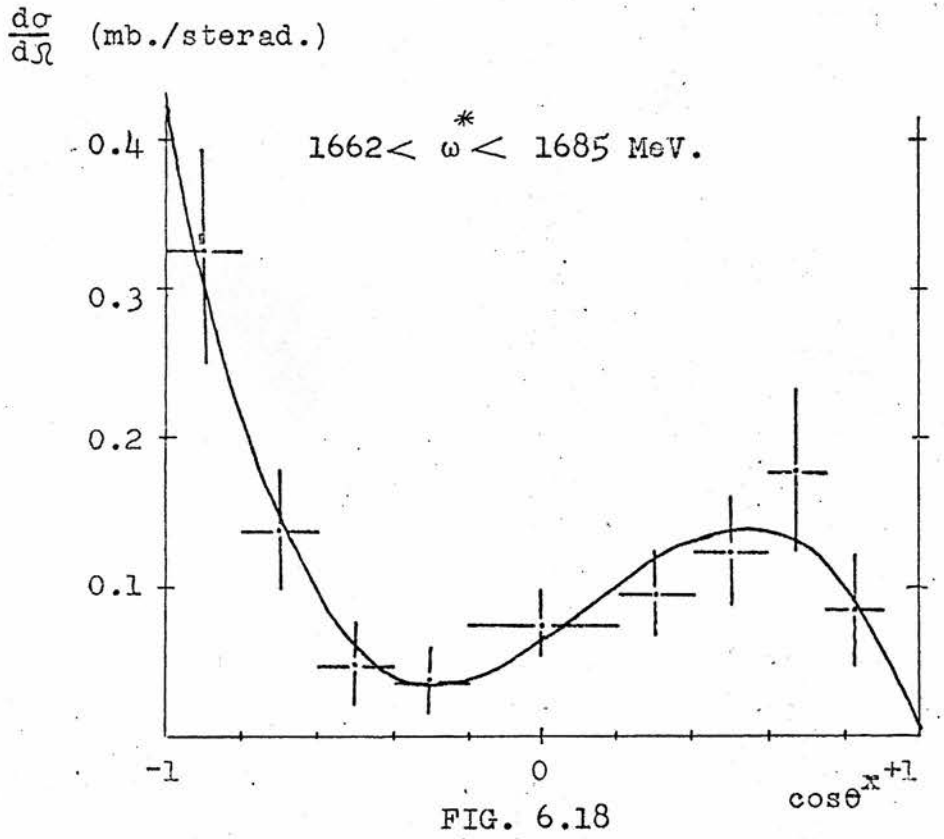

FIG. 6.18

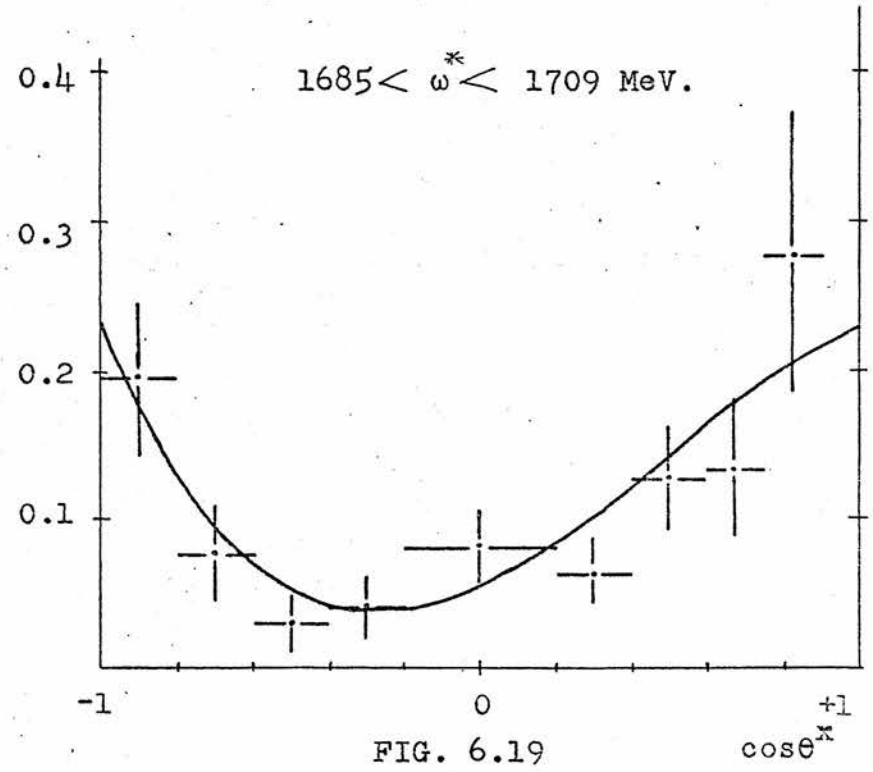

FIG. 6.19

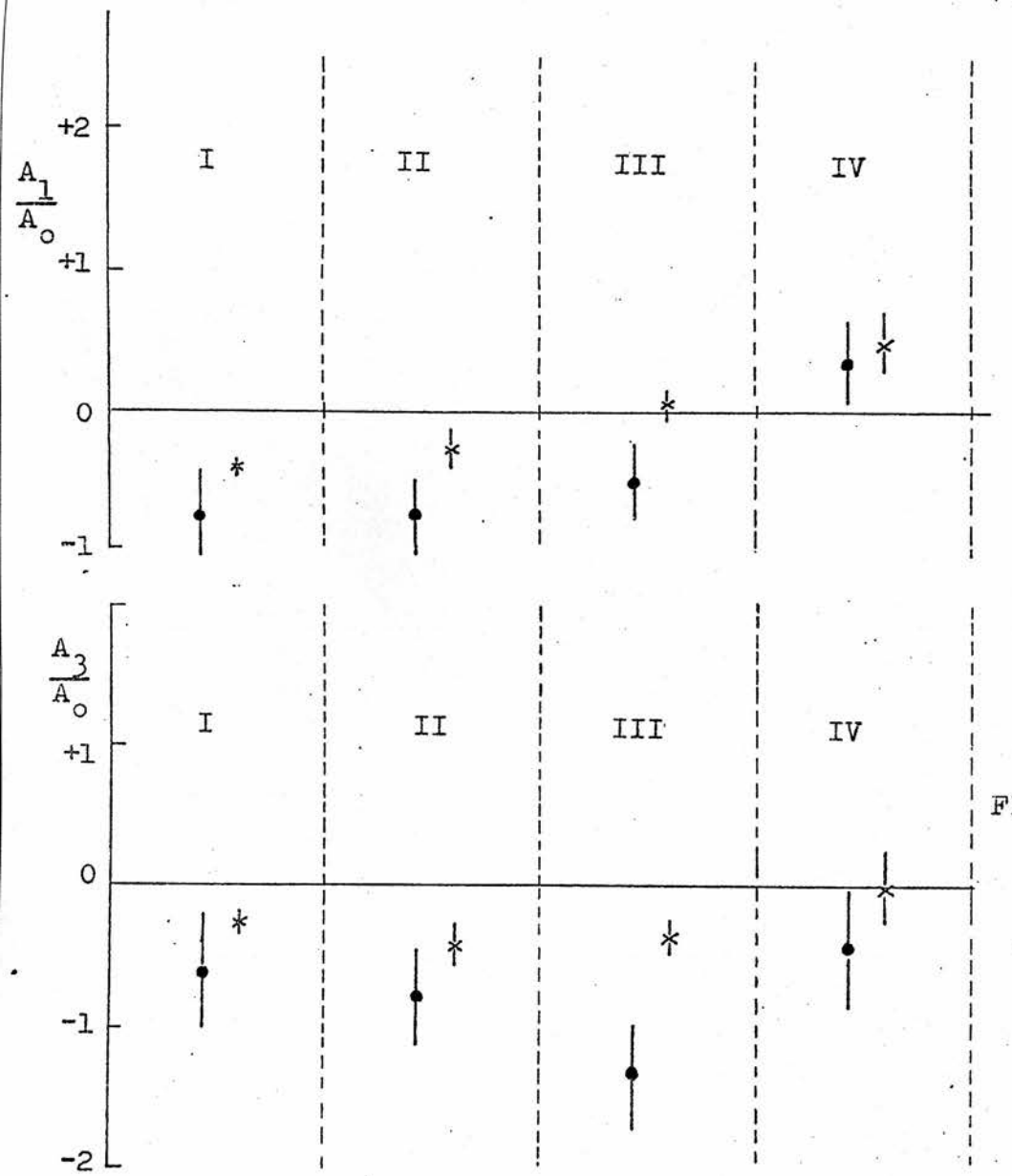

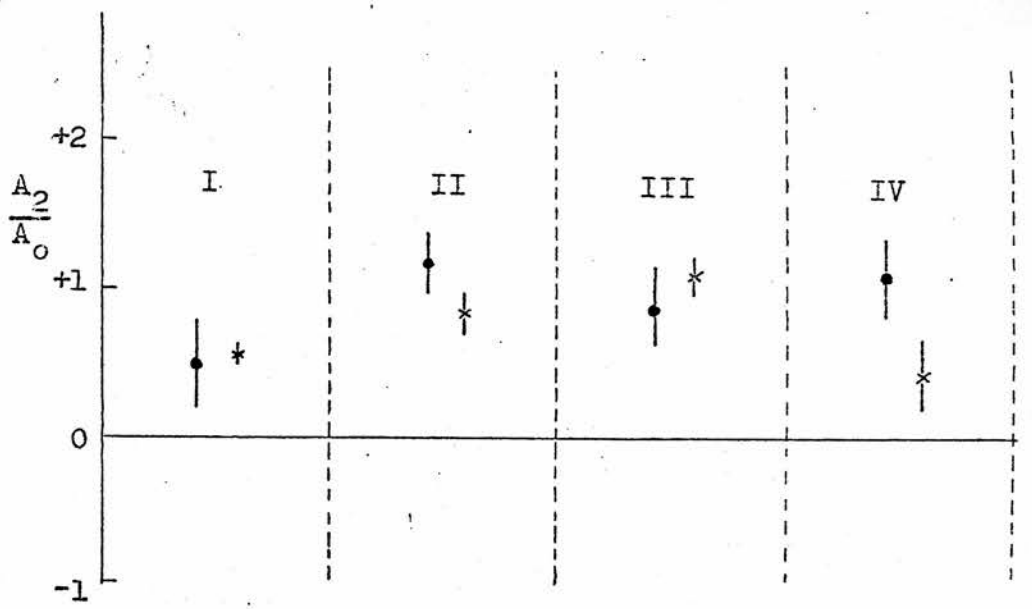

× Armenteros et al.[6]

• This experiment.

FIG. 6.20 The Legendre 'A' Coefficients from the $K^- p \longrightarrow \Sigma^o \pi^o$ differential cross-section fit in each of the 4 energy bands are compared with the values of Armenteros et al.[6].

iii) $\underline{K^- p \longrightarrow \Lambda\, \eta}$

In the $\Lambda\, \eta$ channel 50 events were fitted to the hypothesis:- $K^- p \longrightarrow \Lambda \eta$, $\eta \longrightarrow \gamma\gamma$ with an average event weight of 12.6. The fit probability distribution is shown in Figure 6.21 and peaks at low values. For this channel it was assumed that the nuclear background was the same as that calculated for the $\Lambda\, \pi^o$ channel, and hence a 7°/o subtraction was made. The wrong-fit background was estimated as less than 1°/o.

The distribution in the centre of mass energy for the $\Lambda\, \eta$ fits showed a sharp peak just above the threshold value of 1665 Mev and a rapid decrease with increasing energy, as shown in Figure 6.22. A similar peak in the $K^- p \longrightarrow \Lambda\, \eta$ cross-section had been previously noted by Bastien et al.[32] and later by Berley et al.[33], who considered several possible interpretations. Fits to $S_{1/2}$ and $P_{1/2}$ resonances, and to $S_{1/2}$ and $P_{1/2}$ scattering length models were tried and the peak finally attributed to the presence of an $S_{1/2}$ resonance, which gave the best fit. As yet, no detailed analysis of the $\Lambda\, \eta$ data has been performed in this experiment.

The cross-sections quoted in Table 6.2 pertain to the neutral decay modes of the η and were calculated from the measured value for the 2γ decay mode by assuming the ratio $\frac{\eta \longrightarrow 2\gamma}{\eta \longrightarrow \text{neutrals}}$ to have a value of 0.534 ± 0.013 [13].

The $K^- p \longrightarrow \Lambda\, \eta$ (neutrals) cross-sections of Table 6.2 are compared with the values of Armenteros et al. in Figure 6.23 and show reasonable agreement in the highest energy band, 1685-1709 Mev, but the Armenteros value is somewhat larger in the region 1662-1685 Mev.

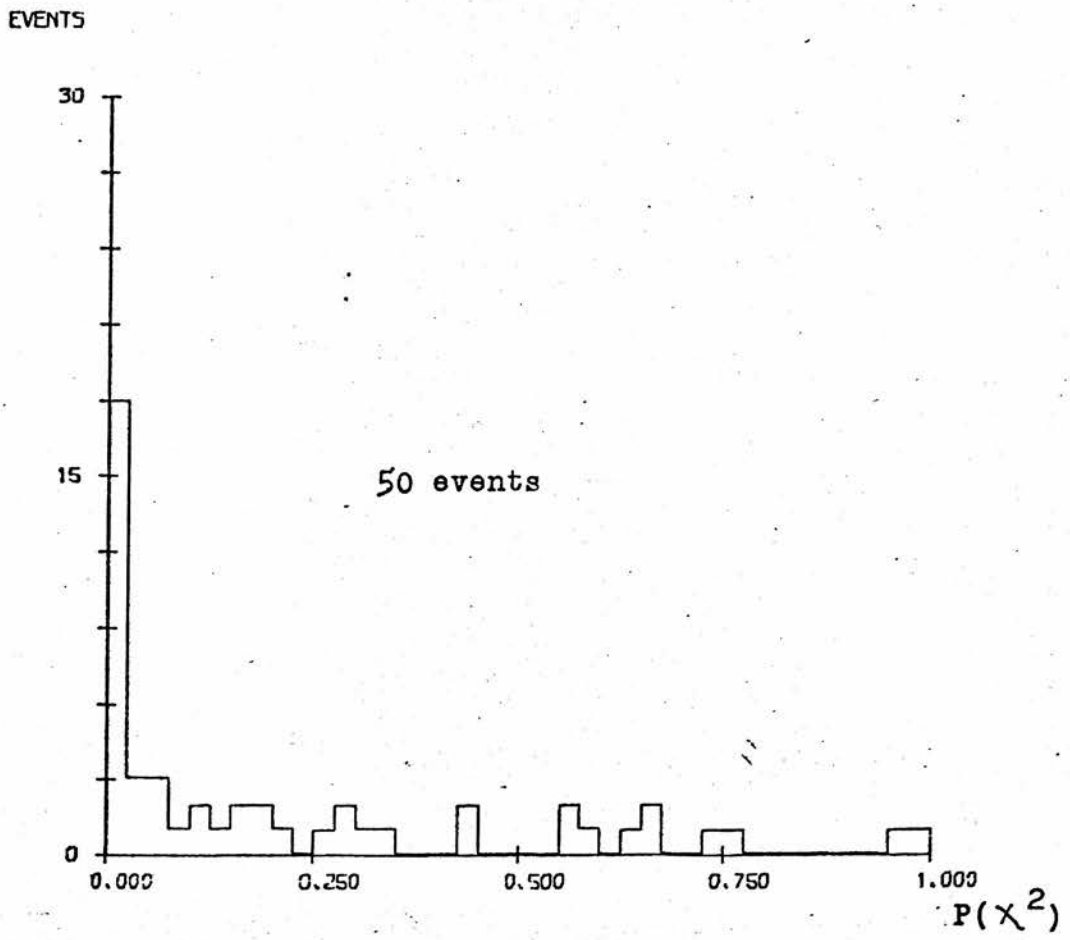

FIG. 6.21 Fit probability distribution for events fitting $K^- p \longrightarrow \Lambda \eta$.

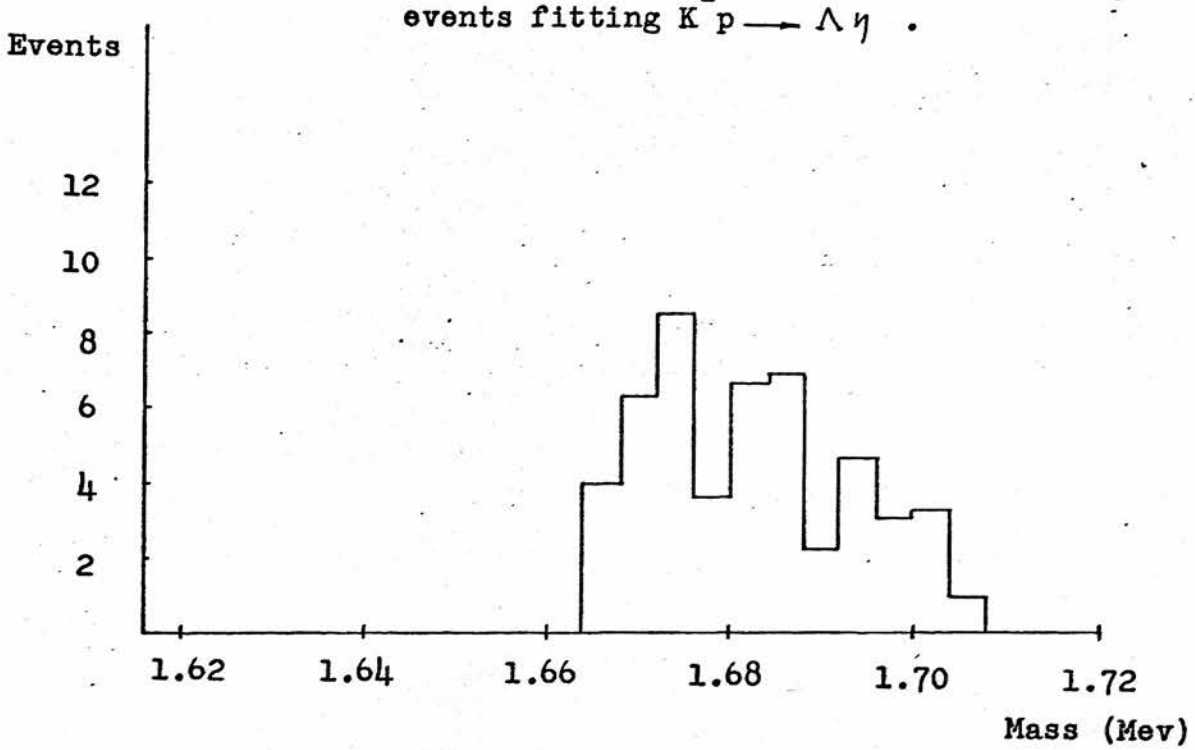

FIG. 6.22 Distribution of c.m. energy for the $\Lambda\eta$ fits.

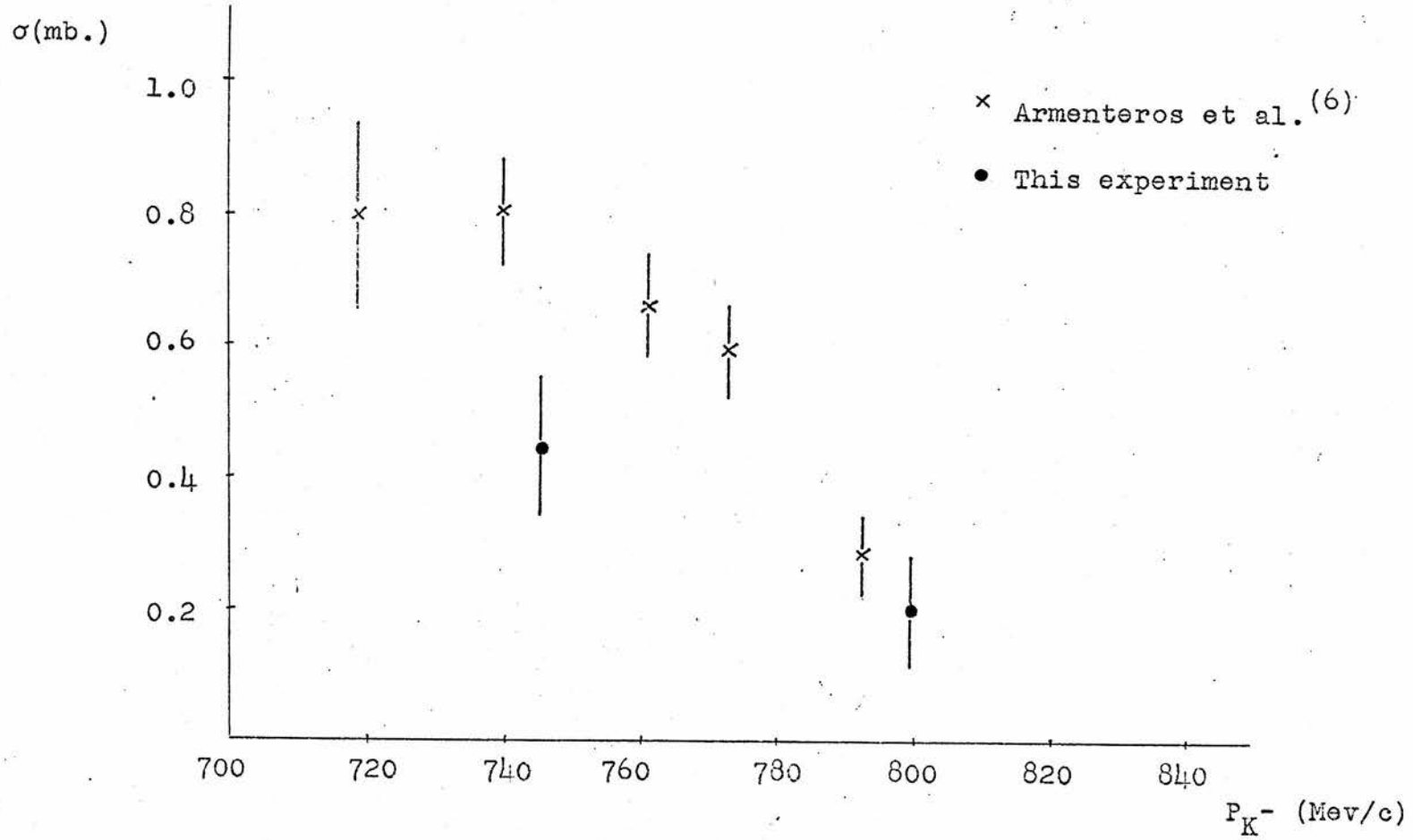

FIG. 6.23 Comparison of $K^- p \longrightarrow \Lambda \eta$ (neutrals) cross-sections with those of Armenteros et al.[6].

6.5 Analysis of the 3- and 4-Body Channels

i) $K^- p \longrightarrow \Lambda \pi^0\pi^0$, $\Sigma^0\pi^0\pi^0$

The numbers of events in the $\Lambda\pi^0\pi^0$ and $\Sigma^0\pi^0\pi^0$ channels were 170 and 29 with mean weights of 14.4 and 29.8 respectively. The fit probability distributions are shown in Figures 6.24 and 6.25. These channels have not yet been studied in detail although cross-sections have been calculated and are shown in Table 6.2. The values given have been corrected for a nominal 80°/o fit-plus-selection efficiency and a 10°/o nuclear background subtraction. No allowance has as yet been made for spurious γ, or for missing γ background. As mentioned in Section 6.2 a small correction to allow for the loss of events having a Λ of momentum less than 175 Mev was made by extrapolating the Λ and Σ momentum distributions from phase space. (For $\Lambda\pi^0\pi^0$ this correction was 1°/o and for $\Sigma^0\pi^0\pi^0$ negligible).

These cross-section values are among the first direct measurements of these reactions, and are compatible with the results of a recent experiment[34] performed at the Argonne National Laboratory in a heavy liquid mixture of 80°/o to 20°/o propane to freon using a K^- beam varying in momentum from 730-900 Mev/c. In this case the improved resolution allowed missing γ fits to be made, although the decreased γ detection efficiency (radiation length 39 cm. in a 40" chamber) reduced the numbers of fits with all γ's seen and increased the cross-section errors.

It is proposed to do a more detailed Dalitz plot analysis in the near future, to provide more accurate cross-

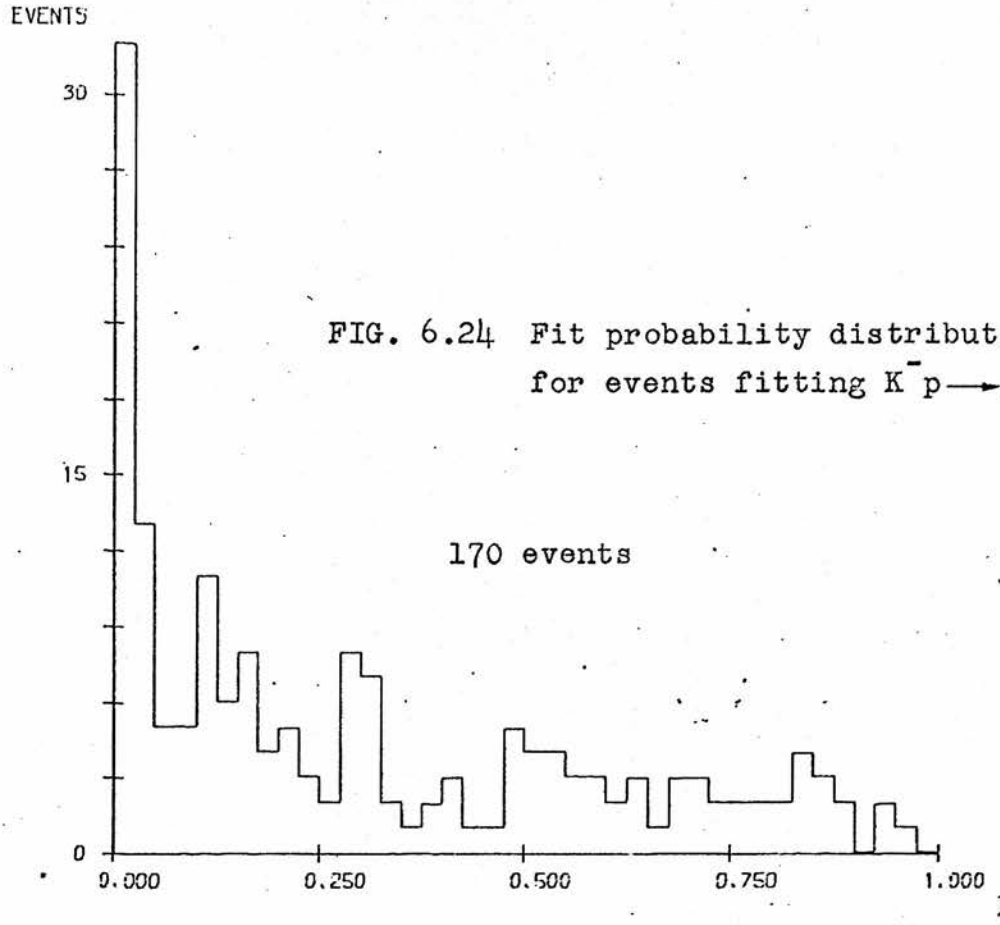

FIG. 6.24 Fit probability distribution for events fitting $K^- p \longrightarrow \Lambda \pi^o \pi^o$

170 events

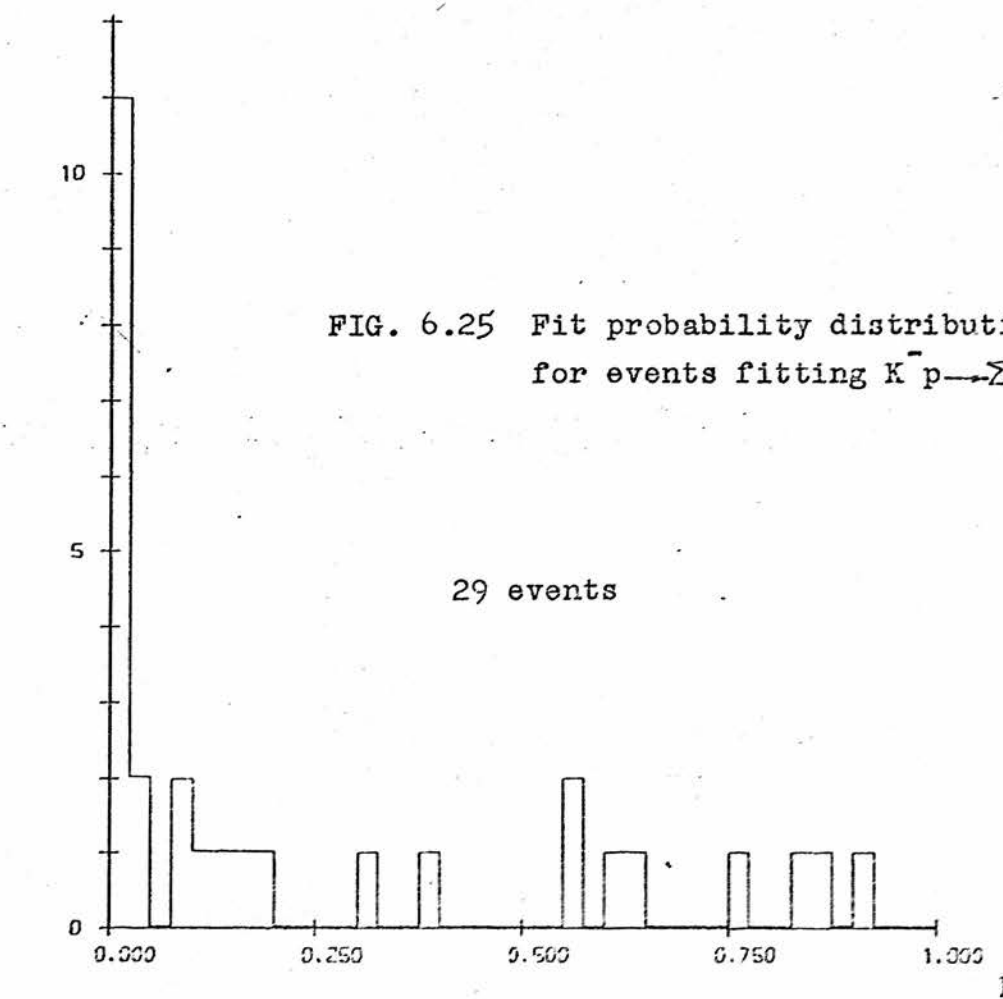

FIG. 6.25 Fit probability distribution for events fitting $K^- p \longrightarrow \Sigma^o \pi^o \pi^o$.

29 events

section values for these channels.

ii) $\underline{K^- p \longrightarrow \Lambda \pi^o \pi^o \pi^o}$

A total of 3 events was observed in this channel, with an average event weight of 55.8. The $3\pi^o$ effective mass values for these events was compatible with that of the η, implying that the events were consistent with the reaction:-

$$K^- p \longrightarrow \Lambda \eta \longrightarrow \pi^o \pi^o \pi^o$$

The branching ratio:-

$$\frac{\eta \longrightarrow 3\pi^o}{\eta \longrightarrow 2\gamma}$$

was calculated to be 0.5 ± 0.3, compatible with the value of Devons et al.[35] of 0.75 ± 0.09.

6.6 Negative Search for the Radiative Decay of the $Y_o^*(1327)$.

In a paper by Bozoki et al.[36] describing an experiment performed at Dubna, in which a beam of negative pions at 5.1 Gev/c was allowed to interact on propane, evidence was produced, in the form of an enhancement in the $\Lambda\ \gamma$ invariant mass spectrum for the existence of a $Y_o^*(1327)$ state. A later experiment by Mayeur et al.[37] at R.H.E.L., using a 2.1 Gev/c K^- beam in heavy liquid, however, failed to find any evidence for such a resonance.

A similar search for the radiative decay of the $Y_o^*(1327)$ was made in this experiment on a sample of 200 K photos, with beam momentum varying from 620 to 825 Mev/c. Events were fitted to the hypothesis:-

$$K^- p \longrightarrow \Lambda \pi^o \gamma$$
$$\qquad\qquad\quad \hookrightarrow 2\gamma$$

where all three γ's were seen and all possible γ combinations were tried. For events having more than one acceptable fit, that with the maximum probability was chosen. Figure 6.26 shows the $\Lambda\gamma$ invariant mass of the 286 fits selected, and it can be seen that apart from the Σ^o peak which is clearly seen, there is no evidence for the existence of a $\Lambda\gamma$ mass enhancement in the 1.1 - 1.5 Gev region.

It was found that the background in the 1.3 - 1.5 Gev region was due mainly to three-body events with one or more γ's missing and to $\Sigma^o\pi^o$ events with incorrect γ pairings. The expected distribution of the estimated 90 background events is shown as a solid line in Figure 6.26 and explains the high $\Lambda\gamma$ mass events. In the lower mass region, below 1.3 Gev, the background was attributed to $\Lambda\pi^o$ events with a spurious γ added.

After subtracting the above backgrounds, it was found that in a 60 Mev mass region, around 1327 Mev, 0 ± 6 events remained.

Hence it was concluded that no evidence was seen for the existence of the $Y_o^*(1327)$.

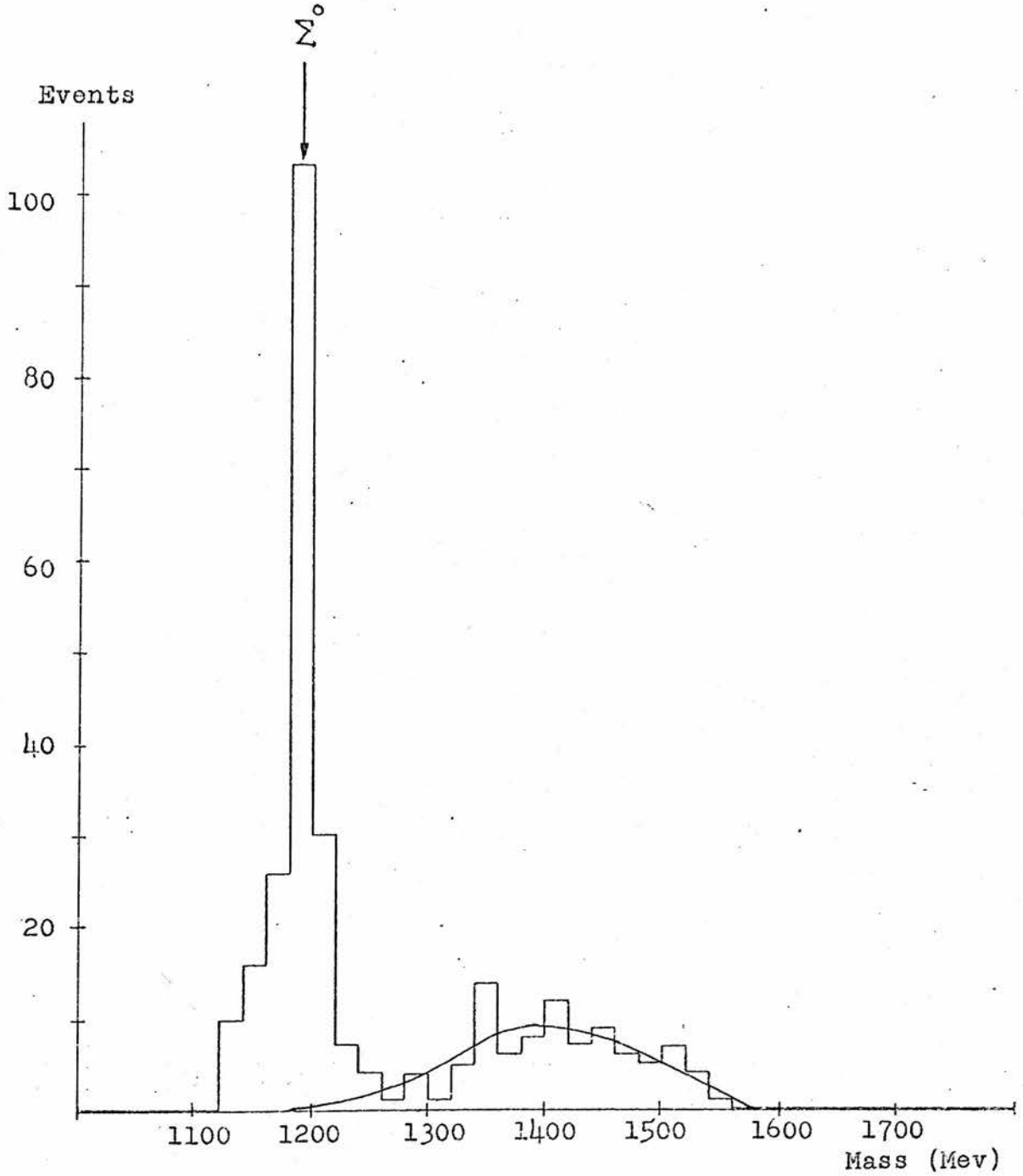

FIG. 6.26 $\Lambda\gamma$ invariant mass distribution for events fitting $K^- p \longrightarrow \Lambda \pi^0 \gamma$. The expected background is shown as a solid line.

6.7 CONCLUSION

The experiment was performed to provide information on the Y_o^* and Y_1^* resonance states in an energy region in which considerable confusion still remains. Although a Partial Wave Analysis has not yet been performed, the many checks and comparisons made with existing hydrogen data indicate that we have obtained a clean sample of events with low background upon which such an analysis can be based.

The main advantage of the heavy liquid method is that by enabling the detection of γ's, the neutral pure $I = 0$ and $I = 1$ states in K^-p interactions can be studied directly, as opposed to the indirect "missing mass" approach necessary in studies made in hydrogen. Specific problems do occur, however, because of the use of heavy liquid, such as the "wrong-fit" backgrounds arising from fits containing spurious γ's or with missing γ's, and from the contamination of events produced on bound proton targets. An extensive Monte Carlo study has shown, however, that for the two-body channels the cuts applied to remove spurious γ's, coupled with the technique of choosing the least complex fit (subject to a probability cut), have been successful in substantially reducing the spurious and missing γ fit backgrounds. A less rigorous study showed that for the three-body channels the wrong-fit background was due mainly to the increased density of spurious γ's, and was reduced by making stronger cuts to remove them.

In the case of the nuclear event background, the kinematic fitting procedure allowed the majority of bound proton events to be rejected, and it was shown that the residual background of nuclear events could be reliably estimated.

Cross-sections were calculated for each of the channels investigated, and for some of these, comparisons made with the results of previous hydrogen experiments. For the $\Lambda\,\pi^{o}$ total and differential cross-sections the agreement was good, an indication that our experimental method was correct. A similar comparison for the $\Sigma^{o}\pi^{o}$ channel, although showing general agreement with some of the previous hydrogen experiments, indicated that the data of Armenteros et al. may contain a contamination of events from the $\Lambda\pi^{o}\pi^{o}$ and $\Sigma^{o}\pi^{o}\pi^{o}$ channels.

Although the background studies for the three-body channels are not yet complete, the cross-sections are compatible with previous hydrogen values and also with the results of a recent heavy liquid experiment performed at the Argonne National Laboratory, using an 80-20^{o}/o propane-freon mixture, which provided the first direct measurement of these cross-sections, but with large errors because of poor statistics.

The success of the experiment to date indicates that the problems inherent in the heavy liquid technique can be overcome to make this method a very useful tool in the search for resonances. This is particularly so in the large bubble chambers such as "Gargamelle" and "BEBC", with their

increased γ materialisation power, or in conjunction with a "Track Sensitive Target" - a hydrogen target which allows the interaction origin to be seen, surrounded by a heavy liquid mixture to provide γ detection.

It is hoped that in addition to ultimately providing information on the resonances within the energy range covered in this experiment, by means of a single channel Partial Wave Analysis, the data will be a useful addition to that already available to enable a much better constrained multi-channel approach in this region.

ACKNOWLEDGEMENTS

I wish to thank Dr. D.J. Candlin for his help and for many interesting discussions during the course of this work. I am also indebted to Dr. G.R. Evans for his encouragement and for his overall supervision, and to Dr. A. Goshaw, Dr. H.W.K. Hopkins and Dr. W. Venus, for their help during my period at C.E.R.N.

I would like to thank the accelerator and bubble chamber staff at C.E.R.N. for enabling the experiment to be performed, and also the scanning teams at Edinburgh and at C.E.R.N., especially Mrs. A. Drummond and Mme. C. Sletten for their assistance with the scanning programs.

I would like to express my appreciation to Professor N. Feather for making available to me the facilities of the Department, and to the Science Research Council for financing the Edinburgh contribution to the experiment and for enabling me to make several journeys to C.E.R.N. I am also grateful to the Northern Ireland Education Authority for providing me with a grant during the course of my study.

Finally I would like to thank my typist, Mrs. R. Chester, for managing to decipher my script, and my wife, Alison for her help and patience during the past three years.

REFERENCES

1. V.F. Weisskopf, 'SU2 SU3 SU6', CERN 66-19, pp. 26-27. (1966) (Unpublished).
2. B.T. Feld, 'The Quark Model of Elementary Particles', CERN 67-21, pp. 16. (1967)(Unpublished).
3. M. Ferro-Luzzi, 'Review of CERN Experimental Program", CERN/D.Ph. II/Phys 71-9 (Unpublished).
4. R. Armenteros et al., 'Hyperon Resonances - 70', Duke University Conference, (Moore Publishing Co., Durham, North Carolina). Editor E.C. Fowler.
5. J.K. Kim, Phys. Rev. Lett. 27, 356 (1971).
6. R. Armenteros et al., Nucl. Phys. B21, 15 (1970).
7. L. Bertanza et al., Phys. Rev. 177, 2036 (1969).
8. P.L. Bastien and J.P. Berge, Phys. Rev. Lett. 10, 188 (1963).
9. K. Soop, CERN Report No. CERN 68-37 (1968) (Unpublished).
10. R. Bock, CERN Report DD/EXP/62/10 (Unpublished).
11. R.D. Tripp, 'Baryon Resonances', CERN 65-7 (1965) (Unpublished).
12. A. Donnachie 'Proceedings of the 1970 CERN School of Physics', CERN 71-7 (1971) (Unpublished).
13. M. Roos et al., Review of Particle Properties, Phys. Lett., 39B (1972).
14. H. Geiger and A. Werner, Zeits. f. Phys. 21, 187 (1924).
15. R.H. Hildebrand and S.E. Derenzo, Nucl. Inst. and Meth. 69, 287 (1969).
16. H.A. Bethe and W. Heitler, Proc. Roy. Soc. A146, 83 (1934).
17. O. Klein and Y. Nishina, Zeits. f. Phys. 52, 853 (1929).
18. A. Abashian et al., Phys. Rev. 104, 855 (1956).
19. K. Aslam and J.R. Rook, Nucl. Phys. B20, 397 (1970).
20. C.E. Wiegand, Phys. Rev. Lett. 22, 1235 (1969).
21. D.H. Davis et al., Nucl. Phys. B1, 434 (1967).

REFERENCES (Contd.)

22. E.H.S. Burhop, Nucl. Phys. B1, 438 (1967).

23. W.M. Bugg et al., Nucl. Phys. A124, 212 (1969).

24. B.W. Allardyce et al., Phys. Lett 41B, 577 (1972).

25. G.A. Jones, Rep. Prog. Phys. 33, 645 (1970).

26. A. Ferrer-Soria, Thesis (Unpublished).

27. B. Rossi, 'High Energy Particles' (Prentice Hall, Englewood Cliffs, New Jersey, 1956).

28. U. Fano, Ann. Rev. Nucl. Sci. 13, 1 (1963).

29. CERN Program Library, D(506) (Unpublished).

30. E. Flaminio et al., CERN/HERA 70-6 (1970) (Unpublished).

31. D.V. Bugg et al., Phys. Rev. 168, 1466 (1968).

32. P.L. Bastien et al., Phys. Rev. Lett. 8, 114 (1962).

33. D. Berley et al., Phys. Rev. Lett. 15, 641 (1965).

34. T.W. Dombeck, Thesis, Argonne National Laboratory Report ANL/HEP 7213) (Unpublished).

35. S. Devons et al., Phys. Rev. D1, 1936 (1970).

36. G. Bozoki et al., Phys. Lett. 28B, 360 (1968).

37. C. Mayeur et al., Phys. Lett. 33B, 441 (1970).